Imperial College London
Department of Materials

Electropulsing of Pearlitic Steels

Bernadette Elliott-Bowman

A dissertation submitted in partial fulfilment of the requirements for the degree of
Doctor of Philosophy at Imperial College London, August 2016

Copyright Declaration

The copyright of this thesis rests with the author and is made available under a Creative Commons Attribution Non-Commercial No Derivatives licence. Researchers are free to copy, distribute or transmit the thesis on the condition that they attribute it, that they do not use it for commercial purposes and that they do not alter, transform or build upon it. For any reuse or redistribution, researchers must make clear to others the licence terms of this work.

Statement of Originality

I, Bernadette Elliott-Bowman, hereby declare that the research contained within this thesis is my own work. All sources used or quoted have been indicated and acknowledged by means of complete referencing.

Abstract

Electropulsing is a process characterised by the application of short duration (~100μs) electrical current pulses. The process is claimed to be capable of stimulating microstructure change [1-3] in a variety of metals at low temperatures and energy levels. In this thesis, electropulsing is applied to examine its potential to produce nanostructured, strong yet ductile pearlitic steel.

Existing grain refinement methods have produced a dual-phase microstructure of equiaxed ferrite and spheroidised cementite in pearlitic steel. Li *et al.* [4] obtained an ultrafine microstructure of this nature by annealing drawn wire, whilst He *et al.* [5] achieved a similar morphology by applying heated equal channel angular pressing to carbon steel. In contrast, electropulsing may offer a method for grain refinement of bulk material with very few processing steps. Grain refinement by electropulsing has previously been reported in pearlitic steel wire by Qin *et al.* [6, 7]. A single electropulse of high current density produced fine cementite spheroidisation from the prior lamellar structure. The mechanisms for the accelerated electropulsing effect have not yet been confirmed in the literature, and theories focus on high rate heating [8, 9] and the athermal "electron wind" [10, 11] as potential driving factors.

This thesis begins with a review of grain refinement and electropulsing literature (Chapter 2), followed by experimental methods (Chapter 3). Chapter 4 describes electropulsing of 0.92wt%C pearlitic plate at room temperature. The chapter identifies the parameters required to induce microstructure change and describes the mechanisms involved. Chapter 5 presents the results of elevated temperature electropulsing tests on 0.73wt%C pearlitic rod, which combined pulsed current treatments with furnace annealing. Simultaneous furnace heating was applied to overcome the initial energy threshold, in order to highlight any microstructural athermal effects. Chapter 6 describes electropulsing treatments conducted at an external facility, where a significantly more powerful electropulse generator was available. The generator provided sufficient current to produce single high current density pulses in the 0.92wt%C pearlitic steel plate.

Chapter 7 describes the conclusions drawn based on the previous chapters. Despite the observation of electropulse-induced microstructure change, athermal effects distinguishable from Joule heating could not clearly be discerned. In addition, the resulting microstructures were not harder than the initial cold-worked pearlite condition. Experiments below a current density threshold or with applied external heating resulted in no microstructural change. It is therefore concluded that the electropulsing process does not offer any processing or mechanical property advantages for bulk pearlitic steel treatments. Furthermore, it does not offer any additional benefits when compared to processes such as flash induction annealing, which is a widely-commercialised technique.

Acknowledgements

Doctoral research is a challenging process and I am incredibly grateful for the invaluable support of friends, family and academic staff at Imperial College. It is not possible to thank everyone individually, but special mention must go to:

~ ~ ~ ~

The Defence Science and Technology Laboratory for funding this project, and Professor Peter Brown for always asking the difficult questions.

Professor Rongshan Qin of the Open University, for giving me the opportunity to undertake this research and providing insight and guidance.

Professor David Dye of Imperial College London, for taking me into his research group, and sharing invaluable knowledge and encouragement in the last year of this project.

Dr. Alex Cook at DSTL for his patience, guidance, science fiction recommendations and grammatical pedantry.

Michele Pettina of Imperial College London for his friendship and support as a fellow DSTL student.

Anna Radecka of Imperial College London, for hours of help in the preparation of atom probe samples and for facilitating experiments at the University of Oxford.

Tomas Martin, Paul Bagot and Michael Moody at the University of Oxford, for assistance with atom probe experiments.

Kang Ji of Imperial College London, for assistance with Gleeble experiments in the Department of Mechanical Engineering.

Ben Wood in the workshop, Mahmoud Ardakani and all the staff at the Harvey Flower EM Suite. Most of all, Ecaterina Ware for her invaluable help with TEM and FIB operation, her friendship and encouragement, and for keeping the coffee shop in business all these years.

Anna A. and Tansel A., for the macchiatos.

Peter E., Jen A., Giuseppe S., Vivian T., Abbi A., Wenjun L., Yongkun L., Xinfang Z., Osas O., and all of my friends at Imperial College for help and conversations (about science or not!).

My parents, for their encouragement and regular “how is your research going?” questions.

~ ~ ~ ~

And finally, to my wife Joy. For always being there, for always knowing what to say on the tough days, for proofreading and advice, and for being the best wife I could ever have asked for. Oh, and for feeding me.

Contents

Copyright Declaration i
Statement of Originality i
Abstract ii
Acknowledgements iii
Contents iv
List of Figures vi
List of Tables xiii
List of Acronyms xvi
List of Experimental Variables xvii
1. Introduction 1
1.1. Electropulsing: process and effects 1
1.2. Foundation for research 2
1.3. Electropulsing in bulk 2
1.4. Electropulsing for grain refinement and workability 2
1.5. Scaling for industry 3
1.6. Identification of mechanisms 4
1.7. Thesis composition 4
2. Literature review 6
2.1. Introduction 6
2.2. Part I – Grain refinement: processing and pearlitic steel 8
2.3. Part II – Electropulsing: mechanisms and microstructure effects 27
3. Experimental methods 49
3.1. Initial material characterisation 49
3.2. Effect of cold work on microstructure and properties 56
3.3. Preparation of samples for treatment 59
3.4. Electropulsing: equipment, parameters and operation 61
3.5. Characterisation techniques 68
4. Electropulsing at ambient temperature 77
4.1. Experimental parameters 77
4.2. Results 79
4.3. Discussion 116
4.4. Summary 123
5. Electropulsing at elevated temperature 125

5.1. Experimental parameters 125
5.2. Results 126
5.3. Discussion 157
5.4. Summary 159
6. High current density electropulsing (non-UK) 160
6.1. Experimental parameters 160
6.2. Results 161
6.3. Discussion 175
6.4. Summary 178
7. Conclusion 180
8. Further work 184
9. References 185
10. Appendix A 196
Decarburisation of a pearlitic steel sample 196
11. Appendix B 198
Convection heating of high carbon steel 198

List of Figures

Figure 1.1. Nanoscale cementite spheroidisation in highly deformed pearlitic steel. A) As-drawn; B) electropulsed [6]. 1

Figure 1.2. Schematic of a recrystallised ferrite matrix, with intergranular spheroidised cementite at triple-points and grain boundaries. 2

Figure 1.3. Schematic of the ECAP process [26]. 3

Figure 2.1. ECAP processing schematic [26]. 10

Figure 2.2. ECAP treatment of 0.8wt%C pearlitic steel [5]. Lamellar microstructure remained after the first pass, transforming to equiaxed ferrite and spheroidised cementite with subsequent passes and increasing dislocation density. 12

Figure 2.3. EBSD showing martensite fragmentation in 0.19wt%C steel as a result of ECAP [35]. 13

Figure 2.4. Schematic showing multilayer rolling. Modified from [80]. 16

Figure 2.5. ARB of 0.0024wt%C steel. AFM images of steel microstructure at three regions across the sample thickness after one to three passes (top). Variation in grain size distribution across the thickness of the sample with number of passes (bottom left). Reproduced from [99]. Additional schematic indicating the regions of subsurface, middle and centre relevant to the bonded sample. 18

Figure 2.6. Correlation of hardness with grain size in 0.0024wt%C steel subjected to three ARB passes. Reproduced from [99]. 19

Figure 2.7. Wire drawing schematic showing dies of decreasing area from A0 to A6. Modified from [103]. 20

Figure 2.8. Reduction in interlamellar spacing of 0.8wt%C pearlitic steel wire with increasing drawing strain. Plotted using data from [106], equivalent plastic strain for cold-drawing calculated using the equation shown [102]. 22

Figure 2.9. Atom probe tomography 3D reconstruction of nanoscale carbon decomposition in 0.81wt%C pearlitic steel drawn to strains of 2 and 5. Carbon atoms are yellow, while iron atoms are blue [109]. 22

Figure 2.10. Atom probe tomography 3D reconstruction showing ferrite subgrains (delineated by carbon (red) at the subgrain boundaries) and spheroidised cementite at triple points. Modified from [4]. 23

Figure 2.11. Borchers and Kirchheim's summary of the drawing strain/tensile strength relationship observed throughout the literature. Replotted from data provided in [38]. References to the original data can also be found in [38]. 24

Figure 2.12. Effect of annealing temperature on mechanical properties of 0.7wt%C drawn pearlitic steel wire. Reproduced from [41]. 25

Figure 2.13. Schematic of the dynamic electropulsing process. Reproduced from [71]. 29

Figure 2.14. SEM micrographs demonstrating spheroidisation of cementite lamellae in deformed pearlitic steel samples after a single electropulse of current density (A,D) $7.73x10^9$ $A{\cdot}m^{-2}$, (B,E) $9.82x10^9$ $A{\cdot}m^{-2}$, and (C,F) $1.07x10^{10}$ $A{\cdot}m^{-2}$ along the cross-sectional and longitudinal directions. Reproduced from [7]..... 31

Figure 2.15. Schematic illustration for grain refinement and ultrafine grained microstructure formation: (I) formation of γ-phase nuclei, (II) formation of γ-phase grains by the growth of γ-phase nuclei, (III) formation of α-phase nuclei, and (IV) formation of α-phase grains by the growth of α-phase nuclei. Reproduced from [15]. 32

Figure 2.16. SEM micrographs of electropulse-induced microstructure transformation in pearlitic steel A) before electropulse and B) after electropulse. Reproduced from Qin et al [6]. 33

Figure 2.17. SEM micrograph showing equiaxial crystal formation at a crack tip. Reproduced from [22]. 39

Figure 2.18. SEM micrographs of crack healing in 1045 steel. Modified from [60]. 40

Figure 2.19. Theoretical healing driving force as a function of current density. Varying tensile strengths represent different materials. Modified from [59]..... 41

Figure 2.20. Recrystallised grain size versus amount of prior cold work as a function of current pulsing. Reproduced from [1]. 41

Figure 2.21. Variation in hardness with increasing amplitude of applied high intensity electric pulses. Vickers hardness values were: as received sample $564HV_{10}$; EP-1 $559HV_{10}$, EP-2 $480HV_{10}$, EP-3 $339HV_{10}$. Reproduced from [7]. 43

Figure 3.1. Initial as-received microstructure of 0.92wt%C steel. A,B) SEM imaging of lamellar regions; C,D) SEM imaging of regions of spheroidised cementite; E,F) Backscatter imaging showing delineation of pearlite colonies. Cementite appears as the lighter phase in SEM images, and darker in backscatter images. 50

Figure 3.2. SEM imaging of initial as-received microstructure of 0.73wt%C steel. A,B) Drawn SA condition; C,D) Drawn FA condition; E,F) Annealed SB540 condition. 53

Figure 3.3. Theoretical relationship between undercooling below the eutectoid temperature (ΔT) and observed interlamellar spacing (S_O) in a binary Fe-C alloy. 53

Figure 3.4. Phase diagrams for A) 0.92wt%C hypereutectoid steel; and B) 0.73wt%C hypoeutectoid steel. Diagrams were generated in Thermo-Calc and redrawn using Inkscape graphic software. 55

Figure 3.5. Characteristics of 0.92wt%C steel after severe plastic deformation. A,B) SEM imaging showing rolling kinks appearing as waves in the lamellar structure; C,D) Backscatter imaging showing subgrain dislocation effects, represented by variation from light to dark regions. 58

Figure 3.6. Relationship between severity of cold rolling reduction and hardness in 0.92wt%C steel plate. 58

Figure 3.7. Schematic showing decarburisation of a rectangular sample with parameters for Equation 3.5. 61

Figure 3.8. SEM imaging of microstructure of multilayer cold-rolled 0.92wt%C steel. 61

Figure 3.9. Electropulsing equipment and circuit layout. Top: Delta Elektronika SM 35-45 D.C. power supply. Middle: Avtech AV108F-3A-B-P series pulse generator. Bottom: Electropulsing components connected with standard digital oscilloscope..... 62

Figure 3.10. Example schematic of a square electropulsing waveform with current amplitude 100A (A), pulse duration 500µs (B), pulse period 1000µs (C) and frequency 1000Hz (not shown). 63

Figure 3.11. Schematic of high temperature electropulsing test. The power supply (A), oscilloscope (B) and pulse generator (C) are shown. The pulse generator connects to a sample which is placed inside the furnace (D). The sample placement is shown in cross-section (F) with copper wires (H) connected. A sheathed probe (G) connects to a thermocouple (E) outside the furnace..... 64

Figure 3.12. Theoretical change in temperature due to a single pulse of electric current in a steel sample (density 7850 $kg \cdot m^{-3}$, specific heat 490 $J \cdot kg^{-1} \cdot K^{-1}$) with pulse duration and current density.... 67

Figure 3.13. APT equipment schematic. Reproduced from [158]. 72

Figure 3.14. A) A Weibull function is applied to fit the cumulative distribution function of the grain size data; B) The Weibull smoothing function can then be used to plot the probability density function and allow statistically meaningful analysis..... 74

Figure 3.15. Use of the circular test line method to measure the ILS of pearlitic steel. 75

Figure 4.1. Representative areas observed of the 0.92wt%C pearlitic steel electropulsed at 10^7 $A \cdot m^{-2}$. Secondary electron imaging on samples etched in 2% nital solution (methanol balance). No effect is observed as a result of electropulsing treatment at high (A) or moderate (B) magnification. 79

Figure 4.2. 0.92wt%C pearlitic steel electropulsed at 10^8 $A \cdot m^{-2}$, f = 20Hz. Treatment parameters: d = 160µs, t = 1 minute (A,B); d = 160µs, t = 15 minutes (C,D). Secondary electron imaging on samples etched in 2% nital solution (methanol balance). 81

Figure 4.3. 0.92wt%C pearlitic steel electropulsed at 10^8 $A \cdot m^{-2}$, f = 50Hz. Treatment parameters: d = 80µs, t = 1 minute (A,B); d = 80µs, t = 15 minutes (C,D); d = 160µs, t = 1 and 15 minutes (representative of martensitic microstructure) (E,F); d = 160µs, t = 15 minutes (G,H). Secondary electron imaging on samples etched in 2% nital solution (methanol balance). 83

Figure 4.4. Backscatter electron imaging of recrystallised α-ferrite microstructure in sample 8-50-80-15-4. Ferrite grains are visible as equiaxed structures of varying shade (an example of which is labelled as 'A'). Globular grains appearing to overlay the ferrite are unresolved spheroidised cementite (indicated by an arrow). 84

Figure 4.5. 0.92wt%C pearlitic steel electropulsed at 10^8 $A \cdot m^{-2}$, f = 100Hz. Treatment parameters: d = 80µs, t = 2 seconds (A-B,C-D); d = 80µs, t = 5 seconds (E-F,G-H). Note that samples used in the 2 second condition were pre-processed as described in Methods Section 3, part ii. Secondary electron imaging on samples etched in 2% nital solution (methanol balance). 86

Figure 4.6. The Dubé morphological classification system [173, 174] as modified by Aaronson [172]. Reproduced from [175]..... 87

Figure 4.7. 0.92wt%C pearlitic steel electropulsed at 10^8 $A \cdot m^{-2}$, f = 100Hz. Treatment parameters: d = 80µs, t = 1 minute (A-B,C-D); d = 80µs, t = 15 minutes (E-F,G-H). Secondary electron imaging on samples etched in 2% nital solution (methanol balance). 89

Figure 4.8. Furnace annealed 0.92wt%C pearlitic steel samples. A) 600°C; B) 650°C; C) 700°C. All samples annealed for 15 minutes and air cooled. Secondary electron imaging on samples etched in 2% nital solution (methanol balance). 91

Figure 4.9. Aspect ratio characteristics of recrystallised microstructure obtained by electropulsing treatment at $4.2x10^8$ $A{\cdot}m^{-2}$ or furnace annealing. Electropulse-induced recrystallisation is compared with annealing treatments at 600°C, 650°C and 700°C. 91

Figure 4.10. Area (left) and major axis length (right) characteristics of recrystallised microstructure obtained by electropulsing treatment at $4.2x10^8$ $A{\cdot}m^{-2}$ or furnace annealing. Electropulse-induced recrystallisation is compared with annealing treatments at 600°C, 650°C and 700°C. 92

Figure 4.11. 0.92wt%C pearlitic steel electropulsed at 10^9 $A{\cdot}m^{-2}$, f = 20Hz, d = 80µs. Representative of treatments at 1 and 15 minutes. Secondary electron imaging on samples etched in 2% nital solution (methanol balance). 95

Figure 4.12. 0.92wt%C pearlitic steel electropulsed at 10^9 $A{\cdot}m^{-2}$, f = 50Hz, d = 80µs, t = 2 seconds. Various microstructures were observed after treatment at these parameters. Secondary electron imaging on samples etched in 2% nital solution (methanol balance). 96

Figure 4.13. 0.92wt%C pearlitic steel electropulsed at 10^9 $A{\cdot}m^{-2}$, f = 50Hz, d = 80µs, t = 5 seconds. Secondary electron imaging on samples etched in 2% nital solution (methanol balance). 97

Figure 4.14. 0.92wt%C pearlitic steel electropulsed at 10^9 $A{\cdot}m^{-2}$, f = 100Hz. Treatment parameters: d = 80µs, t = 2 seconds (A-B,C-D); d = 80µs, t = 5 seconds (E-F,G-H). Secondary electron imaging on samples etched in 2% nital solution (methanol balance). 99

Figure 4.15. A) Temperature-composition relationships for carbon steel [142] (Fig 5.48b, originally [172]). 100

Figure 4.16. Mechanical and electrical properties of samples electropulsed at 10^7 $A{\cdot}m^{-2}$. Microhardness (A-D) tested at 1kg (HV_1). Resistivity values shown (E) represent samples tested over a range of parameters. 103

Figure 4.17. Mechanical and electrical properties of samples electropulsed at 10^8 $A{\cdot}m^{-2}$. Microhardness (A-E) tested at 1 or 2kg (HV_1, HV_2) dependent on sample thickness. Resistivity values shown (F) represent samples tested over a range of parameters. 104

Figure 4.18. Hardness of martensitic microstructure by steel carbon content. Adapted from [177], originally [178]. 106

Figure 4.19. Microhardness of 0.69wt%C plain carbon steel isothermally transformed to a dual phase microstructure of bainite and pearlite. Reproduced from [171], originally [179]. 107

Figure 4.20. Mechanical and electrical properties of samples electropulsed at 10^9 $A{\cdot}m^{-2}$. Microhardness (A-F) tested at 0.5 or 1kg ($HV_{0.5}$, HV_1) dependent on sample thickness. Resistivity values shown (F) represent samples tested over a range of parameters. 113

Figure 4.21. Summary of observed electropulse-induced microstructure effects. ΔT is the Joule heating effect for a single pulse calculated for each sample plotted. The applied pulse time is the actual time that the applied electric current was “on” for each sample. Note that six results with high electropulse-induced heating effects (described in Chapter 6) are also included. 117

Figure 4.22. Transformation regions of electropulse-induced microstructure effects. 118

Figure 4.23. Subcritical annealing regions overlaid on the Fe-C phase diagram. Modified from [42], originally [187]. 120

Figure 4.24. Schematic showing transformation of proeutectoid cementite microstructure. 120

Figure 4.25. Electron configuration of iron and carbon. 121

Figure 5.1. Schematic showing experimental configuration inside the furnace. 125

Figure 5.2. High resolution SEM microscopy of furnace annealed 0.73wt%C pearlitic steel (still air cooled condition) with or without simultaneous electropulsing treatment. A,C) annealing only, 660°C; B,D) annealing and electropulsing, 660°C; E,G) annealing only, 680°C; F,H) annealing and electropulsing, 680°C. 127

Figure 5.3. High resolution SEM microscopy of furnace annealed 0.73wt%C pearlitic steel (still air cooled condition) with or without simultaneous electropulsing treatment. A,C) annealing only, 700°C; B,D) annealing and electropulsing, 700°C; E,G) annealing only, 720°C; F,H) annealing and electropulsing, 720°C. 128

Figure 5.4. High resolution SEM microscopy of furnace annealed 0.73wt%C pearlitic steel (still air cooled condition) with or without simultaneous electropulsing treatment. A,C) annealing only, 740°C; B,D) annealing and electropulsing, 740°C. 129

Figure 5.5. Interlamellar spacing of 0.73wt%C pearlitic steel with SA, FA and SB540 initial microstructure, after austenitisation and eutectoid transformation. Comparison is made after furnace annealing, or furnace annealing with simultaneous electropulsing treatment. 130

Figure 5.6. Ferrite grain area comparison (still air cooled condition) for temperatures 660 – 720°C. 132

Figure 5.7. Ferrite grain major axis length comparison (still air cooled condition) for temperatures 660 – 720°C. 133

Figure 5.8. Ferrite grain aspect ratio comparison (still air cooled condition) for temperatures 660 – 720°C. 134

Figure 5.9. Spheroidised cementite major axis length comparison (still air cooled condition) for temperatures 660 – 720°C. 136

Figure 5.10. Spheroidised cementite aspect ratio comparison (still air cooled condition) for temperatures 660 – 720°C. 137

Figure 5.11. SEM microscopy of furnace annealed 0.73wt%C pearlitic steel (forced air cooled condition) with or without simultaneous electropulsing treatment. A) annealing only, 660°C; B) annealing and electropulsing, 660°C; C) annealing only, 700°C; D) annealing and electropulsing, 700°C; E) annealing only, 740°C; F) annealing and electropulsing, 740°C. 139

Figure 5.12. Ferrite grain area comparison (forced air cooled condition) for temperatures 660 and 700°C. 140

Figure 5.13. Ferrite grain major axis length comparison (forced air cooled condition) for temperatures 660 and 700°C. 141

Figure 5.14. Ferrite grain aspect ratio comparison (forced air cooled condition) for temperatures 660 and 700°C. 142

Figure 5.15. Spheroidised cementite major axis length comparison (forced air cooled condition) for temperatures 660 – 700°C. 143

Figure 5.16. Spheroidised cementite aspect ratio comparison (forced air cooled condition) for temperatures 660 – 700°C. 144

Figure 5.17. SEM microscopy of furnace annealed 0.73wt%C pearlitic steel (salt bath condition) with or without simultaneous electropulsing treatment. A) annealing only, 660°C; B) annealing and electropulsing, 660°C; C) annealing only, 700°C; D) annealing and electropulsing, 700°C; E) annealing only, 740°C; F) annealing and electropulsing, 740°C. 146

Figure 5.18. Ferrite grain area comparison (salt bath condition) for temperatures 660 and 700°C. . 149

Figure 5.19. Ferrite grain major axis length comparison (salt bath condition) for temperatures 660 and 700°C. 150

Figure 5.20. Ferrite grain aspect ratio comparison (salt bath condition) for temperatures 660 and 700°C. 151

Figure 5.21. Spheroidised cementite major axis length and aspect ratio comparison (salt bath condition) for temperature 700°C. 153

Figure 5.22. Comparison of microhardness characteristics of samples furnace treated and simultaneously electropulsed, and furnace treated only. A) SA samples; B) FA samples; C) SB540 samples. Note that hardness data is not provided for the electropulsed FA condition at 720°C due to a sample problem. 155

Figure 6.1. Schematic showing full and partial spheroidisation in cementite lamellae. 162

Figure 6.2. 0.92wt%C pearlitic steel treated with a single electropulse at 4.7×10^9 A·m^{-2}. A,B) control sample, as-received cold-rolled; C,D) spheroidised cementite in electropulsed sample; E,F) recrystallised α-ferrite in electropulsed sample. Secondary electron imaging on samples etched in 2% nital solution (methanol balance). 163

Figure 6.3. 0.92wt%C pearlitic steel treated with a single electropulse at 5.1×10^9 A·m^{-2}, producing a fully martensitic microstructure. Secondary electron imaging on samples etched in 2% nital solution (methanol balance). 163

Figure 6.4. Transmission Electron Microscopy of 0.92wt%C pearlitic steel. A) as-received, cold-rolled lamellar microstructure; B) recrystallised α-ferrite in sample electropulsed at 4.7×10^9 A·m^{-2}. Inset: associated Selected Area Diffraction patterns. 165

Figure 6.5. Atom Probe Tomography (APT) of 0.92wt%C pearlitic steel electropulsed at 4.7×10^9 A·m^{-2}. A) SEM imaging of APT needle after preparation in a Helios NanoLab 600. B-C) APT reconstruction of element distribution in needle (A). B) all elements; C) carbon; vanadium; iron; manganese; phosphorus; sulphur. 168

Figure 6.6. Proxigrams showing composition change at the interface between spheroidised cementite and the bulk matrix in 0.92wt%C steel after electropulsing at $4.7x10^9$ $A{\cdot}m^{-2}$. The plots are shown in combination with the carbon distribution as shown in Figure 6.5 C, and the interfaces are highlighted. 169

Figure 6.7. Gleeble 3800 experimental setup (top). The steel sample is held between two clamps, through which resistive heating is applied (bottom). 172

Figure 6.8. 0.92wt%C pearlitic steel heat treated in a Gleeble 3800 (Dynamic Systems Inc.) resistive heating unit to a peak temperature of 634°C. A,B) Backscatter electron imaging of post-treatment lamellar microstructure; C) Heating profile showing temperature time relationship. Inset: detail of peak temperature region; D) backscatter imaging of a control cold-rolled sample. 173

Figure 6.9. Backscatter electron imaging of sample GL 5 showing lamellar and equiaxed regions. Equiaxed grains are circled. 174

Figure 6.10. Transmission Electron Microscopy of recrystallised grains in 0.92wt%C pearlitic steel sample GL5, subjected to resistive heating in a Gleeble 3800. Inset: associated Selected Area Diffraction patterns..... 175

List of Tables

Table 2.1. Tensile properties of annealed and electropulsed samples, as reported by Zhou et al. (2004), pp.1950 Table 1. 44

Table 3.1. Composition of experimental materials. 49

Table 3.2. 0.92wt%C plate characterisation. 50

Table 3.3. 0.73wt%C wire sample designations. 51

Table 3.4. Initial furnace treatment parameters for 0.73wt%C rod (as supplied by Tata Steel). 51

Table 3.5. 0.73wt%C wire characterisation. 52

Table 3.6. Summary of key transformation temperatures for experimental steels based on ThermoCalc phase diagram simulations (Figure 3.4). T_{SOL} is the solidus temperature, while T_{LIQ} is the liquidus. 55

Table 3.7. Explanation of sample designations for ambient temperature electropulsing experiments. 65

Table 3.8. Explanation of sample designations for elevated temperature electropulsing experiments. 65

Table 3.9. Grinding and polishing regime. 69

Table 3.10. APT experimental parameters. 72

Table 4.1. Electropulsing parameters for ambient temperature tests at J ~ 10^7 A·m^{-2}. 77

Table 4.2. Electropulsing parameters for ambient temperature tests at J ~ 10^8 A·m^{-2}. 78

Table 4.3. Electropulsing parameters for ambient temperature tests at J ~ 10^9 A·m^{-2}. 79

Table 4.4. Breakdown of electropulsing parameters at moderate current density (10^8 A·m^{-2}) and frequency 50Hz (note Area Reduction is abbreviated to AR). 82

Table 4.5. Geometries of samples treated at current density of the order 10^8A·m^{-2}, frequency 50Hz, pulse duration 160µs and test duration 15 minutes. 84

Table 4.6. Breakdown of electropulsing parameters at moderate current density (10^8 A·m^{-2}) and frequency 100Hz (note Area Reduction is abbreviated to AR). 85

Table 4.7. Geometries and applied current parameters of samples treated at current density of the order 10^8A·m^{-2}, frequency 100Hz, pulse duration 80µs and test duration 2 seconds. I_{IN} is the applied current, I_{OUT} is the output current. 88

Table 4.8. Recrystallised α-ferrite grain data. 91

Table 4.9. Breakdown of electropulsing parameters at high current density (10^9 A·m^{-2}) and frequency 20Hz. 94

Table 4.10. Breakdown of electropulsing parameters at high current density (10^9 A·m^{-2}) and frequency 50Hz. 97

Table 4.11. Breakdown of electropulsing parameters at high current density (10^9 A·m^{-2}) and frequency 100Hz. 98

Table 4.12. Microhardness data for samples tested at current density of the order 10^8 A·m^{-2}, frequency 100Hz and pulse duration 80µs for a test duration of 2 seconds. Note that samples in this condition were pre-processed as described in Methods Section 3, pp.58. 107

Table 4.13. Resistivity variation in samples electropulsed at current density of the order 10^8 A·m^{-2}. 110

Table 4.14. Breakdown of hardness data with microstructure for 0.92wt%C steel electropulsed at current density of the order 10^9 A·m^{-2}, pulse frequency 50Hz and pulse duration 80µs. 114

Table 4.15. Breakdown of hardness data in relationship to microstructure for 0.92wt%C steel electropulsed at current density of the order 10^9 A·m^{-2}, pulse frequency 100Hz and pulse duration 80µs. 114

Table 4.16. Resistivity variation in samples electropulsed at current density of the order 10^9 A·m^{-2} and found to contain proeutectoid cementite. 115

Table 4.17. Theoretical heating effects by phase resulting from a single electropulse of current density 10^9 A·m^{-2} and pulse duration 80µs. 121

Table 5.1. Electropulsing parameters for elevated temperature tests at J ~ 10^7 A·m^{-2} 126

Table 5.2. Summary of equiaxed ferrite geometry descriptors (assessed for approximately 75% of measured grains in samples with initial still air cooled microstructure). 131

Table 5.3. Summary of spheroidised cementite geometry descriptors (assessed for approximately 75% of measured grains). 137

Table 5.4. Summary of equiaxed ferrite geometry descriptors (assessed for approximately 75% of measured grains in samples with initial forced air cooled microstructure). 141

Table 5.5. Summary of spheroidised cementite geometry descriptors (assessed for approximately 75% of measured grains). 143

Table 5.6. Volume fraction analysis of 0.73wt%C SB540 samples annealed at 740°C with and without simultaneous electropulsing treatment. 147

Table 5.7. Interlamellar spacing of 0.73wt%C SB540 samples annealed at 720 and 740°C with and without simultaneous electropulsing treatment. 147

Table 5.8. Summary of equiaxed ferrite geometry descriptors (assessed for approximately 75% of measured grains in samples with initial salt bath transformed microstructure). 150

Table 5.9. Summary of spheroidised cementite geometry descriptors in samples with very fine microstructures resulting from initial salt bath treatment. 152

Table 6.1. Geometries of samples treated with a single electropulse at current density of the order $10^9 A \cdot m^{-2}$ 160

Table 6.2. Electropulsing parameters for single pulse tests at current density J of the order 10^9 $A \cdot m^{-2}$. 161

Table 6.3. Estimated Joule heating effect in single pulse tests at current density J of the order 10^9 $A \cdot m^{-2}$. 161

Table 6.4. Volume fraction analysis of sample 9-1-150-S-1 treated with a single electropulse of current density 4.7×10^9 $A \cdot m^{-2}$. 162

Table 6.5. Vickers hardness characteristics of 0.92wt%C pearlitic steel samples treated with a single high current density electropulse with current density J of the order 10^9 $A \cdot m^{-2}$. 167

Table 6.6. Gleeble sample treatment parameters. The heating rate to T_{PEAK} (dT_{PEAK}/dt) and cooling rate from T_{PEAK} to T_{COOL} (dT_{COOL}/dt) are shown. 171

Table 6.7. Electropulsing and Gleeble parameter comparison 172

List of Acronyms

APT – atom probe tomography

AR – as-received

ARB – accumulative roll-bonding

BS / BSE – backscattered electron

CLS – coarse lamella with shear band

CR – cold-rolled

ECAP / ECAE – equal channel angular pressing or extrusion

EP - electropulsed

FA – forced air

FL – fine lamella

FIB – focused ion beam

GBI – grain boundary idiomorphs

GL - Gleeble

IBL – irregularly bent lamella

IF – interstitial-free

IHP – inverse Hall-Petch

ILS – interlamellar spacing

SA – still air

SAD – selected area diffraction

SPD – severe plastic deformation

SB540 – salt bath at 540°C

SEM – scanning electron microscopy

TEM – transmission electron microscopy

UFG – ultrafine-grain

UTS – ultimate tensile strength

List of Experimental Variables

A_o – original cross-sectional area (m^2)

A_f – final cross-sectional area (m^2)

%AR – percent area reduction

C_p – specific heat capacity ($J \cdot kg^{-1} \cdot K^{-1}$)

d – pulse duration (μs)

D – sample depth (mm)

d_c – test circle diameter (nm)

δ – density ($kg \cdot m^{-3}$)

dT_{PEAK}/dt – heating rate ($°C \cdot s^{-1}$)

dT_{COOL}/dt – cooling rate ($°C \cdot s^{-1}$)

f – pulse frequency (Hz)

HV – Vickers hardness (HV)

i – (sample designations)

I – current (A)

I_{IN} – input current (A)

I_{OUT} – output current (A)

J – current density ($A \cdot m^{-2}$)

L – sample length (mm)

$\bar{\lambda}_t$ – mean true interlamellar spacing (nm)

n – number (tests or grains)

N – number of pulses

n_c – number of lamellae intercepted by d_c

R – resistance (Ω)

ρ – bulk resistivity (Ω·m)

ρ_α – resistivity of α-phase (Ω·m)

ρ_β – resistivity of β-phase (Ω·m)

$\bar{\sigma}_d$ – mean spacing in the direction perpendicular to the lamellae (nm)

t – test duration (s or min)

T_p – pulse period (s)

T_T – target furnace temperature (°C)

T_A – actual furnace temperature (°C)

T_{PEAK} – peak Gleeble temperature (°C)

T_{COOL} – Gleeble temperature at end of measurements (°C)

ΔT – change in temperature due to resistive heating (°C or K)

V – voltage (V)

V_α – volume fraction of α-phase (wt%)

V_β – volume fraction of β-phase (wt%)

W – sample width (mm)

1. Introduction

1.1. Electropulsing: process and effects

There have been reports in the literature for many years suggesting that the application of high current density electric pulses, termed electropulsing, can have dramatic effects on the microstructure and properties of metallic materials. Both electrical and environmental factors can alter the effects of electropulsing treatment, but as discussed in the literature review (Chapter 2) current density, pulse frequency and pulse duration are particularly important parameters. These variables relate specifically to the characteristics of the pulsed current, and determine the strength and heating effects of the treatment. Throughout the literature current densities of the order of 10^7 to 10^9 $A{\cdot}m^{-2}$ [2, 7, 12], pulse durations typically ranging between 20 and 500µs [13-15] and frequencies from 1Hz to the order of hundreds [10, 13, 16] have been applied to various metals and alloys and were found to induce a range of effects.

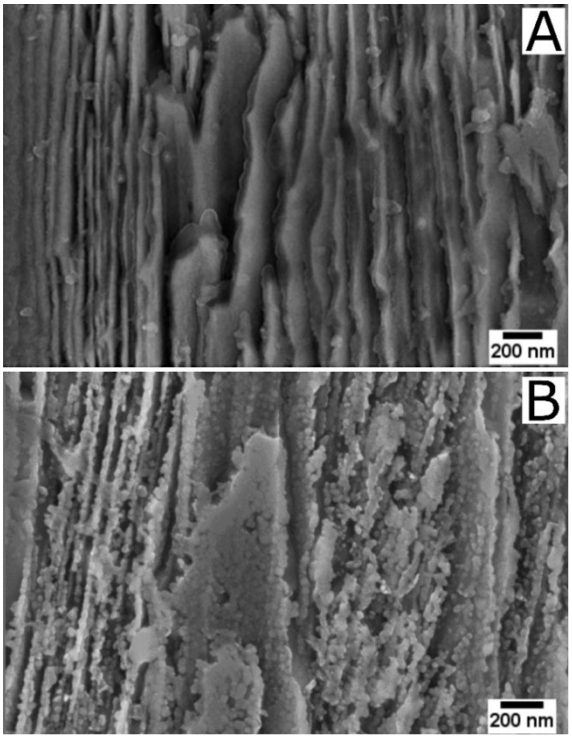


Figure 1.1. Nanoscale cementite spheroidisation in highly deformed pearlitic steel. A) As-drawn; B) electropulsed [6].

Accelerated nanocrystallisation of an iron-based amorphous alloy was reported as a result of high density electropulsing at ambient temperatures [17]. When combined with annealing, electropulsing has also been shown to enhance the recrystallisation rate of cold-worked copper [1, 18, 19]. A diffusive phase transformation was observed in a Cu-Zn alloy after treatment of two pulses at a maximum current density of $1.8x10^{10}$ $A{\cdot}m^{-2}$ [20]. Processing of molten metal with electric current has also been reported, with current density of $1.2x10^5$ $A{\cdot}m^{-2}$ found to remove Mn-S inclusions from liquid 0.74wt%C steel [21]. Recovery of damage, such as crack healing, has also been noted in 1045 steel [22] and a titanium alloy [23, 24].

1.2. Foundation for research

In the present study the effect of electropulsing on cold-deformed pearlitic steel is examined, using initial work by Qin *et al*.[6] as a basis. Those experiments were focused on 0.8wt%C pearlitic steel wire, cold-drawn to a true strain of 1.61 and treated with a single pulse at ambient temperature. The duration of the pulse was less than 1ms and current density was 9.61×10^9 A·m^{-2}. As shown in Figure 1.1 the treatment induced nanoscale cementite spheroidisation, producing globular particles with diameter of approximately 30nm. Earlier work by the same authors reported accelerated cementite spheroidisation in similar pearlitic steel wire cold-drawn to true strain of 3.0. The applied single pulses had a duration of 150μs and current density of 9.82×10^9 A·m^{-2} and 1.07×10^{10} A·m^{-2} [7].

1.3. Electropulsing in bulk

Following from this research, the aim of the current work was to examine the effect of electropulsing on cold-rolled pearlitic steel plate with a view to reproducing and optimising the previously reported grain refinement effects observed in drawn wires. Primarily the focus was on achieving grain refinement at low energies and low heating rates. The high strength characteristics of drawn pearlitic wires are well known and utilised in applications such as automotive tyre cord and wire rope in bridges and ski lifts. Some wires have been shown to possess tensile strengths in excess of 6GPa [4]. However, these effects are typically produced in drawn wires with narrow profiles which limits the applicability of the material. Furthermore, cold working of bulk material such as plate increases hardness and tensile strength at the expense of ductility, ultimately affecting the workability of the piece [25]. This study therefore considers the practicality of employing electropulsing treatment for the development of ductile yet high strength bulk pearlitic material by combining severe deformation with an alternative processing method.

1.4. Electropulsing for grain refinement and workability

A related area of interest was the effect of electropulsing on the α-ferrite phase, as previous work has focused on the carbon phase cementite. The recrystallisation of ferrite resulting from annealing treatments is generally accompanied by a decrease in hardness and tensile strength as grain growth occurs. However, it is possible that nanoscale recrystallisation could offer improvements in those mechanical properties while maintaining a level of ductility.

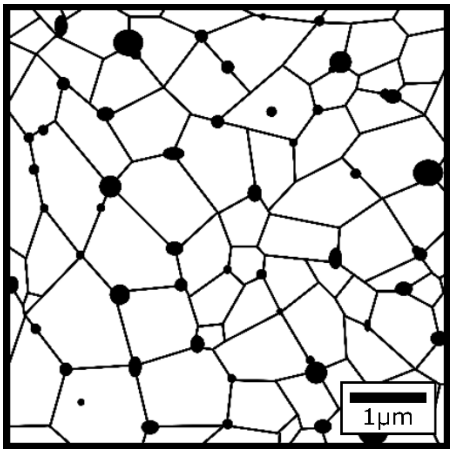


Figure 1.2. Schematic of a recrystallised ferrite matrix, with intergranular spheroidised cementite at triple-points and grain boundaries.

Such ultra-fine grained microstructures (depicted in schematic form in Figure 1.2) have been achieved through processes such as Equal Channel Angular Pressing (ECAP), which induces recrystallisation through extremely high levels of deformation at relatively low temperatures [26]. By forcing a workpiece through an enclosed channel with an angular deviation (see Figure 1.3), strain is induced without significantly affecting the overall geometry of the bulk material and multiple passes can produce extremely fine microstructures.

A study by He *et al.* [5] reported nanoscale ferrite recrystallisation in 0.8wt%C pearlitic steel after four passes through a channel with 30° intersection angle. Treated at 650°C, the microstructure transformed from fully lamellar to a matrix of equiaxed ferrite grains of average grain size of 400nm, interspersed with spheroidised cementite particles of average diameter 350nm. A follow-up study on the effects of the ECAP treatment on the mechanical properties of pearlite showed that final hardness and tensile strength values were slightly lower but comparable to the original pearlite. Importantly, the fracture morphology had changed from brittle to ductile failure, suggesting that the ECAP ultrafine-grained microstructure had an improved strength to ductility ratio compared to undeformed pearlite [27].

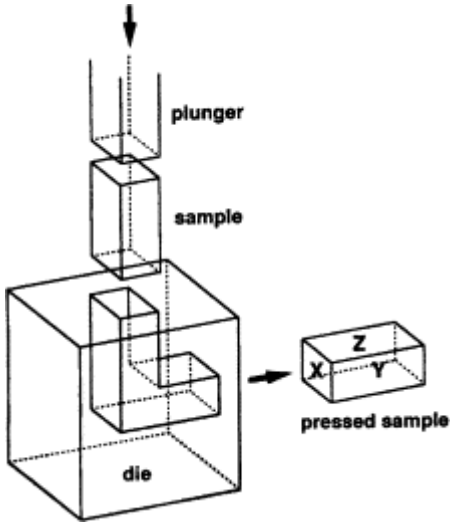


Figure 1.3. Schematic of the ECAP process [26].

While ECAP can produce desirable characteristics, it is an extrusion process that requires long samples, and cannot be applied to plate in bulk. The opportunity for electropulsing treatment would be to produce ultra-fine grained microstructures in pre-deformed plate, allowing manufacture of large workpieces with good strength and workability. However, the main barrier to making this a reality lies in the scalability of electropulsing.

1.5. Scaling for industry

The electropulsing process itself is relatively simple, with experimental variability dictated by pulsing parameters, environment and application of strain. As described previously current density appears to be a key variable in the effectiveness of electropulsing treatments, but it may also act as a limiting factor for industrialisation of the process. As a ratio of applied current to sample cross-section, current

density is dependent on a balance between sample geometry and equipment capacity. Electropulsing a standard steel plate of thickness 0.02m and width 1m would require an applied current of 200kA to achieve a minimum current density of $1x10^7$ $A{\cdot}m^{-2}$, a value that sits at the lower end of those associated with microstructure change in the literature. This shows that the use of electropulsing in its current form at industrial scale must be carefully considered, as such a high-energy process carries implications not only for practicality but also economic feasibility and safety. This project will consider the usefulness of electropulsing in large-scale materials processing, and suggest alterations to the process to improve its applicability to real-world steel treatment.

1.6. Identification of mechanisms

The final and most important driver for initiating research in this area relates to the mechanisms of electropulsing. While electropulsing effects are consistently reported in the literature, the mechanisms proposed to explain those effects are not yet confirmed. Some researchers suggest that both thermal and athermal effects, such as an electron wind, may play a part in microstructure transformation [10, 11, 28]. They theorise that the electron wind may enhance diffusivity of elements such as carbon, to accelerate microstructure change. Alternatively, the proposed null hypothesis would suggest that electropulsing effects are simply thermal in nature. The process involves very high rate heating and cooling, and even lower parameter treatments can be observed to heat metal samples. It is possible that this heating may simply cause recrystallisation in deformed samples through similar mechanisms to traditional annealing. A critical question under examination in this thesis then becomes whether an electropulsing effect can be discerned, over and above that expected simply from Joule heating.

1.7. Thesis composition

Following from the current introduction section, Chapter 2 contains a review of relevant literature on 1) grain refinement processing and 2) electropulsing. Chapter 3 describes experimental methods, including sample preparation, electropulsing equipment operation and electron microscopy.

Experimental Chapters 4 to 6 describe tests carried out at varying environmental conditions and operating parameters. Chapters 4 and 6 describe work on a hypereutectoid 0.92wt%C pearlitic steel plate. Chapter 5 focuses on experiments with hypoeutectoid 0.73wt%C pearlitic rod. Chapter 4 describes electropulsing at ambient temperature, with parameters of current density between 10^7 and 10^9 $A{\cdot}m^{-2}$, frequency up to 200Hz and pulse duration between 80 and 600µs. Chapter 5 presents high temperature experiments, combining annealing treatments up to 800°C with electropulsing. Pulsing parameters of current density between 10^7 and 10^8 $A{\cdot}m^{-2}$, frequency of 1Hz and pulse duration of 60 or 80µs were applied. Chapter 6 describes the use of alternative electropulsing equipment to achieve single pulses of very high current density without intensive

pre-processing via cold rolling to produce samples of small cross-section. Using more powerful equipment current densities of approximately $5x10^9$ $A \cdot m^{-2}$ were achieved in the hypereutectoid steel plate. Chapter 7 summarises the research and states the conclusions drawn.

2. Literature review

2.1. Introduction

For many years, grain refinement in materials science has been an area of intense and consistent research interest. The importance of grain size to the mechanical properties of crystalline materials was first quantified by Hall and Petch [25], who independently determined that the tensile strength was inversely proportional to the grain size. They found that a reduction in grain size increased the volume of grain boundaries, which acted as barriers to dislocation motion and hence increased the resistance of a material to deformation. Later research by Gleiter [29] highlighted the possibility of even finer grains, spurring research into ultrafine grain processing methods and inadvertently opening a new area of research when it was discovered that the Hall-Petch relationship did not hold for ultrafine grain sizes [30-32].

Synthesis of submicron and ultrafine-grained microstructures can be readily achieved through small-scale processes such as inert gas condensation, powder compaction and electrodeposition. These so-called “bottom-up” production methods are able to produce fine grain sizes by constructing a small amount of material atom by atom [33]. However, processing of bulk materials in this manner is impractical and likely impossible due to the inherent nature of the processes and the time and cost involved. “Top-down” manufacturing is more appropriate for bulk material synthesis, and involves the refinement of a pre-existing grain structure via severe plastic deformation (SPD).

Various methods for top-down production have been developed, and three key processes will be assessed in the course of this review. Equal Channel Angular Pressing [5, 34, 35], multilayer rolling [36, 37] and wire drawing [38-40] have all been successfully applied to steels to induce submicron or ultrafine-grained microstructure. Each is an SPD process that introduces very high strain to the workpiece, which is reflected in the mechanical properties obtained.

In many cases the material of interest in SPD processes is pearlitic steel [4, 5, 27, 39, 41]. As its initial microstructure has excellent inherent strength and toughness characteristics [42], a further refined pearlitic microstructure could possess enhanced properties. A stronger yet more ductile steel might emerge from the combination of hard cementite and ductile ferrite in an ultrafine configuration. Previous attempts to produce such a microstructure using ECAP have yielded an improved tensile strength, while reducing the ductility [27].

Electropulsing combined with severe deformation has been proposed as a potential grain refinement technique for pearlitic steel. Researchers have studied the effects of electropulsing since the 1960s, and the process can be described simply as the passage of electric current through a material. Troitskii pioneered the topic and applied the electropulsing technique to many highly deformed metals [43, 44]. Subsequent electropulsing studies have been carried out on a variety of metals and alloys [3, 10, 23, 45-52]. Throughout this body of research, many different electropulsing effects have been observed. An accelerated microstructural recrystallisation process is consistently reported across a range of metallic materials, generally described as stemming from an enhanced nucleation rate, which leads to phase transformation and varying degrees of grain refinement [1-3, 18, 19, 47, 53-56].

Changes to the mechanical properties associated with altered microstructure in electropulsed materials are also well documented [6, 7, 51, 56-58]. Additionally, electropulsing has been successfully used to heal microcracks and to reduce defects in a number of metals [22, 51, 59-62]. The treatment has also been applied in combination with other processing methods to achieve various effects. Ivanov *et al.* [63] combined electropulsing treatment with high energy electron beams and applied the processing to various alloys. Ye *et al*. [64] combined electropulsing with ultrasonic shock, which significantly improved the surface quality of treated alloys.

A recent review by Qin highlighted several outstanding issues in electropulsing processing [65]. Despite a wealth of research, the underlying mechanism remains unclear. Some theories suggest that the effects of electropulsing are produced by the high heating and cooling rates associated with the process [9, 52, 57, 66]. Others focus on properties inherent to the electric current such as current density, additional free energy and the effect of the current on the movement of electrons [6, 7, 11, 15, 28, 67-69]. More recently, multi-factor theories such as those describing the combination of thermal and athermal effects have been developed. In addition, the amount of pre-deformation must also be considered, as studies have shown that the effects of electropulsing on recrystallisation can be magnified in pre-deformed materials [1, 7, 28, 70]. Finally, the specific processing conditions are also important. The effects of static electropulsing (where electropulsing is applied separately to any deformation or heating process) have been shown to differ to those of dynamic electropulsing (where electropulsing is applied in combination with deformation) [71, 72].

The following literature review is divided into two parts. The first focuses on grain refinement, and describes the theory, mechanisms and processing methods currently used to obtain refined microstructures in bulk. When discussing material synthesis the focus will be placed on treatment of pearlitic materials where possible. The second part presents an overview of the progression of

research on electropulsing. It summarises key literature on grain refinement through phase transformation and recrystallisation and includes research on the effects of pre-deformation. The mechanical properties of electropulsed materials are discussed, and processing conditions will be considered throughout the review. For completeness a section on crack healing induced by electropulsing is also included.

2.2. Part I – Grain refinement: processing and pearlitic steel

2.2.1. Nanoscale strengthening mechanisms

2.2.1.1. The Hall-Petch relationship

Strengthening by grain size reduction is a well-known phenomenon that is described by the Hall-Petch relationship (Equation 2.1) [25]. The yield strength σ_y varies with average grain diameter d, and the variables σ_0 and k_y are chemical and microstructural material constants, respectively.

$$\sigma_y = \sigma_0 + k_y d^{-\frac{1}{2}} \qquad 2.1$$

The relationship states that the yield strength of a material will increase with decreasing average grain size. The mechanism of the Hall-Petch effect was originally explained as relating to the increased volume of grain boundaries as a result of grain refinement. Grain boundaries impede dislocation motion and cause dislocation pile-up at the grain interface. A larger volume of grain boundaries results in more dislocation accumulation, which increases the yield strength, or resistance of the material to further deformation. A review by Cordero *et al.* [73] summarises subsequent research and further derived equations that aim to more completely explain the mechanisms involved in Hall-Petch strengthening.

Based on Equation 2.1 it should be theoretically possible to achieve a maximum yield strength when the grain size is minimised. As a result, research into the properties and synthesis of ultra-fine grained (UFG) materials has escalated since the 1980s and the publication of a seminal review article by Gleiter on the topic [29]. However at very small grain sizes the Hall-Petch relationship has been found to become nonlinear, with the rate of yield strength increase (or hardening) slowing with further reduced grain size [30-32]. The behaviour is referred to as the Inverse Hall-Petch effect. This is represented by a decrease in the material constant k_y, which determines the slope of the Hall-Petch plot [74]. The minimum grain size at which the Hall-Petch relationship remains valid varies with material, however a study by Horita *et al*. [75] is highlighted to give an indication of the scales under consideration. Equal Channel Angular Pressing (ECAP, described in section 2.2.2.1) of aluminium alloys Al1100 and Al3004 produced grain sizes ranging between approximately 250nm and 30μm. Based on comparison of grain size with 0.2% proof stress it was found that the material obeyed the Hall-Petch relationship down to

the smallest observed average grain size of 250nm. The Hall-Petch relationship in BCC steels has been found to extend to the sub-micrometre scale, but a decrease in the value of k_y and subsequent deviation from the linear relationship has been observed [74].

2.2.1.2. Ultrafine grains and the Hall-Petch relationship

Theories have been proposed to explain the Inverse Hall-Petch (IHP) behaviour using dislocation, diffusion and grain boundary shearing mechanisms [33, 76]. Several theories are derived from the original grain boundary dislocation pile up mechanism described by Hall and Petch [25]. They suggest that the size of the ultrafine grains prevents them from storing dislocations, or affects the interaction between dislocations and the grain boundaries [73]. Argon and Yip [77] proposed a model that aims to identify the "strongest size", i.e. the nanoscale grain size at which the peak material strength occurs. The authors applied two mechanisms, grain boundary shear and dislocation plasticity, to explain the reduction in strength with decreasing grain size at the nanoscale. Simulations have shown that the dislocation flux required for plastic flow is restricted when the grains fall below a certain size (preventing dislocation strengthening), and that plastic strain production is determined by grain boundary shear (affecting the contribution of grain boundaries to strengthening by inhibition of dislocation motion). The combination of these mechanisms causes the material strength to peak and then invert with further decreasing grain size.

In contrast to theories that attempt to explain the breakdown of the Hall-Petch relationship at small grain sizes in metallurgical or microstructural terms, other researchers have proposed a new fitting exponent that is able to explain deviations more readily than the original. Papers by Dunstan and Bushby [78] and Li *et al*. [79] considered whether the Hall-Petch strengthening effect was a unique phenomenon, or a manifestation of other size-related strengthening effects observed in the literature in thin foils, micropillars and other small samples. As opposed to the original inverse square root fit the researchers suggested a simple inverse fit of the form shown in Equation 2.2, where ℓ is the sizing variable (i.e. for this application, ℓ is equivalent to the grain diameter d).

$$\sigma = \sigma_0 + k\ell^{-1} \qquad 2.2$$

Comparison of both the inverse and inverse square root fits using multiple data sets from various materials revealed that there was no conclusive evidence that the original Hall-Petch fit was any better than the simple inverse fit. In addition, when the simple inverse was used the values of the material constant k for various materials converged to a single value. This suggested to the authors that differentiation between materials in the strengthening equation was attributable to only the chemical

constant σ_0. As a result, the authors concluded that the Hall-Petch relationship could be classified in the same category as other sizing effects, rather than a stand-alone phenomenon.

2.2.1.3. Summary

Despite sixty years of research and data, the mechanisms involved in Hall-Petch strengthening are yet to be fully understood. Research in both microstructural and mathematical directions continues, and an in-depth analysis of the theories involved is outwith the scope of this review. Instead, the focus will now shift to that which has caused such complexity for researchers in terms of the Hall-Petch relationship – processing of ultrafine grains.

2.2.2. Materials processing for ultrafine-grained (UFG) materials

Various production methods are available for the synthesis of UFG materials, the most common methods including inert gas condensation, mechanical alloying of powders, electrodeposition, optimised heat treatments for crystallisation from amorphous solids, and severe plastic deformation [33]. Most of these techniques are suitable for processing of UFG materials in small quantities. However as the focus of this thesis was bulk processing of pearlitic steel, the literature review will similarly focus on bulk synthesis. Severe plastic deformation (SPD) techniques are most relevant in this case [80]. The following sections will discuss the SPD methods equal channel angular pressing, multilayer rolling and drawing processes with reference to pearlitic steel.

2.2.2.1. Equal Channel Angular Pressing (ECAP)

Equal Channel Angular Pressing (ECAP) or extrusion (ECAE) is a deformation method whereby a workpiece is repeatedly forced through a die at a severe angle in order to induce high strain [26]. A schematic of the process is shown in Figure 2.1. The advantage of the ECAP process lies in the design of the processing method – it allows very large strains to be introduced to the workpiece while maintaining its original shape. Other deformation methods such as rolling or drawing are limited in that dislocations and strain are produced at the cost of altered material geometry.

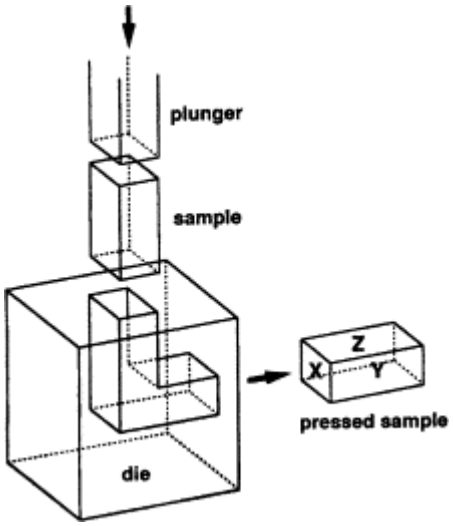


Figure 2.1. ECAP processing schematic [26].

The process is repeated multiple times with the workpiece rotated at each pass to achieve the required properties or grain refinement. The grain refinement is achieved by introducing an increasing volume of dislocations into the microstructure that transform with each pass into a network of subgrains [26]. The technique can be conducted at ambient or elevated temperatures and the grain size obtained by ECAP has been found to increase with processing temperature in low carbon steel [81], aluminium and al-alloys [82] and copper [83] as a result of dynamic recovery and grain growth.

ECAP treatments are governed by several key parameters, including treatment temperature, pressing speed, the angle of intersection between the die channels, and the direction and number of sample rotations between passes [84, 85]. These parameters affect the severity of the applied strain, the final grain size and homogeneity of microstructure transformation. The following literature review will focus on the effects of temperature as the remaining parameters are process-specific and thus difficult to meaningfully compare with other deformation processes.

ECAP and steels

ECAP has been used to alter the microstructure of steels of varying carbon contents. He *et al*. [5] used ECAP at 650°C to refine the grain size of a commercial 0.8wt%C high carbon pearlitic steel. The cylindrical samples (8.3mm diameter and 49mm length) were deformed through four passes, and were rotated 90° along the longitudinal axis after each pass. The intersecting angle between the insertion and extrusion channels was 120°. After four passes the lamellar microstructure was refined to equiaxed ferrite grains of average diameter 400nm and spheroidised cementite particles of average diameter 150nm (Figure 2.2). The microstructure was altered as a result of severe deformation combined with dynamic recrystallisation at an elevated temperature.

A comparable study by Shin *et al*. [81] applied ECAP at temperatures between 350 and 600°C to two grades of low carbon 0.15wt%C steel with pearlitic regions in the as-received microstructure. Four passes through an intersection angle of 90° produced a microstructure of equiaxed ferrite grains in cylindrical samples (diameter 18mm, length 130mm) of both steel grades. The grain size increased with temperature and the finest grains of approximately 300nm diameter were observed at 350°C. As in the study by He *et al*. [5], the transformation was attributed to the effects of high strain rate and rapid recovery. The cementite phase was less easily identified than in the previous study as a result of the variation in carbon content. However, fine cementite spheroidisation was observed at higher pressing temperatures.

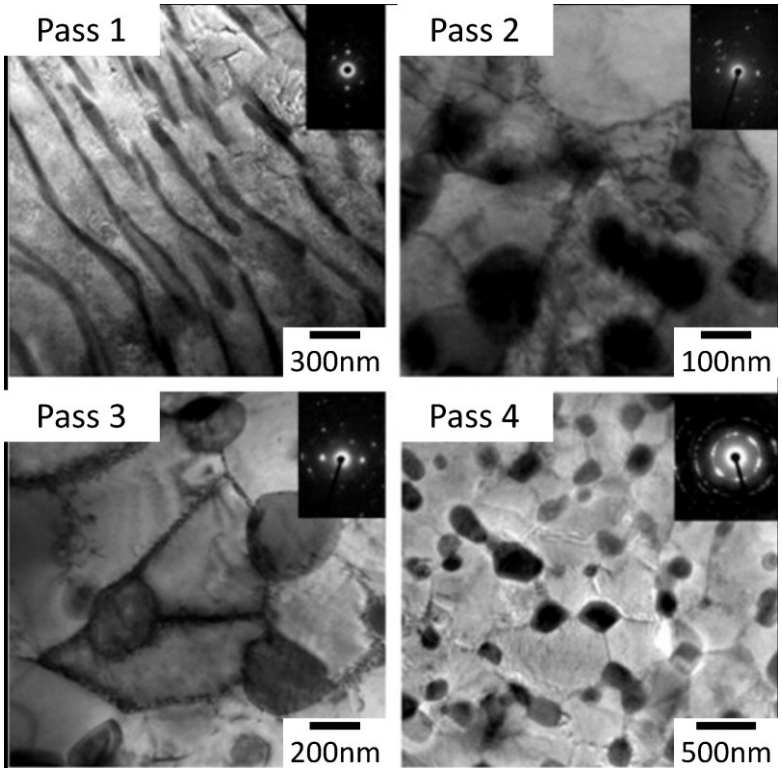


Figure 2.2. ECAP treatment of 0.8wt%C pearlitic steel [5]. Lamellar microstructure remained after the first pass, transforming to equiaxed ferrite and spheroidised cementite with subsequent passes and increasing dislocation density.

Ambient temperature ECAP processing can also be used to refine the grain structure of carbon steels. Fukuda *et al*. [34] applied ECAP to a 0.08wt%C ferrite-pearlite steel at room temperature through three passes, with an intersecting angle of 90° and a channel diameter of 10mm. The microstructure transformed to equiaxed grains after three passes, with the grains showing elongation after one and two passes. The average grain diameter after three passes was approximately 200nm. Low angle subgrain boundaries that developed after one and two passes were found to have resulted from the introduction of large volumes of dislocations due to intense plastic strain. The dislocations then rearranged into a network of grain boundaries. With further deformation after three passes equiaxed grains with high angle boundaries were formed. In this case the grain refinement observed is purely due to severe plastic deformation, as no external heat was applied to induce recovery or grain growth. Note that the authors do not offer any indication of the effects of ECAP on the cementite phase, with the analysis focusing on ferrite recrystallisation.

ECAP has also been applied to martensitic microstructures in order to produce grain refinement. Yang *et al.* [86] researched the effects of a single ECAP pass at room temperature on 0.15wt%C aged martensitic steel. The intersecting angle of the channels was 90°, and cylindrical samples of length 45mm and diameter 8mm were tested. After one pass the martensitic microstructure had fragmented

into subgrains and dislocation cells. On subsequent aging at temperatures between 640 and 720°C ultrafine grains were formed as a result of recovery processes.

A similar study by Pang *et al.* [35] on 0.19wt%C steel with martensitic microstructure obtained comparable results. The researchers found that the average size of martensite grains decreased by 40% after a single pass followed by heat treatments,[1] and continued to decrease gradually with further passes (Figure 2.3). The experiments were conducted at room temperature and up to four passes were applied to the samples. In both martensite papers the UFG microstructure was described as being a product of ECAP-induced fragmentation followed by recovery at high temperatures.

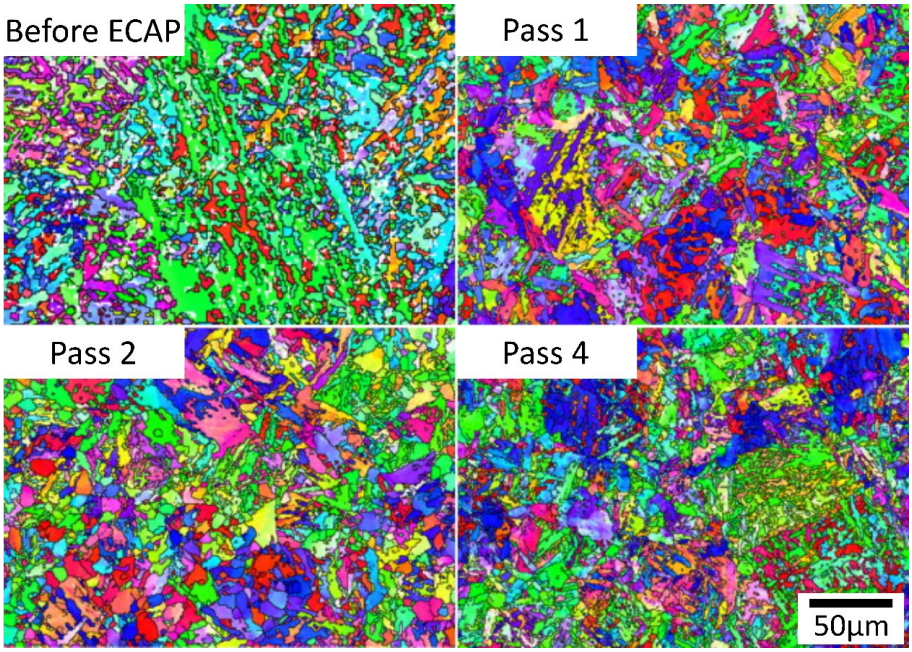


Figure 2.3. EBSD showing martensite fragmentation in 0.19wt%C steel as a result of ECAP [35].

Mechanical properties after ECAP

ECAP involves both high deformation and more often than not, elevated temperatures. It might then be expected that the mechanical properties of ECAP-processed samples would vary with the number of passes (the level of deformation) and the applied temperature (the driving force for recrystallisation). A study by Xiong *et al.* [27] on 0.8wt%C pearlitic steel processed in an identical manner to that described by He *et al*. [5] found that after two passes the microhardness and ultimate tensile strength (UTS) increased from the as-received lamellar pearlite state. The peak values achieved as a result of work hardening were 355HV and 0.912GPa, respectively. After a third pass the hardness and UTS were found to decrease due to dynamic recrystallisation. The fourth and final pass produced refinement of the recrystallised grains, and the hardness and UTS increased slightly as a result

[1] After one to four ECAP passes at room temperature the samples were heated at 780°C for 10 minutes and quenched in water, followed by tempering at 200°C for 120 minutes.

(although the values were lower than the original lamellar pearlite). The ductility of the third and fourth pass ECAP samples was increased from the lamellar pearlite state. This was an effect of the distribution of cementite in the microstructure – after multiple ECAP passes the cementite was spheroidised and homogeneously distributed through the ferrite matrix, thus improving the workability of the steel.

The mechanical properties of low carbon steel after room temperature ECAP were considered by Fukuda *et al*. [34]. After three passes the Vickers microhardness of both the ferrite phase and pearlite colonies was increased significantly. However, the majority of the hardness increase occurred after the first pass while the subsequent passes produced only a small increase. Similarly, the UTS and 0.2% proof stress of the bulk material were clearly improved after a single pass and saw only moderate increase (UTS) or stabilisation (proof stress) with further passes. It should be noted that the overall UTS value increased by over 0.4GPa after three passes, a significant improvement on the as-received material. The ductility of the bulk material was found to decrease after ECAP, corresponding to the increase in strength. The mechanical property variations were attributed to the effects of strain hardening at ambient temperature, which increased the strength and hardness of the material at the cost of ductility as large numbers of dislocations were introduced to the crystal structure.

Yang *et al.* [86] observed that after a single pass of ECAP treatment at room temperature, the UTS and yield strength of 0.15wt%C martensitic steel increased significantly while the ductility decreased. After aging heat treatment, the UTS and yield strength fell but remained greater than that of the as-received sample. Conversely, the ductility increased after aging with one sample comparable to the as-received value, one lower and one higher. In some cases (dependent on heat treatment profile) ECAP was able to produce a martensitic bulk material with both improved strength and ductility properties. This was ascribed to both the refined microstructure produced by ECAP, and the improved distribution of fine carbides.

Pang *et al.* [35] found a variation in the mechanical property effects of ECAP with the number of passes similar to Xiong *et al*. [27] in pearlitic steels. After two passes and subsequent heat treatment the fatigue strength of 0.19wt%C martensitic steel peaked at 0.46GPa. Subsequent ECAP passes caused the fatigue strength to decrease. In contrast to Yang *et al*. [86], no significant yield strength effects were observed after any number of ECAP passes. The tensile strength increased only slightly after one pass then decreased and stabilised with further passes. The mechanical property behaviour was described as resulting from the initiation of cracks with subsequent ECAP passes, which affected the strength of the material.

Summary - ECAP

The effects of ECAP treatment on the mechanical properties of steel samples result from strain hardening and dislocation subgrain network formation. It has been shown that ECAP at ambient temperatures can increase the strength characteristics of carbon steels by introducing severe plastic deformation. The large volumes of dislocations associated with the deformation increase the hardness of the material by impeding dislocation motion, and as a result improve the resistance of the material to further deformation while reducing its ductility. With further ECAP passes, the dislocations coalesce into subgrain boundaries to produce deformation-induced grain refinement. When ECAP is conducted at elevated temperatures (or ECAP samples are subsequently heat treated) the grain structure undergoes dynamic recovery, recrystallisation or grain growth (or the static heating equivalent). This produces a more equiaxed microstructure generally with improved ductility and strength characteristics compared to the as-received material.

The number of ECAP passes is a key parameter in terms of the mechanical property effects produced. Studies have shown that peak strengthening by ECAP is often achieved after one or two passes, and that subsequent passes do not always produce beneficial property effects [27, 34, 35]. This must be taken into account particularly at room temperature, when the mitigating effects of heat treatment are not applied. If the main aim of ECAP treatment is mechanical property strengthening then a smaller number of passes at ambient temperature is recommended. However, if a homogeneous microstructure of equiaxed grains is required then a multi-pass course of elevated temperature ECAP is more appropriate.

2.2.2.2. Multilayer rolling

Multilayer rolling is an SPD process that uses solid-state additive roll-bonding to manufacture bulk, highly strained material. The technique has evolved from standard cold rolling, and uses the same basic mechanisms to produce deformation. On the first pass a metallic plate is rolled to a certain reduction. The plate is then cut into sections, stacked and rolled again. A schematic of multilayer rolling is shown in Figure 2.4 [80]. The process is repeated until a bulk material of extremely thin sheets is produced. The sheets are bonded by pressure-induced diffusion [87]. High pressure rolling causes interfacial voids between the surfaces to collapse, allowing them to interact on an atomic scale and facilitating inter-diffusion and adhesion [88]. The key parameters for effective bonding vary by material and are described in a review by Li *et al.* [89]. They include sufficient rolling pressure, bonding temperature, and appropriate surface preparation and contamination removal.

Two variations of multilayer rolling exist, although the major process is identical. Accumulative Roll-Bonding (ARB) introduces a surface treatment step before stacking at each pass to enhance the

bonding process, while repeated cold rolling does not apply surface treatment in order to maximise shear strains during rolling due to frictional forces [90, 91].

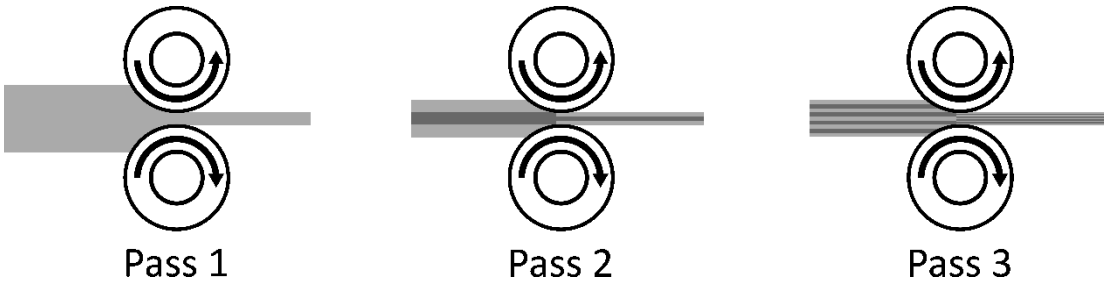


Figure 2.4. Schematic showing multilayer rolling. Modified from [80].

Critically, multilayer rolling is able to introduce very large strains while maintaining the original dimensions of the bulk plate. Saito *et al*. [92] calculated that the equivalent plastic strain associated with the ARB process at 50% reduction[2] per cycle was equal to 0.8n, where n is the number of passes. ARB processing can therefore produce significant strain with a relatively small number of passes. This is a significant improvement on traditional cold rolling, which severely alters the geometry of the workpiece and therefore affects the potential applications of the material. Multilayer rolling can be conducted both at room temperature [89] and with applied heating [91] (where the temperature is less than the recrystallisation temperature of the material being bonded to prevent strain removal).

Instances of the application of multilayer rolling to steels in the literature are limited to certain compositions. Cold multilayer processes have been found to be most successful in ductile materials with FCC crystal structure [89], perhaps due to the larger interstitial sites available for diffusion in FCC than BCC configurations [42]. Elevated temperature single roll bonding of low carbon steel has been achieved [93], but at the cost of exceeding the recrystallisation temperature and thus removing the applied strain and increasing the grain size. Low carbon steel has also been roll-bonded to austenitic steel, but as a result of an equally high heating course [94]. The higher content of brittle carbon combined with the BCC crystal structure of ferrite at ambient temperature appear to prevent the successful use of multilayer rolling for bulk synthesis of UFG material in pearlitic steels. The literature that does exist is focused on ultralow carbon compositions, which will be described in the following sections.

Multilayer rolling for UFG microstructures

As pioneers of the process [92], Tsuji *et al*. have conducted a large volume of research on ARB and its application to various materials [95-97]. In each case, the steels successfully treated by the researchers using ARB have a very low carbon content. One such study on an interstitial-free (IF) 0.0031wt%C steel

[2] At 50% reduction the original dimensions of the bulk material can be maintained with each pass.

with titanium additions described the production of a bulk steel using ARB [36]. Up to seven cycles of ARB were applied to the steel, which was rolled at a temperature of 500°C and had an initial grain size of 27µm. The reduction in thickness per cycle was 50% with an equivalent strain of 0.8 and a mean strain rate of $46s^{-1}$. After seven cycles the equivalent strain was 5.6. It was found that dislocation cell substructures formed after one to two passes. After four passes UFG microstructure was observed, and after seven passes the microstructure was almost entirely UFG with mean grain size of 420nm.

A further study by Kamikawa *et al.* [98] using identical processing methods (excluding the mean strain rate, which was $19s^{-1}$) applied to a 0.002wt%C IF steel further analysed the microstructure. The UFG structure after seven passes was found to have a pancake-shape, with average thickness of 210nm and length of 930nm. The distribution of grain size and misorientation through the thickness of the material was uniform. However, the distribution of texture across the material thickness was complex as a result of the repeated application of shear strain to various surfaces.

Costa *et al.* [99] again applied ARB to ultralow carbon steel, in this case with 0.0024wt%C. The steel was rolled at 500°C for three passes, with a mean strain rate of $21.5s^{-1}$. The accumulated true strain was 2.08, and the initial grain size was 15µm. As previously reported the grain size was found to decrease with increasing number of ARB passes, as shown in Figure 2.5. The distribution of grain size is also shown in Figure 2.5, which reveals a significant variation in grain size with distance from the centre of the ARB workpiece after one and two passes. After three passes the ultrafine grains found in the subsurface in the previous pass have shifted to the centre of the workpiece due to the stacking order, resulting in an almost homogeneous distribution of UFG microstructure with average grain size of 350nm.

Post-ARB annealing treatments have been applied to ultralow carbon steels to alter the grain structure and mechanical properties. Tsuji *et al*. [37] applied ARB to two 0.002wt%C compositions, one having phosphorus added. The ARB was conducted at 400°C through five passes up to a total equivalent strain of 4. The ARB process was then followed by annealing treatments ranging from 500 to 700°C for 30 minutes in argon atmosphere. An additional 100 minute treatment at 400°C was also applied in order to enhance phosphorus segregation before final annealing. After ARB treatment the microstructure of both compositions was found to contain a refined sub-micrometre elongated grain structure. The ARB-only microstructure was less equiaxed than other research described previously, which was thought to result from the lower temperature applied during the process. After the 100 minute, 400°C grain boundary segregation treatment the microstructure was found to have become increasingly equiaxed, which was attributed to dislocation recovery and grain boundary migration. Finally, annealing treatments between 500 and 700°C induced further grain growth and an almost-equiaxed

structure. The equiaxed microstructure occurred at a slightly higher temperature in the phosphorus-added composition, and the element was described as inhibiting grain growth.

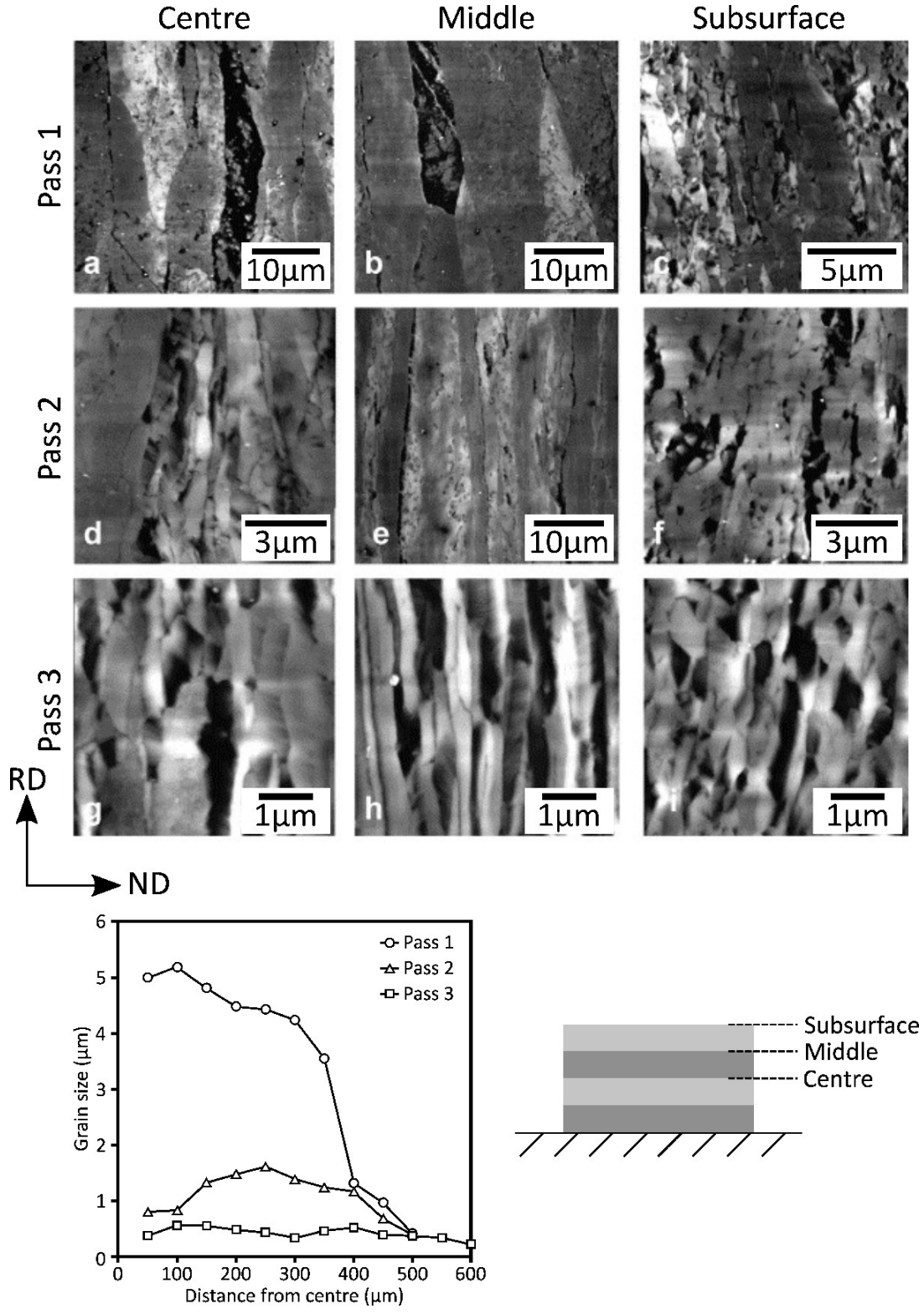


Figure 2.5. ARB of 0.0024wt%C steel. AFM images of steel microstructure at three regions across the sample thickness after one to three passes (top). Variation in grain size distribution across the thickness of the sample with number of passes (bottom left). Reproduced from [99]. Additional schematic indicating the regions of subsurface, middle and centre relevant to the bonded sample.

Mechanical properties of bulk multilayer materials

The effects of ARB on the mechanical properties of the bulk materials it produces are well documented, and correlate with those observed for other strain-based grain refinement methods such as ECAP. Tsuji *et al*. [36] observed an increase in tensile strength with subsequent ARB passes in a 0.0031wt%C steel, accompanied by a decrease in ductility. The ductility dropped most severely after the first pass, and continued to fall at a much slower rate with further treatment.

Costa *et al*. [99] observed a direct correlation between grain size and hardness in 0.0024wt%C steel. After three passes of ARB an UFG microstructure was obtained, but some variation in the grain sizes was observed. Hardness values measured across the thickness of the sample were plotted alongside the grain size at the same point to highlight the relationship as shown in Figure 2.6. The hardness was found to be inversely proportional to the grain size as predicted by the Hall-Petch relationship.

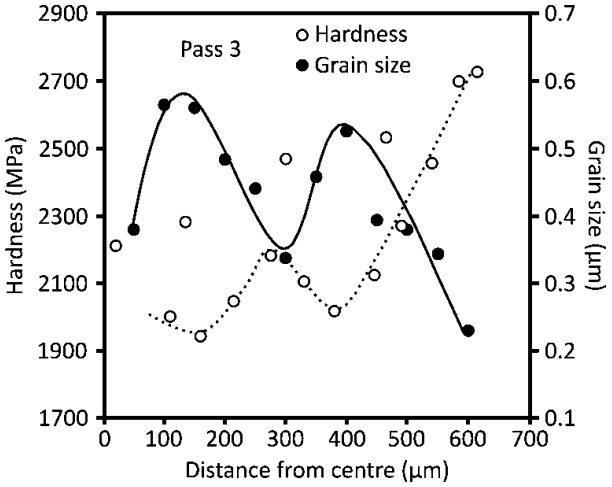


Figure 2.6. Correlation of hardness with grain size in 0.0024wt%C steel subjected to three ARB passes. Reproduced from [99].

Krallics *et al.* [100] assessed the mechanical properties of a 0.002wt%C steel treated with five passes of ARB at 515°C and a strain rate of $20s^{-1}$. After the fifth pass the hardness had increased to 293HV from 111HV in the as-received state. The first pass was observed to induce the most significant hardening effect (as observed by Tsuji *et al*. [36]) with subsequent passes increasing the hardness but less significantly so. Similarly, the tensile and yield strength increased with further ARB-induced strain but the largest increase occurred after the first pass. The ductility correspondingly decreased with the same characteristics.

As might be expected, annealing of ARB bulk material was found by Tsuji *et al.* [37] to reduce the strength while increasing the ductility. This behaviour occurred as a result of recrystallisation and grain growth at elevated temperatures, which reduced the strain in the material. Comparable results for ECAP-treated material are described in section 2.2.2.1.

Summary – Multilayer rolling

Multilayer rolling treatments are capable of producing highly strained bulk material through a several-stage process. Sub-micrometre and UFG microstructures can be obtained using the method, and as a result the mechanical properties of the material produced are enhanced compared to the as-received

condition. However, the application of multilayer methods to steels is limited by composition and crystal structure. Cold rolling of high carbon steels can require high rolling force after relatively few passes, which then requires significantly more powerful rolling equipment. In addition, higher carbon compositions require significantly higher temperatures to achieve diffusion bonding, which reduces the effectiveness of the grain refinement by exceeding the recrystallisation temperature. As a result, multilayer rolling has been limited to steels with ultralow compositions, and is therefore difficult to compare with other SPD methods that are able to escape this issue.

A critical number of passes are required to obtain a relatively homogeneous microstructure distribution in ARB materials. This is a result of the shearing forces applied to the material and the stacking order used, which can essentially produce a confused microstructure of elongated and equiaxed grains without sufficient passes. Furthermore, the process is dependent on multiple parameters that determine the success of the diffusion bonding and ultimately the final mechanical properties of the bulk material. It is unclear whether the method can be industrialised in a manner that reduces the time required to produce bulk ARB metals when the surface preparation, heating and cutting stages are taken into account.

2.2.2.3. Drawn materials

Wire drawing involves severe plastic deformation of a workpiece by extrusion to reduce its cross-sectional area and increase the length. To achieve this the wire is drawn through a series of successively smaller diameter dies as shown in Figure 2.7. Drawn high carbon pearlitic steel wires are one of the strongest materials available and are used in the construction of suspension bridges [101] and other high-strength applications including tyre reinforcement [102]. Wire drawing is an effective method of introducing very high strain and is capable of producing UFG microstructure in a single extrusion, unlike the cold-rolling process which requires multiple passes to achieve the same microstructure [102].

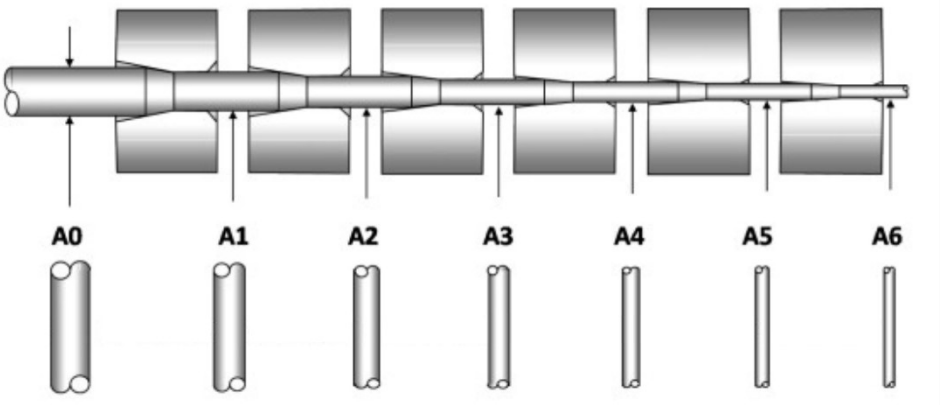


Figure 2.7. Wire drawing schematic showing dies of decreasing area from A0 to A6. Modified from [103].

Strengthening mechanisms in drawn pearlitic steel

High strength steel wire is typically produced from compositions of 0.7 to 1.0wt%C in two stages. Bulk material is drawn to an intermediate reduction and subsequently heat treated to produce pearlitic microstructure. The patented rod is then cold-drawn to the final reduction [38]. The popularity of pearlitic steel as the drawing medium results from the strengthening characteristics that can be achieved due to the response of the initial lamellar microstructure to strain and the dissolution of the carbon phase during drawing.

The strength of pearlitic steel is inversely proportional to the interlamellar spacing [104, 105] and wire drawing is known to significantly reduce this material property. Toribio and Ovejero [106] observed that with increasing strain the interlamellar spacing decreased in 0.8wt%C pearlitic steel wire (Figure 2.8). This was described as resulting from axial tensile and radial compressive stresses associated with the drawing process. Furthermore, the lamellae rotate during drawing to align parallel with the drawing direction [106-108], resulting in anisotropic mechanical properties [38, 108]. Zelin [108] identified the mechanisms involved in colony rotation as being linked to operation of dislocation slip systems, localised shearing and localised failure of lamellae resulting from severe strain.

Li *et al.* [109] reported a decrease in the lamellar thickness with increasing drawing strain. The behaviour was observed in both the cementite and ferrite phases, with the former reducing from 17 to 2nm and the latter from 56 to 10nm when as-patented 0.81wt%C wire was drawn to a strain of 5. The reduction in thickness was caused by a combination of lamellar adjustment to accommodate axial elongation and deformation-induced carbon dissolution, described in further detail below.

Severe deformation has been found to induce nanoscale carbon dissolution, as shown by Hono *et al*. [39] and Li *et al.* [109]. Research conducted by Hono *et al*. on 0.97wt%C steel wire drawn to a true strain of 5.1 and tensile strength of 5.17GPa found via atom probe tomography that severe strain caused complete dissolution of the cementite lamellae. The strengthening mechanism of the wire was thought to result from both the supersaturation of ferrite with carbon, and the refinement of ferrite into nanoscale fibres separated by sub-boundaries.

Atom probe tomography was also used by Li *et al*. [109] to analyse carbon decomposition in 0.81wt%C pearlitic steel wires drawn to true strains between 0.93 and 5.4. It was found that with increasing drawing strain from 2 to 5, the carbon concentration in cementite fell while concurrently increasing in ferrite. As the carbon concentration in the cementite dropped, the thickness of the cementite lamellae decreased. It was also reported that a calculated saturation limit of 1.46at%C existed at a drawing strain of 3.47 for cementite decomposition in the bulk material, indicated by the continuing

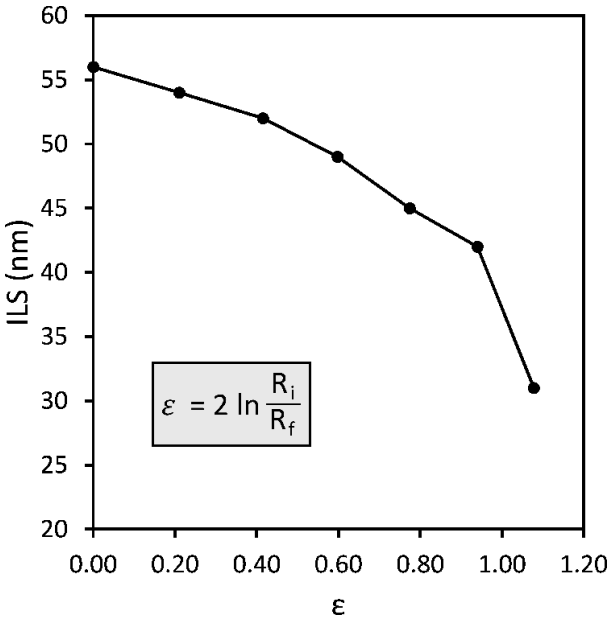


Figure 2.8. Reduction in interlamellar spacing of 0.8wt%C pearlitic steel wire with increasing drawing strain. Plotted using data from [106], equivalent plastic strain for cold-drawing calculated using the equation shown [102].

presence of a lamellar structure at even higher drawing strains. As previously suggested by Gavriljuk [110], the researchers found that the distribution of carbon in the ferrite phase was heterogeneous, and was associated with the distribution of dislocation substructure in the ferrite.

Note that this research is in contrast to that of Hono *et al*. [39]. While the earlier research observed full decomposition of the cementite lamellae, Li *et al*. [109] reported a saturation limit of carbon in ferrite and found cementite lamellae even at high strain. The variation in the results is difficult to quantify due to the differences in material composition and treatment methods.

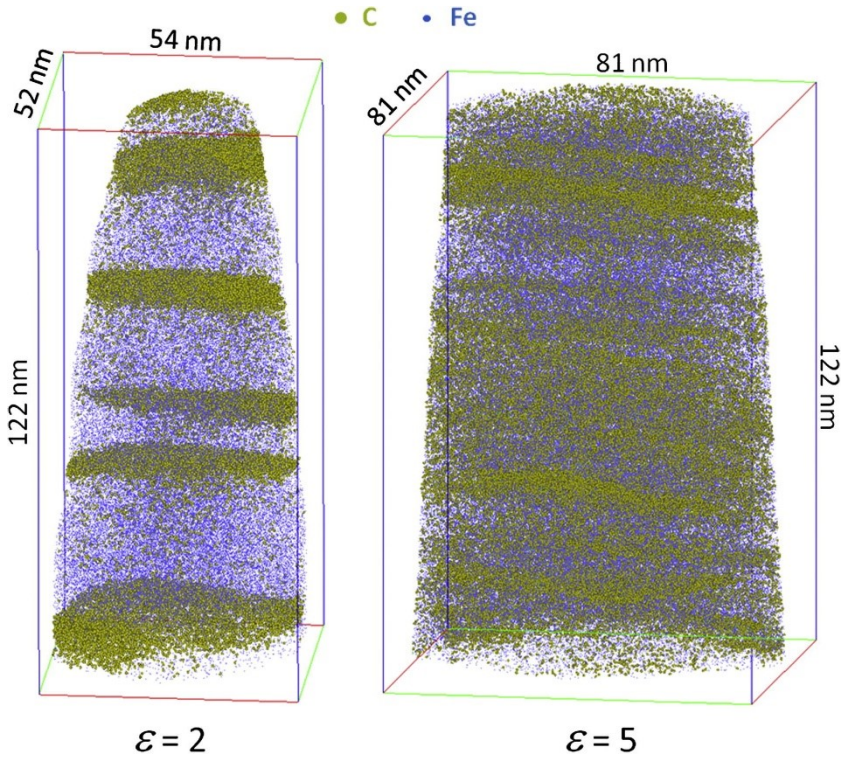


Figure 2.9. Atom probe tomography 3D reconstruction of nanoscale carbon decomposition in 0.81wt%C pearlitic steel drawn to strains of 2 and 5. Carbon atoms are yellow, while iron atoms are blue [109].

Severe drawing has also been found to produce a refined subgrain microstructure, as described by Li *et al.* [111]. Pearlitic wire of carbon composition 0.98wt%C was cold-drawn to strains of up to 6.52, with the highest strain producing a tensile strength of 7GPa. Atom probe tomography showed that with increasing strain, carbon decomposition occurred and resulted in supersaturated ferrite. Furthermore, a microstructure of deformation-induced subgrain ferrite was obtained, with the grains appearing almost equiaxed at the highest strain. The average grain diameter at strain of 6.52 was 10nm along the transverse cross-section of the drawn wire, and the grain shape was columnar along the drawing direction. The researchers found that the very high strength at high strain was associated with stabilisation of the ferrite subgrains by decomposed cementite at the grain boundaries, as opposed to a lamellar strengthening mechanism.

In a similar manner to tempering processes after ECAP treatments (see section 2.2.2.1), annealing of cold-drawn pearlitic steel wires can also produce desirable microstructure characteristics. Li *et al*. [4] annealed pearlitic steel wire at intervals between 150 and 450°C for 30 minutes. The 0.98wt%C wire had been drawn to a true strain of 6.02. Using atom probe tomography, it was found that the drawn lamellar structure persisted until 200°C. At 400°C the lamellae had transformed to a network of ferrite subgrains with spheroidised cementite located at the triple points (Figure 2.10). The ferrite grains were elongated in the drawing direction and were not equiaxed. Furthermore, their average dimensions were significantly smaller (at 400°C the major axis length of the elongated subgrains was 70nm) than those typically produced by recrystallisation processes (on the order of micrometres). As a result, their appearance was attributed to recovery of the deformed microstructure rather than recrystallisation.

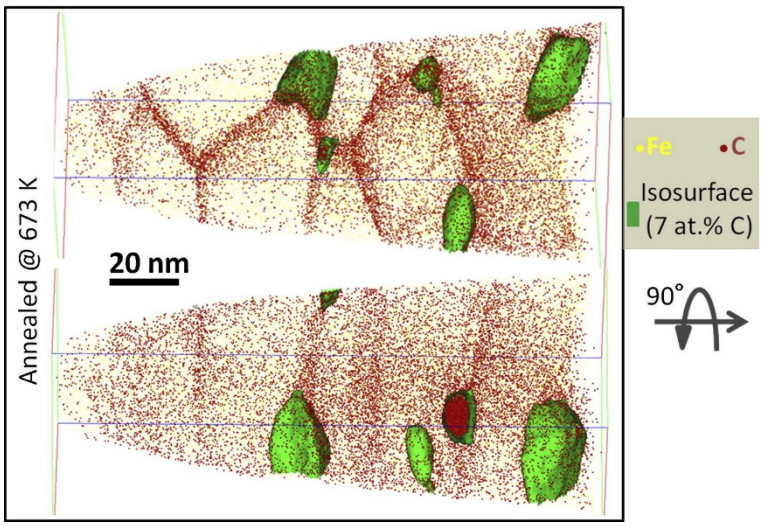


Figure 2.10. Atom probe tomography 3D reconstruction showing ferrite subgrains (delineated by carbon (red) at the subgrain boundaries) and spheroidised cementite at triple points. Modified from [4].

Mechanical properties of cold-drawn pearlitic steel wires

As a result of the combined effects of carbon decomposition and lamellar refinement and reorientation, drawn pearlitic steel wires can reach exceptional strengths. In an extensive review Borchers and Kirchheim [38] summarised the linear relationship between tensile strength and true drawing strain reported throughout the literature, and highlighted that with increasing drawing strain tensile strengths approaching 7GPa could be obtained.

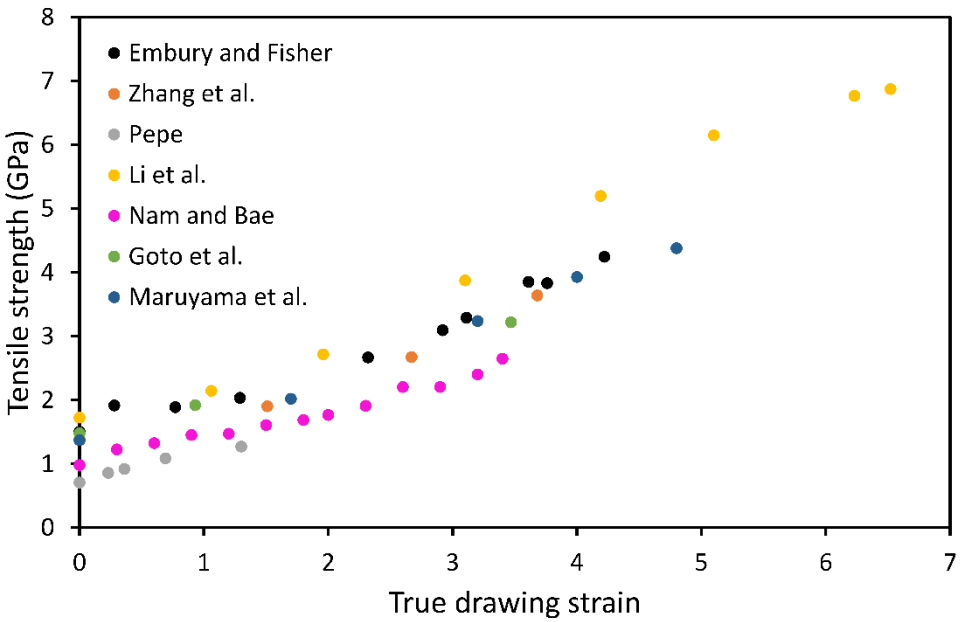


Figure 2.11. Borchers and Kirchheim's summary of the drawing strain/tensile strength relationship observed throughout the literature. Replotted from data provided in [38]. References to the original data can also be found in [38].

Research by Languillaume *et al.* [41, 112] characterised the as-drawn and annealed mechanical properties of a 0.7wt%C pearlitic steel wire (Figure 2.12). Heat treatments ranging between 100 and 680°C were applied for an hour to wire that had been strained to 3.5, resulting in an as-drawn tensile strength of 2.9GPa. The as-drawn properties were attributed to an increase in dislocations and a reduced interlamellar spacing as a result of the applied strain. The annealing results showed an increase in tensile strength and yield stress with an accompanying decrease in ductility from the as-drawn condition up to 200°C. At temperatures higher than 200°C both the tensile strength and yield stress decreased with annealing temperature, while the ductility was gradually recovered.

Analysis of the microstructure revealed that below 200°C the lamellar structure was maintained, and the heat treatment did not affect the thickness or strain levels of the ferrite lamellae. However, fine cementite spheroidisation had formed between the ferrite lamellae in much greater numbers than in the as-drawn condition. The increase in strength at low temperature annealing was then described as resulting from interactions between cementite particles and dislocations (precipitation hardening).

Above 200°C the microstructure had undergone dislocation recovery and ferrite recrystallisation, reducing the grain boundary volume and hence softening the bulk material.

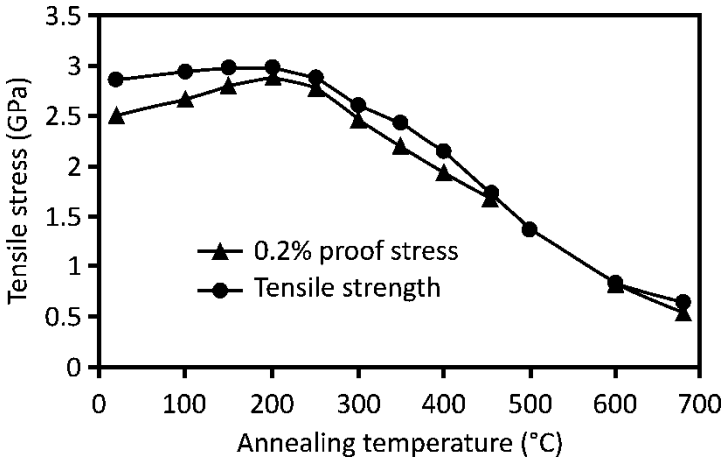


Figure 2.12. Effect of annealing temperature on mechanical properties of 0.7wt%C drawn pearlitic steel wire. Reproduced from [41].

Li *et al*. [4, 40] used a similar experimental method to assess the properties of a 0.98wt%C pearlitic steel wire of 6.35GPa tensile strength after cold-drawing. The tensile strength was found to decrease with increasing annealing temperature. From room temperature to 450°C, the tensile strength reduced from 6.35 to 2.92GPa. The softening behaviour was attributed to dislocation recovery and subgrain coarsening leading to a reduction in grain boundary volume during annealing as shown in Figure 2.10. The authors did not describe any hardening behaviour at lower annealing temperatures as observed by Languillaume *et al*. [41], and the lowest temperature tested was 150°C. It is possible that variations in strain and composition may account for this difference. It should also be noted that the recovery process in both papers appears to begin at relatively similar temperatures (150 and 200°C).

Summary – Drawn materials

Drawing of pearlitic steel wire has been highlighted as an effective method for producing large plastic strains and as a result, very high strength structural materials. The properties obtained are directly related to the level of applied strain and can be further modified by post-deformation annealing in a similar manner to the ECAP treatments described in section 2.2.2.1. UFG microstructure is readily obtained as a result of the development of dislocation substructures as well as the decomposition of carbon at high strains, and contributes to the mechanical properties of the material. The strength of drawn pearlitic steel wire is generally greater than that of ECAP steel and can be achieved in significantly less passes (usually a single wire drawing pass is sufficient, while multiple passes of ECAP can be necessary). The strengthening mechanisms are related to the interlamellar spacing and orientation of the pearlite, the dislocation substructure and the saturation of carbon in ferrite.

However, the mechanical properties of wire are anisotropic, limiting the bulk material to specific applications.

2.2.3. Conclusion

Part I of the literature review describes grain size strengthening mechanisms and some of the difficulties associated with modelling UFG microstructures using the Hall-Petch relationship. A brief introduction is given to the ongoing research seeking to explain the mechanisms behind the breakdown of the effect at the smallest lengthscales. Current research focuses on microstructural or mathematical solutions, through theories that include descriptions of dislocation storage limits in small grains, to adjustments of the scaling factor in the equation itself.

The production of ultrafine grains in steels can be difficult, depending on the carbon composition of the steel and therefore the temperatures required to achieve significant deformation through SPD processes such as ECAP or ARB. However, UFG pearlite microstructure can be achieved through ECAP or wire drawing. The microstructures obtained vary depending on applied strain, treatment temperature and post-processing annealing treatments. The grain structure of cold-drawn pearlitic steel wire is severely elongated, and has been found through high-resolution processes such as atom probe tomography to contain fine ferrite dislocation substructures supersaturated with deformation-decomposed carbon. ECAP-induced pearlite microstructure can evolve from elongated grains to equiaxed ferrite at ambient temperatures.

ARB is limited in its application to certain materials due to the processes involved. Roll-bonding has been achieved in low carbon steels (as opposed to ultralow) but only at temperatures so high that recrystallisation occurred and nullified the grain refinement effects of ARB. As a result, no pearlitic ARB-processed microstructure could be found in the literature and all of the research described is related to ultralow carbon compositions. Post-deformation annealing of steels treated with the SPD processes described produced a dual-phase microstructure of equiaxed ferrite and spheroidised cementite in each case. This behaviour is typical of heat treatments applied to deformed microstructures and is a result of dislocation recovery and grain growth of dislocation substructures.

The mechanical properties of steel can be enhanced by SPD, and exceptionally high strengths can be achieved depending on the process. However, this generally comes at the expense of a loss in ductility which can be mitigated by short post-SPD annealing treatments. It is difficult to compare the mechanical properties obtained through the three SPD processes described. Two are applicable to pearlitic steels, while a third is not. Two produce bulk material in plate form, while the third produces wire. An in-depth comparison of the mechanical properties obtained is, in this case, meaningless.

2.3. Part II – Electropulsing: mechanisms and microstructure effects

2.3.1. Recrystallisation and enhanced nucleation rate

Many studies have demonstrated the capacity for electropulsing treatment to accelerate recrystallisation through enhanced nucleation rate, such as the investigations by Conrad *et al.* [1, 18, 19] into the effects of electric current pulses on recrystallisation in copper. In each study, it was found that the application of multiple high density DC electric current pulses (current density 8.0×10^8 A·m^{-2}, frequency 2Hz and duration 90μs) during the annealing of cold-worked copper enhanced the recrystallisation rate and reduced the frequency of twinning. Grain refinement was observed at lower annealing temperatures [1], while grain growth was enhanced at higher temperatures [18]. Electric current was also thought to affect the rate of nucleation of new strain-free grains, by enhancing subgrain coalescence[3] associated with improved dislocation mobility [19]. It was also considered that localised heating effects and electron-defect interaction might influence the response of copper microstructure under electropulsing [18]. Finally, it was shown that a continuous 1×10^7 A·m^{-2} DC current of equivalent Joule heating rate[4] to the pulsed condition did not produce the same effects on recrystallisation and recovery [19].

Further research by Lai *et al.* [56] demonstrated the effects of electropulsing on the recrystallisation of iron-based amorphous alloys. The authors noted that low temperature recrystallisation was achieved using different electropulsing parameters for two separate alloys. They proposed that there was some direct action by the electric current over a short pulsing time and the effect could not be attributed to thermal excitation alone. Teng *et al.* [3] found that high current density electropulsing was capable of producing nanocrystallised grains in amorphous $Fe_{78}B_{13}Si_9$; enhanced nucleation rate was thought to be the critical factor here. Similarly, Ma *et al.* [2] observed localised nanocrystalline γ-Fe structure in boron steel after electropulsing at current density 8.9×10^8 A·m^{-2}. This effect was also attributed to an enhanced nucleation rate resulting from reduction of the thermodynamic barrier through additional free energy supplied by the applied current.

A review by Conrad [114] discusses the recrystallisation of cold-worked metals and alloys by electropulsing. As part of the review, Conrad stated that the most significant effect of the application of electric current was on the nucleation rate of new grains, as the majority of papers reported the influence of both electropulsing and continuous DC current on the rate of early-stage recrystallisation. Barnak *et al.* [53] cited electropulsing-induced undercooling combined with irregular lamellar spacing

[3] Subgrain coalescence refers to a method of subgrain growth resulting from the dissolution of sub-boundaries. Alternatively, subgrain growth may occur through boundary migration, in which large subgrains consume smaller ones (Sandström, 1977).

[4] Joule heating is an effect that results from the interaction between electrons and atoms as electric current passes through a metal.

reduction as evidence for the effect of nucleation on colony or grain size in Pb-Sn alloy samples. They went on to discuss theories that might explain an electropulsing-enhanced nucleation rate at a relatively low temperature. The authors speculated that the effect of electropulsing on nucleation rate may stem from an increase in liquid-solid interfacial energy, or a reduced free energy difference between the two states. In addition it was found that skin and pinch effects[5] were limited in their effect on the nucleation rate of the samples. This is supported by Okazaki *et al.'*s earlier work [115] on the electroplastic effect,[6] in which skin and pinch effects were found to have very little influence on electroplasticity in polycrystalline titanium during electropulsing.

Electron wind is a well-known phenomenon in electromigration theory, used to explain electropulsing-induced recrystallisation [49, 116-121]. First modelled in the 1960s by Fiks [122, 123] and Huntington and Grone [124], the electron wind is a driving force for electromigration and results from the scattering of electrons by atoms or defects [123]. As current passes through a conductor, electrons collide with the constituent atoms of the material. Each collision transfers momentum from an electron to an atom, encouraging the atom to move from its location in the crystal lattice and hence contributing to the electromigration effect. In its most fundamental form, the electron wind is a function of the electron density, the average electron velocity, and the cross-section of the atom available for collision with electrons [125]. Electromigration (and hence the electron wind) have become an important research area in recent decades due to the rise of microelectronics. Very narrow wires and components can suffer from electromigration-induced void formation, resulting in system failure [126-128].

The electropulsing literature describes the electron wind as providing an additional force that acts on dislocations in a material. The literature states that it can enhance the mobility of dislocations by providing heterogeneous electromagnetic shielding, which provides an additional driving force during dislocation movement resulting from the interaction with drift electrons [47, 129]. In studies focussing on recrystallisation and grain refinement in titanium alloys and pure titanium sheet, Song and Wang [47, 54] discuss the effect of electron wind force on nucleation rate and dislocation mobility. They describe how reduction in dislocation density and improved mobility of dislocations, induced by the electron wind force, enhanced the nucleation rate of recrystallisation and produced a refined microstructure.

[5] Skin and pinch effects are, respectively, the concentration of current in the proximity of the material surface, and the appearance of radial compressive stresses as a result of magnetic field-induced pressure.
[6] The electroplastic effect describes the interaction between electrons and dislocations.

In a review of the theory of electroplasticity, Conrad [129] noted that reduced flow stress had been observed in metals as a result of high density electropulsing. Conrad compared calculated and experimentally determined values of the electron wind and determined that the reduced flow stress was a product of the electroplastic effect. Conrad proposed that the high density electropulsing produced an interaction between the electron wind and dislocations that improved the dislocation mobility, resulting in a reduced flow stress.

Zhang *et al.* [71] studied dynamic electropulsing-induced phase transformations in AZ91 magnesium alloy. The term 'dynamic' refers to the simultaneous application of electropulsing and rolling deformation; a schematic of the apparatus is shown in Figure 2.13. For comparison, static electropulsing was also conducted [121]. It was found that electropulsing was capable of inducing β-phase decomposition with increasing pulse frequency. However, while β-phase decomposition was observed in dynamic electropulsing samples, the static electropulsing samples showed a more accelerated phase transformation.

The authors suggested that the accumulation and annihilation of defects in the alloy produced by the electropulsing-induced electron wind resulted in a reduced dislocation density with increasing frequency. Zhang *et al.* believed that as the electric current acted to reduce the dislocation density, Gibbs free energy associated with the electropulsing process was used up through interaction between electrons and defects formed as a result of mechanical deformation. The authors state that the dynamic samples therefore possessed a lower total energy than the static specimens, thus reducing the capacity of the dynamic electropulsing process for acceleration of phase transformation.

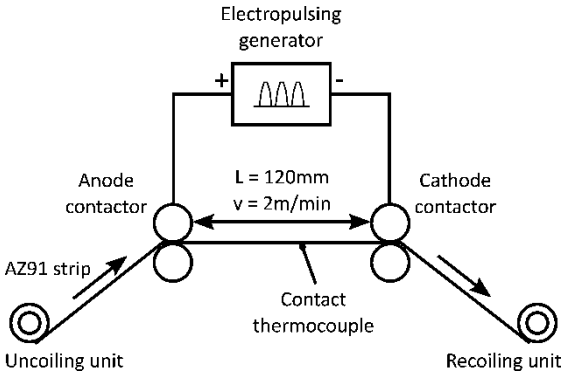


Figure 2.13. Schematic of the dynamic electropulsing process. Reproduced from [71].

Xu *et al*. [49] also offer an explanation for a reduction in dislocation density, through the action of the electron wind pushing dislocations towards grain boundaries and resulting in an accumulation of defects. Simultaneously, annihilation of the accumulated defects was thought to occur as a result of the combined action of thermal and electromigration effects.

Similar findings presented by To *et al.* [72] focus on the application of dynamic electropulsing to a eutectic Zn-Al based alloy during tensile deformation. In this case, multiple electropulses of current density ranging between 3.58×10^7 and 1.04×10^8 $A \cdot m^{-2}$ produced increasing levels of decomposition of

the zinc-rich η's phase with increasing current density. When the rate of phase transformation of static and dynamic electropulsing samples were compared, To *et al.* also found that the acceleration of phase transformation observed was much higher in static samples than in dynamic samples. However, it is not clearly stated in this paper whether accelerated phase transformation in the static electropulsing samples was obtained with or without prior deformation.

2.3.2. Current density

Research by Hao *et al.* [67] on electropulse-induced nanocrystallisation in amorphous alloys suggests that current density may be a critical factor in the crystallisation process. The study found that electropulse-induced low temperature recrystallisation in amorphous alloys a-$Cu_{50}Ti_{50}$, a-$Pd_{80}Si_{20}$ and a-$Zr_{60}Cu_{30}Al_{10}$ was observed when initial current density surpassed a critical threshold value. The authors suggest that the mechanism for this behaviour may revolve around an athermal process based on collective motion of atoms. Such concentrated electromigration behaviour was thought to enhance atomic diffusion. Further work by Mizubayashi *et al.* [68] concluded that inherent current density fluctuations exist in amorphous alloys and that high density regions experience a resonant collective motion of atoms due to electropulsing. Similarly to Hao *et al.*, the authors suggest that this resonant collective motion of atoms may induce dynamic atomic diffusion, thereby modifying the thermodynamic free energy of phases.

In a study on the effects of electropulsing on the microstructure of a heavily deformed pearlitic steel, Samuel *et al.* [7] observed accelerated spheroidisation of the lamellar eutectoid structure. Spheroidisation is described as the breakdown of cementite lamellae in pearlite colonies into smaller globular grains and is visible in the micrographs in Figure 2.14. The amount of spheroidisation was found to increase with the amplitude of the current density. The authors described the enhanced spheroidisation process as a function of rapid temperature increase associated with increasing current density. It was thought that high rate heating introduced a large number of vacancies into the steel, which migrated into the grains and enhanced the ability of elements to diffuse.

Zhou *et al.* [15] found that current density, in combination with high heating and cooling rate, was highly influential in determining the final refined grain size in low-carbon steel. They found that increased current density and average heating rate led to a decrease in average grain size. The grain refinement process is described in a schematic illustration, shown in Figure 2.15.

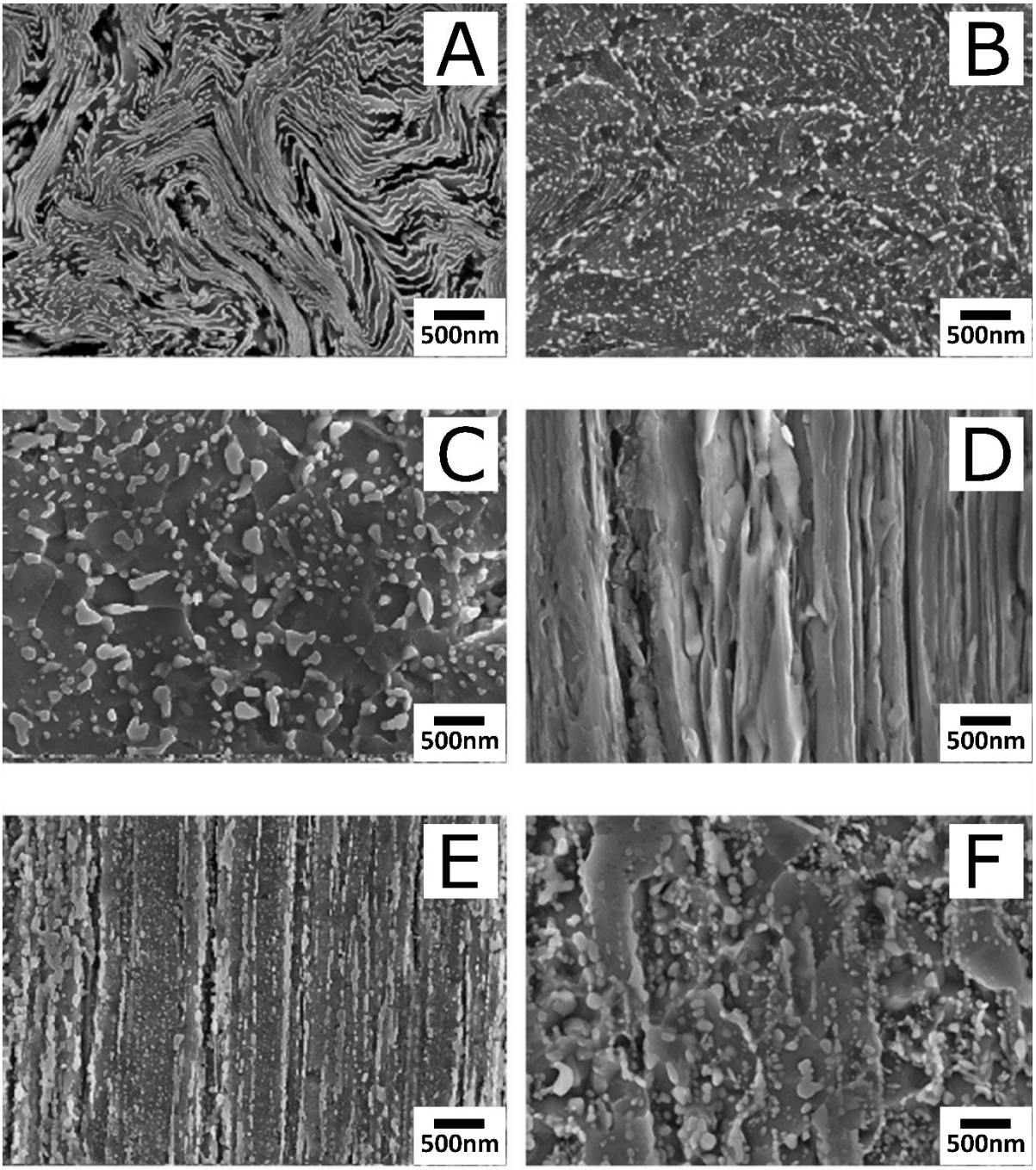


Figure 2.14. SEM micrographs demonstrating spheroidisation of cementite lamellae in deformed pearlitic steel samples after a single electropulse of current density (A,D) 7.73x10^{9} A·m^{-2}, (B,E) 9.82x10^{9} A·m^{-2}, and (C,F) 1.07x10^{10} A·m^{-2} along the cross-sectional and longitudinal directions. Reproduced from [7].

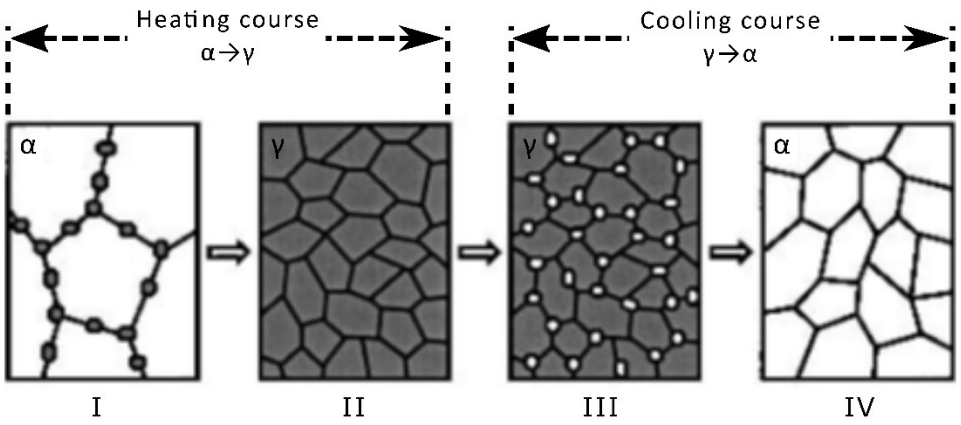


Figure 2.15. Schematic illustration for grain refinement and ultrafine grained microstructure formation: (I) formation of γ-phase nuclei, (II) formation of γ-phase grains by the growth of γ-phase nuclei, (III) formation of α-phase nuclei, and (IV) formation of α-phase grains by the growth of α-phase nuclei. Reproduced from [15].

The authors stated that due to the Joule heating effect and a decrease in the thermodynamic barrier, very small γ-phase nuclei formed at an accelerated rate in the grain boundaries of the α-phase over the heating course. Grains of γ-phase then formed from the γ-phase nuclei but the short treatment time prevents grain growth, causing the grains to be very fine as the α-phase fully transforms into γ-phase. The inherent short treatment time necessary for grain refinement here suggests an important advantage to the electropulsing process over more time-consuming processes such as annealing.

Over the cooling course, the process acts in reverse. The α-phase nucleates at the grain boundaries of γ-phase grains at an accelerated rate due to the increased grain boundary volume fraction provided by the fine γ-phase grains. Finally, the γ-phase completely changes to refined α-phase grains. However, while Zhou *et al.* did emphasise the dominance of current density, heating and cooling rate in determining final grain size, they also stated that a decreased thermodynamic barrier and an enhanced nucleation rate contributed to the effects observed.

Qin *et al.* [6] found that the application of a single electropulse of highest density 9.61×10^9 $A \cdot m^{-2}$ was capable of producing nanoscale particles in cold-drawn pearlitic steel, Figure 2.16. The application of electropulsing resulted in the formation of fine (approximately 30nm) spheroidised cementite particles that were distributed homogeneously across the sample. The refinement of the cementite particles was thought to stem from the additional free energy provided by the electropulsing process. An increased level of free energy provided a larger interface area for microstructural transformation, enabling finer particles to form. Further work by Samuel *et al.* [7] supported these findings, demonstrating the same microstructural spheroidisation and grain refinement with increasing current density.

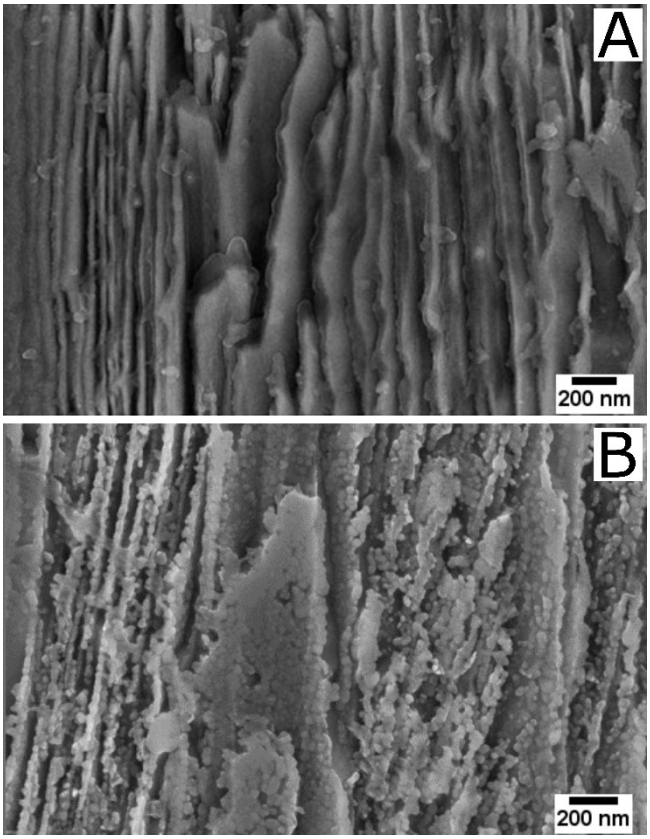


Figure 2.16. SEM micrographs of electropulse-induced microstructure transformation in pearlitic steel A) before electropulse and B) after electropulse. Reproduced from Qin et al [6].

Conrad [114] also highlighted the significance of current density in successful acceleration of solid state phase transformations, stating that a current density greater than approximately $1x10^7$ $A{\cdot}m^{-2}$ could accelerate phase transformations using both continuous current and electropulsing. However, work by Teng *et al.* [3] serves to highlight the complexity of the mechanisms describing recrystallisation behaviour in electropulsed samples. High current density electropulsing of $1.8x10^9$ $A{\cdot}m^{-2}$ and pulse duration 40µs was applied to two amorphous $Fe_{78}B_{13}Si_9$ samples. One sample (pulse frequency 20Hz for 65 minutes, producing an average Joule heating temperature of 220°C) was fully recrystallised. The second (treated in two stages with pulse frequency 18 and 14Hz for 5 and 8 minutes, producing average Joule heating temperatures of 210 and 175°C respectively) was partially recrystallised. Fine nanocrystallised grains were formed in both samples as a result of the electropulsing treatment. As the current density and pulse duration remained constant for both samples, this study suggests that other factors can affect the rate of crystallisation in metallic materials.

The research by Teng *et al.* [3] presents differences in crystallisation rate that appear to be linked to the variation of pulse frequency, total pulsing time and average temperature rise due to Joule heating. An earlier study by Conrad *et al.* [130] found a similar dependence on pulse frequency. Grain growth in copper was inhibited by electropulsing and the observed effect increased with pulse frequency over

the range 0.07 to 7Hz. Furthermore, Conrad *et al.* observed that pulse duration had limited influence on the magnitude of electropulsing effects beyond a certain saturation time. As it was observed that the effects of electropulsing were not directly proportional to the number of drift electrons passing through a unit area, the occurrence of which might suggest a dependence on the pulse duration, Conrad *et al.* concluded that the effects of electropulsing were most significant when applied in pulse durations less than 50μs.

It is clear that while current density seems to be a critical factor in initiating recrystallisation, it is not the only component affecting the recrystallisation rate. The research described here shows that other variables, such as heating rate and processing method, are capable of affecting the recrystallisation behaviour of metallic materials. These factors will be considered in the following sections.

2.3.3. High-rate heating and cooling

The importance of high rate heating and cooling in enhancing recrystallisation has been discussed in depth throughout the literature. Joule heating has been suggested as a critical factor affecting the acceleration of recrystallisation.

The earliest example of electropulsing applied as a rapid heating process was published in 1967 by Wallbridge and Parr [131]. The authors used electric current heating to treat low carbon steels of carbon composition between 0.06 and 0.12wt%C. Few details on the pulsing process are provided but the heating rate was approximately 1000°C·s^{-1}, the quench rate 2000°C·s^{-1} and holding times ranged between 0.15 and 30 seconds. Heating temperature ranged between 775 and 1050°C. The applied electric current was found to induce martensitic microstructure and improve the tensile strength of the material, but the authors do not offer any electropulse-focused argument for the behaviour.

Later research by Xu *et al.* [57] on recrystallisation in cold-worked α-Ti combined electropulsing with furnace heating. They found that when the combined temperature of the processes was maintained below 600°C for 30 minutes, low current density electropulsing of 1x10^{7} A·m^{-2} produced grain refinement resulting from an enhanced nucleation and recrystallisation process. The authors conclude that the enhanced nucleation observed was a result of high heating rate produced by an electron wind.[7] Xu *et al.* also observed that when the temperature was maintained at 600°C for 30 minutes, electropulsing produced coarser grains. Increasing current density was thought to enhance the rate of impurity migration, thus encouraging grain coarsening.

[7] In this case the electron wind is described as a transfer of momentum between electron drift and the crystal lattice.

Results presented by Lai *et al.* [9] suggest that a minimum temperature rise induced by the Joule heating effect is necessary for the initiation of low temperature crystallisation. In tests on various iron-based amorphous alloys, samples cooled to lower the Joule heating effect to below an average temperature of 115°C did not exhibit any microstructural change, while low temperature crystallisation was observed in samples that experienced an average Joule heating-induced temperature rise of between 353 and 395°C.

Zhang *et al.* [66] used an electric current pulse of maximum current intensity $2.6x10^4$ A and pulse duration 400µs to induce a martensitic phase transformation in a titanium alloy. After electric current was applied, initial α-Ti grains were found to contain lamellae of both α-Ti and β-Ti phase. The martensitic phase transformation observed by Zhang *et al.* was stated as being the result of rapid heat treatment. In addition, Takemoto and Mizubayashi [52] found that when crystallisation occurred quickly at higher temperatures (above approximately 337°C) in amorphous $Cu_{50}Ti_{50}$, nucleation at the early stage of crystallisation was accelerated. This behaviour was observed when an electric current of current density below $5x10^7$ $A{\cdot}m^{-2}$ was applied to the samples.

Research carried out by Zhou *et al.* [20, 132, 133] seems to confirm that as previously discussed, high heating and cooling rate alone is not sufficient to induce recrystallisation, phase transformation or grain refinement in metallic materials. The authors attempted to establish the role of high heating and cooling rate in producing enhanced recrystallisation behaviour in a Cu-Zn alloy by presenting a comparison of the effects of electropulsing with those produced by pulsed laser of equivalent heating rate. Initial research describes an electropulsing regime that produced a heating rate of $1x10^6$ $°C{\cdot}s^{-1}$, with pulse duration 800µs, peak pulse period 120µs and maximum current density $1.8x10^{10}$ $A{\cdot}m^{-2}$. A similar heating rate was achieved by a 1000µs pulse from an Nd:glass laser. It was found that an increased number of small, homogeneous β'-phase precipitates developed in the electropulsed samples, but no microstructural changes were observed in the laser samples despite the similarity in heating and cooling rates [133]. The increased nucleation rate was thought to have been achieved through a reduction of the thermodynamic barrier as a result of the electropulsing treatment, rather than the rapid heating and cooling rates associated with the process.

A second paper by Zhou *et al.* [132] using a similar electropulsing and laser treatment arrangement also reported the diffusion of atoms between α-phase and β'-phase during electropulsing treatment. Furthermore, Zhou *et al.* observed α-phase ultrafine-grained microstructure in electropulsed samples, but not in those treated by laser pulsing. The authors stated that their results indicated that the generation of ultrafine-grained microstructure was dependent on solid-state phase transformations present in the α-phase but absent in the β'-phase, as no β'-phase ultrafine-grained microstructure was

observed. Finally, a third paper by Zhou *et al.* [20] describes the observation of a diffusive phase transformation from α and β' phases to β in electropulsed samples, but no transformation in laser pulsed samples. It is important to point out that it is unusual to observe this type of phase transformation under rapid heating conditions, as long-range diffusion is required. The authors theorize that an enhanced diffusion coefficient resulting from the applied electric field may have produced the observed phase transformation.

Further work by Zhou *et al.* [58] found that high rate heating, combined with enhanced dislocation mobility and atom migration, accelerated the nucleation rate of recrystallisation. In addition, Zhou *et al.* [134] also found that electropulsing produced nanostructured γ-Fe in an initially coarse-grained low-carbon steel over a short treatment time. They suggested that the phase transformation may have resulted from high heating and cooling rates induced by electropulsing. The enhanced nucleation rate of the γ-phase occurred through reduction of the thermodynamic barrier during electropulsing.

Pan *et al*. [8] conducted electropulsing experiments on a medium carbon 0.45wt%C steel with initial martensitic microstructure. A capacitor discharge unit was used to apply pulsed current of maximum current density $2x10^{10}$ $A{\cdot}m^{-2}$ at the narrowest part of the sample. The duration of each sinusoidal-shaped pulse was 160μs, the pulse frequency was 0.25Hz and the duration of the treatment was 40 minutes. The researchers found that electropulsing did not produce any microstructure change in terms of grain orientation or size. However, the tensile strength was shown to increase from 695MPa as-quenched to 1180MPa after electropulsing. The tensile strength of the electropulsed samples was also greater than that of furnace-tempered control samples. As no grain size or texture variation was observed, the improved tensile properties were ascribed to a reduction in dislocation density and residual stresses. Based on dislocation density measurements the authors found that the effect of the electron wind force was very small, while the Joule heating was a primary factor in the dislocation activation rate.

The literature shows that high rate heating is an important factor capable of influencing the characteristics of electropulsing treatment. However, the literature cannot definitively identify it as the sole driving force in electropulsing treatments. This suggests that the combined effects of current density and high rate heating might produce the electropulsing behaviours described.

2.3.4. Thermal and athermal effects

More recently, the multi-factor mechanism theory of thermal and athermal effects has been given significant consideration in the literature. Mechanisms that describe the thermal and athermal effects revolve around the co-operative actions of electron wind and Joule heating as discussed previously, combining electromigration with a rapid temperature increase. An early study carried out by

Sprecher *et al.* [11] gave some indication of the nature of the relationship between these components by investigating the factors governing the electroplastic effect. While thermal expansion due to Joule heating was found to be the most significant component of the reversible strain, other factors were also found to enhance the rate of plastic flow, due to an interaction between drift electrons and dislocation motion. Sprecher *et al.* concluded that while dislocations were affected by the athermal electron wind under high density DC current pulses, drift electrons may also have affected other parameters. These parameters were said to include strain rate, activation enthalpy and the effective stress.

Guan *et al.* [28] applied an electropulsing treatment to AZ31 magnesium alloy and concluded that thermal and athermal effects were responsible for the enhanced nucleation rate observed. In this case, the pulsed Joule heating produced a compressive stress gradient, while the athermal effects were attributed to the electron wind. This combination of factors was thought to enhance grain boundary migration as a result of accelerated interchange of vacancies and atoms through the increased driving pressure provided by electropulsing. Accelerated boundary migration then enhanced early stage nucleation and inhibited subsequent grain growth.

Research on the recrystallisation behaviour in electropulsed cold-rolled silicon steel strips by Hu *et al.* [10] described a similar theory of electron wind-accelerated dislocation climb leading to an enhanced nucleation rate and retarded recrystallised grain growth. Grain refinement was observed in the electropulsed sample (grain size 0.5-2.0µm) when compared to a non-electropulsed, heat treated sample (grain size 2-6.0µm). Electron migration was thought to be an important factor in electropulse-induced low temperature recrystallisation; this atomic flux was attributed to the thermal and athermal effects. Similar conclusions were drawn in earlier work by Xu *et al.* [135] focussing on dynamic electropulsing of copper wire. In this study, enhanced mobility of vacancies through the combination of thermal and athermal effects was also assumed to be a key factor in promoting dislocation climb and annihilation, leading to an enhanced nucleation rate and retarded growth of recrystallised grains.

Increased atomic flux resulting from the thermal and athermal effects was also stated as being the probable cause of accelerated nucleation rate observed by Jiang *et al.* [12] in a study describing the effects of electropulsing on Mg-9Al-1Zn alloy strip. In this case, fine recrystallised grains were formed over a very short amount of time. Further work by Jiang *et al.* [136] attempted to provide greater detail on the nature of the relationship between the thermal and athermal effects. The authors found that the rate of accelerated recrystallisation observed in the Mg-9Al-1Zn alloy could only be achieved when the thermal effect due to Joule heating was large enough to accelerate dislocation climb and

subgrain growth. The influence of the athermal effect on these factors was too small to induce recrystallisation behaviour alone.

A dynamic electropulsing experiment conducted by Xu *et al.* [119] on an Mg-Al-Zn alloy produced similar results, and here the authors went further in their explanation of the combined influence of thermal and athermal effects. They stated that the enhanced mobility of dislocations and vacancies induced by the athermal effect acts to decrease the density of piled-up dislocations at grain boundaries, and described the electron wind force as being able to untangle sections of dislocations. The high temperature Joule heating activates dislocations on non-basal planes, rearranging the dislocation structure. The density of dislocations was thought to be reduced by the coupled action of the thermal and athermal effects. Similarly, Liao *et al.* [137] observed that the novel dynamic thermo-electropulsing rolling (TER) process accelerated dynamic recrystallisation in AZ31 magnesium alloy by reducing the dislocation density through annihilation, climb and cross-slip resulting from self-diffusion-controlled thermal and athermal effects.

The thermal and athermal effects mechanism combines high rate heating with electric current-associated phenomena, experimental factors which have both been shown to alter the effects of electropulsing in some form during testing. This multi-factor mechanism therefore seems to be the most valid mechanism theory as yet proposed in the field, but further research is required to fully understand the processes involved.

2.3.5. Crack healing

When a material experiences damage or fatigue, microcracks develop. These cracks may grow and accumulate, eventually causing the material to fracture and fail. It has been shown by a number of papers that the application of electropulsing to metallic materials can slow, prevent and even heal cracks, often lengthening the lifespan of the material. Early research by Conrad *et al.* [62] suggested that electropulsing was capable of increasing the fatigue life and reducing the amount of intergranular cracking in polycrystalline copper. These improvements were thought to result from a reduction in the geometry and separation of fatigue-induced persistent slip bands, also referred to as an increased homogenization of slip. Electron-dislocation interaction or electromigration effects[8] were proposed as mechanisms for the enhanced mobility required.

A study conducted by Zhou *et al.* [22] focused on the potential crack healing abilities of electropulsing in damaged 1045 steel samples. It was observed that the growth rate of cracks, formed during water

[8] Electromigration is the term used to describe the directed motion of atoms resulting from an applied electric field (Conrad, 1998). Zhou *et al* believed that electromigration was capable of reducing the volume of vacancies in a material.

quenching after heating to 840°C, was reduced after electropulsing treatment of pulse duration 0.2ms. Furthermore, equiaxial crystals were formed at crack tips, which acted to partially fill or heal the damaged sections as shown in Figure 2.17.

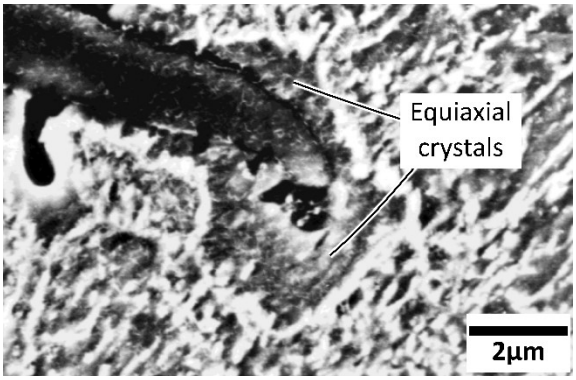


Figure 2.17. SEM micrograph showing equiaxial crystal formation at a crack tip. Reproduced from [22].

The researchers also noted the selective behaviour of electropulsing, observing more pronounced effects in damaged areas than in undamaged sections. This property is explained by regional resistivity and electric current detour distance. A damaged area would demonstrate a higher regional resistivity compared to an undamaged section, due to the greater volume of cracks and microstructural defects. As current moves through and detours around an area of higher resistance, a local increase in temperature is induced that acts to increase the observed effects of electropulsing.

Zhou *et al.* also discuss the conditions necessary to achieve crack filling under electropulsing. Rapid heating and thermal compressive stress resulting from delayed thermal expansion were thought to be capable of producing the effect. The authors proposed three mechanisms for the process: dislocation fill, diffusion fill and compression fill.[9] This theory was later used by Song *et al.* [23, 24] to explain the healing of primary defects and damage resulting from plastic deformation observed in TC4 titanium alloy sheet. Wang and Song [138] also suggested that local recrystallisation due to electropulse-induced temperature increase and thermal compressive stress produced microcrack healing in TA15 titanium alloy sheet. Continued research by Zhou et *al.* has reported similar findings, highlighting the effects of electropulsing on crack healing in steels. Crack healing observed in 1045 steel, as shown in Figure 2.18 (label A), was attributed to the effects of temperature and thermal compressive stress [60].

Crack healing in a steel sample was described by a further paper as resulting from low temperature plasma produced by electrical breakdown of the crack, or the motion of effective atoms towards the crack. The motion of effective atoms was dependent on sufficient reduction of the crack face separation distance as a result of thermal expansion [61]. Here, the motion of atoms theory expands

[9] During dislocation fill, dislocations experiencing enhanced mobility due to the applied electropulsing current transfer into the crack. During diffusion fill, the diffusional ability of atoms is enhanced by the electropulsing process and atoms diffuse towards the crack. Compression fill involves the movement of atoms into the crack through a thermal compressive stress.

on the idea of diffusion fill previously proposed by the authors. It is also noted that the selective properties of the healing process remove the need for information on location and geometry of a crack prior to healing, as damaged regions are self-identifying due to their higher local resistivity.

Evidence of the healing effect of electropulsing in other metallic materials can also be found in the literature. In addition to the work by Conrad *et al.* [62] on polycrystalline copper, research by Qiao *et al.* [51] suggests that damage or work hardening in aluminium alloys 4043 and 2024 was partially healed by electropulsing treatment. In this case, the authors theorised that the damage recovery resulted from a decrease in the volume of defects in the samples due to electropulse-induced recrystallisation.

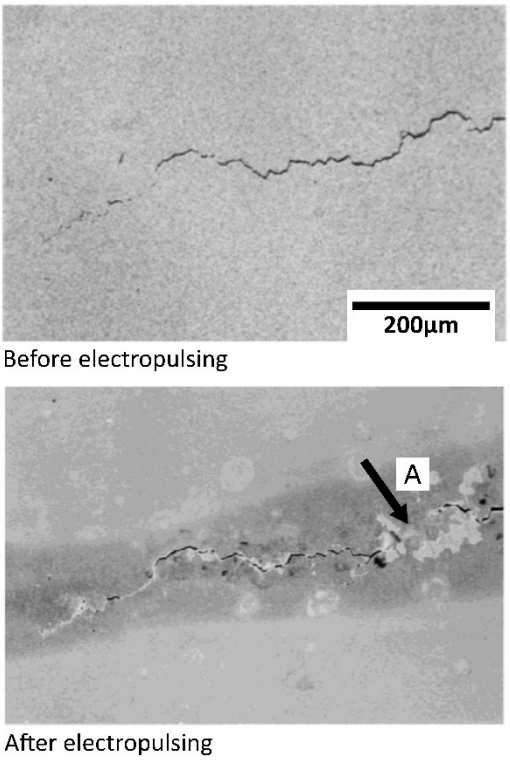


Figure 2.18. SEM micrographs of crack healing in 1045 steel. Modified from [60].

A theoretical study conducted by Qin and Su [59] produced a thermodynamic model of crack healing, incorporating the relationship between current density, crack geometry and healing driving force. Different materials were modelled by varying the tensile strength used in the calculation. The researchers suggested that a critical current density exists, beyond which crack healing may occur in a range of materials.[10] The application of current was thought to reduce the driving force for crack growth, and increase the driving force for healing, causing the crack to shrink. Figure 2.19 suggests that the critical current density lies between approximately 3 and 6×10^5 $A \cdot m^{-2}$ for the range of metals considered. A critical current density is also proposed by papers focussing on electropulsing-induced phase transformations, discussed previously [67, 114].

[10] In this study a range of materials were represented through variation in the value of Young's modulus applied in the calculations. Young's moduli of 80, 100, 150 and 200GPa were selected, with the actual Young's modulus of a steel and an Ni-Ti alloy measured as approximately 200GPa and 83GPa respectively.

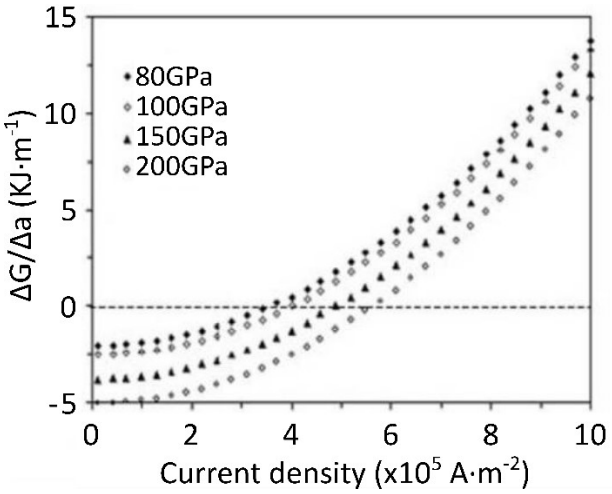


Figure 2.19. Theoretical healing driving force as a function of current density. Varying tensile strengths represent different materials. Modified from [59].

2.3.6. Pre-deformation effects

Several studies have shown that pre-deformation of metallic samples, most commonly through cold work, can affect the response of the sample to electropulsing treatment. Early research by Conrad *et al.* [1] studied how cold drawing affected the recrystallisation behaviour of copper during electric current pulsing. Pulses of current density $8x10^8$ A·m^{-2} and 90µs duration were applied at a rate of two pulses per second to specimens of varying reductions. Increasing cold work produced a corresponding decrease in recrystallisation temperature in both annealed-only and electropulsed samples. However, while the electropulsed samples exhibited enhanced recovery and recrystallisation rates compared to annealed-only samples, the observed effects were less noticeable with an increasing amount of pre-deformation. Conrad *et al.* also observed that electropulsing produced a finer recrystallised grain size, but similarly, while cold work enhanced the response of the copper samples to electropulsing, microstructural changes were less pronounced with increasing cold work as demonstrated by Figure 2.20. The effects of cold work on the recrystallisation behaviour were explained by Conrad *et al.* to be a result of electric current-enhanced strain-free grain nucleation through subgrain coalescence. With increasing prior cold work, the amount of coalescence required decreases and hence the observed effect of electric current pulsing is lower.

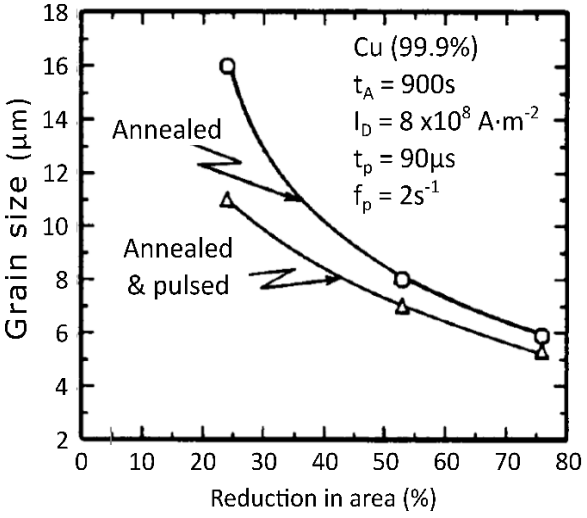


Figure 2.20. Recrystallised grain size versus amount of prior cold work as a function of current pulsing. Reproduced from [1].

Valeev and Kamalov [70] observed similar thermally-activated recrystallisation results through their work on the structure evolution of copper. Samples were cold-rolled to strains of ε = 0.3 and 0.8, defined in terms of the initial and final strip thickness, and electropulsed. As for annealed-only samples, the recrystallisation temperature of the electropulsed copper samples was observed to decrease with increasing pre-deformation. However, a reduction in the response of the recrystallisation behaviour with increasing cold work as described by Conrad *et al.* [1] was not considered in this case.

More recently, Guan *et al.* [28] assessed texture evolution through electropulsing of cold-rolled AZ31 magnesium alloy strips, of rolling reduction 10%, 22% and 31% respectively. It was observed that at low rolling reduction (10% deformation), incomplete recrystallisation focussed around the grain boundaries occurred while at high rolling reduction (31% deformation), recrystallisation progressed until completion. Similar to previously described crack healing mechanisms, it was thought that the thermal and athermal effects were stronger in areas of higher defect volume due to the increased resistivity and enforced current detour in these regions. Therefore, the thermal and athermal effects would be expected to appear more powerful in the high rolling reduction samples which contain a larger volume of defects. Due to the selective effect of electropulsing a greater driving force is produced, thereby enhancing the rate of recrystallisation.

Guan *et al.* also describe potential recrystallisation mechanisms to explain the variation of recrystallisation rate with cold work observed. The authors state that Strain Induced grain Boundary Migration (SIBM), in which an area experiencing strain in one grain boundary initiates the nucleation of previous grain boundaries, is a key factor in low rolling reduction recrystallisation. Fine grained microstructure is formed during electropulsing treatment as SIBM changes to the twin recrystallisation method, in which nucleation sites begin to appear in twins and shear bands.

Samuel *et al.* [7] applied high intensity electropulsing to pearlitic steel deformed to various strain rates. It was found that the application of electropulsing to cold-drawn pearlitic steel induced spheroidisation in the lamellar structure of the material, an effect that increased with current density. Furthermore, the authors observed that samples cold-drawn to a higher true strain rate exhibited an enhanced spheroidisation process. As processes such as cold drawing introduce microstructural defects and dislocations, thus increasing the stored strain energy in the metal, the authors theorised that the energy storage associated with the deformation process is critical to the enhancement of spheroidisation. The spheroidisation enhancement effect increased with reduction in sample area and therefore the increased stored strain energy.

2.3.7. Mechanical Properties

The application of electropulsing has been found to have various effects on the mechanical properties of different metallic materials. Samuel *et al.* [7] observed that increasing the amplitude of current density produced a corresponding decrease in the Vickers hardness of severely deformed pearlitic steel samples, as shown in Figure 2.21. This effect was explained as resulting from microstructural change induced by electropulsing. The observed fine and coarse spheroidisation of pearlite lamellae and cementite particles, respectively, were associated with the decrease in Vickers hardness.

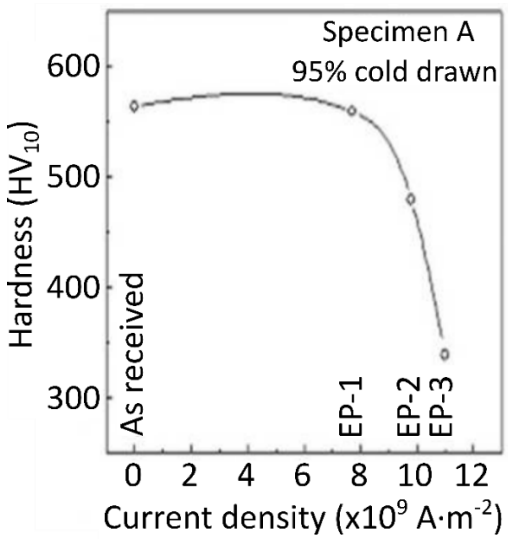


Figure 2.21. Variation in hardness with increasing amplitude of applied high intensity electric pulses. Vickers hardness values were: as received sample 564HV$_{10}$; EP-1 559HV$_{10}$, EP-2 480HV$_{10}$, EP-3 339HV$_{10}$. Reproduced from [7].

Similar behaviour was observed by Xu *et al.* [57] in α-Ti that was simultaneously electropulsed and furnace heated. A decrease in hardness was observed with increasing current density. Zhang *et al.* [121] also note that the Vickers hardness of cold-rolled AZ91 alloy was reduced with increasing pulse frequency. In this case, the authors attribute the reduced hardness to the reduction in dislocation density associated with electropulsing treatment.

Conversely, Qin *et al.* [6] found that Vickers hardness increased after electropulsing in a cold-drawn pearlitic steel, rising from 415HV$_{10}$ to 460HV$_{10}$ after a single pulse of highest current density 9.61x10^{9} A·m^{-2}. In this case, the authors state that the increase in hardness correlated with the observed grain refinement. In their study on electropulsing of iron-based amorphous alloys, Lai *et al.* [56] found that the hardness of the alloys increased slightly after electropulsing treatment of current densities 1.54x10^{9} A·m^{-2} and 7.58x10^{8} A·m^{-2} respectively. More recently, Lai *et al.* [9] also found that in general, the microhardness of iron-based amorphous alloys decreased and then increased with the application of electropulsing. However, the authors found no significant difference between the hardness of the electropulsed samples and samples that had simply been heated in a furnace to the same temperature [9]. This suggests that if the application of electric current is indeed capable of enhancing the hardness of metallic materials, the increase may be close to that observed in similarly annealed samples. If this is the case, then the main advantage inherent to electropulsing

lies in the processing time required to produce such an effect, compared to more traditional methods such as annealing.

Table 2.1. Tensile properties of annealed and electropulsed samples, as reported by Zhou et al. (2004), pp.1950 Table 1.

Sample	Treatment conditions	Tensile strength, σ_b *(MPa)*	Yield strength, $\sigma_{0.2}$ *(MPa)*	Elongation *(%)*
A	Annealed – 30mins @ 570°C	383	176	41
B	Annealed – 30mins @ 650°C	350	113	47
C	Electropulsed – max current density $1.7x10^{10}$ $A{\cdot}m^{-2}$, approx. Joule heating 600°C	395	214	45

Zhou *et al.* [58] found that electropulsing was able to affect a number of mechanical properties of cold-worked brass. As shown in Table 2.1, electropulsed sample C demonstrated improved properties when compared with annealed samples A and B. In this case it was shown that electropulsing was able to produce improved tensile and yield strength and equivalent percent elongation over the annealing process. Zhou *et al.* attributed the improvement of mechanical properties in brass to the smaller, more uniform grain size formed through the application of electropulsing treatment.

Hu *et al.* [10] produced similar results by electropulsing cold-rolled silicon steel strips. They found that an electropulsed sample exhibited equivalent tensile strength and elongation properties to a traditionally heat treated sample after both samples had undergone full recrystallisation. However, research by Qiao *et al.* [51] described increased elongation in aluminium alloys, but a decrease in ultimate tensile strength. Wang and Song [138] suggested that electropulsing was capable of optimising the relationship between ductility and tensile strength in cold-rolled TA15 titanium alloy sheet. The process produced samples with improved elongation yet no obvious decrease in tensile strength when compared with samples that had not experienced any electropulsing.

It is also important to consider the effects of static and dynamic electropulsing, as some studies have shown significant differences in the mechanical properties resulting from this processing variation. Zhu *et al.* [118] observed that the elongation of a Zn-Al alloy sample dynamically electropulsed at current intensity 10A (current density $8.13x10^{6}$ $A{\cdot}m^{-2}$) increased by 437% when compared with a non-electropulsed sample. A supporting paper by Zhu *et al.* [120] found that while static electropulsing of a Zn-Al alloy was also capable of enhancing the plastic elongation by 57%, the dynamic electropulsing process was more effective in enhancing the elongation of the material. However as previously discussed, static electropulsing has been found to be more effective in accelerating phase

transformation than dynamic electropulsing [71, 72]. These findings suggest that it is necessary to give careful consideration to the processing methods used. In this case, improved mechanical properties and accelerated processing must be balanced to achieve the desired material characteristics.

2.3.8. Discussion

Numerous studies have shown that electropulsing is capable of affecting or altering the microstructure and properties of various metallic materials. The literature available supports the idea that electropulsing can induce phase transformation through enhanced nucleation and recrystallisation rates, often resulting in grain refinement and enhanced mechanical properties. A number of factors have been shown to affect the recrystallisation behaviour of a range of metallic materials. In particular, research suggests that appropriate manipulation of current density is an important consideration when determining electropulsing parameters. Some studies have shown that with increasing current density, the rate of nucleation and phase decomposition may increase and the average grain size may decrease. Furthermore, it is possible that low temperature recrystallisation and the associated effects of electropulsing may only be observed above a certain threshold current density. However, studies in which low temperature recrystallisation and/or grain refinement are observed tend to involve a combination of high current density and high heating and cooling rate often resulting from the Joule heating effect.

Other theories available in the literature suggest that additional Gibbs free energy provided by electropulsing treatment may act to reduce the thermodynamic barrier, thus accelerating the nucleation rate. In addition, the range of electropulsing parameters applied across the literature often vary; while some information is available on optimised operating procedure, further research is required to produce appropriate application parameters for specific materials. However, in this respect some theories appear to hold constant over a range of materials. For example, pulse duration is thought to have limited effect on the electropulsing process beyond a saturation point, allowing advantageously short processing times. The majority of studies are able to produce recrystallisation in samples using extremely short pulse duration, suggesting that this variable can be neglected as a critical factor. Similarly, predeformation has been shown to enhance the effects of electropulsing in a range of materials, suggesting that the influence of deformation can be assumed to be relatively constant in that enhanced electropulsing behaviour is observed to different degrees in different materials.

The separation of the effects of key factors such as current density and heating rate is a complex process but the theory of thermal and athermal effects has been developed in an attempt to clarify the critical components of the electropulsing mechanism. Research in this area uses specific aspects

of current and heating rate to produce a multi-factor mechanism theory. Generally, it is thought that the athermal electron wind effect acts to enhance the mobility and reduce the density of dislocations, introducing a force on the dislocations and resulting in their accumulation and annihilation at grain boundaries. The combination of electron wind with the thermal Joule heating effect results in an enhanced nucleation and recrystallisation rate. Mechanisms defined via the thermal and athermal effects may have particular merit, as numerous studies have highlighted the fact that no single parameter can determine the effectiveness of an applied electropulsing treatment. Moreover, a significant amount of the literature demonstrates that high rate heating and electromigration through high current density electropulsing are critical and interlinked parameters. Therefore a multi-factor mechanism such as the thermal and athermal effects theory is particularly appealing.

Research on the influence of pre-deformation in electropulsing studies highlights an interesting opportunity for further optimisation of the process. A number of papers have observed the variation of electropulsing-induced recrystallisation behaviour with the rate of deformation. For each case considered in this review, the recrystallisation temperature under electropulsing was reduced when some form of pre-deformation was applied prior to treatment. Early research also suggests that an upper limit for pre-deformation rate exists, beyond which saturation of the effect occurs. In this case, optimisation of the processing parameters (strain rate or percent elongation/reduction) would be necessary to improve the time and energy efficiency of electropulsing treatment. A number of theories that seek to explain the exact effects of pre-deformation on recrystallisation temperature under electropulsing are presented in this review. The selective effect of electropulsing is particularly interesting as evidence for the behaviour has been observed through both crack healing and pre-deformation research independently. Furthermore, the fact that no previous information on crack geometry or location is required before healing may begin is a particular advantage. While it is clear that the selective healing property of electropulsing encompasses particular inherent procedural efficiencies that might encourage further development of an associated healing process for use in the field, the complete mechanism describing crack healing in metallic materials is not yet clear.

While the exact mechanisms behind the electropulsing process are yet to be clarified, it is evident that the microstructural changes induced by such treatment often result in altered mechanical properties. Critically the mechanical property enhancements observed in electropulsed materials have been observed to equal or surpass those obtained by more traditional heat treatment processes such as annealing, which generally require much longer processing times. In particular, the literature highlights elongation as a property consistently enhanced by electropulsing treatment in a range of

metallic materials. It is thought that this enhancement is a result of the finer, more uniform grain structure often observed in electropulsed materials.

However, it is also important to remember that any improvement in ductility should theoretically result in a decrease in tensile strength, and vice versa. Despite this, the literature suggests that in some cases ductility can be improved by electropulsing with little or no detrimental effect on the tensile strength. Some research also theorises that electropulsing may be capable of producing an optimum balance between elongation and tensile strength, but further research is required to clarify this behaviour. A process capable of producing a high tensile strength metal with high ductility would have potential advantages for the manufacture and forming of, for example, high impact structures and armour. Electropulsing has also been observed to affect the hardness properties of a range of metallic materials, but the effects are still unclear as various studies have demonstrated both increasing and decreasing hardness as a result of electropulsing. Further research is necessary to understand these effects, as in both cases of increased and decreased hardness, grain refinement is cited as most likely to cause the observed change.

2.3.9. Conclusion

Throughout the literature, a number of factors have been identified as having some effect on the outcome of electropulsing treatment. However, it seems increasingly clear that no single factor can be identified as governing the mechanism behind the process. The theory of thermal and athermal effects seems to be the most robust mechanism theory available in the literature to date, as it takes into account multiple factors that have been shown by previous studies to have some effect on recrystallisation behaviour in metallic materials. However, theories focused on the addition to the system of electropulsing-induced Gibbs free energy must not be ignored; our limited current understanding of the mechanisms involved prevents the theory of enhanced nucleation resulting from a lowered thermodynamic barrier from being excluded.

Further research is required to fully understand and clarify the mechanisms underlying the electropulsing process. It would also be advantageous to optimise the processing parameters for individual materials in order to fully utilise the potential advantages of short processing time and low energy manufacture over traditional methods such as annealing. Research must be carried out to clarify the varying mechanical property changes observed across the literature, as the process cannot be feasibly applied in industry without such data. Finally, further work in the area of crack healing could be implemented, as a fully developed damage recovery process could potentially be utilised in industry in a number of pre-existing applications. Crack healing is a reactive process ultimately intended to be applied to a work hardened operational material and, as such, it is possible that there

would be limited or no requirement for alterations to current infrastructure or material manufacturing methods.

3. Experimental methods

3.1. Initial material characterisation

3.1.1. Material summary and composition

The bulk of experimental work was carried out on pearlitic steel plate of carbon composition 0.92wt%C. As the carbon content is greater than the eutectoid composition of 0.8wt%C, this plate can be referred to as a hyper-eutectoid steel [139]. Further tests at certain parameters were conducted on additional material, a hypo-eutectoid 0.73wt%C steel rod. Both the plate and rod had fully pearlitic microstructure, and their compositions are listed in Table 3.1. The following sections describe each steel composition in greater detail and include microstructure and property characterisation.

Table 3.1. Composition of experimental materials.

Description	C	Si	Mn	P	S	N	V
	(wt%)						
Hyper-eutectoid pearlite plate	0.92	0.9	0.86	0.010	0.012	-	0.110
Hypo-eutectoid pearlite rod	0.73	0.2	0.5	0.013	0.007	0.0028	-

3.1.2. As-received microstructure

3.1.2.1. Hyper-eutectoid plate (0.92wt%C)

The initial microstructure of 0.92wt%C pearlitic steel plate is shown in Figure 3.1, with microstructure and property characteristics summarised in Table 3.2. The micrographs show a fully pearlitic microstructure with a dominant lamellar configuration of average interlamellar spacing (ILS) 194nm (images A, B). Regions of lamellar breakdown and spherical cementite particles were also observed across the microstructure (images C, D). The average major axis length of spherical cementite in as-received material was 232±144nm. The volume fraction of ferrite and cementite was 0.72 to 0.28. The presence of spheroidised regions is a result of prior annealing treatments by the manufacturer during material processing.

Mechanical and electrical properties were assessed through Vickers hardness and resistance testing (as described in the section “Mechanical and electrical properties”, pp.75). Average hardness of the untreated, as-received material was found to be 317 HV_{10}, while resistance measurements produced a calculated electrical resistivity of 2.87×10^{-7} Ω·m.

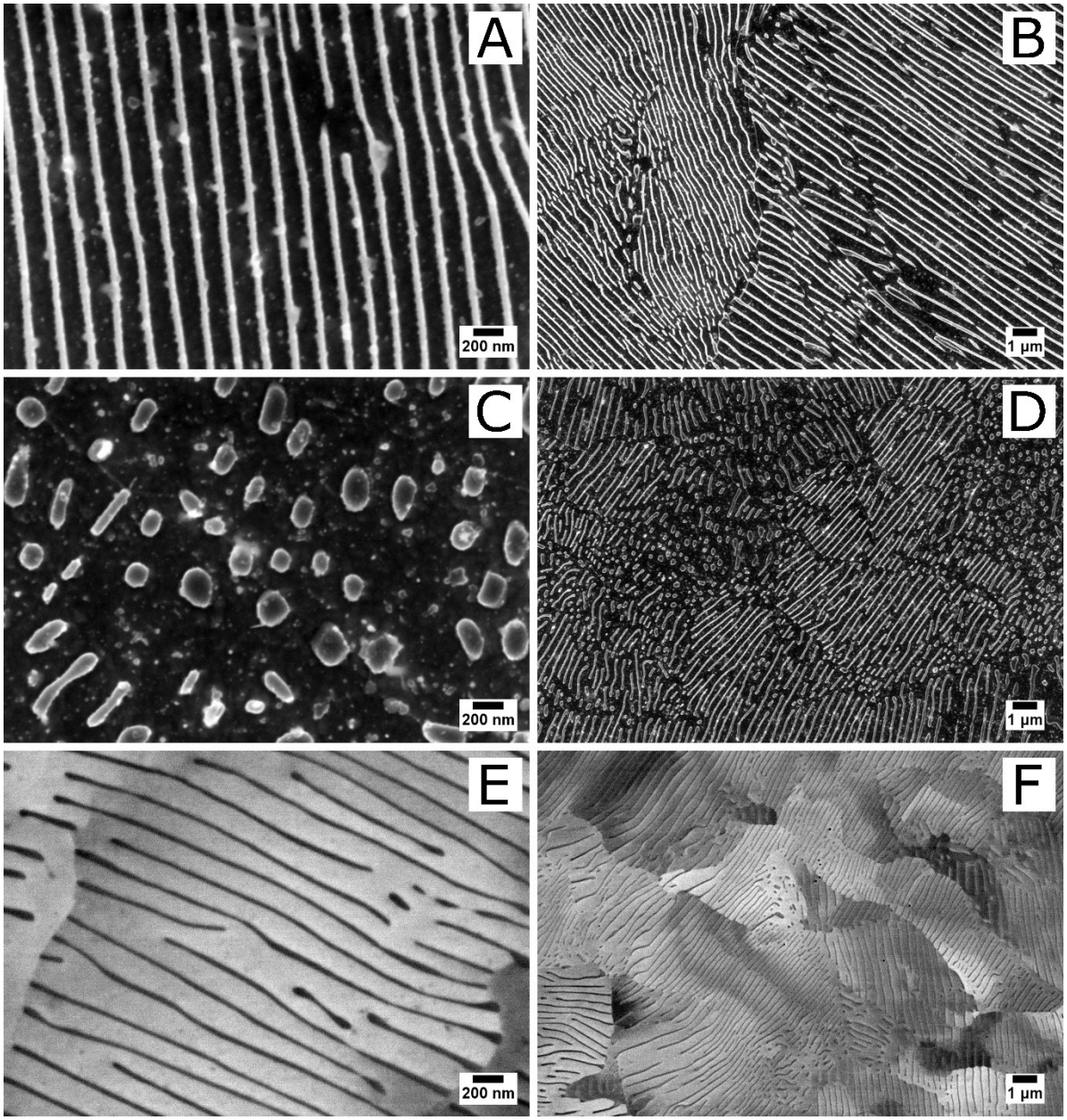


Figure 3.1. Initial as-received microstructure of 0.92wt%C steel. A, B) SEM imaging of lamellar regions; C, D) SEM imaging of regions of spheroidised cementite; E, F) Backscatter imaging showing delineation of pearlite colonies. Cementite appears as the lighter phase in SEM images, and darker in backscatter images.

Table 3.2. 0.92wt%C plate characterisation.

Average ILS *(nm)*	194±38
Volume fraction *(ferrite, %)*	0.72
Volume fraction *(cementite, %)*	0.28
HV_{10}	317±16
ρ *($x10^{-7}$ Ω·m)*	2.87±0.07

The resistivity of individual phases (ρ_α, ρ_β) at ambient temperature can be estimated from the volume fraction (V_α, V_β) and bulk resistivity value (ρ) using Equation 3.1 [25]. Taking the resistivity of α-ferrite to be 0.98×10^{-7} Ω·m [140, 141], the resistivity of the cementite phase can be approximated to be 7.7×10^{-7} Ω·m.

$$\rho = \rho_\alpha V_\alpha + \rho_\beta V_\beta \quad (3.1)$$

The distribution of pearlite colonies can be clearly observed through backscatter electron imaging, as shown in Figure 3.1 (images E, F). The variation in contrast observed results from differences in orientation between the colonies, allowing their boundaries to be clearly delineated. Contrast is also visible as a result of phase differences between the ferrite and cementite matrix. The appearance of the pearlite colonies is non-uniform, with widespread variation in dimensions, circularity and orientation. As the focus of this thesis was on the effects of electropulsing on the individual phases rather than the overall colony, no further information is provided on pearlite colony characteristics.

3.1.2.2. Hypo-eutectoid rod (0.73wt%C)

Three processing variants of drawn 0.73wt%C steel rod were supplied by the manufacturer. Table 3.3 identifies the simplified processing methods and associated labels.

Table 3.3. 0.73wt%C wire sample designations.

Label	Definition
SA	Still air cooled
FA	Forced air cooled
SB540	Salt bath at 540°C

All supplied rods were initially produced from 5.5mm diameter rod material that had undergone austenitisation and transformation to pearlite as described in Table 3.4. The first two rod variants were derived from this stage – SA rod was slow cooled after heat treatment, while FA rod was fast cooled.

Table 3.4. Initial furnace treatment parameters for 0.73wt%C rod (as supplied by Tata Steel).

	SA *(d = 5.5mm)*	**FA** *(d = 5.5mm)*
Heat treatment	Austenitised at 900°C for 3 minutes	
Cooling rate *(°C/s)*	~10	25-30

Table 3.5 details material processing after the initial annealing treatment. All rods were cold-drawn to 2mm diameter, and the final area reduction percentages of the SA and FA conditions are included in

the table. Further processing of SB540 rod is also described in Table 3.5. This condition was austenitised for a second time to remove drawing strain, and subjected to slow cooling rates.

Table 3.5. 0.73wt%C wire characterisation.

	SA *(d = 2mm)*	**FA** *(d = 2mm)*	**SB540** *(d = 2mm)*
Treatment 1	Drawn to 2mm from 5.5mm SA rod	Drawn to 2mm from 5.5mm FA rod	Drawn to 2mm from 5.5mm rod (SA or FA)
Treatment 2	-	-	Austenitised at 900°C for 3 minutes and salt bath patented at 540°C for 80s
Final %AR	58*	61*	-
Average ILS *(nm)*	99±17	66±4	43*
HV_2	403±6	461±15	382±8
ρ *($x10^{-7}$ Ω·m)*	1.34±0.09	1.28±0.07	1.35±0.1

* Data supplied by TATA Steel.

Final microstructures of the three rod variants SA, FA, and SB540 are shown in Figure 3.2. Interlamellar spacing,[11] hardness and electrical resistivity values for all conditions are also included in Table 3.5. From Figure 3.2, the effects of drawing on the SA (images A, B) and FA (images C, D) conditions are clearly observed. Cold deformation has heavily distorted the lamellar structure and aligned the lamellae in the drawing direction across much of the microstructure. As a result, the interlamellar spacing appears reduced. The apparent average ILS in the SA condition was measured to be 99nm, while in the FA condition the value was 66nm. Fragmentation and breakdown of some lamellae is also present.

Interlamellar spacing can be considered theoretically in terms of its relationship with the level of undercooling below the eutectoid temperature. For a binary Fe-C alloy the observed lamellar spacing S_O varies inversely with undercooling, as described in Equation 3.2 [142]. A graphical representation of the relationship plotted in Figure 3.3 shows asymptotic behaviour.

$$S_O \propto \Delta T^{-1} \qquad 3.2$$

[11] Refer to section 3.5.3.3 for comment on the use of interlamellar spacing measurements with rolled microstructure.

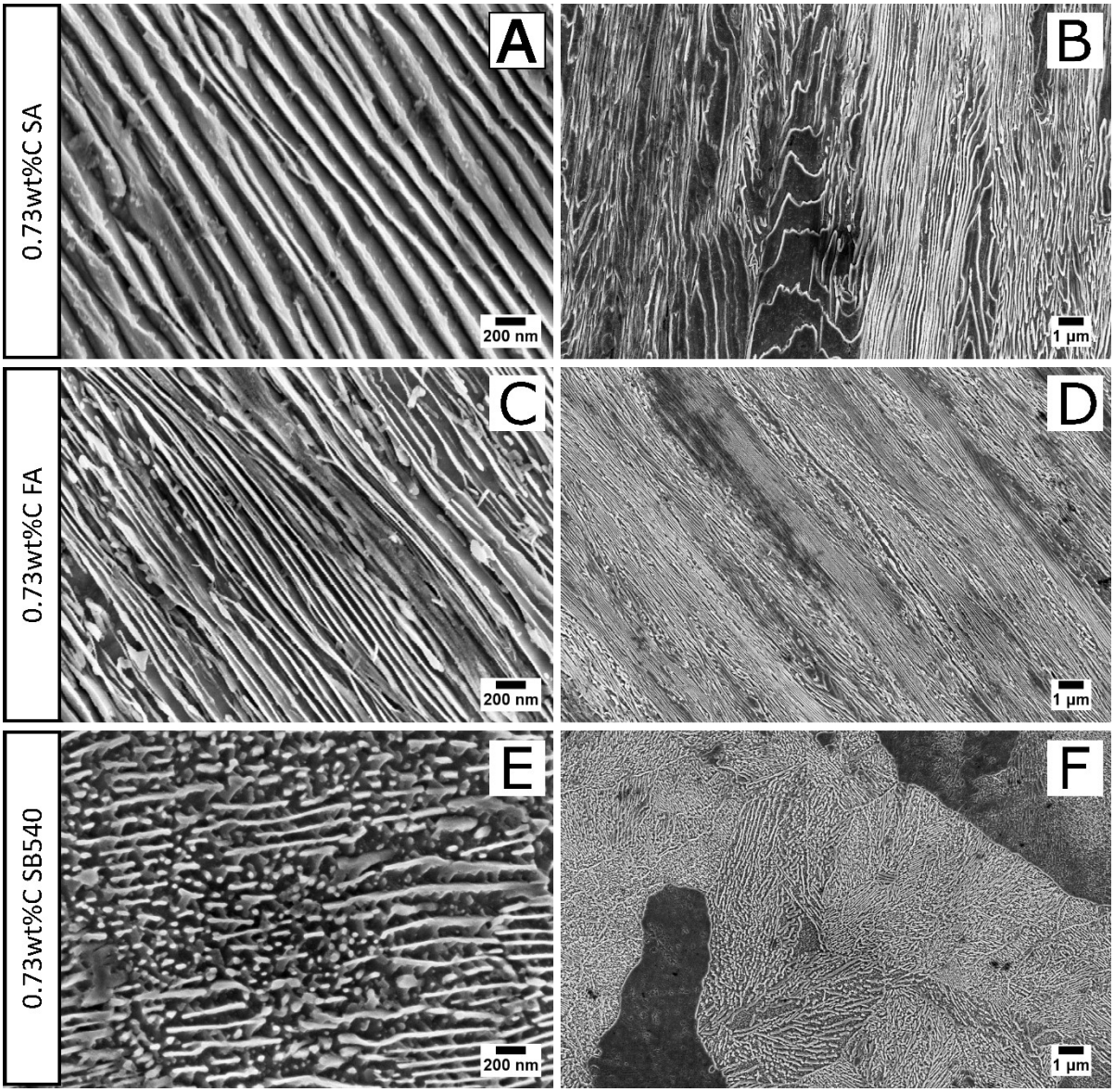


Figure 3.2. SEM imaging of initial as-received microstructure of 0.73wt%C steel. A, B) Drawn SA condition; C, D) Drawn FA condition; E, F) Annealed SB540 condition.

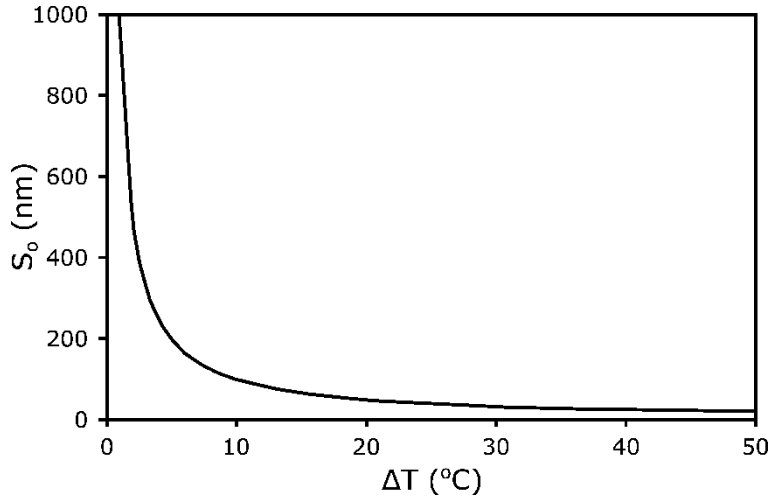


Figure 3.3. Theoretical relationship between undercooling below the eutectoid temperature (ΔT) and observed interlamellar spacing (S_O) in a binary Fe-C alloy.

At higher transformation temperatures (low undercooling) there is greater driving force for the diffusive pearlite transformation. This increases the potential carbon diffusion distance and allows thicker lamellae of both phases to form. With greater undercooling the driving force for diffusion is reduced, preventing longer range carbon diffusion and producing finer lamellae to compensate for this [25]. The behaviour is demonstrated in Figure 3.3 where it can be seen that with increasing undercooling, the observed interlamellar spacing is reduced. As the FA condition experienced greater undercooling, its interlamellar spacing would be expected to be smaller than that of the SA condition. This can be extrapolated to the drawn condition as the level of cold-drawing between the two conditions is comparable.

The SB540 condition (images E, F) is also shown in Figure 3.2. As this condition underwent heat treatment after drawing, the microstructure appears unstrained. The lamellar pearlite has no texture and there are no observable orientation effects as seen in the SA and FA conditions. The SB540 rod contained regions of fine spheroidised cementite and fragmented cementite lamellae as a result of the applied heat treatment.

Salt bath patenting is generally applied as an interrupted quench technique. After heating to above the austenitisation temperature the steel section is then quenched in a salt bath and held at a temperature within the pearlite formation region. The use of a salt bath allows even cooling and should guarantee full transformation to pearlitic microstructure when an appropriate temperature is selected. The SB540 condition was quenched to 540°C, which should produce a relatively fine interlamellar spacing as the undercooling below the eutectoid temperature is significant. The short holding time (80 seconds) is appropriate as the geometry of the rod is small [143].

3.1.2.3. Phase properties

At ambient temperature pearlitic steel is a dual phase alloy of BCC α-ferrite and orthorhombic cementite (Fe_3C). The phases interact to form colonies of interpenetrating layers, producing a material with excellent natural strength properties due to the combined ductility of iron and hardness of carbon. The composition of the steel determines the temperature at which it will transform to FCC γ-ferrite or austenite. A steel with composition 0.8wt%C typically transforms at 723°C [139], decomposing through a eutectoid transition from single phase austenite to dual phase pearlite.

The high carbon 0.92wt%C steel used in this research was theoretically and experimentally determined to austenitise at temperatures above 728°C (see Figure 3.4 A and Table 3.6). The composition contains a high proportion of silicon (0.9wt%) in combination with phosphorus and vanadium. These elements restrict the formation of austenite and act to expand the ferrite phase field, thus raising the austenitisation temperature of the steel.

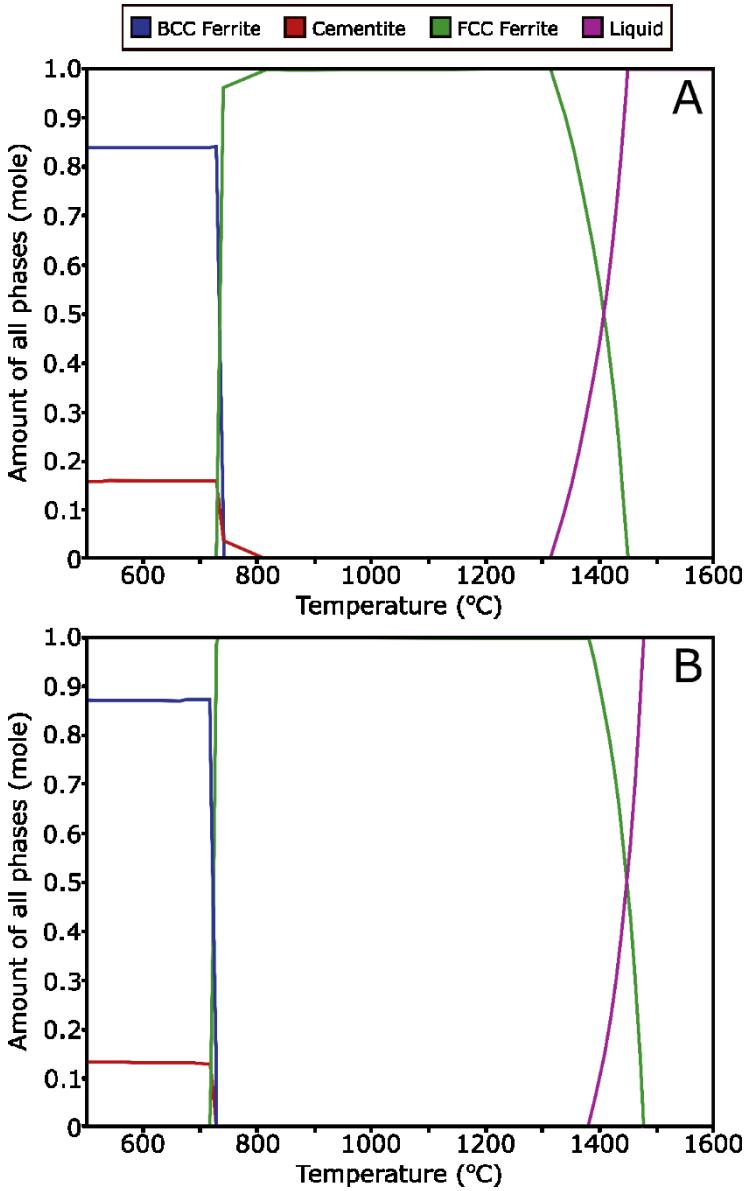


Figure 3.4. Phase diagrams for A) 0.92wt%C hypereutectoid steel; and B) 0.73wt%C hypoeutectoid steel. Diagrams were generated in Thermo-Calc and redrawn using Inkscape graphic software.[12]

Table 3.6. Summary of key transformation temperatures for experimental steels based on ThermoCalc phase diagram simulations (Figure 3.4). T_{SOL} is the solidus temperature, while T_{LIQ} is the liquidus.

	T (°C)			
	A_{e1}	A_{cm}	T_{SOL}	T_{LIQ}
Hyper-eutectoid pearlite plate (0.92wt%C)	728	811	1310	1446
Hypo-eutectoid pearlite rod (0.73wt%C)	714	730	1376	1473

[12] Thermo-Calc is a thermodynamic simulation software used to produce phase diagrams based on the material composition provided. Further information is available at *http://www.thermocalc.com/products-services/software/thermo-calc/*. Inkscape is an open-access graphic software that can be used to create and edit diagrams and schematics. Further information is available at *https://inkscape.org/en/*.

The 0.73wt%C steel is closer to eutectoid carbon composition but has a eutectoid transformation temperature of 714°C (see Figure 3.4 B and Table 3.6). This steel composition contains nitrogen and manganese, austenite stabilising elements that depress the austenite transformation temperature [42, 139].

The mechanical and electrical properties of a steel are also affected by the phase composition. A higher carbon content means a larger proportion of cementite in the steel. Cementite has a hardness in excess of 1000HV [141, 144] and electrical resistivity of 7.87×10^{-7} Ω·m [141]. In comparison, the hardness of iron can range between approximately 95 and 150HV [145] while its electrical resistivity has been measured to be 0.98×10^{-7} Ω·m [140]. The higher carbon content of the 0.92wt%C steel would therefore be expected to produce a harder, less electrically conductive material than the 0.73wt%C steel. This is confirmed by experimental measurements, which showed that the 0.92wt%C steel had an average as-received resistivity of 2.87×10^{-7} Ω·m while the 0.73wt%C composition was found to have an average value of 1.35×10^{-7} Ω·m or less across the three microstructure conditions. Note that the 0.73wt%C resistivity values are calculated based on measurements from the deformed material, which suggests that the resistivity of the true as-received value may be even lower.

3.2. Effect of cold work on microstructure and properties

As described in the literature review, research suggests that dislocations play a key role in the electropulsing mechanism [1, 7, 28, 70]. Based on these findings, all[13] electropulsed samples described in this thesis underwent some form of cold work to introduce dislocations to the crystal lattice. The effect of this cold work was observed in both the microstructure and mechanical properties of the steels. Figure 3.5 images A-D show the microstructure of the 0.92wt%C steel after cold rolling to more than 60% cross-sectional area reduction. In each case, morphological artefacts of the cold rolling process are visible. The pearlite lamellae are kinked and bent, and shear bands are visible (A, B). The shear bands are generated at a tangent to the rolling direction, as shown in Figure 3.5 B. The microstructure also appears flattened and elongated in some regions (C, D). Tagashira *et al*. [146] identified three morphological characteristics of cold-rolled pearlitic steel – irregularly bent lamella (IBL, regions of Figure 3.5 D), coarse lamella with shear band (CLS, Figure 3.5 A) and fine lamella (FL). Fine lamella regions as defined by Tagashira *et al.* are extremely elongated with very fine interlamellar spacing. These regions are typically observed in drawn wires, and were not observed in the cold-rolled 0.92wt%C microstructure as the rolling reduction was not severe enough.

[13] Excluding salt bath treated (SB540) 0.73wt%C rod which underwent austenitisation after being cold-drawn by the manufacturer, TATA Steel.

During any cold deformation the lamellae of a pearlitic microstructure will align with the direction in which the deformation is occurring, if it is severe enough [38, 108, 146]. Tensile wire drawing demonstrates this phenomenon more readily than compressive cold rolling, as shown in Figure 3.2 C-D in 0.73wt%C drawn steel rod. Wire drawing can produce very fine interlamellar spacings [106] and as a result, very strong materials [4]. This is correlated by measurements taken by TATA Steel from the steel rod supplied for this research, which state that the ultimate tensile strength of the still air cooled rod was 1.8GPa, while the forced air condition was 2.0GPa.

The effects of cold work on the mechanical properties of the cold-rolled 0.92wt%C steel plate are shown in Figure 3.5 E. With increasing cold work the Vickers hardness is found to increase, from approximately 320HV in the undeformed condition to over 500HV at 77% cross-sectional area reduction. This is a result of an increasing volume of dislocations in the crystal structure introduced by the cold work, known as strain hardening. As the dislocation density increases, the number of dislocation-dislocation interactions also increases. As these interactions are generally repulsive, dislocation motion is limited by the presence of other dislocations. This means that the applied stress required to deform the material further must increase, and subsequently the material becomes harder [25].

Defects are also known to affect the electrical properties of metals. Cold deformation increases the electrical resistivity of various metallic materials [147, 148]. Dislocations and vacancies in the crystal lattice increase the scattering of electrons, inhibiting their movement through the material and therefore increasing the net resistivity. The thermal conductivity of a metal can be affected in a similar way by cold work. Dislocations inhibit the motion of heat-carrying electrons, increasing the probability of collisions between those electrons and elements of the crystal lattice. The collisions pass along heat energy, and local resistivity effects such as dislocation clusters can increase the heating effect observed.

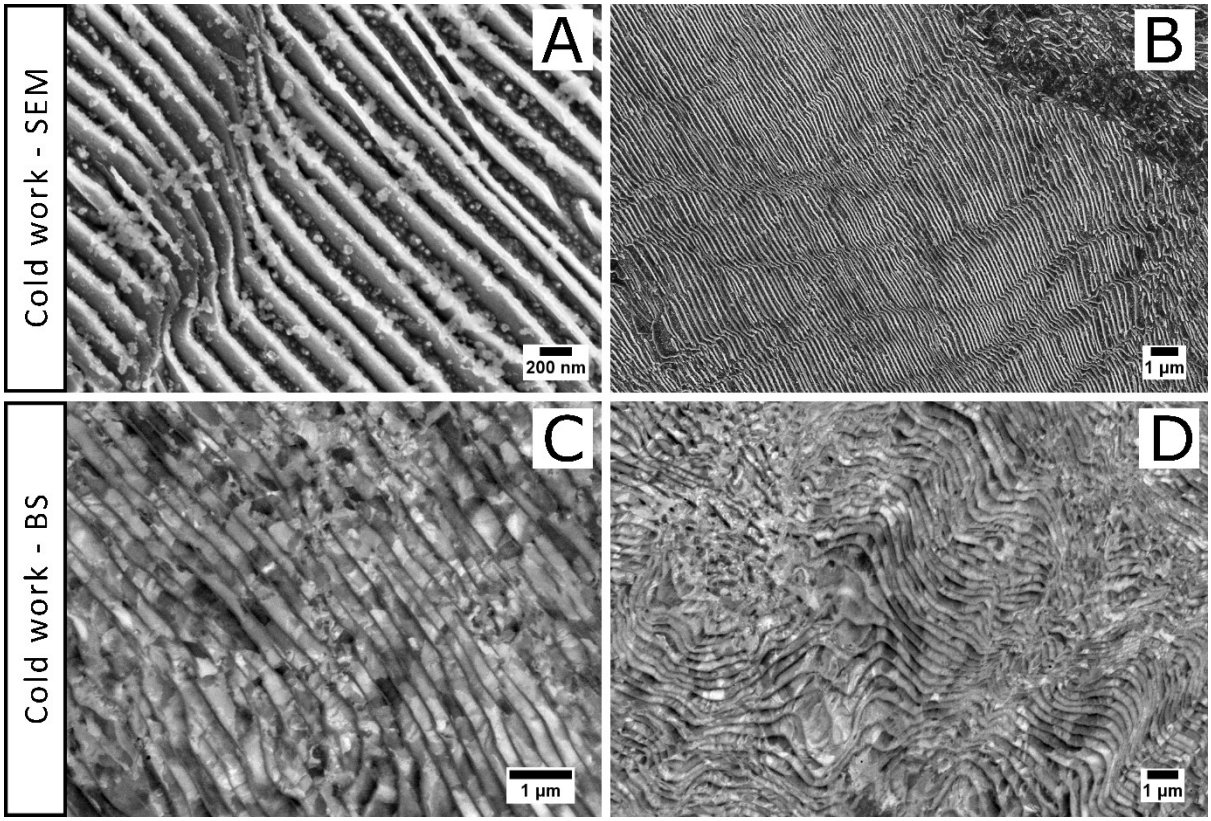


Figure 3.5. Characteristics of 0.92wt%C steel after severe plastic deformation. A, B) SEM imaging showing rolling kinks appearing as waves in the lamellar structure; C, D) Backscatter imaging showing subgrain dislocation effects, represented by variation from light to dark regions.

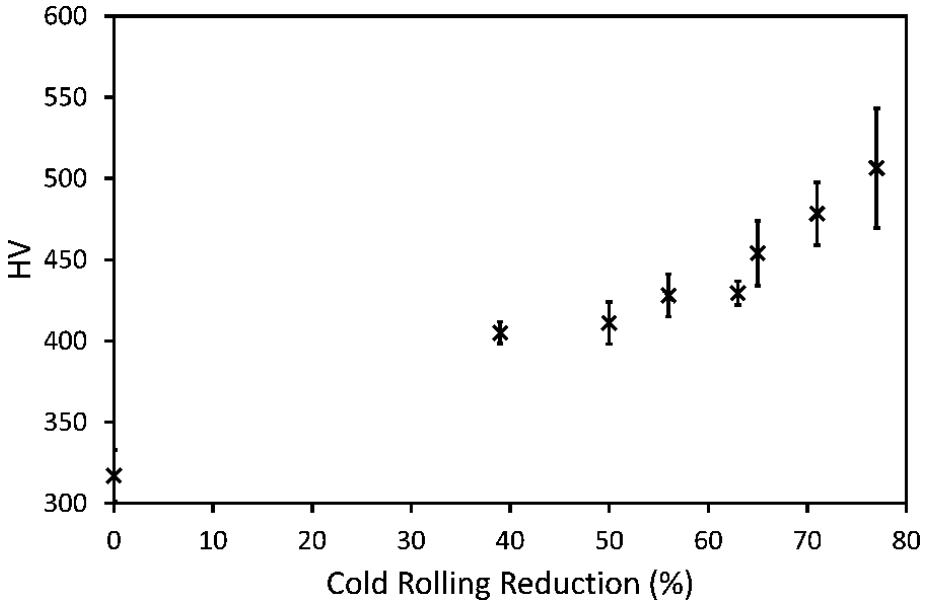


Figure 3.6. Relationship between severity of cold rolling reduction and hardness in 0.92wt%C steel plate.

3.3. Preparation of samples for treatment

3.3.1. Milling

Material sectioning was completed using a selection of coarse and precision cutting mills. An ATM Brillant 200 and Buehler AbrasiMet 250 abrasive cutter were used for bulk cutting of large sections. For smaller-scale cutting with low precision requirements a Buehler IsoMet 5000 linear precision saw was utilised. Fine precision cutting with minimal sample damage was achieved using a Struers Accutom 50 with a low feed rate (0.010mm·s^{-1}).

3.3.2. Plastic deformation

3.3.2.1. Low and moderate current density samples, $A_f > 0.2mm^2$

Plastic deformation of the majority of samples was achieved through cold rolling. As the target current density was between 10^7 and 10^8 A·m^{-2}, extreme reductions were not required. A small manually operated mill was utilised for moderate to high cross-sectional area reductions, while two larger mechanised mills were used when very high reductions were required. All plate rolling reductions discussed in this thesis are described in terms of the cross-sectional area reduction (*%AR*) and, when appropriate, the applied compressive strain (ε_c). When referring to drawn wires, the drawing strain (ε_d) is stated. Note that all wires were drawn by the material supplier, TATA Steel. Equations 3.3 and 3.4 describe the rolling deformation parameters, where A_o is the original cross-sectional area, A_f the final cross-sectional area, D_o the original depth and D_f the final depth.

$$\%AR = \frac{A_o - A_f}{A_o} \times 100 \qquad 3.3$$

$$\varepsilon_c = \frac{D_o - D_f}{D_o} \qquad 3.4$$

3.3.2.2. High current density samples, $A_f < 0.2mm^2$

The maximum current density applied to any sample described in this thesis was of the order 10^9 A·m^{-2}. This uppermost limit was determined by three factors. The original research by Qin *et al*. [6, 7] was conducted at 10^9 A·m^{-2} and set a precedent for this work. Furthermore, with increasing current density, the practicality of scaling up any technique developed through this research is diminished. Finally, a combination of inherent material and equipment limitations prevents current densities greater than 10^9 A·m^{-2} from being achieved.

In order to achieve the maximum current density, a modified plastic deformation method was applied to the material. This method was used to produce very small samples from centimetre-scale steel plate. The thickness of the samples was sequentially reduced by mechanical processes (rolling,

grinding and milling) with an intermediate austenitisation stage to improve the workability of the plate for final rolling requirements. The process steps were as follows:

- As-received 0.92wt%C steel plate of depth 4.5mm was cut by wire electrical discharge machining (EDM) to approximately half its original depth (2.25mm). The rolled section was then cut into smaller pieces for cold rolling.
- Initial cold rolling with an average cross-sectional area reduction of 45% was applied to the cut samples.
- The cold-rolled samples were austenitised above 800°C for two hours to remove the rolling strain then air cooled.
- Mechanical grinding was applied to remove the surface oxidisation and carbon film formed during furnace treatment.
- The austenitised samples were cold-rolled again to an average cross-sectional area reduction of 69% and cut into smaller sections.
- Manual grinding using 320 grit silicon carbide paper was applied to the samples to further reduce their depth.
- The final sample dimensions were obtained by fine rotary saw milling using a Struers Accutom 50 at the slowest feed rate (0.005mm·s^{-1}).

The microstructure produced by the modified plastic deformation regime was a combination of pearlite lamellae and large ferrite grains, shown in Figure 3.8. This is a result of decarburisation inside the furnace combined with relatively thin sample size [149]. Decarburisation occurs at the surface of the sample during austenitisation, where carbon reacts with the furnace atmosphere. When this process occurs, a diffusion gradient is introduced and the carbon moves to the surface. The carbon is converted to a gaseous phase and lost from the steel composition [149, 150]. The carbon content at the centre of a sample after decarburisation can be estimated using Equation 3.5 [25], assuming that the carbon content before diffusion was uniformly distributed.

$$\frac{C_s - C_x}{C_s - C_o} = erf\left(\frac{x}{2\sqrt{Dt}}\right)$$

3.5

The variables of the equation are shown visually in Figure 3.7. The reduction in carbon composition (C_x, *wt%C*) from the original composition (C_o, *wt%C*) at a particular depth inside the sample (x, *mm*) after a time (t, *s*) can be calculated using the diffusion coefficient of carbon in austenite (D = 2.3x10^{-5} mm^2·s^{-1} [25]). The carbon concentration at the surface (C_s, *wt%C*) is assumed to be 20% of the overall steel composition after decarburisation [151]. After approximately two hours in a

furnace above the austenitisation temperature, the carbon content at the centre of a typical 0.92wt%C steel sample is estimated to have fallen to 0.61wt%C (see Appendix A). This calculation explains the ferrite-pearlite microstructure observed in Figure 3.8, which is more readily associated with a hypoeutectoid composition.

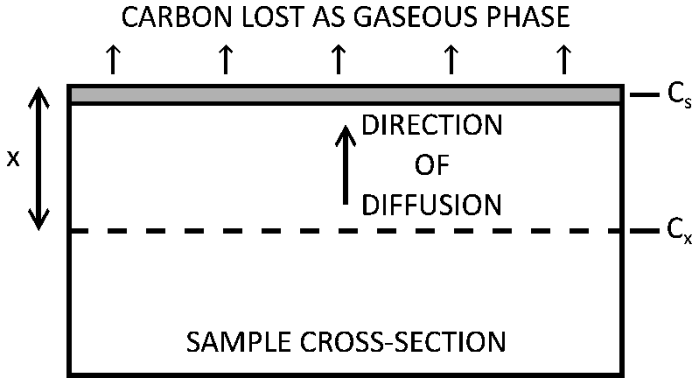


Figure 3.7. Schematic showing decarburisation of a rectangular sample with parameters for Equation 3.5.

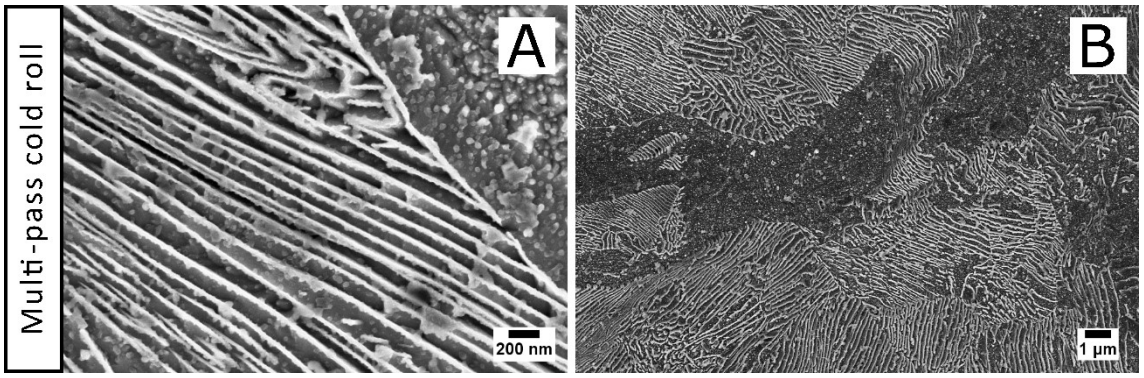


Figure 3.8. SEM imaging of microstructure of multilayer cold-rolled 0.92wt%C steel.

3.4. Electropulsing: equipment, parameters and operation

3.4.1. Electropulsing equipment

Electropulsing at Imperial College London was carried out using a three-component system. DC power was supplied by a Delta Elektronika SM 35-45 unit, operating with a current range of 0-45A and voltage range 0-35V. Process parameters were controlled via an Avtech AV-108F-3A-B-P pulsed constant current generator with maximum output current 200A. The Avtech unit monitored the actual output current with an accuracy of ±3% [152]. The unit supplied square wave pulses with a rise time of 10µs. Pulse waveform was monitored using a standard digital oscilloscope. Schematics of the power supply and pulse generator are shown in Figure 3.9, with a simple circuit diagram showing the connected system. Connection between pulse generator and sample was made using standard 40mm insulated crocodile clips or 0.9mm diameter copper wire depending on the expected heating effects. Copper wire was manually crimped to the sample to ensure a good connection. Note that this section refers to UK-based electropulsing only. Very limited information is available on alternate electropulsing

equipment used to treat samples described in Chapter 6. All known processing information is described in that chapter.

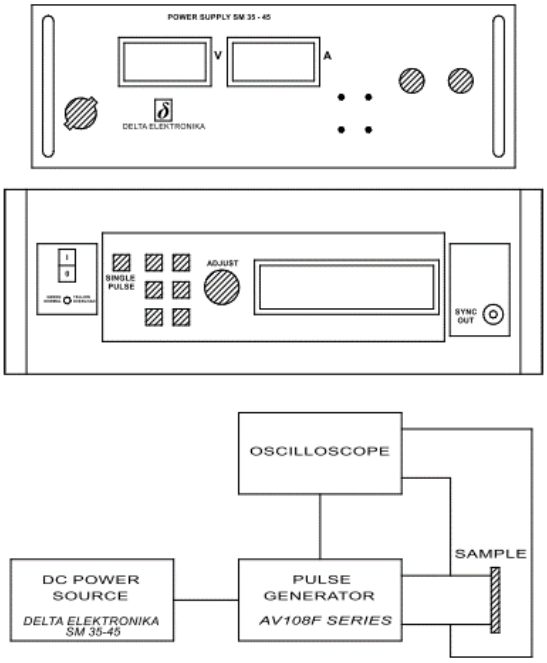


Figure 3.9. Electropulsing equipment and circuit layout. Top: Delta Elektronika SM 35-45 D.C. power supply. Middle: Avtech AV108F-3A-B-P series pulse generator. Bottom: Electropulsing components connected with standard digital oscilloscope.

3.4.2. Parameters and operation

The electropulsing parameters varied as part of the experimental process are listed below and represented visually in Figure 3.10. All pulsing treatments were applied as a square waveform (also shown in Figure 3.10).

- **Input current, I_{IN}** (*A*): The target value of current applied to the sample, generally set to the maximum 200A (an equipment limit) but varied for smaller samples to achieve particular current densities.
- **Output current, I_{OUT}** (*A*): The actual current achieved during electropulsing. Multiple readings of output current were taken during testing dependent on experiment duration, giving an average output value.
- **Pulse frequency, f** (*Hz*): The pulsing rate of the applied electropulsing treatment, as defined by Equation 3.6 where T_P is the pulse period (s). The pulse period is defined as the length of time between the start of subsequent pulses (labelled (C) in Figure 3.10). In this method of treatment pulse period is determined by the selected frequency and is not controlled directly.

$$f = \frac{1}{T_P} \tag{3.6}$$

- **Pulse duration, d** (μs): The width of a single pulse, describing the period of time for which the pulse is applied, or "on" (labelled (B) in Figure 3.10).

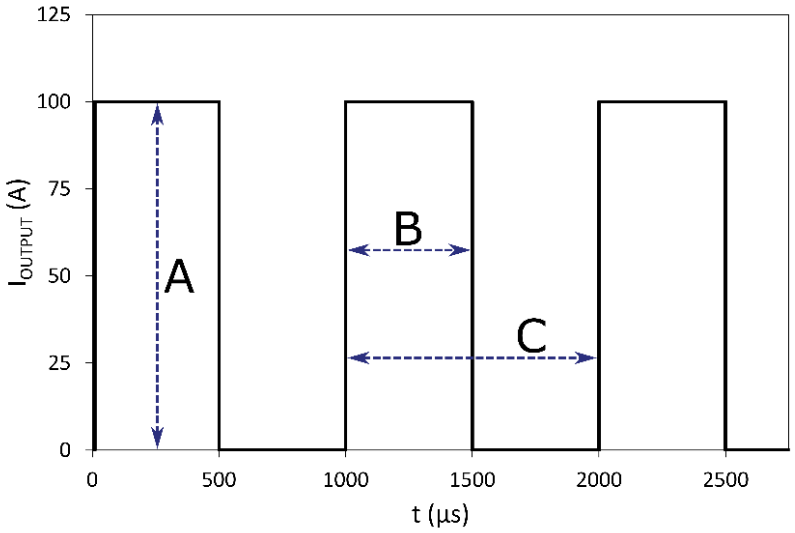


Figure 3.10. Example schematic of a square electropulsing waveform with current amplitude 100A (A), pulse duration 500µs (B), pulse period 1000µs (C) and frequency 1000Hz (not shown).

During electropulsing, the output current I_{OUT} (A) was constantly monitored and recorded. The output current is the actual current amplitude achieved through the sample (labelled (A) in Figure 3.10) and as such is critical for accurate current density calculations. The value may differ to the applied input current due to losses associated with the wired connection, conductivity of the sample surface and heating effects during treatment.

All output current values were converted to a current density value to reflect the strength of the electropulsing treatment relative to sample size. The relationship between current density J ($A \cdot m^{-2}$), output current and cross-sectional area of the sample A (m^2) is described by Equation 3.7.

$$J = \frac{I_{OUT}}{A} \qquad 3.7$$

3.4.3. Combined furnace and electropulsing treatments

Electropulsing at high temperature was achieved using the same circuit arrangement as described above, combined with a standard Lenton EF 11/8B or similar chamber furnace. The equipment was arranged as shown in Figure 3.11, with 0.9mm copper wire electrodes and a high temperature sheathed thermocouple probe fed through the furnace door. Early tests were conducted with each electrode encased in a non-conductive heat resistant ceramic tube to prevent contact between the wires and furnace during treatment. However, further calibration tests showed that the output current was not affected by contact with the furnace door. Furnace tests were conducted following the steps described below.

- **Furnace preheating**: The furnace was set to the required value and chamber temperature was monitored using an external thermocouple with high temperature sheathed probe inserted through the chamber door.
- **Sample insertion**: The experimental sample (with an as-received cold-worked control sample for comparison) is placed in the centre of the chamber in as short a time as possible to ensure the required furnace temperature is maintained. The electrodes and thermocouple are fed out through the furnace door in a manner preventing contact between the wires. The furnace is allowed to return to the required temperature before electropulsing begins.
- **Electropulsing**: Electropulsing treatment begins, with regular recordings of output current and furnace temperature.
- **End of test**: The electropulsing treatment is stopped after a predetermined period and both samples are removed from the furnace for air or water quench cooling as required.

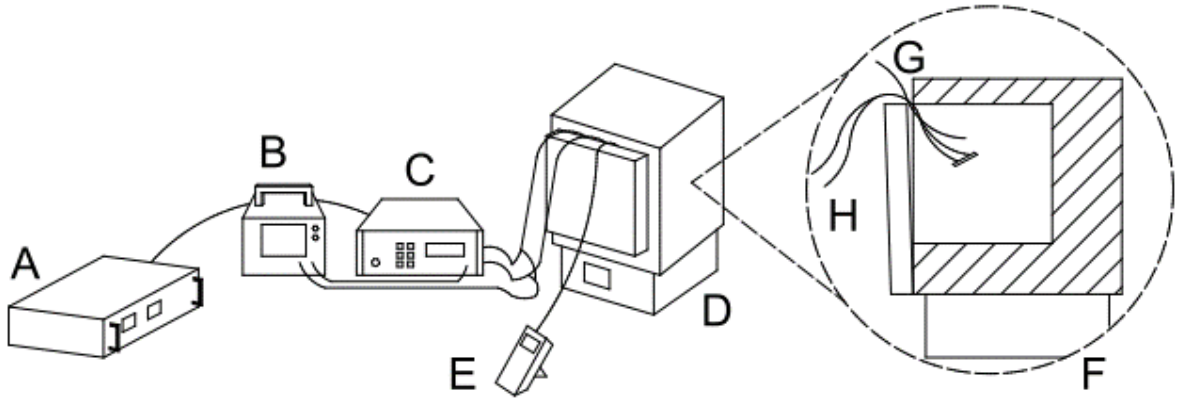


Figure 3.11. Schematic of high temperature electropulsing test. The power supply (A), oscilloscope (B) and pulse generator (C) are shown. The pulse generator connects to a sample which is placed inside the furnace (D). The sample placement is shown in cross-section (F) with copper wires (H) connected. A sheathed probe (G) connects to a thermocouple (E) outside the furnace.

3.4.4. Sample designations

3.4.4.1. Ambient temperature tests

Sample codes for 0.92wt%C steel plate electropulsed at ambient temperature were generated based on the applied parameters, as shown in Table 3.7. Designations include information on all key electropulsing variables.

The sample codes are included as a footnote in each experimental chapter for ease of reference.

Table 3.7. Explanation of sample designations for ambient temperature electropulsing experiments.

Annealing temperature *(if applicable)*		***Order of magnitude of current density***		***Frequency***		***Pulse duration***		***Test duration***		***Sample identifier***
F650	-	8	-	50	-	80	-	1	-	1
		7	-	100	-	160	-	5s	-	3
		9	-	1	-	80	-	S	-	2
T (°C)		**J (A·m^{-2})**		**f (Hz)**		**d (µs)**		**t (min)**		**i**
								Second notation added when required.		
								S refers to single pulse		

3.4.4.2. Elevated temperature tests

Sample codes for 0.73wt%C steel rod electropulsed at elevated temperatures are detailed in Table 3.8. The designations include less detail than those for ambient temperature as the electropulsing parameters used were identical between tests. Codes describe key test parameters associated with temperature and initial material conditions.

Table 3.8. Explanation of sample designations for elevated temperature electropulsing experiments.

Initial cooling condition		***Annealing temperature***		***As-received or electropulsed***		***Test duration***
SA	-	F740	-	EP	-	15
FA	-	F660	-	AR	-	30
		T (°C)				**t (min)**

3.4.5. Heating effects and temperature monitoring

It is well established that application of electric current to a metallic material will produce resistive heating effects [153] due to the interaction of excited electrons with the crystal lattice. The resistive heating associated with a single application of current (a single pulse) can be estimated using Equation 3.18, referred to as the Joule heating equation. The equation is derived from Ohm's law and the

electric power equation as shown in Equations 3.8 to 3.10, relating applied voltage (V, *V*), current (I, *A*), resistance (R, *Ω*), and power (P, *W*).

$$V = IR \tag{3.8}$$

$$P = IV \tag{3.9}$$

$$P = I^2R \tag{3.10}$$

Equation 3.10 is combined with the formulae for electrical energy (Q, *J)* (Equation 3.11), resistivity (ρ, *Ω·m*) (Equation 3.12) and current density (J, $A \cdot m^{-2}$) (Equation 3.13). The result is shown in equation 3.14 and comprises sample length (L, *m*), cross-sectional area (A, m^2) and duration of applied current (t, *s*).

$$Q = Pt \tag{3.11}$$

$$R = \frac{\rho L}{A} \tag{3.12}$$

$$I = JA \tag{3.13}$$

$$Q = J^2A\rho Lt \tag{3.14}$$

A relationship for the change in temperature due to resistive heating[14] (ΔT, *K*) can then be obtained by substituting the energy term (Equation 3.14) for the thermal energy (Equation 3.15) and incorporating the mass-volume-density relationship (Equation 3.17). The final Joule heating equation (Equation 3.18) is determined by both the specific heat capacity of the material (C_p, $J \cdot kg^{-1} \cdot K^{-1}$) and its density (δ, $kg \cdot m^{-3}$).

$$Q = C_p m \Delta T \tag{3.15}$$

[14] Note that while the initial derivation of Equation 3.18 gives the temperature increase in Kelvin, the value can also be described in degrees Celsius. From this point onwards, the temperature increase due to Joule heating will therefore be stated with units of °C.

$$\Delta T = J^2 A \rho L t \left(C_p m\right)^{-1}$$

3.16

$$m = \delta A L$$

3.17

$$\Delta T = \frac{J^2 \rho t}{C_p \delta} = J^2 \rho t \left(C_p \delta\right)^{-1}$$

3.18

Figure 3.12 shows the theoretical change in temperature in a steel sample relative to variable pulse duration and current density. While increasing the pulse duration increases the calculated temperature change, the current density has a much more significant effect due to its squared term.

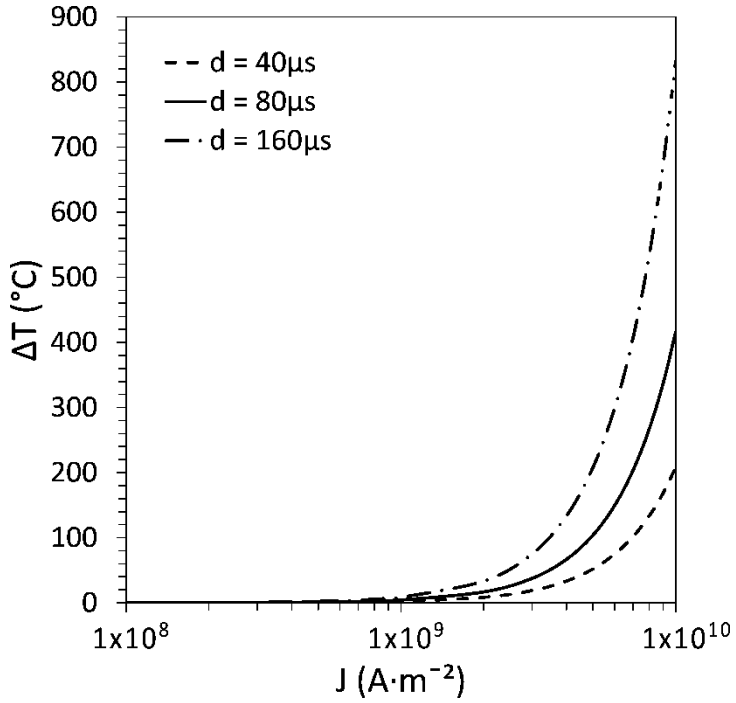


Figure 3.12. Theoretical change in temperature due to a single pulse of electric current in a steel sample (density 7850 kg·m^{-3}, specific heat 490 J·kg^{-1}·K^{-1}) with pulse duration and current density.

The Joule heating equation is only appropriate for estimating resistive-heating induced temperature increase for a single electropulse. The equation does not take into account cumulative heating and cooling, or resistivity changes during the treatment. In order to assess the temperatures of samples treated with multiple electropulses, a thermocouple would normally be used. However, several factors prevented the use of thermocouples in this research.

Welding of the thermocouple to the sample surface was rejected as the heating effects of the process might affect the microstructure in small samples. Furthermore, initial attempts to use a thermocouple during electropulsing treatment altered the expected microstructure effects. For example, attaching

a thermocouple using clips to samples treated under electropulsing conditions that had previously induced heating and microstructure change, prevented those effects from occurring. The thermocouple affected the flow of current and the heating effects of the treatment. A pyrometer was also used to attempt to remotely measure the temperature increase during electropulsing, but was not successful. The pyrometer uses a reflected laser source to assess the temperature of materials. However, the laser spot size of the pyrometer was generally wider than the samples under treatment, thus preventing an accurate reading from being taken.

3.4.6. Comparative heat treatments[15]

In order to give a comparison with other high rate heating methods, a Dynamic Systems Inc. Gleeble 3800 was used to heat a small number of pearlitic steel samples (see Chapter 6, pp.170). Gleeble systems use resistive heating for physical simulation of metallurgical processes [154]. They are applied for longer duration annealing simulations but are also capable of short pulse heating profiles. Depending on sample size the Gleeble 3800 can generate a maximum heating rate of $10000C{\cdot}s^{-1}$.

The sample is held inside the machine by two copper grips. The high thermal conductivity of the grips facilitates both high rate heat transfer and rapid cooling. The Gleeble chamber is temperature controlled and a fine thermocouple connection can be spot welded to the surface of a sample.[16] The heating and cooling profile is recorded by custom software, and the temperature values obtained are valid 3mm to either side of the thermocouple weld position.

3.5. Characterisation techniques

3.5.1. Surface preparation

3.5.1.1. Mechanical polishing

Samples were hot mounted in Struers Multifast non-conductive thermosetting resin before surface preparation for microscopy. A Struers Tegramin 20 automatic preparation system was used to complete grinding and polishing, following the regime detailed in Table 3.9. Polishing was conducted down to 1µm grain size using diamond materials for standard SEM (Scanning Electron Microscopy) and light microscopy. For backscatter imaging a further colloidal silica polishing stage was added.

[15] Gleeble treatments were conducted by Kang Ji of Imperial College London. For more information see Chapter 6.

[16] The size of the Gleeble samples was larger than those typically electropulsed using the equipment at Imperial College London, which allowed the use of a small spot-welded thermocouple.

Table 3.9. Grinding and polishing regime.

Surface	Solution	Grain size *(μm)*	Force *(N)*		Time *(mins)*
			D < 0.5mm	D > 0.5mm	
Struers MD Piano	Water	15	10-15	30	10-12
Struers MD-Dac	Struers DiaPro Dac	3	10-15	30	10-12
Struers MD-Nap	Struers DiaPro Nap B	1	10	25	10-12
Struers OP-Chem	OP-S (70%) H_2O_2 (30%)	0.04	5	5	60-120

3.5.1.2. Etching

A nital solution was used to etch the sample surface before secondary electron imaging. The solution was comprised of 2-4% nitric acid, with methanol balance to 100ml. The nital etchant is commonly applied to plain carbon and low alloy steels [155]. According to the American Society for Testing and Materials (ASTM International) [156], nital solution can be used to delineate ferrite grain boundaries and general microstructure in iron-carbon alloys containing less than 1wt% carbon and less than 4wt% in alloying elements. Both experimental steel compositions used in this research possess less than 1wt% carbon, while alloying elements make up 2.8wt% of the hypereutectoid composition and 1.5wt% of the hypoeutectoid composition (including carbon). Therefore, nital is an appropriate etchant for use with both compositions of steel.

During application, the nitric acid component chemically attacks individual ferrite grains. The attack effect is most effective when the grains have differing crystallographic orientations. The effect is less noticeable when the grains have similar orientation, and hence the step at the grain boundary is shallower [155]. For this reason, the overall etching response of a steel to nital etchant can vary in quality.

In relation to the steels used in this work, the required nital etching time was very short (1-2 seconds). The nital etchant was selected as it is a simple, effective and relatively safe etchant for the steels that were studied. After etching, samples were washed in water and isopropanol and dried using Kimtech Science Lens Cleaning Microfibre Wipes.

3.5.2. Microscopy and characterisation

3.5.2.1. Scanning Electron Microscopy

Scanning electron microscopy (SEM) first became commercially available in 1965 and has rapidly become a standard microstructural imaging technique [157]. Applying a high energy electron beam to a sample surface causes large numbers of low energy secondary electrons to be emitted. When these electrons are collected by an in-lens detector, high resolution nanometre scale images can be obtained [158]. During this project samples were subjected to high resolution SEM for microstructure

characterisation. As the effects associated with previous electropulsing treatments were on the micro- and nanoscale, SEM was an appropriate imaging method.

A Carl Zeiss LEO Gemini 1525 FEGSEM was used to obtain SEM images at an accelerating voltage of 5kV. Images of magnification up to 85000X were collected from a minimum of three regions distributed across the sample surface. Additional SEM imaging was conducted on a Carl Zeiss Auriga Crossbeam (see section 3.5.2.3, Backscatter Electron Imaging). Before SEM imaging the sample surface was prepared as described in Table 3.9, and etched in 2% nital solution.

3.5.2.2. Transmission Electron Microscopy

The first transmission electron microscope (TEM) was developed in Germany by Ernst Ruska in 1933 [158], a breakthrough which earned a Nobel Prize in physics in 1986 [159]. The technique focuses and transmits a beam of high energy electrons through a thin foil sample. The interactions between the electrons and the material during transmission resulting from variations in material density and atomic properties are recorded and converted to a final visible image [158]. The intensity of the electron scattering (the spatial distribution) provides information on the structural characteristics of the sample [160]. TEM allows a more complete image of the local microstructure to be observed as it offers very high resolution imaging and provides information on the grain structure, distributions and defects.

A JEOL 2000FX TEM was used to obtain images and selected area diffraction (SAD) patterns from Focused Ion Beam (FIB)-prepared foils (see section 3.5.2.4). The electron source was a heated tungsten filament and the accelerating voltage used was 200kV. The location of the TEM foil was randomly selected during FIB processing. As the foil size is very small, the entire surface could be reviewed during the TEM imaging and several regions of interest observed. For each TEM bright field image a matching dark field SAD pattern from the same location was obtained.

3.5.2.3. Backscatter Electron Imaging

Backscatter Electron (BSE) imaging is conducted in a similar manner to SEM imaging. The difference lies in the type of electron that is emitted and detected as a result of an incident high energy electron beam. Backscattered electrons are emitted in smaller numbers than secondary electrons but are higher energy, allowing crystallographic information to be obtained. However, BSE imaging is of a lower resolution than secondary electron imaging due to a difference in the origin depth of the detected electrons [158]. The BSE technique also allows microstructure characterisation of microscale samples without the need for etching prior to imaging.

BSE imaging of selected samples was conducted to observe the microstructure free of etching effects, and to highlight grain orientation. A Carl Zeiss Auriga Crossbeam was employed to carry out

backscatter imaging at an accelerating voltage of 10kV with an aperture size of 60µm. Backscatter images of magnification up to 30000X were collected from randomly distributed regions across the sample surface. Before imaging samples were polished down to 0.04µm grain size as described in Table 3.9.

3.5.2.4. Focused Ion Beam microscopy

Focused Ion Beam (FIB) microscopy is often used for TEM sample preparation because nanometre-scale machining is possible using the technique. A high energy ion beam fed from a liquid gallium source is used to sputter atoms from the surface of a sample with an accuracy of 1-2nm. A tungsten needle with a tip radius small enough to generate very high electric fields induces field evaporation of the liquid metal source, producing a focused ion beam [158].

An FEI Helios NanoLab DualBeam 600 FIB microscope was used to mill and thin samples for TEM imaging. During milling the sample was observed via a secondary SEM detector at an accelerating voltage of 5kV. The accelerating voltage applied to the FIB source was 30kV. Samples used for FIB milling were previously prepared for SEM (polished to 1µm grain size and lightly etched in nital as described in section 3.5.1). As the TEM sample is cut from the bulk material and thinned, the etched surface is not observed in the final sample. Previous light surface etching therefore does not affect the quality of the TEM sample.

3.5.2.5. Atom Probe Tomography[17]

Atom probe tomography (APT) is an experimental technique offering atomic-scale resolution and chemical composition analysis. The method is destructive, and uses a high energy laser or voltage pulse to induce field evaporation of atoms from the tip of a needle-shaped sample. The strength of the electric field (F, $V{\cdot}m^{-1}$) generated by the pulses is dependent on the tip radius (R, m) of the sample and the applied voltage (V) as shown in Equation 3.19. As a result, APT samples are designed to have nanometre-scale tip radii. The variable k is a geometry factor that varies with sample shape [161].

$$F = \frac{V}{kR} \qquad 3.19$$

During APT the time of flight of each ion is recorded in order to determine its charge-to-mass ratio, along with the incident position of the ion on a plate detector (the x-y co-ordinates of the ion) and the pulse time increment (used as the z-co-ordinate) [158]. This data is then used to create a 3D

[17] Atom probe tomography sample preparation and data post-processing were conducted by Dr. A. Radecka of Imperial College London and Rolls Royce. The APT experiments were conducted by members of the University of Oxford atom probe group. Further details can be found in Chapter 6.

reconstruction of the sample that reveals the constituent elements and their distribution, atom by atom. An example of the APT equipment configuration is shown in Figure 3.13.

Sample preparation for APT is complex and requires a specialised technique to produce materials of appropriate quality. Sections are cut from the bulk material using FIB milling and individually mounted on a silicon post. Each mounted section is then sculpted into a needle shape using FIB techniques, with a tip radius of less than 100nm and length 4 to 6µm. Several hours of FIB milling are required to produce four to five samples. An image of an APT needle sample is provided in Chapter 6, pp.168, Figure 6.5. The needles are easily damaged and care must be taken during transport.

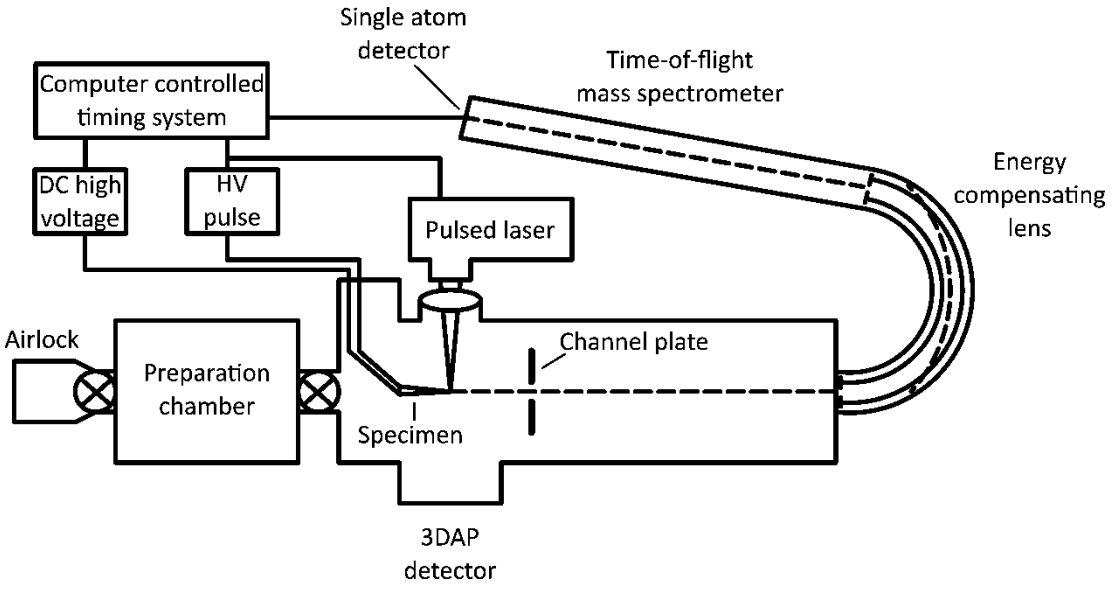


Figure 3.13. APT equipment schematic.[18] Reproduced from [158].

A Cameca Local Electrode Atom Probe (LEAP) 3000X HR located at the University of Oxford was used to conduct atom probe analysis on pearlitic steel samples (see Chapter 6, pp.167). Three samples were tested, one in laser mode and two in voltage mode. Laser mode is less likely to fracture the sample than voltage mode, and as a result was applied first. The experimental parameters are listed in Table 3.10.

Table 3.10. APT experimental parameters.

Tip	Mode	Frequency *(kHz)*	Temperature *(°C)*	Number of detected ions
1	Laser	200	-223	6.75×10^6
2	Voltage	200	-218	12.3×10^6
3	Voltage	200	-218	5.7×10^6

[18] The APT schematic and others were produced using QCad open source 2D Design software. Further information is available at *http://www.qcad.org/en/*.

Laser mode was found to cause microstructural changes in the steel. The carbon in the sample was found to have aligned along the axis of the needle due to laser-induced heating. Laser mode tests were discontinued and voltage mode was used for further analysis. Post-processing of the data gathered from the two voltage mode samples was conducted using specialist APT software, IVAS by Cameca.

3.5.3. Microstructure analysis methods

3.5.3.1. Grain size and volume fraction

Grain size and volume fraction analysis were conducted using the open source software ImageJ.[19] Various methods were considered for grain size analysis as described in ASTM Standard E112-13 [162]. However, due to the often fragmented nature of the partially recrystallised grain structures under analysis (not to mention the dual-phase nature of the steel), these methods were not applicable and therefore discounted. Manual measurements of recrystallised ferrite grains were conducted using ImageJ tools, while thresholding of binarised images enabled semi-automated measurements of spheroidised cementite particles. Three grain characteristic descriptors were measured – surface area, major axis length and aspect ratio. The surface area measures the area of the visible grain surface. The major axis length provides an upper limit for the diameter of grains. Aspect ratio gives an indication of the shape of the grain and therefore the extent of recrystallisation.

Volume fraction values were obtained using a simple point counting method [158]. This is an appropriate method for a dual-phase material, as it can differentiate between the phases. ImageJ allows the user to overlay a grid of specified dimensions onto a micrograph, enabling simple and accurate volume fraction calculations.

3.5.3.2. Weibull Cumulative Distribution Function

Grain size and volume fraction analysis generates many data points and is best represented in histogram form, with appropriate binning parameters. However, a basic histogram does not allow statistically significant analysis of anomalies and may not be sufficient to highlight distribution trends. A distribution curve can be fitted to the data to allow more meaningful and accurate analysis. In this case, a Weibull distribution was selected for the purpose as it has been previously shown to have good applicability to particle size data [163, 164].

The Weibull distribution was first applied to grain size measurements in 1933 by Rosin, Rammler and Sperling and has since become a commonly used distribution function [165]. The technique utilised in

[19] ImageJ is a free to download, open source software developed by Wayne Rasband at the US National Institutes of Health. At the time of writing the current stable version of the software is 1.50i, released on 26/03/2016 at http://rsb.info.nih.gov/ij/.

this thesis uses a three-parameter Weibull smoothing method to fit a distribution curve to the cumulative distribution function (the cumulative percentage representation of the frequency distribution, Figure 3.14 A). In this way a second plot can then be generated to allow comparison between the raw frequency data and the statistically significant probability density function (Figure 3.5 B).

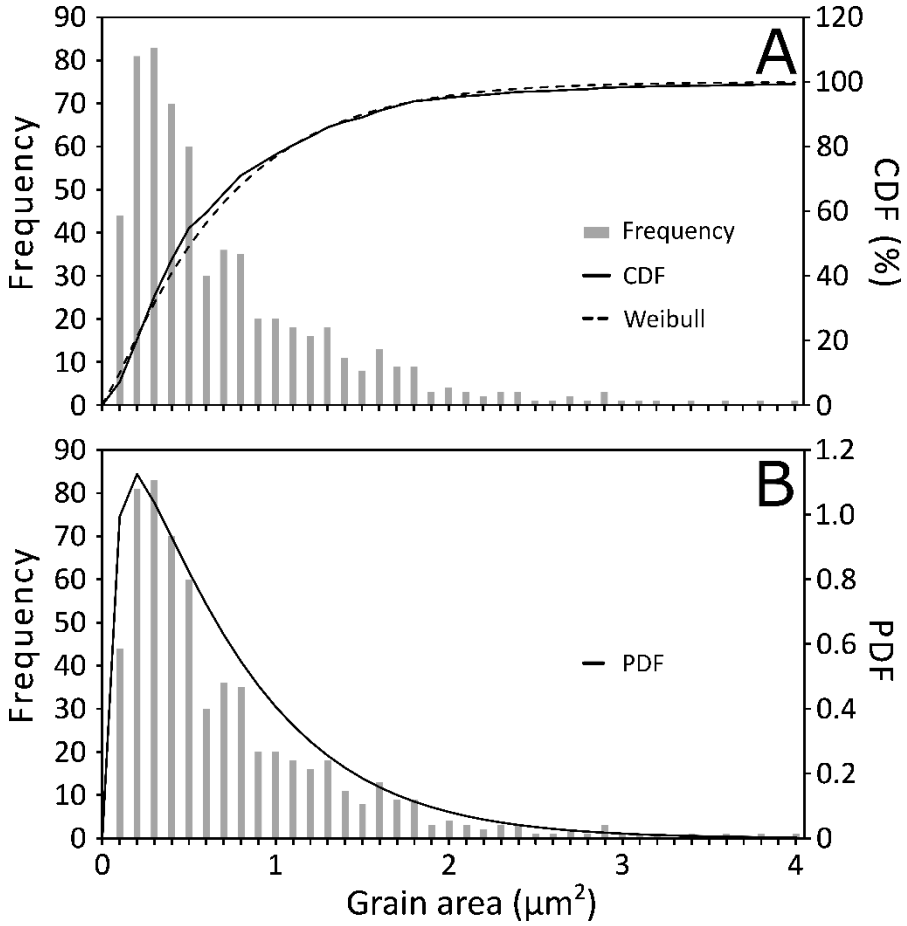


Figure 3.14. A) A Weibull function is applied to fit the cumulative distribution function of the grain size data; B) The Weibull smoothing function can then be used to plot the probability density function and allow statistically meaningful analysis.

3.5.3.3. Interlamellar spacing

As previously described, the spacing of lamellae in a pearlitic steel determines the strength of the material. The interlamellar spacing (ILS) can be calculated in order to give an indication of the lamellar refinement that has occurred as a result of the cooling rate from the austenite phase. The mean true ILS ($\bar{\lambda}_t$, *nm*) is defined by a circular test line method using Equation 3.20. The mean spacing in the direction perpendicular to the lamellae ($\overline{\sigma}_d$, *nm*) is the ratio of the test circle diameter (d_c, *nm*) to the number of cementite lamellae (n_c) intercepted by the diameter of the circle (Equation 3.21) [166].

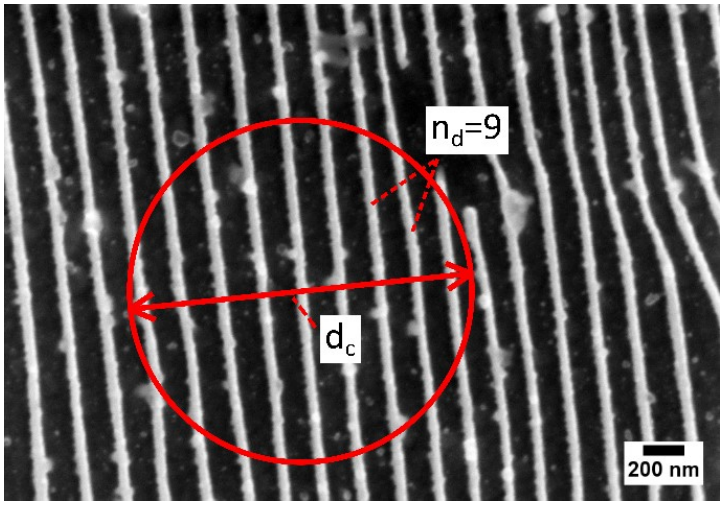


Figure 3.15. Use of the circular test line method to measure the ILS of pearlitic steel.

$$\bar{\lambda}_t = \frac{\pi}{4}\bar{\sigma}_d \qquad 3.20$$

$$\bar{\sigma}_d = \frac{d_c}{n_d} \qquad 3.21$$

Interlamellar spacing measurements can be affected by sample deformation [162], which produces distortion in the lamellae that can be misidentified in microscopy as widening or thinning of the lamellae. This effect can be mitigated by taking measurements across a range of colony orientations. However, the accuracy of the ILS measurement technique in severely cold-rolled samples is limited. As a result, ILS measurements in this thesis are generally restricted to undeformed and annealed steel samples.

3.5.4. Mechanical and electrical properties

3.5.4.1. Hardness

Two pieces of equipment were used to test Vickers hardness of the steel samples. Larger samples were assessed using a Zwick Roell Indentec Macro 6030LKV Vickers hardness indenter using a 10kg load, 10X objective surface magnification and 10 second dwell time. Smaller samples were tested with a Zwick Roell Indentec Micro ZHV Vickers hardness tester with a loads of 0.5-2kg, 10X objective surface magnification and 10 second dwell time. The procedure followed was as described in ASTM Standard E384-11$^{\varepsilon 1}$ (Section 8) [167] with tests conducted on mounted and lightly etched samples using a square-based pyramidal-shaped indenter at room temperature. Each sample was subjected to a minimum of four indentations.

Error in Vickers hardness values generally results from the indent measurement stage, which relies on the accuracy of the human operator. A 0.5% error in the measurement of the indent results in a 1%

error in the HV value (calculated using Equation 3.22, where P is the applied force (*gf*) and d_I is the mean diagonal length of the indentation (μm)) [167].

$$HV = 1854.4 \times \frac{P}{{d_I}^2} \quad 3.22$$

The hardness values stated in the experimental chapters are bulk values. They do not take into account the dual phase nature of lamellar pearlite, or any microstructure derivatives produced by electropulsing treatments. Bulk measurements give an overall, combinatorial representation of the mechanical characteristics and a more readily comparable value for analysis.

3.5.4.2. Resistivity

Resistance testing was conducted on steel samples using a Seaward Cropico DO5001 Micro-Ohmmeter. Before resistance testing, each sample was hand-ground on silicon carbide paper in three steps from 800 to 2000 grit with water as lubricant. This process ensured a clean surface for acquisition of accurate test values. Each sample was tested to obtain four resistance measurements. Equation 3.23 was used to calculate the resistivity (ρ, $\Omega \cdot m$) of the material, where R is the average resistance value (Ω), A the cross-sectional area of the sample (m^2) and L the sample length (m).

$$\rho = \frac{RA}{L} \quad 3.23$$

The accuracy of resistance measurements taken using the DO5001 series ohmmeter is stated by the manufacturer as ±0.03% of the resistance reading [168]. This translates to essentially an insignificant effect on the calculated resistivity value due to equipment accuracy. The resistivity calculation is then most significantly affected by sample geometry measurement accuracy. Standard digital callipers are typically accurate to approximately ±0.02mm. Any additional surface cleaning of samples after electropulsing also produced a minimal variation from the original measured geometry, giving an error of approximately -0.05mm. In this case a negative-only error is given, as the sample size could only be reduced by the cleaning process.

4. Electropulsing at ambient temperature

4.1. Experimental parameters

Electropulsing at ambient (room) temperature was conducted on cold-rolled 0.92wt%C pearlitic steel plate at current densities ranging across three orders of magnitude. These current densities are referred to as low (J ~ 10^7 A·m^{-2}), moderate (J ~ 10^8 A·m^{-2}) and high (J ~ 10^9 A·m^{-2}) for ease of reference in the results and discussion sections.

Treatments were varied by pulse frequency, pulse duration and test duration. Frequencies (f) of 20, 50 or 100Hz were used, with a small number of additional tests at higher frequencies. Pulse duration (d) was tested at 80 or 160µs in order to allow duration effects to be observed. A small number of tests at very high pulse duration were also conducted under single pulse conditions (see pp.78, Table 4.3). Test duration (t) ranged in length from single pulse up to 15 minutes. All samples were allowed to cool to ambient temperature in air on conclusion of the electropulsing treatment.

4.1.1. Low current density, J ~10^7A·m^{-2}

Table 4.1 describes test parameters applied to steel samples during treatment at low current density. All samples were first cold-rolled to a cross-sectional area reduction (AR) of approximately 77%. Current density (J) values were maintained between 7 and 8 x10^7 A·m^{-2}. This was possible due to small sample size and low current density requirements, which allowed greater control over the applied current. The average sample dimensions were L 41mm x W 0.82mm x D 0.56mm.

Table 4.1. Electropulsing parameters for ambient temperature tests at J ~ 10^7 A·m^{-2}.

Area reduction *(%)*	**J** *(x10^7 A·m^{-2})*	**f** *(Hz)*	**d** *(µs)*	**t** *(min)*	**N** *(#)*	**n** *(#)*
77	7.0 – 7.1	20	80	1	1200	3
77	7.8 – 7.9	20	80	15	18000	3
77	7.1	20	160	1	1200	3
77	7.1 – 7.2	20	160	15	18000	3
77	7.1	50	80	1	3000	3
77	7.9 – 8.0	50	80	15	45000	3
77	7.1	50	160	1	3000	3
77	7.0 – 7.2	50	160	15	45000	3
77	7.9 – 8.0	100	80	1	6000	3
77	8.0	100	80	15	90000	3
77	7.1 – 7.2	200	80	1	12000	3

Three tests were conducted at 200Hz in order to assess elevated frequency effects in low current density treatments. All tests were a minimum of 1 minute in duration. The number of pulses (N) and number of tests (n) at each condition are stated in Table 4.1.

4.1.2. Moderate current density, J ~10^8A·m^{-2}

Experimental parameters of moderate current density electropulsing treatments are described in Table 4.2. By Equation 3.18 (see Methods, pp.67) electropulsing at 10^8 A·m^{-2} is expected to induce more significant heating effects than at 10^7 A·m^{-2}. Similar effects are expected at higher and lower pulse durations and frequencies, as a result of increasing applied pulse time and cumulative heating. As a result, a number of tests described in Table 4.2 focus on short test duration, lower frequency (20 – 50Hz) and shorter pulse duration.

The majority of electropulsing treatments were conducted on samples cold-rolled to a cross-sectional area reduction of approximately 77%. Material and equipment availability led to a small number of tests being carried out on steel prepared for higher current density tests, having an approximate cross-sectional area reduction of 69%. The average dimensions of 77% reduced samples were L 28mm x W 0.60mm x D 0.52mm, and 69% samples L 41mm x W 0.77mm x D 0.23mm.

Table 4.2. Electropulsing parameters for ambient temperature tests at J ~ 10^8 A·m^{-2}.

Area reduction *(%)*	**J** *(x10^8 A·m^{-2})*	**f** *(Hz)*	**d** *(µs)*	**t** *(min)*	**N** *(#)*	**n** *(#)*
77	6.6 – 7.9	20	80	1	1200	3
77	5.9 – 7.6	20	80	15	18000	3
77	7.3 – 7.8	20	160	1	1200	3
77	6.7 – 7.6	20	160	15	18000	3
77	6.6 – 9.7	50	80	5s	250	2
77	5.6 – 6.9	50	80	1	3000	3
77	6.0 – 7.4	50	80	15	45000	3
77	5.0 – 5.5	50	160	1	3000	3
77	5.5 – 5.6	50	160	15	45000	2
69	9.6	100	80	2s	200	2
69 - 77	6.2 – 9.0	100	80	5s	500	4
77	4.8 – 6.3	100	80	1	6000	3
71 - 77	1.2 – 5.5	100	80	15	90000	4

4.1.3. High current density, J ~10^9A·m^{-2}

Electropulsing at high current density was conducted on cold-rolled samples with approximate cross-sectional area reduction of 69%. The average sample dimensions were L 38mm x W 0.65mm x D 0.18mm. Table 4.3 describes the applied test parameters, which broadly fall into two categories; high frequency with low pulse and test duration, or low frequency with high pulse or test duration. These parameter combinations were determined in order to control heating effects

and maintain sample integrity. Initial tests at 100Hz and 160µs resulted in excessive heating and immediate sample failure.

Single pulse tests were conducted at high current density and high pulse duration in an attempt to repeat the microstructure effects observed by Qin *et al*. [6] in pearlitic steel wire after a single electropulse at 10^9 A·m^{-2} (see Literature review, pp.33).

Table 4.3. Electropulsing parameters for ambient temperature tests at J ~ 10^9 A·m^{-2}.

Area reduction *(%)*	**J** *(x10^9 A·m^{-2})*	**f** *(Hz)*	**d** *(µs)*	**t** *(min)*	**N** *(#)*	**n** *(#)*
69	1.2 - 2.2	1	200	-	1	4
69	1.1 - 2.2	1	200	10s	10	4
69	1.6 – 2.3	1	600	-	1	3
69	1.4	1	1000	-	1	1
69	1.5 – 1.8	1	80	15	900	3
69	2.0 – 2.3	20	80	5s	100	3
69	1.0 – 1.5	20	80	1	1200	3
69	1.2	20	80	15	18000	3
69	1.1 - 1.7	50	80	2s	100	6
69	1.4 - 2.8	50	80	5s	250	5
69	1.0 – 1.9	100	80	2s	200	5
69	1.0 – 1.6	100	80	5s	500	4

4.2. Results

4.2.1. Microscopy and grain size analysis

4.2.1.1. Low current density, J ~10^7A·m^{-2}

Figure 4.1 shows micrographs obtained from a sample treated at current density of the order 10^7 A·m^{-2}. The micrographs are representative of the microstructure observed after all electropulsing treatments at this current density, independent of frequency, pulse or test duration.

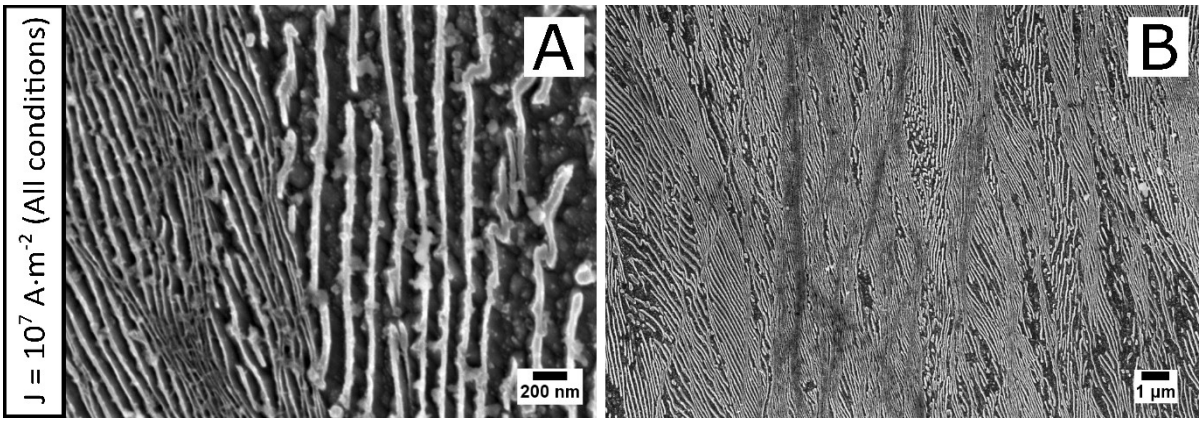


Figure 4.1. Representative areas observed of the 0.92wt%C pearlitic steel electropulsed at 10^7 A·m^{-2}. Secondary electron imaging on samples etched in 2% nital solution (methanol balance). No effect is observed as a result of electropulsing treatment at high (A) or moderate (B) magnification.

The rolled lamellar structure is evident and shows no variation to the original un-electropulsed microstructure. Rolling kinks are particularly visible at lower magnification in Figure 4.1 B, appearing as thick vertical waves. The presence of these defects shows that low current density electropulsing treatment did not induce any relaxation or recrystallisation behaviour quantifiable by Scanning Electron Microscopy (SEM).

The effects of electropulsing on interlamellar spacing are not described here as the microstructure maintains its deformed characteristics. As such the interlamellar spacing measurement technique described on pp.74 is not applicable and its use would generate inaccurate values in this case.

4.2.1.2. Moderate current density, J ~10^8A·m^{-2}

Experimental results from samples treated at 10^8 A·m^{-2} are described in the following sections, and are categorised by pulse frequency.

Pulse frequency = 20Hz

Figure 4.2 shows samples pulsed at 20Hz and 160µs for 1 or 15 minutes. At both test durations the lamellar structure was still visible but significant breakdown and spheroidisation of cementite lamellae was also observed. The electropulse-induced transformation produced regions of both fine and coarse spheroidisation. The fragmentation and spheroidisation followed the path of the prior intact lamellae and was distributed homogeneously across the sample surface.

In addition to spheroidisation of the cementite phase, regions of partial α-ferrite recrystallisation were observed after treatment of 15 minutes duration (Figure 4.2 C and D). The recrystallised ferrite is delineated by the presence of carbon at the newly formed grain boundaries. Approximate measurements of the major axis length of equiaxed ferrite grains gave a range between 100 and 400nm.

No microstructure effects were observed at the same frequency (20Hz) and lower pulse duration (80µs). Deformed lamellar microstructure was maintained, with no additional cementite spheroidisation observed. Results at frequency of 20Hz show a critical dependence on elevated pulse duration when the pulse frequency is low. Microstructure change was observed at the highest pulse duration condition only.

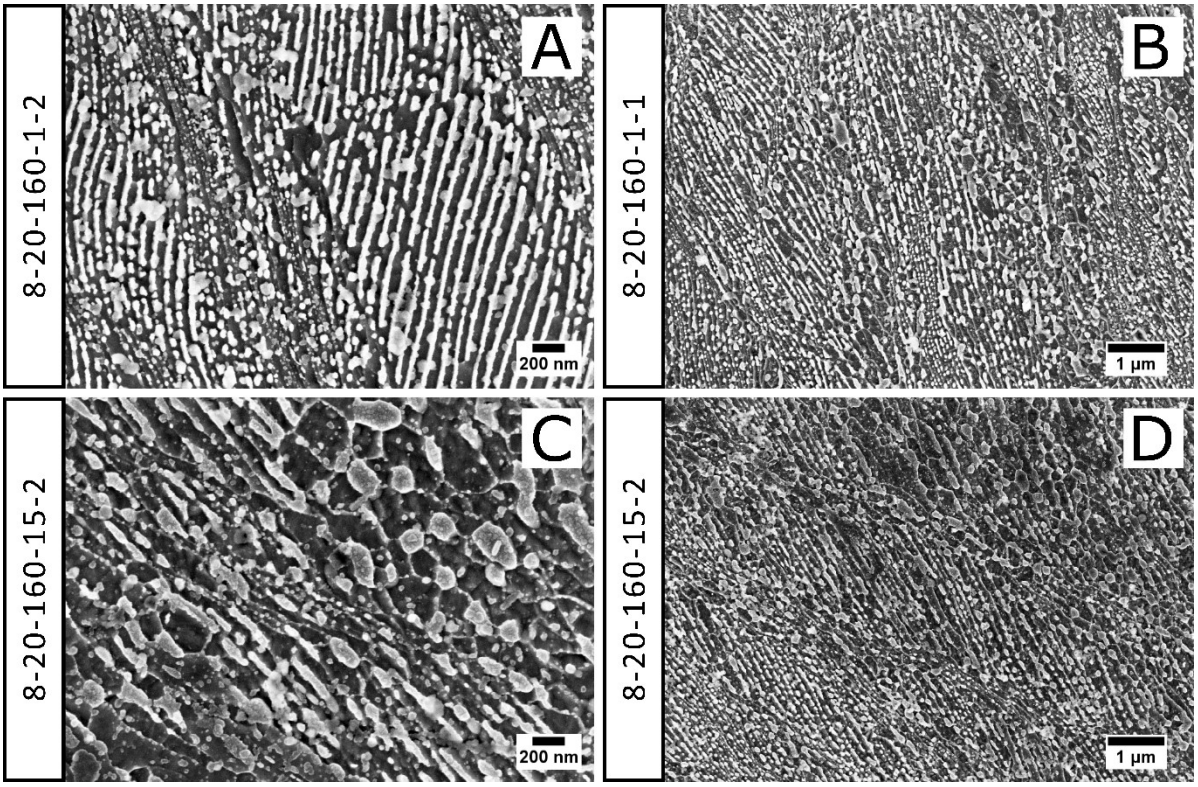


Figure 4.2. 0.92wt%C pearlitic steel electropulsed at 10^8 A·m^{-2}, f = 20Hz. Treatment parameters: d = 160µs, t = 1 minute (A,B); d = 160µs, t = 15 minutes (C,D). Secondary electron imaging on samples etched in 2% nital solution (methanol balance).

Pulse frequency = 50Hz

Electropulsing at higher frequency induced further microstructure change, as shown in Figure 4.3. Samples treated at frequency of 50Hz and pulse duration of 80µs for 1 (A,B) and 15 (C,D) minutes showed significant cementite spheroidisation distributed across the microstructure. The spheroidisation followed the prior lamellar structure, often appearing in linear columns. After 1 minute the spheroidisation was relatively large, with some regions of fine particles.

Treatment of 15 minutes duration produced a microstructure of larger globular particles with major axis length of 200 - 300nm. After both 1 and 15 minute treatment conditions the prior lamellar structure of the pearlite was still visible, and regions of incomplete spheroidisation were visible. The appearance of spheroidisation was largely observed to follow the prior lamellar structure. Regions of recrystallised ferrite microstructure were also observed in one sample (8-50-80-15-4, Figure 4.4), replacing the deformed lamellar pearlite microstructure.

Electropulsing at frequency of 50 Hz and pulse duration 160µs produced martensitic microstructure after treatments of both 1 and 15 minutes duration in two samples (Figure 4.3 E,F). Lenticular, angular features are clearly observed and no lamellar pearlite structure remains. The phase transformation was homogeneous and volume fraction was 100%. A single sample treated for 15 minutes

(8-50-160-15-3) was found to contain a lamellar microstructure that differed to the original lamellar structure (Figure 4.3 G,H). The transformation that occurred in the sample was a result of austenitisation followed by a slightly slower ambient cooling rate than the other samples treated at 160μs pulse duration, producing a coarse lamellar structure.

Table 4.4. Breakdown of electropulsing parameters at moderate current density (10^8 A·m^{-2}) and frequency 50Hz (note Area Reduction is abbreviated to AR).

Sample code	AR (%)	J ($x10^8$ A·m^{-2})	f (Hz)	d (μs)	t (min)	N (#)	Microstructure
8-50-80-5s-1	77	6.6	50	80	5s	250	Lamellar (no change)
8-50-80-5s-2	77	9.7	50	80	5s	250	Lamellar (no change)
8-50-80-1-1	77	5.6	50	80	1	3000	Spheroidised cementite
8-50-80-1-2	77	6.9	50	80	1	3000	Spheroidised cementite
8-50-80-1-3	77	6.3	50	80	1	3000	Spheroidised cementite
8-50-80-15-1	77	6.3	50	80	15	45000	Spheroidised cementite
8-50-80-15-2	77	7.4	50	80	15	45000	Spheroidised cementite
8-50-80-15-3	77	6.0	50	80	15	45000	Spheroidised cementite
8-50-80-15-4	71	7.5	50	80	15	45000	Spheroidised cementite / recrystallised α-ferrite
8-50-160-1-1	77	5.5	50	160	1	3000	Martensite
8-50-160-1-2	77	5.3	50	160	1	3000	Martensite
8-50-160-1-3	77	5.0	50	160	1	3000	Martensite
8-50-160-15-1	77	5.6	50	160	15	45000	Martensite
8-50-160-15-2	77	5.5	50	160	15	45000	Martensite
8-50-160-15-3	77	5.3	50	160	15	45000	Transformed pearlite

Bainite is a transitionary phase between pearlite and martensite, transforming from austenite at a temperature between that of the two phases (for a eutectoid composition steel, between approximately 250 and 550°C [169]). Bainite can appear in two forms, upper and lower, depending on transformation temperature and carbon content. Upper bainite is formed between 400 and 550°C, and lower bainite between 250 and 400°C [169]. The lamellar microstructure observed in Figure 4.3 (G,H) may have formed close to the martensite start (M_S) temperature, at the lower limit of the bainite formation temperature range. Note that studies have shown that upper bainite is unable to form in plain carbon steels of very high carbon content (0.85 to 1.8wt%C) [170, 171] which suggests that the microstructure observed here can be identified as coarse pearlitic or lower bainite.

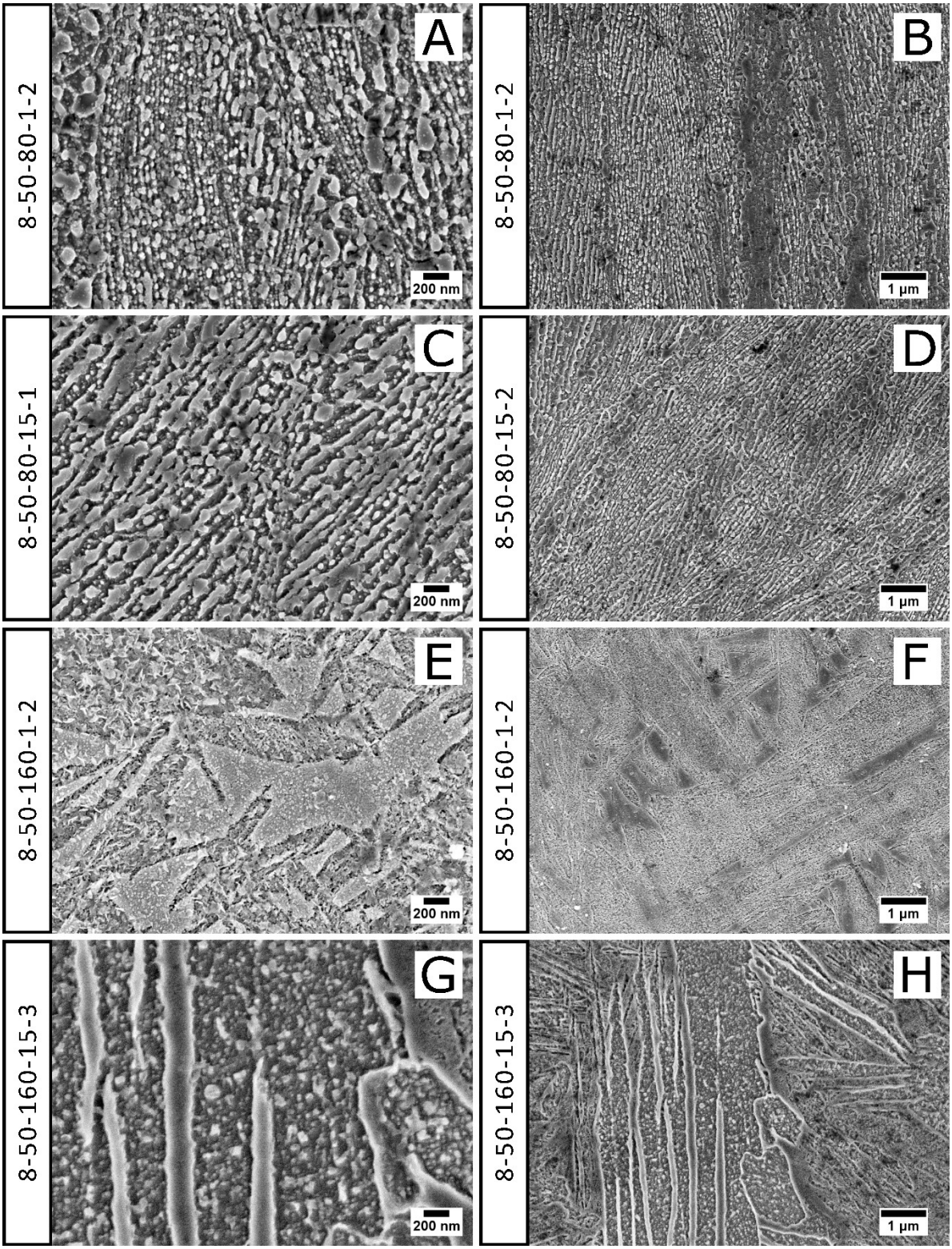


Figure 4.3. 0.92wt%C pearlitic steel electropulsed at 10^8 A·m^{-2}, f = 50Hz. Treatment parameters: d = 80µs, t = 1 minute (A,B); d = 80µs, t = 15 minutes (C,D); d = 160µs, t = 1 and 15 minutes (representative of martensitic microstructure) (E,F); d = 160µs, t = 15 minutes (G,H). Secondary electron imaging on samples etched in 2% nital solution (methanol balance).

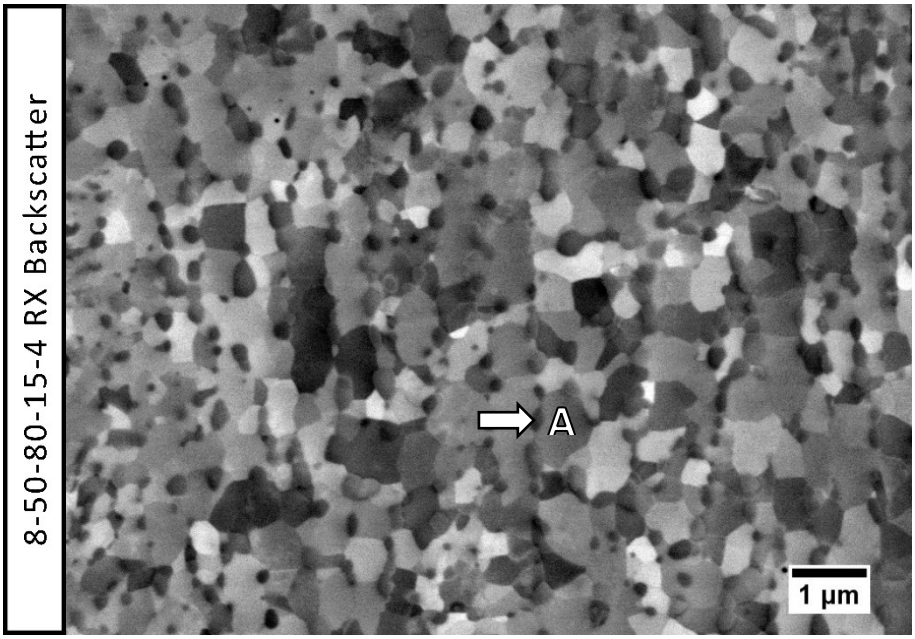


Figure 4.4. Backscatter electron imaging of recrystallised α-ferrite microstructure in sample 8-50-80-15-4. Ferrite grains are visible as equiaxed structures of varying shade (an example of which is labelled as 'A'). Globular grains appearing to overlay the ferrite are unresolved spheroidised cementite (indicated by an arrow).

A slight variation in cooling rate due to environmental factors such as a fluctuation in ambient temperature between the martensitic and bainitic samples could produce the differing microstructures. The temperature achieved during electropulsing was comparable between the samples, as all three were austenitised before assuming their final microstructure. Sample geometry effects in terms of heating or cooling are a factor that could have caused the microstructure variation between bainite and martensite. Geometries of the three samples were comparable, as shown in Table 4.5, although the bainitic sample was slightly larger than the samples that transformed to martensite.

Table 4.5. Geometries of samples treated at current density of the order $10^8 A \cdot m^{-2}$, frequency 50Hz, pulse duration 160µs and test duration 15 minutes.

Sample code	**L** *(mm)*	**W** *(mm)*	**D** *(mm)*	**A** *(mm^2)*
8-50-160-15-1	28.2	0.86	0.25	0.22
8-50-160-15-2	28.2	0.87	0.23	0.20
8-50-160-15-3	27.2	0.88	0.39	0.34

No microstructure effects were observed after 5 second treatments at frequency 50Hz and pulse duration 80µs. The lamellar structure was fully intact and no quantifiable morphology change was observed. Results at frequency of 50Hz show the progression of microstructure change with increasing pulse duration or treatment time. At low pulse and test duration no effects were observed despite moderate current density and frequency conditions. With increasing test duration spheroidised cementite was produced. An additional increase in pulse duration lead to martensitic microstructure.

Pulse frequency = 100Hz

Variable electropulsing effects were observed as a result of electropulsing treatments at frequency of 100Hz, as shown in Figure 4.5. Table 4.6 provides a breakdown of the electropulsing parameters associated with each sample treated at frequency of 100Hz. Note that pulse duration was not varied at these frequency and current density settings. Initial tests at pulse duration 160µs produced immediate sample failure due to heating effects, and subsequent experiments were discontinued as a result.

Table 4.6. Breakdown of electropulsing parameters at moderate current density (10^8 A·m^{-2}) and frequency 100Hz (note Area Reduction is abbreviated to AR).

Sample code	**AR** *(%)*	**J** *(x10^8 A·m^{-2})*	**f** *(Hz)*	**d** *(µs)*	**t** *(min)*	**N** *(#)*	**Microstructure**
8-100-80-2s-1	69	9.6 (9.64)	100	80	2s	200	Proeutectoid cementite
8-100-80-2s-2	69	9.6 (9.56)	100	80	2s	200	Lamellar (no change)
8-100-80-5s-1	77	9.0	100	80	5s	500	Martensite
8-100-80-5s-2	77	6.2	100	80	5s	500	Fine spheroidisation / recrystallisation
8-100-80-5s-3	77	8.8	100	80	5s	500	Fine spheroidisation / recrystallisation
8-100-80-5s-4	69	8.5	100	80	5s	500	Fine spheroidisation
8-100-80-1-1	77	5.2	100	80	1	6000	Martensite
8-100-80-1-2	77	6.3	100	80	1	6000	Martensite
8-100-80-1-3	77	4.8	100	80	1	6000	Coarse spheroidisation / recrystallisation
8-100-80-1-4	71	5.7	100	80	1	6000	Martensite
8-100-80-15-1	71	4.6	100	80	15	90000	Coarse spheroidisation / recrystallisation
8-100-80-15-2	71	5.5	100	80	15	90000	Martensite
8-100-80-15-3	71	4.2	100	80	15	90000	Coarse spheroidisation / recrystallisation
8-100-80-15-4	77	1.2	100	80	15	90000	Lamellar (no change)

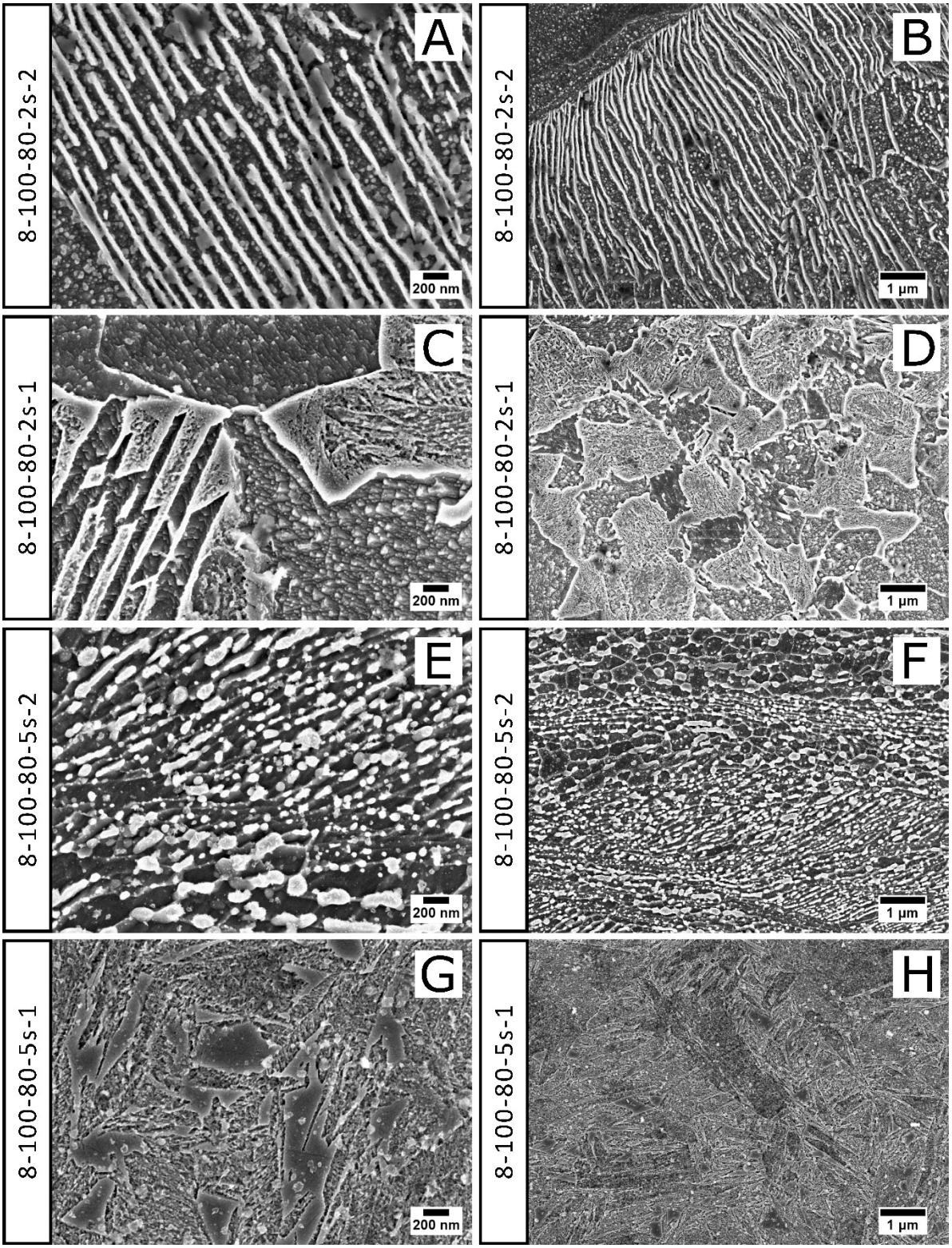


Figure 4.5. 0.92wt%C pearlitic steel electropulsed at 10^8 A·m^{-2}, f = 100Hz. Treatment parameters: d = 80µs, t = 2 seconds (A-B,C-D); d = 80µs, t = 5 seconds (E-F,G-H). Note that samples used in the 2 second condition were pre-processed as described in Methods Section 3, part ii. Secondary electron imaging on samples etched in 2% nital solution (methanol balance).

After treatment duration of 2 seconds, lamellar (Figure 4.5 A,B) or proeutectoid cementite (Figure 4.5 C,D) microstructure was observed.

Using the modified Dubé morphological system [172] the proeutectoid cementite formed can be classified as a combination of idiomorphic and Widmanstätten structures formed along the prior grain boundaries. Further description of proeutectoid cementite microstructure is given on page 97. Note that 2 second tests were carried out on material pre-prepared for high current density electropulsing, and as a result had an initial ferritic-pearlitic microstructure. Both samples were treated at higher current densities than any other in the 100Hz condition. The samples achieved comparable average current densities (9.56 and 9.64x10^{8} A·m^{-2}) and were treated at identical frequency and pulse duration. The difference in the microstructures observed could then result from two possible factors; 1) variation in treatment time, and 2) sample dimension measurement error.

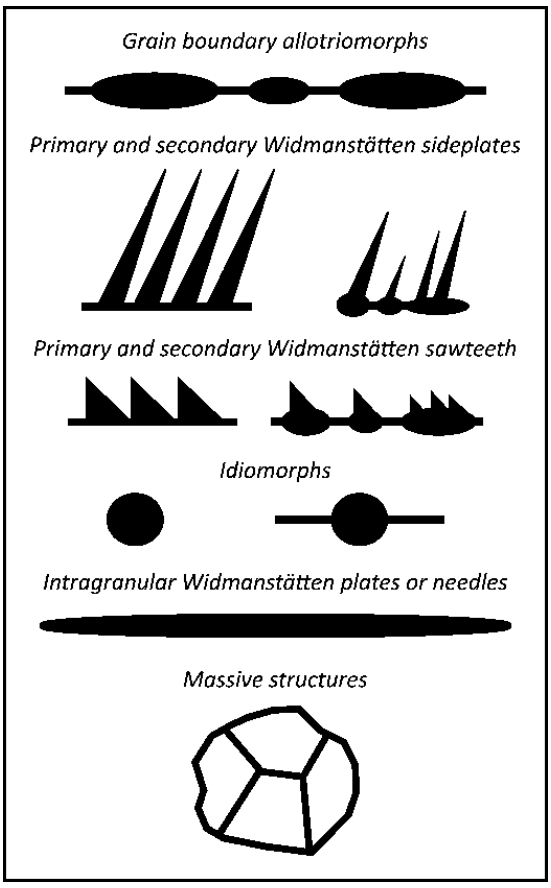


Figure 4.6. The Dubé morphological classification system [173, 174] as modified by Aaronson [172]. Reproduced from [175].

As the duration of the test was particularly short and mechanical electropulsing treatment timing was not a function of the equipment used, slight variation in treatment time at this test duration may have occurred. This difference in treatment time would be in the order of milli- or microseconds dependent on the accuracy of the human operator. Sample dimensioning errors may have occurred due to inhomogeneity of sample geometry or inaccuracies in the measuring equipment used. A closer investigation of sample geometry (Table 4.7) shows that proeutectoid cementite was obtained in the smaller of the two samples, which may explain a faster heating rate in the sample.

Table 4.7. Geometries and applied current parameters of samples treated at current density of the order $10^8 A \cdot m^{-2}$, frequency 100Hz, pulse duration 80µs and test duration 2 seconds. I_{IN} is the applied current, I_{OUT} is the output current.

Sample code	L (mm)	W (mm)	D (mm)	A (mm^2)	I_{IN} (A)	I_{OUT} (A)
8-100-80-2s-1	37.7	0.37	0.15	0.06	200	54
8-100-80-2s-2	41.3	1.2	0.16	0.19	200	179

Experiments of duration 5 seconds were also found to produce variable microstructure. At the highest of the four test current densities ($9.0x10^8$ $A \cdot m^{-2}$) homogeneous martensitic microstructure was observed (Figure 4.5 G,H), while at three lower current densities ($6.2 – 8.8x10^8$ $A \cdot m^{-2}$) fine cementite spheroidisation and α-ferrite recrystallisation were produced under the same pulsing parameters (Figure 4.5 E,F).

Microstructure change resulting from 1 and 15 minute electropulsing treatments is shown in Figure 4.7. After 1 minute, current densities of $5.2x10^8$ $A \cdot m^{-2}$ or greater induced homogeneous martensitic phase transformation (Figure 4.7 C,D). A lower current density of $4.8x10^8$ $A \cdot m^{-2}$ produced coarse cementite spheroidisation and regions of α-ferrite recrystallisation (Figure 4.7 A,B).

Similarly, a 15 minute treatment at current density of $5.5x10^8$ $A \cdot m^{-2}$ induced martensitic transformation (Figure 4.7 G,H), while current density of $4.2 - 4.6x10^8$ $A \cdot m^{-2}$ produced coarse cementite spheroidisation and α-ferrite recrystallisation (Figure 4.7 E,F). The α-ferrite recrystallisation was more developed after 15 minutes of treatment than after 1 minute. As a result one sample was selected for comparison with furnace annealed pearlitic steel to assess the development of α-ferrite recrystallisation, described on page 90.

A single sample showed no electropulsing effects after 15 minutes at a frequency of 100Hz. The applied current density was $1.2x10^8$ $A \cdot m^{-2}$, a particularly low value compared to other treatment conditions. This low current density was insufficient to induce any quantifiable microstructure change, independent of the elevated frequency applied.

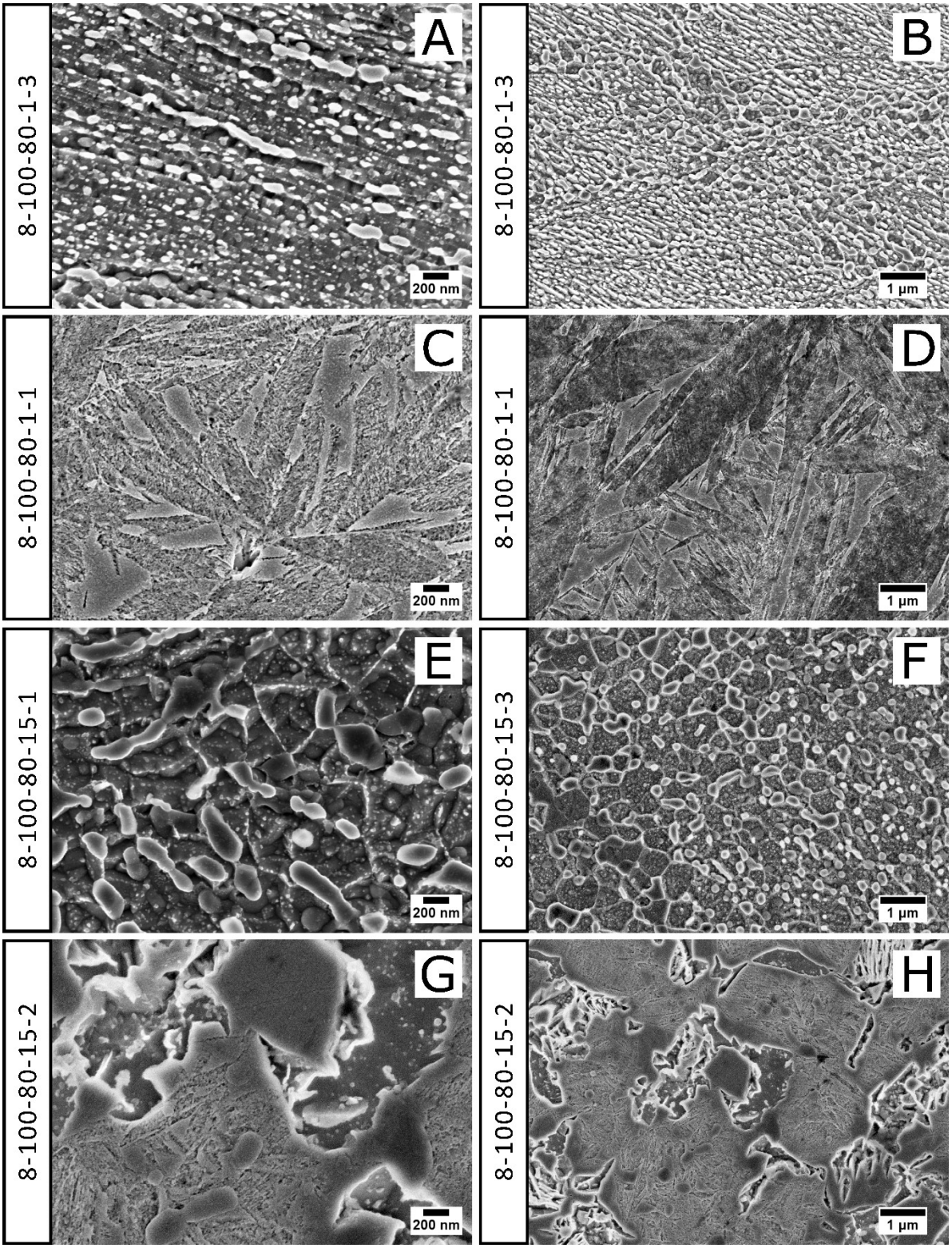


Figure 4.7. 0.92wt%C pearlitic steel electropulsed at 10^8 A·m^{-2}, f = 100Hz. Treatment parameters: d = 80µs, t = 1 minute (A-B,C-D); d = 80µs, t = 15 minutes (E-F,G-H). Secondary electron imaging on samples etched in 2% nital solution (methanol balance).

Grain size analysis (f = 100Hz, d = 80µs)

Comparison of α-ferrite recrystallisation was undertaken between electropulsed and furnace annealed samples, in order to assess the development of recrystallisation due to electropulsing and to give a broad estimate of the temperatures involved. Welded thermocouples were rejected for the purpose of temperature measurement; the reasoning behind this is given in the Methods section (pp.65).

Grain size analysis was conducted on a sample electropulsed at frequency 100Hz, pulse duration 80µs and test duration 15 minutes (Figure 4.7 F). Comparison was made with three furnace treated samples at 600, 650 and 700°C (Figure 4.8). According to the 0.92wt%C steel phase diagram (Methods, pp.54), α-ferrite recrystallisation would be expected to occur within this temperature range, which falls just below the eutectoid temperature. All samples, electropulsed or furnace annealed, were treated for 15 minutes and allowed to cool in still air (ambient conditions). Grain measurements were conducted as described on pp.73 and a Weibull distribution (see Methods, pp.73) was fitted to histograms generated from the data. Ferrite grain aspect ratio distribution is shown in Figure 4.9, and area and major axis length are shown in Figure 4.10. Additional data on measured grains and volume fraction are summarised in Table 4.8.

From the grain distribution histograms in Figure 4.9 and Figure 4.10 the characteristics of recrystallised grains can be observed. The aspect ratio, used to describe the development of equiaxed recrystallised grains, was comparable between the four samples (Figure 4.9). This was to be expected as the grains measured were all recrystallised to some degree, leading to aspect ratios of 1 to 2.5 in all conditions.

Grain surface area was found to increase with annealing temperature across the three furnace treated samples (Figure 4.10). At 600°C grain area distribution was concentrated between 0.05 and 0.19µm^2 (with an upper limit of approximately 0.5µm^2). The concentrated area distribution range increased to between 0.075 and 0.325µm^2 (with an upper limit of approximately 1µm^2) at 700°C. This behaviour was accounted for by grain growth after recrystallisation of new strain free grains in the microstructure [25]. The electropulsed sample was most closely comparable to the 650°C and 700°C conditions (Figure 4.10). The largest concentration of the electropulsed sample grain area distribution fell between 0.1 and 0.325µm^2. The grain area distribution extended up to approximately 0.85µm^2, which was between the distribution extremes of the two furnace conditions.

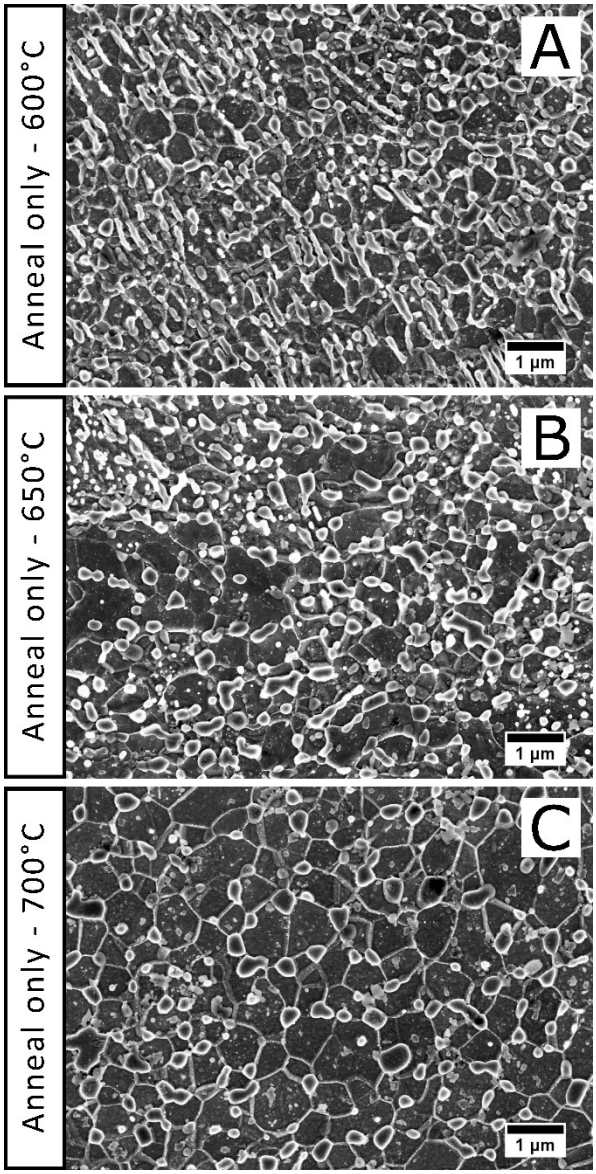


Figure 4.8. Furnace annealed 0.92wt%C pearlitic steel samples. A) 600°C; B) 650°C; C) 700°C. All samples annealed for 15 minutes and air cooled. Secondary electron imaging on samples etched in 2% nital solution (methanol balance).

Table 4.8. Recrystallised α-ferrite grain data.

Condition *(t = 15mins)*	**n** *(#)*	**Volume fraction** *(%)*
Electropulsed at 100Hz, 80µs, 10^8 A·m^{-2}	585	18
Furnace T_T = 600C (T_A = 601)	608	30
Furnace T_T = 650C (T_A = 653)	421	13
Furnace T_T = 700C (T_A = 704)	1186	37

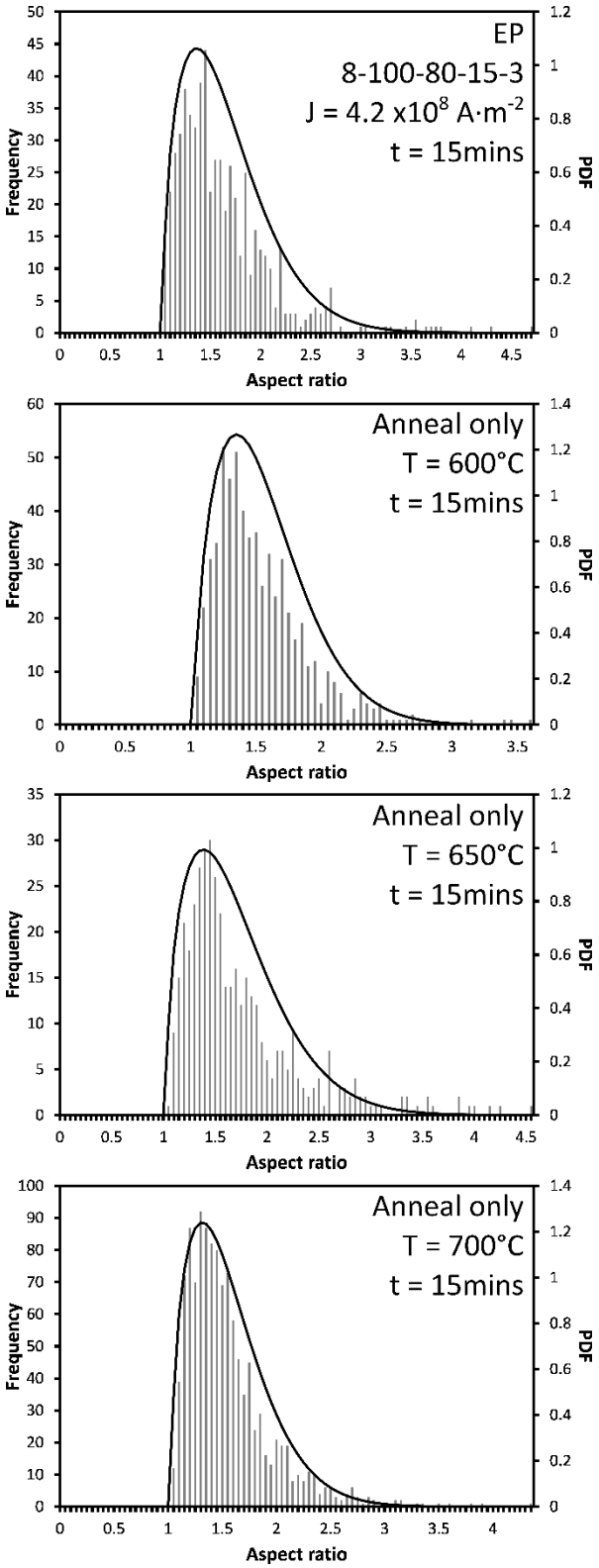


Figure 4.9. Aspect ratio characteristics of recrystallised microstructure obtained by electropulsing treatment at 4.2x10^8 A·m^{-2} or furnace annealing. Electropulse-induced recrystallisation is compared with annealing treatments at 600°C, 650°C and 700°C.

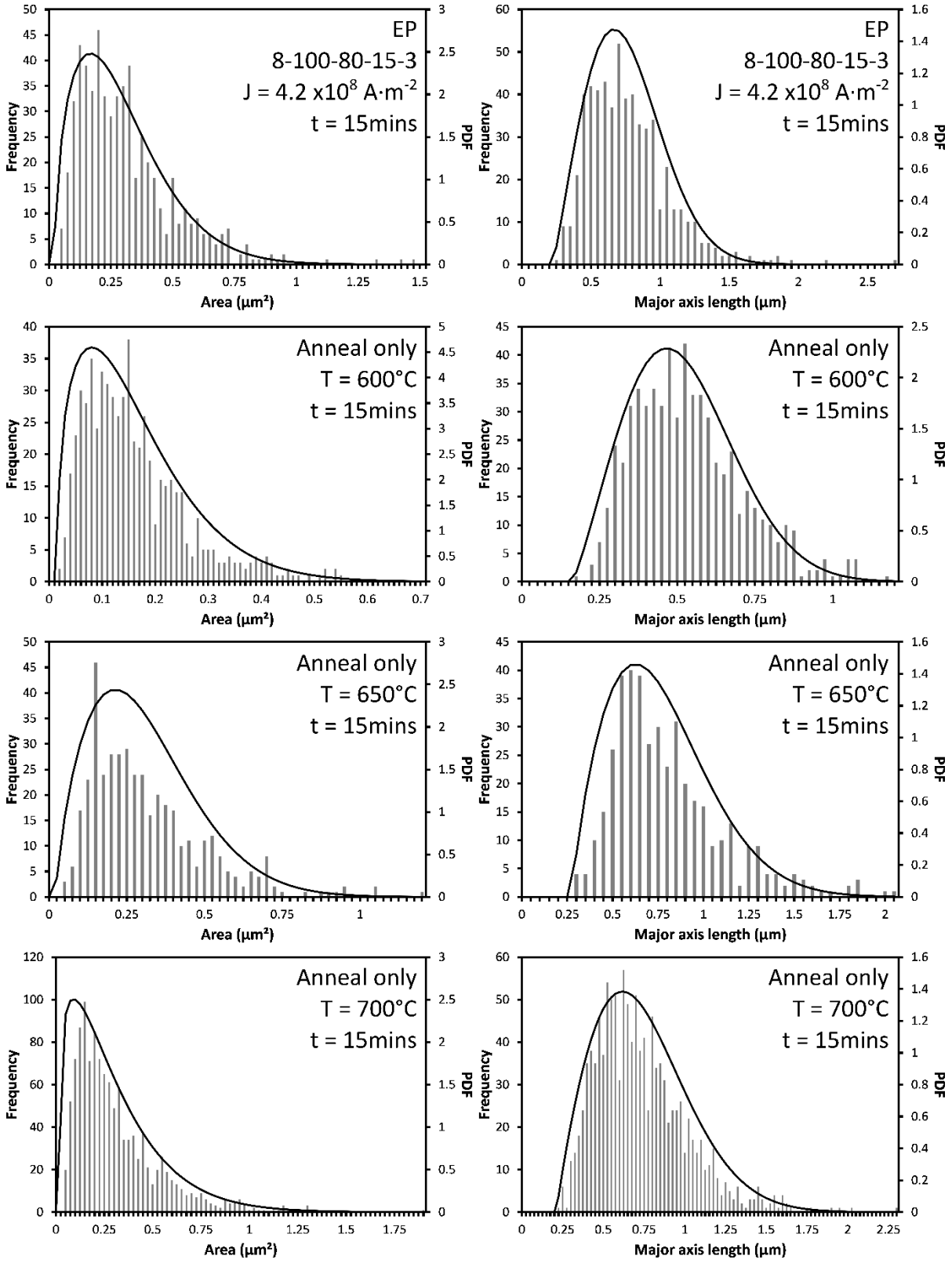


Figure 4.10. Area (left) and major axis length (right) characteristics of recrystallised microstructure obtained by electropulsing treatment at 4.2x10^{8} A·m^{-2} or furnace annealing. Electropulse-induced recrystallisation is compared with annealing treatments at 600°C, 650°C and 700°C.

The major axis length of recrystallised α-ferrite grains was also found to increase with annealing temperature (Figure 4.10). At 600°C the distribution was focused between approximately 0.35 and 0.6µm, extending up to a limit of 1.075µm. At 650°C the distribution concentration shifted up to between 0.5 and 0.85µm, with an upper limit of 1.85µm. The distribution at 700°C was similar to that of 650°C. An increase in major axis length echoed the findings reported on grain area.

During grain growth, both the surface area and hence the major axis length would be expected to increase. The electropulsed sample had a major axis length distribution concentrated between 0.45 and 0.95µm, the upper limit extending to approximately 1.55µm (Figure 4.10). The distribution of major axis length in the electropulsed sample was again most similar to that of the 650°C and 700°C furnace annealed samples.

In summary, α-ferrite recrystallisation induced by electropulsing treatment of frequency 100Hz, pulse duration 80µs and test duration 15 minutes was found to have comparable microstructural features to similar samples treated at 650 and 700°C in a furnace. Grain size analysis with three microstructure descriptors (aspect ratio, surface area and major axis length) was used to confirm the observation.

4.2.1.3. High current density, J ~10^9A·m^{-2}

SEM analysis of samples treated at current density of the order 10^9 A·m^{-2} are detailed in the following pages. As in the previous section, the results are categorised by pulse frequency. Note that at frequencies of 20Hz and above, pulse duration was not varied. As described previously (pp.85) the heating effects associated with the combination of high frequencies, pulse durations and current densities produced sample failure in initial tests. As a result it was determined that tests at current density of the order of 10^9 A·m^{-2} would be conducted at a lower pulse duration (80µs).

Pulse frequency = 1Hz

Single pulse tests were conducted at 10^9 A·m^{-2} to assess whether longer pulse duration could induce microstructure effects independently of frequency at high current densities. Eight tests at pulse durations between 200µs and 1000µs (1ms) and current densities between 1.1 and 2.3x10^9 A·m^{-2} failed to produce any observable microstructure effects. Four further tests at 200µs and frequency 1Hz for a duration of 10 seconds also had no effect. In all cases the lamellar structure remained in a deformed state and no lamellar breakdown as a result of electropulsing was observed.

Pulse frequency = 20Hz

Figure 4.11 shows microstructure effects in 0.92wt%C steel after electropulsing at current density of the order 10^9 A·m^{-2}, frequency 20Hz and pulse duration 80µs for 1 (A,B) and 15 minutes (C,D). After 1 minute regions of fine cementite breakdown and spheroidisation were observed. The regions were randomly distributed, and the remaining unaltered microstructure was intact lamellar. After

15 minutes fine cementite breakdown was also observed, but spheroidisation was not visible. The microstructure change was again inhomogeneous, and distributed randomly across the observed area. The remaining microstructure was lamellar, identical to that after 1 minute of electropulsing.

Table 4.9. Breakdown of electropulsing parameters at high current density (10^9 A·m^{-2}) and frequency 20Hz.

Sample code	AR (%)	J ($x10^9$ A·m^{-2})	f (Hz)	d (µs)	t (min)	N (#)	Microstructure
9-20-80-5s-1	69	2.02	20	80	5s	100	Lamellar (no change)
9-20-80-5s-2	69	2.25	20	80	5s	100	Lamellar (no change)
9-20-80-5s-3	69	2.03	20	80	5s	100	Lamellar (no change)
9-20-80-1-1	69	1.03	20	80	1	1200	Fine lamellar breakdown
9-20-80-1-2	69	1.52	20	80	1	1200	Fine lamellar breakdown / spheroidisation
9-20-80-1-3	69	1.32	20	80	1	1200	Fine lamellar breakdown / spheroidisation
9-20-80-15-1	69	1.24	20	80	15	18000	Fine lamellar breakdown
9-20-80-15-2	69	1.23	20	80	15	18000	Fine lamellar breakdown
9-20-80-15-3	69	1.17	20	80	15	18000	Fine lamellar breakdown

Table 4.9 details the applied electropulsing parameters at frequency 20Hz and current density 10^9 A·m^{-2}. After 1 or 15 minutes it can be seen that the regions of more developed lamellar breakdown and spheroidisation occur in samples treated at relatively higher current densities ($1.32x10^9$ A·m^{-2} and above), while at $1.24x10^9$ A·m^{-2} and below the microstructure effect is less significant. Test duration did not appear to significantly affect the progression of microstructure change after 15 minutes at lower current densities.

No quantifiable microstructure effects were observed after tests of 5 seconds duration. This is despite a higher current density in each of three tests at 5 seconds, than any other 20Hz frequency test. In each case the prior deformed lamellar structure was maintained. At a low frequency and test duration, there was insufficient time and driving force for microstructure effects to manifest.

Experiments at 20Hz show the dependency of electropulse-induced microstructure effects on a balance between the applied parameters. Insufficient current density, frequency, and test duration were all found to affect successful microstructure transformation.

Pulse frequency = 50Hz

Figure 4.12 shows varied microstructure effects in 0.92wt%C steel samples treated at frequency 50Hz, test duration 2 seconds and current density 10^9 A·m^{-2}. Figure 4.12 demonstrates the range of microstructure change observed, which included coarse lamellar regions (A,B), fine cementite breakdown and spheroidisation (C) and unaltered lamellar structure (D). In some cases, all three morphologies were observed in the same sample. The distribution of microstructure effects

with treatment parameters is described in Table 4.10, where "Various" refers to those samples with multiple morphologies present.

The table shows that the observed variations can be correlated with the applied treatment parameters. Treatments of current density 1.03 and 1.16×10^9 $A \cdot m^{-2}$ did not produce any quantifiable microstructure change. The deformed lamellar structure remained intact after electropulsing.

Electropulsing at higher current density (between 1.25 and 1.70×10^9 $A \cdot m^{-2}$) was found to produce a variable microstructure of coarse lamellar regions, fine cementite breakdown and spheroidisation, and prior lamellar structure. The appearance of the microstructure was inhomogeneous, with each morphology randomly distributed throughout the sample.

The underdeveloped, fragmented and partially unaffected microstructure observed is likely a result of the short treatment time. Over 2 seconds there was insufficient time for meaningful microstructure change to occur, leading to only partially transformed samples. The short treatment time is also more sensitive to slight variations in test end time due to a human operator, resulting in marginally different treatment times. A difference of milliseconds could introduce slight variations in morphology at high electropulsing

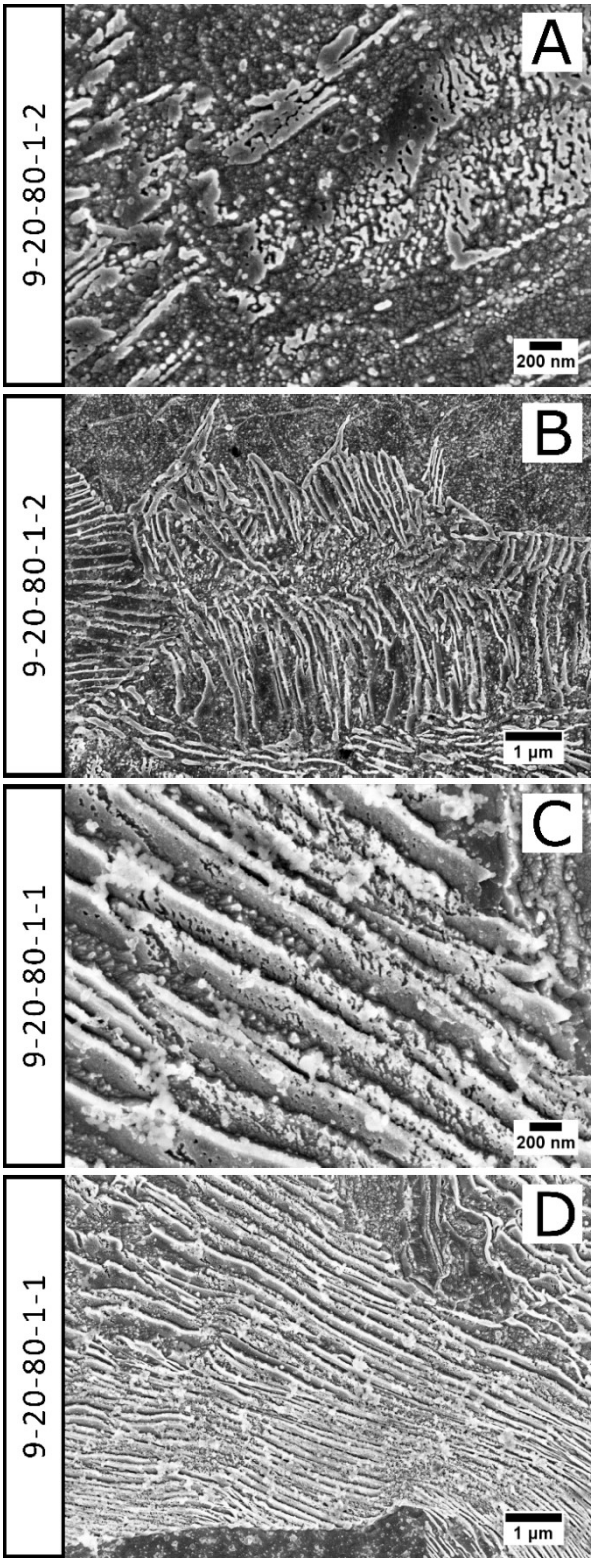


Figure 4.11. 0.92wt%C pearlitic steel electropulsed at 10^9 $A \cdot m^{-2}$, f = 20Hz, d = 80µs. Representative of treatments at 1 and 15 minutes. Secondary electron imaging on samples etched in 2% nital solution (methanol balance).

parameters, and may explain the variable microstructure observed.

After treatments of 5 seconds, the microstructure changes observed are more uniform. As shown in Figure 4.13, fine spheroidised cementite was consistently produced after electropulsing of current densities between 1.44 and 2.75x10^9 A·m^{-2}. The microstructure change was homogeneous in four of five samples, with the fifth showing spheroidised regions.

The variation in the development of spheroidisation in a single sample (9-50-80-5s-5) does not appear to correlate with the electropulsing parameters applied. The current density of the treatment (1.64x10^9 A·m^{-2}) lies within the range stated previously (1.44 to 2.75x10^9 A·m^{-2}) and all other electropulsing parameters were identical. As described previously some variation in treatment time may occur in short test durations due to human error.

However, the uniformity of morphology in the remaining four samples suggests that this is unlikely to have been the cause of inhomogeneity in this case. It is therefore suggested that sample 9-50-80-5s-5 is anomalous, perhaps the result of a faulty connection or poor surface cleanliness.

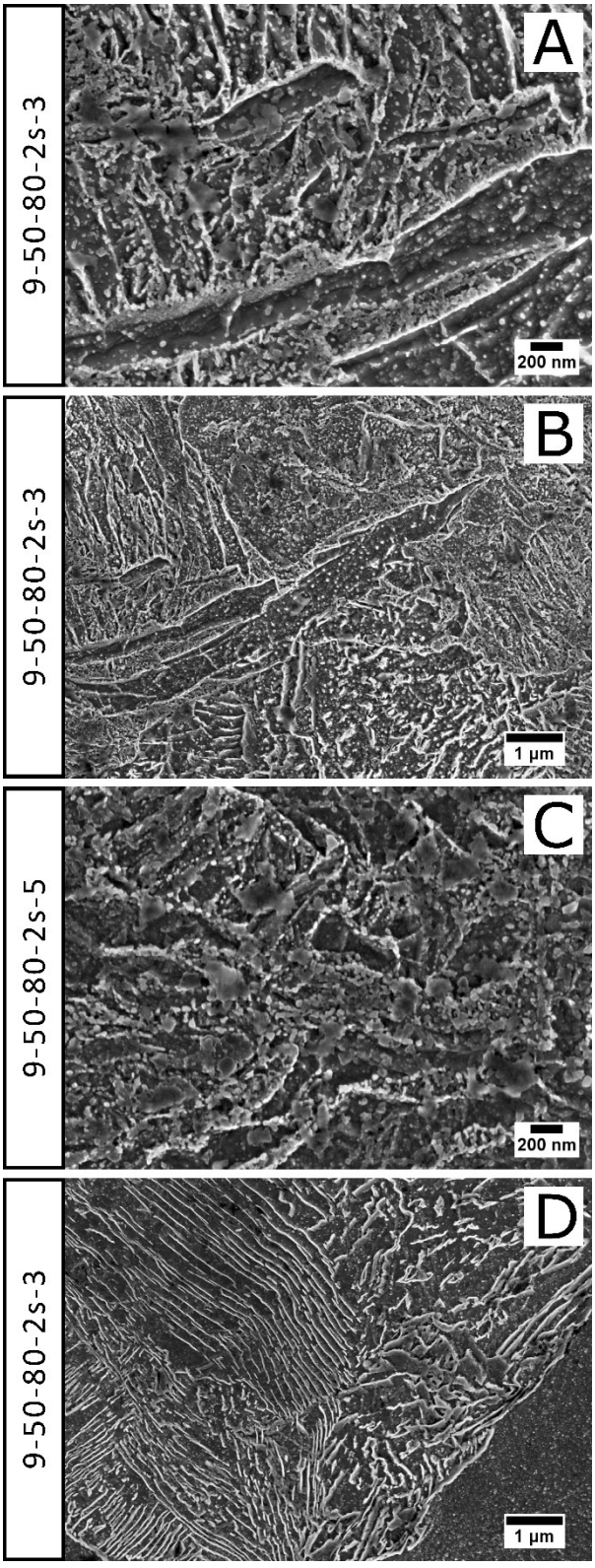


Figure 4.12. 0.92wt%C pearlitic steel electropulsed at 10^9 A·m^{-2}, f = 50Hz, d = 80µs, t = 2 seconds. Various microstructures were observed after treatment at these parameters. Secondary electron imaging on samples etched in 2% nital solution (methanol balance).

Table 4.10. Breakdown of electropulsing parameters at high current density (10^9 A·m^{-2}) and frequency 50Hz.

Sample code	AR (%)	J ($x10^9$ A·m^{-2})	f (Hz)	d (µs)	t (min)	N (#)	Microstructure
9-50-80-2s-1	69	1.05	50	80	2s	100	Lamellar (no change)
9-50-80-2s-2	69	1.30	50	80	2s	100	Various
9-50-80-2s-3	69	1.70	50	80	2s	100	Various
9-50-80-2s-4	69	1.41	50	80	2s	100	Various
9-50-80-2s-5	69	1.25	50	80	2s	100	Various
9-50-80-2s-6	69	1.16	50	80	2s	100	Lamellar (no change)
9-50-80-5s-1	69	1.58	50	80	5s	250	Fine spheroidisation
9-50-80-5s-2	69	2.75	50	80	5s	250	Fine spheroidisation
9-50-80-5s-3	69	1.44	50	80	5s	250	Fine spheroidisation
9-50-80-5s-4	69	1.90	50	80	5s	250	Fine spheroidisation
9-50-80-5s-5	69	1.64	50	80	5s	250	Fine spheroidisation (regions)

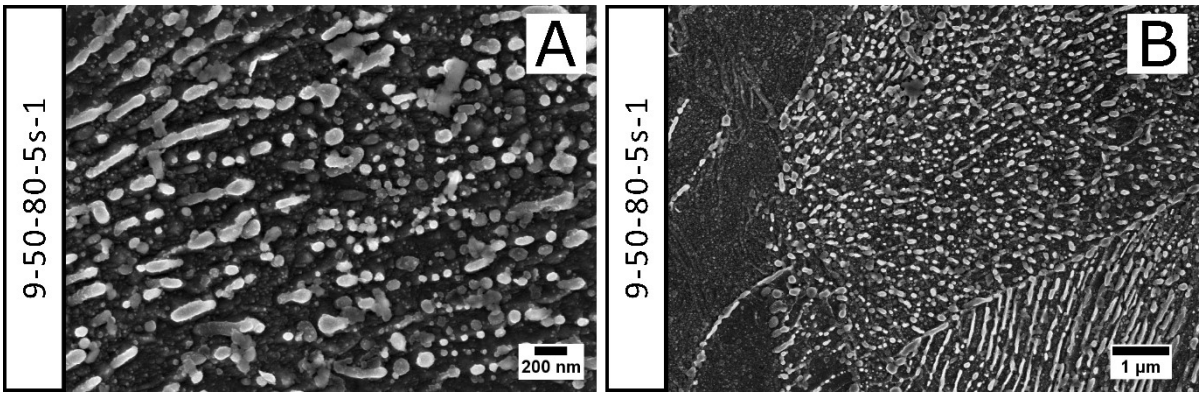


Figure 4.13. 0.92wt%C pearlitic steel electropulsed at 10^9 A·m^{-2}, f = 50Hz, d = 80µs, t = 5 seconds. Secondary electron imaging on samples etched in 2% nital solution (methanol balance).

Pulse frequency = 100Hz

Microstructure effects after electropulsing treatment at current density of the order 10^9 A·m^{-2} and frequency 100Hz are shown in Figure 4.14. Similar to results described in the previous section for 50Hz tests (pp.94), variable microstructures were observed. The results and experimental parameters are summarised in Table 4.11.

Tests of 2 seconds duration and 80µs pulse duration at frequency 100Hz and current density 10^9 A·m^{-2} were found to produce particularly variable microstructure effects. Of the five samples tested, three contained fine spheroidised cementite (Figure 4.14 A,B) distributed across the microstructure. The location of the cementite varied, with some grains following the prior lamellar structure while others were randomly distributed within the prior pearlite colony boundaries. One spheroidised sample was also found to contain regions of α-ferrite recrystallisation.

Table 4.11. Breakdown of electropulsing parameters at high current density (10^9 A·m^{-2}) and frequency 100Hz.

Sample code	AR (%)	J ($x10^9$ A·m^{-2})	f (Hz)	d (µs)	t (min)	N (#)	Microstructure
9-100-80-2s-1	69	1.18	100	80	2s	200	Fine spheroidisation
9-100-80-2s-2	69	1.20	100	80	2s	200	Proeutectoid cementite
9-100-80-2s-3	69	1.91	100	80	2s	200	Fine spheroidisation
9-100-80-2s-4	69	1.28	100	80	2s	200	Fine spheroidisation / recrystallisation
9-100-80-2s-5	69	1.02	100	80	2s	200	Proeutectoid cementite
9-100-80-5s-1	69	1.64	100	80	5s	500	Proeutectoid cementite
9-100-80-5s-2	69	1.06	100	80	5s	500	Proeutectoid cementite / spheroidisation
9-100-80-5s-3	69	1.03	100	80	5s	500	Fine spheroidisation
9-100-80-5s-4	69	1.17	100	80	5s	500	Proeutectoid cementite

The remaining two samples were observed to have a dual-phase microstructure of Widmanstätten cementite and coarse cementite idiomorphs in a ferrite matrix (Figure 4.14 C,D). The microstructure is characterised by thick wedge-shaped plate protrusions of Widmanstätten cementite emerging from extremely coarse regions of pro-eutectoid cementite idiomorphs nucleated along the grain boundaries, as shown schematically in Figure 4.15 B and C. Grain boundary idiomorphs (GBIs) were the dominant morphology in the observed prior pearlitic regions, with Widmanstätten cementite distributed in areas across the observed microstructure.

The structure of Widmanstätten cementite is fine (Figure 4.15 B) or coarse (Figure 4.15 C) dependent on the level of undercooling. The microstructures observed are analogous to those found in hypoeutectoid steel compositions, producing Widmanstätten ferrite and ferrite GBIs. Pro-eutectoid cementite in the form of GBIs is nucleated between the eutectoid and A_{cm} temperature, existing in dual phase with austenite. Above the A_{cm} temperature the microstructure is that of single phase austenite [175]. As shown in Figure 4.15 A, at small undercoolings below A_{cm}, cementite idiomorphs nucleate on austenite grain boundaries while greater undercooling produces finer Widmanstätten structures [142]. The transformation from GBIs to Widmanstätten cementite is not yet fully understood and explanation of the phenomenon is not within the scope of this thesis. However, existence of both morphologies within electropulsed samples gives an indication of the temperatures achieved by the process. From Figure 3.4, the A_{cm} temperature for steel of carbon content 0.92wt%C and composition as described in Table 3.6 was estimated to be 811°C.

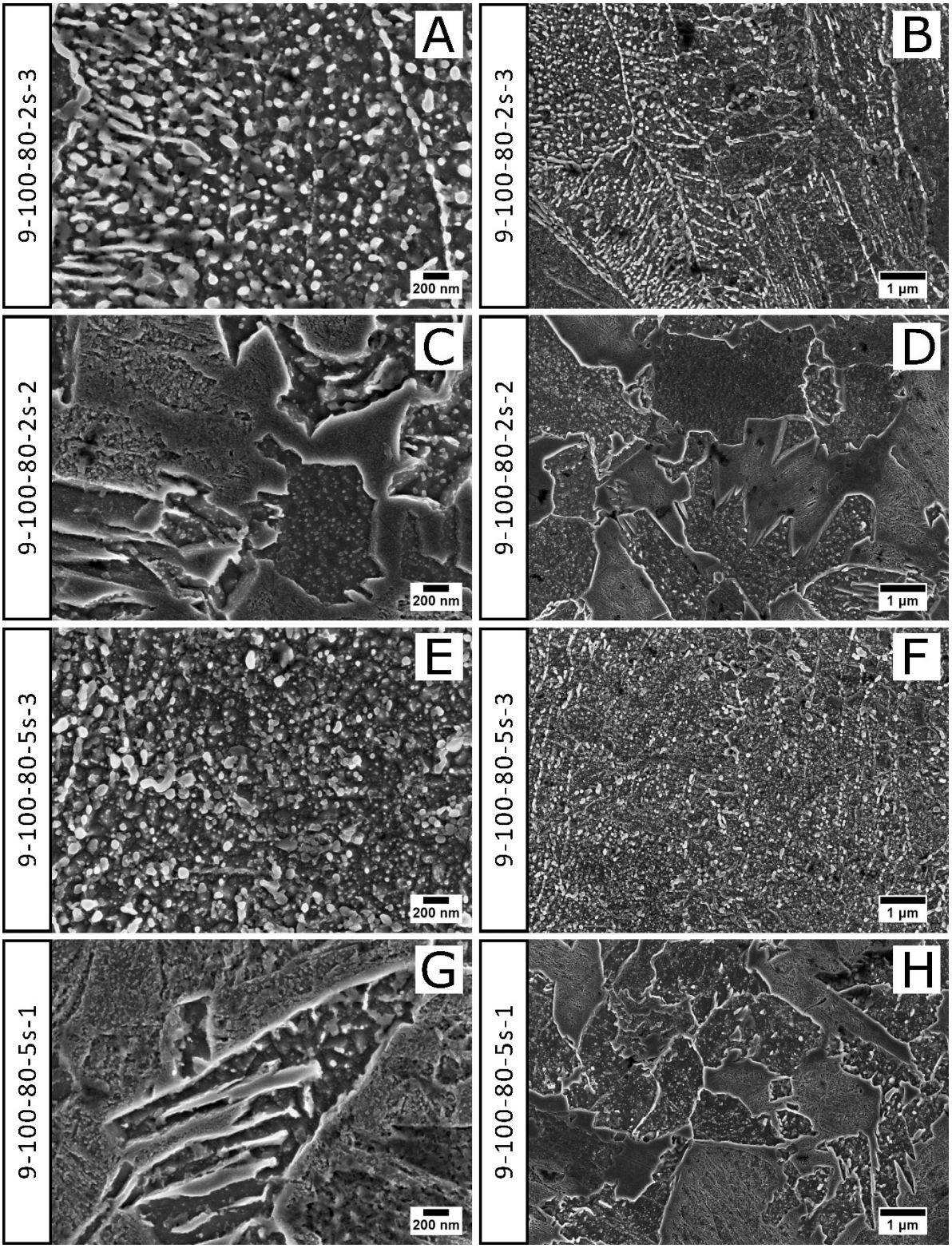


Figure 4.14. 0.92wt%C pearlitic steel electropulsed at 10^9 A·m^{-2}, f = 100Hz. Treatment parameters: d = 80µs, t = 2 seconds (A-B,C-D); d = 80µs, t = 5 seconds (E-F,G-H). Secondary electron imaging on samples etched in 2% nital solution (methanol balance).

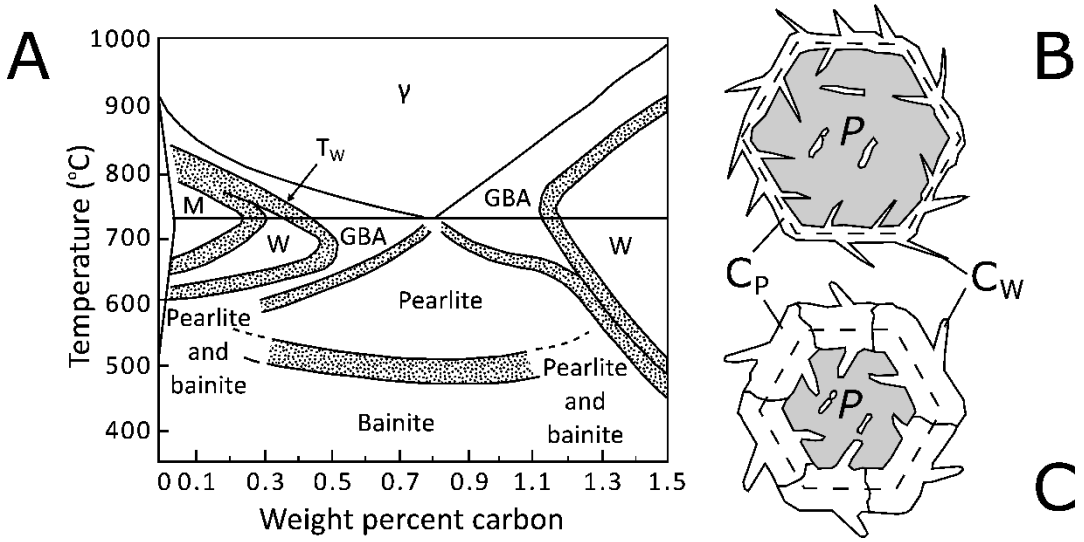


Figure 4.15. A) Temperature-composition relationships for carbon steel [142] (Fig 5.48b, originally [172]). T_W - temperature below which Widmanstätten (W) plates predominantly form, and above which grain boundary allotriomorphs (GBAs) and idiomorphs form (M = massive ferrite).
B,C) Schematics of fine (B) and coarse (C) Widmanstätten structures in a hypereutectoid steel, with pearlitic (P), peripheral (proeutectoid) cementite (C_P) and Widmanstätten cementite (C_W) regions [176].

The dual-phase ferrite-proeutectoid cementite microstructure shown in Figure 4.14 C, D, G and H can be theorised in terms of the initial, pre-electropulsed microstructure. As shown in Figure 3.8, the microstructure before treatment was dual-phase pearlite-ferrite. In order to produce the microstructure shown in Figure 4.14 C, D, G and H, the electropulsing treatment would have been required to induce temperatures high enough to peak inside the unstable austenite-cementite region between A_{e1} and A_{cm}. Within this region the austenite transformation is incomplete, and areas of both pro-eutectoid cementite and α-ferrite (according to Figure 3.4, up to 742°C) may coexist. Recrystallisation was induced in the initial α-ferrite microstructure on elevation to a temperature between 728 and 742°C, while cementite GBIs formed along the ferrite grain boundaries. Only very small pearlitic regions were observed in the samples containing GBI morphology, having formed from austenite that had achieved equilibrium composition.

Correlation of microstructure with electropulsing parameters is weak after electropulsing for a duration of 2 seconds. Widmanstätten cementite and cementite GBIs are expected to appear at temperatures in excess of the A_{e1} temperature and below the A_{cm} temperature, for this composition specifically between 728 and 811°C. Cementite spheroidisation is known to occur in a subcritical region below the A_{e1} temperature [139], in this case below 728°C. It would therefore be expected that pro-eutectoid cementite morphologies would be achieved in samples that experienced higher current density electropulsing (and therefore higher current-induced heating). However, cementite spheroidisation was observed in two samples treated at 1.28 and 1.91×10^9 $A \cdot m^{-2}$

(9-100-80-2s-4 and -3, respectively) while pro-eutectoid morphologies were found in samples treated at lower current densities of 1.02 and 1.20x10^9 A·m^{-2} (9-100-80-2s-5 and -2, respectively).

Experiments of 2 seconds duration at frequency 100Hz experienced identical sensitivity issues to tests conducted at 50Hz and current density of the order 10^9 A·m^{-2} (see pp.94). The effects of slight variation in treatment time or sample cross-section are magnified at increased frequency, resulting in unpredictable variations in morphology. Consistent and reproducible microstructure effects should not be expected in multiple pulse electropulsing treatments at duration of 2 seconds or less without the use of a mechanical timing method and uniform sample dimensions.

Experiments at frequency 100Hz, pulse duration 80µs and current density of the order 10^9 A·m^{-2} gave more predictable results after electropulsing for a duration of 5 seconds. The microstructures obtained are shown in Figure 4.14 (E-H), and are similar to those reported after tests of 2 seconds duration. Fine cementite spheroidisation (Figure 4.14 E,F) was reported in one sample. A dual-phase microstructure of cementite GBIs in an α-ferrite matrix (Figure 4.14 G,H) was observed in the remaining three samples. One sample containing GBI microstructure also had regions of fine spheroidisation distributed randomly across the observed surface.

The key difference between these results and those obtained after 2 seconds test duration lies in the correlation between pulsing parameters and morphology. As detailed in Table 4.11, the microstructures achieved were more consistent relative to the applied treatments. The sample containing fine spheroidisation only was obtained after electropulsing at the lowest current density of the four, 1.03x10^9 A·m^{-2}. The sample containing both spheroidised cementite and cementite GBIs was treated at 1.06x10^9 A·m^{-2}. The remaining two dual-phase GBI-α-ferrite samples were treated at the highest current densities, 1.17 and 1.64x10^9 A·m^{-2}. In this case there is clear correlation between pulsing parameters and obtained microstructure – with increasing current density (and as a result, increasing heating effect) the microstructure alters from sub-eutectoid morphologies to austenite derivatives.

4.2.2. Mechanical and electrical properties

Vickers microhardness testing was conducted as described in the Methods section (pp.75) to assess the mechanical properties of electropulsed samples. Microhardness testing was carried out at loads of 0.5, 1 or 2kg depending on sample size, at an optical magnification of 10X and a dwell time of 10 seconds. Each sample typically underwent five to six hardness tests at regions distributed across the sample surface, and an average value was calculated. A minimum of three tests were conducted in all cases. Figures 4.16, 4.17 and 4.20 show microhardness values plotted by pulsing parameter. The results are grouped by current density, then by pulse and test duration, and finally by frequency.

Sample codes for each parameter group are stated. The average as-received, cold-rolled microhardness value is shown on each plot as a dashed line.

Resistance tests were carried out using a micro-ohmmeter as described in the Methods section (pp.76) to characterise the electrical properties of electropulsed steel. Note that in each case resistance and hardness tests were both conducted on the same sample. Four tests were conducted on each sample and an average value calculated. The average value was then used to calculate the material resistivity (pp.76). The resistivity values shown in Figure 4.16, 4.17 and 4.20 are not plotted with error bars. In all cases each of the four resistance readings per sample were essentially identical and the calculated test error was negligible. Error associated with sample measurement is detailed in section 3.5.4.2. As a large number of resistivity values were collected, the values plotted in Figures 4.16, 4.17 and 4.20 are representative. The results are grouped by current density, then frequency, then pulse duration followed by test duration. The as-received and post-electropulsing resistivity value for each sample is plotted.

4.2.2.1. Low current density, J ~10^7A·m^{-2}

Hardness

Microhardness tests of samples pulsed at a current density of the order 10^7 A·m^{-2} showed no significant variation from the average as-received, cold-rolled value of 511±22 HV_1 (Figure 4.16 A-D). The microhardness of electropulsed samples ranged between 473 and 575HV_1, a 7.4% decrease and 12.5% increase respectively on the as-received cold-rolled value. These values do not correlate with any particular pulsing parameter, and are not significant. Of all 32 samples shown, only four fall outside the region of error of the as-received cold-rolled average value. The variation stems from natural differences in pearlitic structure and localised deformation effects.

Resistivity

Electrical resistivity tests showed no significant variation after electropulsing treatment. Of the twelve samples plotted in Figure 4.16 E, two saw a slight increase in resistivity after electropulsing, while the remaining ten saw slight decrease. However, the resistivity variation observed was very small - the largest variation observed was a decrease of 3.9x10^{-9} Ω·m after electropulsing treatment, in sample 7-100-80-1-2. Additionally the correlation between electropulsing parameters and sample resistivity was not consistent, with both increase and decrease in resistivity observed in samples treated at comparable pulse parameters.

Summary

The microhardness and electrical resistivity behaviour observed is in agreement with high resolution SEM, which shows no quantifiable microstructure change. The mechanical and electrical property

results confirm no underlying electropulsing effect at current density of the order $10^7 A \cdot m^{-2}$, independent of variation in pulse frequency, pulse duration and test duration.

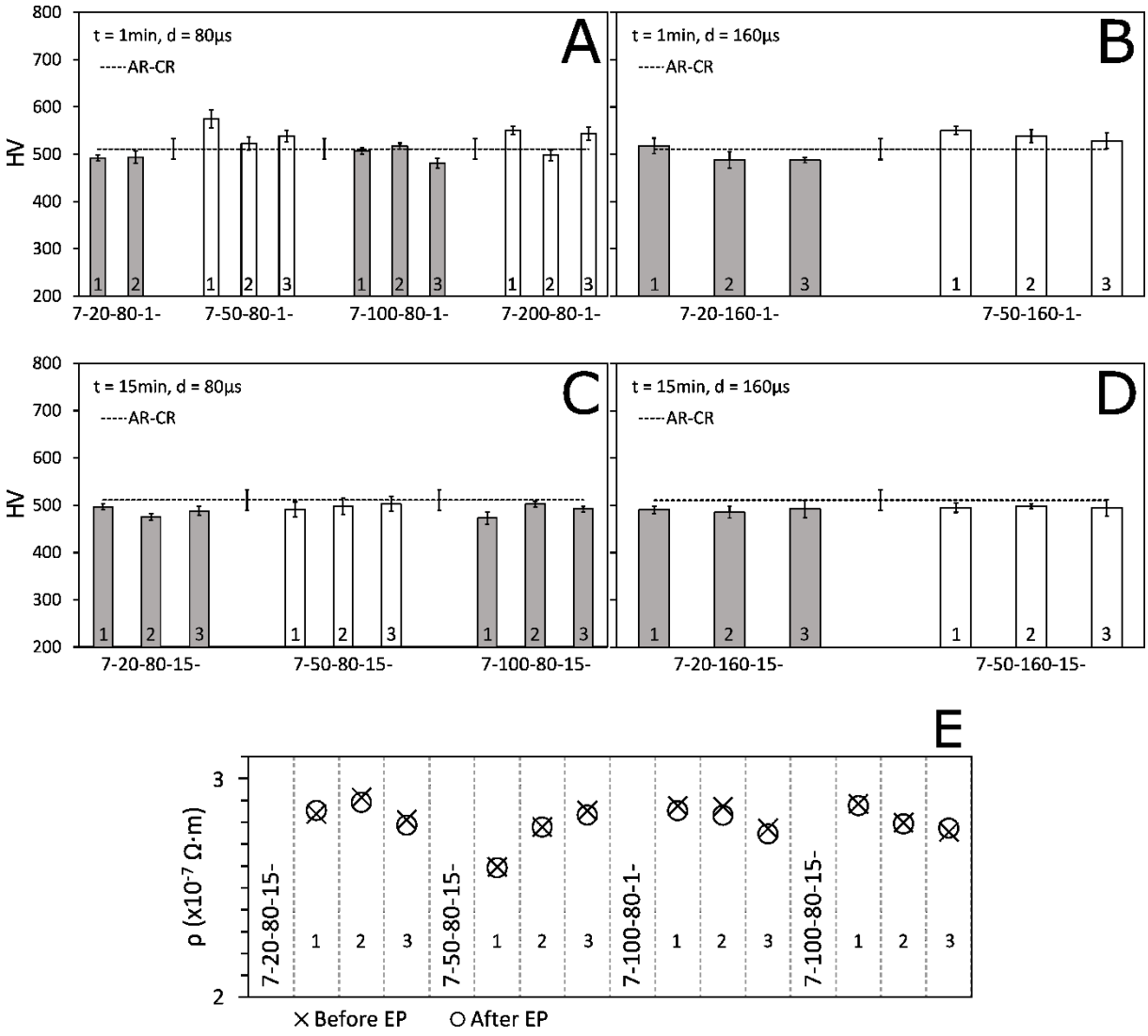


Figure 4.16. Mechanical and electrical properties of samples electropulsed at 10^7 A·m^{-2}. Microhardness (A-D) tested at 1kg (HV_1). Resistivity values shown (E) represent samples tested over a range of parameters.

4.2.2.2. Moderate current density, J ~10^8A·m^{-2}

Electropulsing at current density of the order $10^8 A \cdot m^{-2}$ was conducted on pearlitic steel having an average as-received cold-rolled microhardness of 503±45HV_1. Variation of hardness results was observed with electropulse-induced microstructure change. Resistivity variation is presented on a case-by-case basis with before and after electropulsing values.

Hardness - Pulse frequency 20Hz

Figure 4.17 B-E shows microhardness results for samples electropulsed at 20Hz with various pulse and test durations. Microhardness values for samples treated at 80µs for 1 (B) and 15 (C) minutes, and 160µs for 1 (D) and 15 (E) minutes are plotted. No clear variation from the unelectropulsed cold-rolled

state is observed. The hardness properties of samples electropulsed at 160µs for 1 or 15 minutes and 80µs for 1 minute fall within the region of error of the as-received cold-rolled average value.

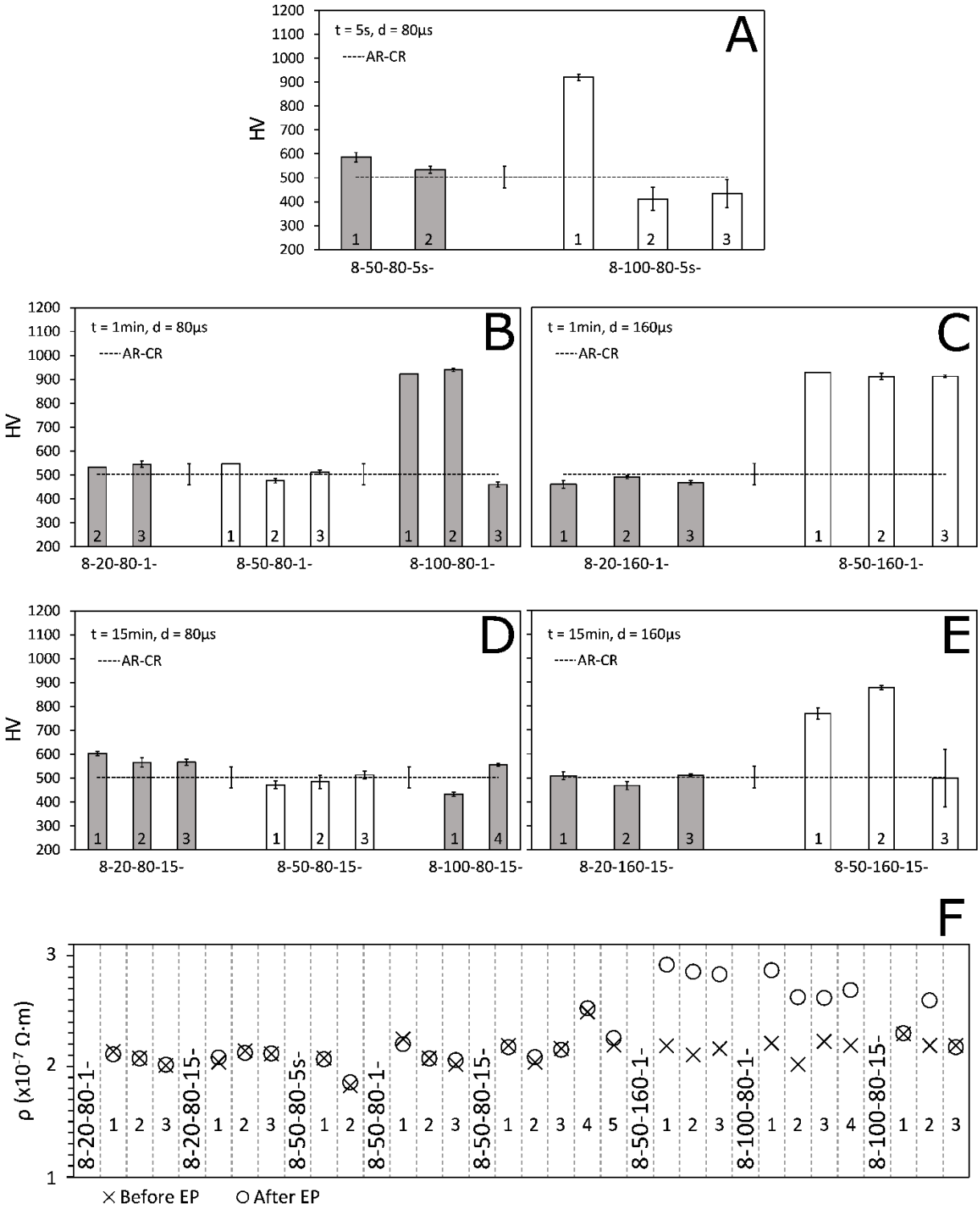


Figure 4.17. Mechanical and electrical properties of samples electropulsed at 10^8 A·m^{-2}. Microhardness (A-E) tested at 1 or 2kg (HV_1, HV_2) dependent on sample thickness. Resistivity values shown (F) represent samples tested over a range of parameters.

High resolution SEM revealed that samples electropulsed at 80µs for 1 minute did not contain any quantifiable microstructure effects, which correlates with the hardness results obtained. Those samples treated at 160µs at either test duration were found to contain a microstructure of fine spheroidised cementite and lamellar breakdown. Some variation in hardness in these samples could be expected due to the observed fine grained morphology, or the coarse breakdown of the lamellar structure in the initial stages of spheroidisation. The former should act to increase the hardness of the material by inhibiting dislocation motion through a greater number of grain boundaries. The latter should act to decrease the hardness by reducing the grain boundary area and enabling dislocation motion [25]. The fact that there is no clear variation in the hardness values observed may suggest that the microstructure transformation was not sufficiently developed to significantly affect the mechanical properties of the steel.

Samples that underwent treatment at 80µs for 15 minutes showed a slight increase in hardness but this behaviour does not correlate with any observable microstructure effects (see pp.80). Structural relaxation would be the most likely electropulsing effect not visible to the SEM, and would have resulted in a reduction rather than an increase in hardness. The variation observed at 20Hz could be anomalous, stemming from inherent differences in pearlite structure and localised work hardening effects such as surface scratches.

Hardness - Pulse frequency 50Hz

Microhardness results for samples electropulsed at 50Hz are shown in Figure 4.17 A-E. Samples treated at a pulse duration of 80µs for 5 seconds, 1 or 15 minutes do not show significant variation from the as-received cold-rolled average hardness value. Of the eight samples tested across these parameters, only one (8-50-80-5s-1, Figure 4.17 A) falls outside the error region of the control sample. The slightly higher hardness of this sample can be explained in a similar manner to other previously described anomalous samples - by localised work hardening effects and natural variations in pearlitic microstructure. This sample was not expected to show any variation in hardness based on its SEM imaging, which showed no quantifiable microstructure effects. Conversely, samples treated at 80µs and 1 or 15 minutes were expected to show hardness variation as all six samples treated under these conditions were found to contain significant spheroidisation. As the particles were found to be coarse, a reduction in hardness was expected to occur, and the absence of this behaviour indicates that the spheroidisation transformation was incomplete.

Hardness values of samples treated at frequency 50Hz and pulse duration 160µs for 1 or 15 minutes test duration are shown in Figure 4.17 C and E. A clear increase in hardness was observed in five of six samples, with values falling between $769HV_1$ and $929HV_2$. These results correlate with the SEM

imaging of the samples, which suggested martensitic transformation as a result of electropulsing treatment. The high hardness characteristics of martensite are well documented, and are known to range between 850 and 920HV (Figure 4.18) for a steel of approximately 0.9wt%C [177, 178]. These hardness characteristics are thought to result from retarded dislocation motion resulting from both pinning by interstitial carbon atoms and limited slip systems due to the phase's body-centred tetragonal (BCT) crystal structure [25].

The sixth sample (80-50-160-15-3), which was observed through SEM to have a coarse lamellar or lower bainite microstructure, had a hardness of 499±119HV_2. Bainite is typically harder than pearlite due to its finer α-ferrite and cementite microstructure. As shown in Figure 4.19, over the approximate transformation temperature region of lower bainite (250 to 400°C) the microhardness in plain carbon steel (0.69wt%C) can range from 360 to 650HV [171, 179].

The standard deviation of the microhardness obtained from sample 80-50-160-15-3 is large. Three of four microhardness values obtained fell between 407 and 444HV_2, while the fourth was 704HV_2. The variation in microhardness observed across the sample leading to this large standard deviation may stem from partial bainite transformation.

Research has shown that bainite can form isothermally below the M_S temperature in 0.66wt%C steel, producing a dual phase lower bainite-martensite microstructure [180]. A partial bainite-martensite transformation explains the variation in the hardness values obtained in sample 80-50-160-15-3.

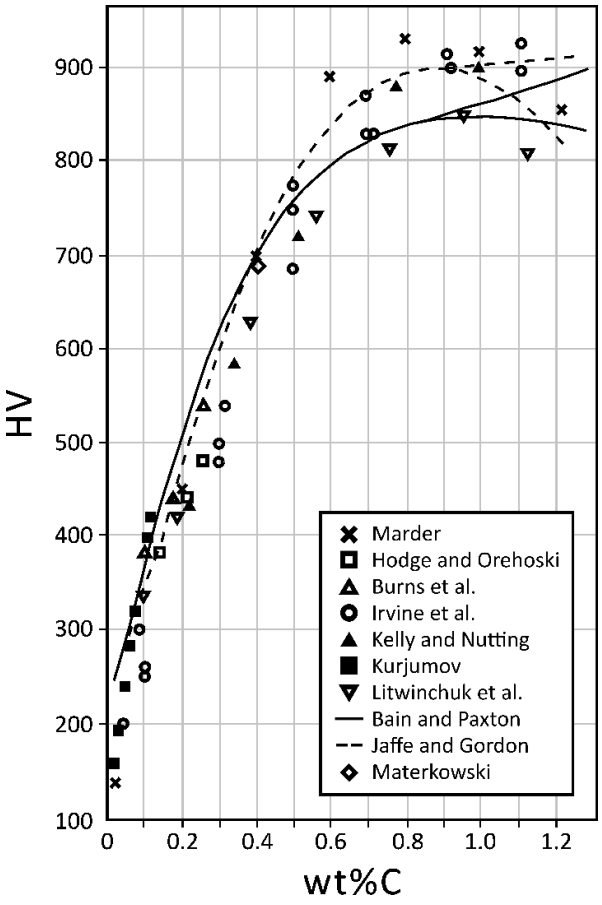


Figure 4.18. Hardness of martensitic microstructure by steel carbon content. Adapted from [177], originally [178].

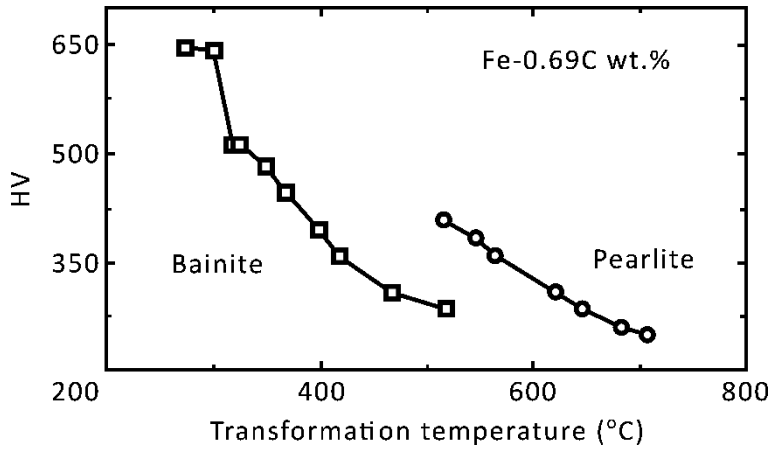


Figure 4.19. Microhardness of 0.69wt%C plain carbon steel isothermally transformed to a dual phase microstructure of bainite and pearlite. Reproduced from [171], originally [179].

Hardness - Pulse frequency 100Hz

Microhardness of samples treated at current density of the order 10^8 A·m^{-2}, frequency 100Hz and pulse duration 80µs are shown in Figure 4.17 A,B and D. Additionally, hardness values associated with samples treated under these conditions for a duration of 2 seconds are detailed in Table 4.12. These samples were not included in Figure 4.17 because their initial microstructure (dual phase ferrite-pearlite) differed from the remaining samples (pearlite only) due to pre-processing (see Methods Section 3, pp.59 for the processing description).

Table 4.12. Microhardness data for samples tested at current density of the order 10^8 A·m^{-2}, frequency 100Hz and pulse duration 80µs for a test duration of 2 seconds. Note that samples in this condition were pre-processed as described in Methods Section 3, pp.59.

Sample code	**Load** *(kg)*	**HV**
Control	1	442±24
8-100-80-2s-1	1	385±21
8-100-80-2s-2	0.5	337±28

Samples electropulsed for 2 seconds showed a slight reduction in hardness from the average cold-worked control value. When standard deviation was taken into account the difference remained significant in both cases, with minimum reductions of 12 (8-100-80-2s-1) and 53$HV_{0.5-1}$ (8-100-80-2s-2). SEM of both samples revealed two different microstructures. Sample 8-100-80-2s-2 had a morphology of cementite grain boundary idiomorphs (GBIs), while sample 8-100-80-2s-1 appeared to have maintained a microstructure of lamellar pearlite.

Studies of the effect of Widmanstätten structures have largely focused on hypoeutectoid steel compositions and proeutectoid ferrite. Research on the various proeutectoid cementite morphologies have become more common in recent years but these works have focused on the formation and

crystallographic nature of the structures, rather than their effects on the mechanical properties of the bulk material [175, 181]. The reduction in hardness observed in sample 8-100-80-2s-2 is significant, and identifies mechanical property softening effects resulting from a microstructure of coarse GBIs in a ferrite matrix. Some studies on proeutectoid ferrite in steels found that while microstructures containing Widmanstätten structures exhibited improved strength and toughness, this behaviour was a result of refinement in the ferrite matrix rather than the proeutectoid ferrite structures [182, 183]. It is possible that the microstructure effects observed in sample 8-100-80-2s-2 are similarly a result of strain removal and recrystallisation in the ferrite phase.

The reduction in hardness observed in sample 8-100-80-2s-1, which possessed a microstructure of lamellar pearlite, is a result of recovery occurring in the deformed microstructure. The heating induced by electropulsing in this particular sample was insufficient to produce diffusive microstructure change over the short treatment time, either via austenitisation or annealing. However the heating that was achieved was sufficient to induce diffusive recovery mechanisms in the deformed microstructure, reducing the stored internal strain energy through limited dislocation motion and untangling. The presence of residual deformation artefacts in the microstructure of sample 8-100-80-2s-1 confirms the softening mechanism as recovery, rather than nucleation of new strain-free pearlite (which would have occurred at a higher temperature, above A_{e1}). Recovery generally occurs in the region of 150 to 350°C in cold-worked microstructure, and its temperature (T_{GR}) can be approximately estimated from the recrystallisation temperature (T_R) using Equation 4.1 [184].

$$T_{GR} = T_R - 300\ [°\mathrm{C}] \qquad 4.1$$

The recrystallisation temperature of 0.92wt%C steel was experimentally determined to fall between 500 and 600°C by standard furnace annealing of similarly cold-rolled samples for a duration of 15 minutes. At 500°C fine spheroidisation of cementite was observed to follow the prior lamellar structure, which remained clearly visible. No α-ferrite recrystallisation was found at this temperature. At 600°C α-ferrite recrystallisation had begun to replace the prior lamellar structure, and cementite spheroidisation was coarser.

The driving force for recovery (and recrystallisation) is increased by introducing strain energy via deformation. In this case, the high cold-rolling reduction in these samples (69%AR) accelerated the recovery process and the microhardness was reduced as a result. Recovery does not overtly change the microstructure of the material. This correlates with SEM images that confirm an intact deformed lamellar microstructure.

After electropulsing at the same parameters (J ~ 10^8 A·m^{-2}, d = 80µs, f = 100Hz) for 5 seconds, the hardness values obtained showed significant variation (Figure 4.17 A). Of the three samples that underwent mechanical testing,[20] one (8-100-80-5s-1) possessed a hardness of 921±14HV_1. The remaining two samples gave average values of 412±49HV_1 (8-100-80-5s-2) and 434±60HV_1 (8-100-80-5s-3), falling slightly below the average as-received cold-rolled value of 503±45HV_1. These values correlate well with the microstructures observed through SEM (Figure 4.5 E-H), which showed a martensitic microstructure for sample 8-100-80-5s-1. Samples 8-100-80-5s-2 and -3 contained a combination of fine cementite spheroidisation and α-ferrite recrystallisation. Softening in these samples was a result of the removal of plastic strain via the recrystallisation process.

Electropulsing for 1 minute produced similar hardness variations resulting from the same microstructure transformations. Hardness values for samples 8-100-80-1-1 and -2 were found to be 923±7HV_2 and 939±11HV_2 respectively, while sample 8-100-80-1-3 was 460±48HV_2. As in the 2 second condition, the microstructures obtained were martensitic in samples 8-100-80-1-1, -2 and -4. Cementite spheroidisation with α-ferrite recrystallisation was observed in sample 8-100-80-1-3.

The described hardness trends continued after electropulsing treatments of 15 minutes duration. Two of four samples underwent hardness testing,[21] and values of 434±9HV_2 (8-100-80-15-1) and 556±6HV_2 (8-100-80-15-4) were recorded. The higher hardness of sample 8-100-80-15-4 is explained by SEM imaging. No discernible microstructure change occurred in this sample, and the morphology remained that of deformed lamellar pearlite. As such, residual strain was not removed from sample 8-100-80-15-4, whereas recrystallisation and spheroidisation of phases in sample 8-100-80-15-1 produced a strain-free crystal structure. The hardness of sample 8-100-80-15-1 was 69HV less than the average as-received cold-rolled value, while sample 8-100-80-15-4 was 53HV greater. Taking into account standard deviation error limits, sample 8-100-80-15-1 was 15HV less than the as-received cold-rolled value, while sample 8-100-80-15-4 was 14HV greater. The variation observed in the lamellar sample is likely a result of localised strain hardening due to the applied cold rolling or surface defects.

[20] Hardness values for the fourth sample in this experimental condition are not included. Sample 8-100-80-5s-4 was pre-prepared for higher current density tests as described in the Methods section. As such the initial microstructure of this sample differed to the others in this test condition, and is not comparable. The sample is included for SEM comparison of pearlitic regions only.

[21] Samples 8-100-80-15-2 and -3 were destroyed during surface preparation for hardness testing.

Resistivity

Resistivity values were calculated for 27 samples tested within the moderate current density range (10^8 A·m^{-2}) (Figure 4.17 F). Of those samples, 9 showed an increase in resistivity after electropulsing treatment. Those samples and their observed microstructures are listed in Table 4.13.

Table 4.13. Resistivity variation in samples electropulsed at current density of the order 10^8 A·m^{-2}.

Sample code	f (Hz)	d (µs)	t (min)	ρ (x10^{-7} Ω·m)		%Increase	Microstructure
				Before	After		
8-50-160-1-1	50	160	1	2.19	2.92	33	Martensite
8-50-160-1-2	50	160	1	2.10	2.85	36	Martensite
8-50-160-1-3	50	160	1	2.16	2.83	31	Martensite
8-100-80-1-1	100	80	1	2.21	2.87	30	Martensite
8-100-80-1-2	100	80	1	2.02	2.62	30	Martensite
8-100-80-1-3	100	80	1	2.23	2.62	17	Coarse spheroidisation / recrystallisation
8-100-80-1-4	100	80	1	2.19	2.69	23	Martensite
8-100-80-15-2	100	80	15	2.19	2.60	19	Martensite

It is clear that the resistivity changes observed are associated with the martensitic transformation reported in samples treated at higher pulse frequency and pulse duration. Carbon remains in solid solution throughout the phase transformation from austenite to martensite. As the less conductive phase, the presence of carbon in solid solution will have a significant effect on the conductivity of the bulk material as reported. Carbon acts to inhibit electron motion, increasing the rate of electron scattering and reducing the conductivity of the material.

A single sample, 8-100-80-1-3, was found to have increased resistivity despite having an electropulse-induced microstructure of coarse cementite spheroidisation. After an annealing treatment of cold-worked metal it would normally be expected that any change observed in electrical properties would be a decrease in resistivity. Cold work introduces large volumes of dislocations which act to impede electron motion and hence increase the resistivity of the metal [185]. Annealing treatment removes dislocations from the crystal structure and should therefore reduce the resistivity of the material. The resistivity increase observed in sample 8-100-80-1-3 cannot be explained by the observed morphology, and the hardness value is characteristic of a spheroidised microstructure. It is suggested that the resistivity value reported is anomalous, resulting from sample surface contamination. The lack of resistivity decrease in other spheroidised samples is not unexpected, as the effect of deformation on the cold-worked microstructure is not as significant as other factors such as temperature or alloying elements [25]. The resulting decrease in resistivity associated with spheroidisation treatment would then be expected to be similarly small.

Summary

Significant hardness and electrical resistivity changes were observed in samples electropulsed at current density of the order 10^8 A·m^{-2} with high pulse frequency and pulse duration combinations (f = 50-100Hz, d = 80-160µs). Samples that showed consistent mechanical and electrical effects were those that were confirmed by SEM to contain martensitic microstructure. Carbon in solid solution in the martensite produced elevated hardness and resistivity values. Structural relaxation and softening due to annealing effects (cementite spheroidisation and ferrite recrystallisation) were also observed.

4.2.2.3. High current density, J ~10^9A·m^{-2}

Electropulsing at current density of the order 10^9A·m^{-2} was conducted on pearlitic steel having an average as-received cold-rolled microhardness of 442±24HV_1. Hardness testing was conducted on the majority of samples but was prevented in some cases by material thickness. Micro-ohmmeter facilities were not available for a small section of experiments due to equipment location. A representative sample of resistivity values are presented.

Hardness - Single pulse and pulse frequency 1Hz

Hardness values of samples treated at low frequency are presented in Figure 4.20 A, B and F. The samples shown were treated at a current density of the order 10^9 A·m^{-2} and pulse duration 80, 200 or 600µs. The test duration was a single pulse, 10 seconds or 15 minutes. A reduction in hardness was observed in all 24 samples tested, compared to the average as-received cold-rolled value. Hardness values across the treatment parameters stated decreased by up to 118$HV_{0.5\text{-}1}$. When regions of error were considered, the minimum reduction values for each sample fell between 11 and 87$HV_{0.5\text{-}1}$.

Evaluation of microstructure using SEM had revealed no discernible microstructure effects. The deformed lamellar microstructure appeared intact. Hardness results would suggest that diffusion-based structural relaxation in the form of reduced dislocation clusters and dislocation density had occurred as a result of electropulsing treatment. As described previously, structural relaxation of this nature would have no obvious microstructural effect that could be observed through SEM, and would manifest as a reduction in hardness due to the reduced strain energy in the material.

Hardness - Pulse frequency 20Hz

Samples electropulsed at frequency 20Hz are presented in Figure 4.20 D-F. All samples were electropulsed at a pulse duration of 80µs for a test duration of 5 seconds, 1 or 15 minutes. Of nine samples tested, all were found to have decreased in hardness. The measured hardness reduction of the electropulsed samples was between 48 and 95$HV_{0.5\text{-}1}$ compared with the average as-received cold-rolled value. Error-corrected minimum values also showed a decrease in hardness between 6 and 61$HV_{0.5\text{-}1}$. No statistically significant variation by test duration was noted.

SEM imaging of the samples had revealed that after 5 seconds of electropulsing treatment, no microstructure effects could be observed. After 1 and 15 minute treatments fine spheroidised cementite was distributed across the samples. The hardness reduction observed correlates with the microstructure obtained via microscopy. Structural relaxation had occurred in the lamellar samples, while more developed diffusional transformation had softened samples showing fine spheroidisation of the cementite phase. It might be expected that the hardness reduction of samples with fine spheroidised cementite morphology would differ to that of the lamellar samples that had simply undergone structural relaxation. This variation could have occurred due to more extensive reduction of strain energy via nucleation of new strain free grains, producing a lower hardness. Alternatively, a very fine grained structure may have increased the hardness via the Hall-Petch strengthening mechanism [25].

The lack of variation between the lamellar and spheroidised microstructure suggests that the cementite spheroidisation observed after 1 and 15 minute treatments was not developed sufficiently to offer strength improvement. The fine cementite microstructure was still inherently linked with the prior lamellar structure, which remained clearly visible. The softening effect was comparable between the varying treatment parameters, suggesting that similar structural relaxation occurred in all samples. The additional treatment time of the 1 and 15 minute duration tests allowed further microstructural change to occur via diffusive spheroidisation mechanisms.

Hardness - Pulse frequency 50Hz

Electropulsing at frequency 50Hz and current density of the order 10^9 $A{\cdot}m^{-2}$ was conducted at pulse duration 80µs and test duration 2 or 5 seconds. Under both experimental conditions the hardness was observed to decrease compared to the average as-received cold-rolled value. After treatment hardness was reduced by between 39 and 98$HV_{0.5\text{-}1}$ in all 11 samples tested. Accounting for standard deviation the reduction in hardness was between 13 and 58$HV_{0.5\text{-}1}$ with one sample falling within the region of error of the control sample.

Samples treated for 5 seconds show consistently lower hardness values than both the control and 2 seconds conditions. This behaviour correlates with the reported microstructure of cementite spheroidisation in all five samples accompanied by removal of dislocations by diffusive mechanisms. The difference in treatment time between the conditions can account for this variation, as a longer duration test would allow the diffusive spheroidisation process to progress further. Similarly, more dislocations can be annihilated by diffusive mechanisms after a longer treatment time.

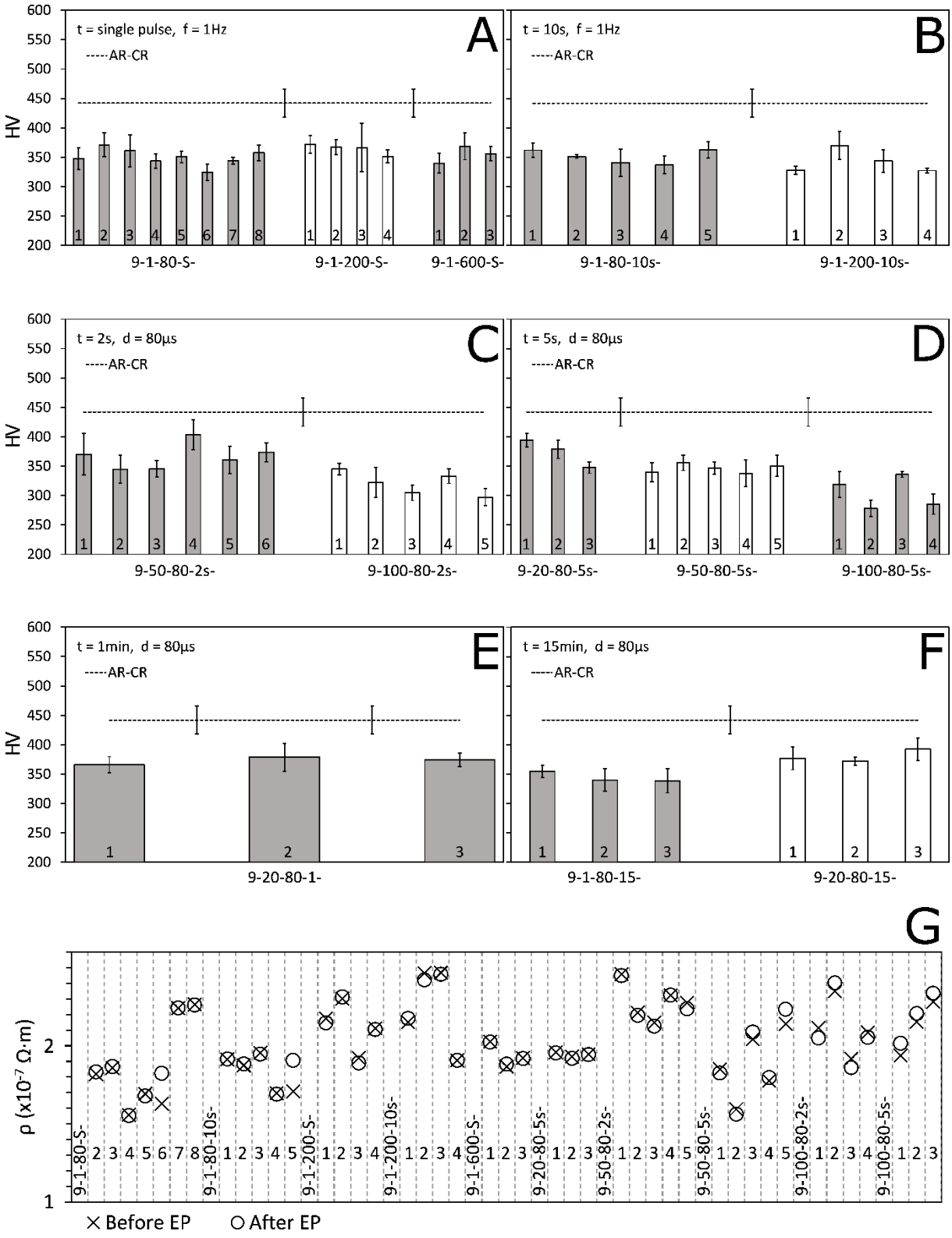


Figure 4.20. Mechanical and electrical properties of samples electropulsed at 10^9 A·m^{-2}. Microhardness (A-F) tested at 0.5 or 1kg ($HV_{0.5}$, HV_1) dependent on sample thickness. Resistivity values shown (F) represent samples tested over a range of parameters.

Table 4.14. Breakdown of hardness data with microstructure for 0.92wt%C steel electropulsed at current density of the order 10^9 A·m^{-2}, pulse frequency 50Hz and pulse duration 80µs.

Sample code	Microstructure	$HV_{0.5-1}$
9-50-80-2s-1	Lamellar (no change)	370±35
9-50-80-2s-2	Various	345±24
9-50-80-2s-3	Various	346±14
9-50-80-2s-4	Various	403±25
9-50-80-2s-5	Various	361±23
9-50-80-2s-6	Lamellar (no change)	374±16
9-50-80-5s-1	Fine spheroidisation	339.8±16
9-50-80-5s-2	Fine spheroidisation	355.8±13
9-50-80-5s-3	Fine spheroidisation	347±11
9-50-80-5s-4	Fine spheroidisation	338±22
9-50-80-5s-5	Fine spheroidisation (regions)	351±18

Hardness - Pulse frequency 100Hz

Short duration tests of 2 or 5 seconds at 100Hz frequency were found to induce reduced hardness in all samples. Compared to the average as-received cold-rolled hardness of 442±24HV_1, the hardness of the electropulsed samples fell by up to 164HV. Taking into account the error margin, the reduction in hardness was found to be up to 126HV, and a minimum of 63HV. The reduction in hardness correlates with the loss of the strong lamellar structure in favour of the lower energy configuration of spheroidisation and globular grain boundary cementite.

A slight variation is observed between the 2 and 5 second conditions, with the longer duration tests having a slightly lower average hardness of 305HV compared with 320HV resulting from the shorter duration tests. As described previously, this is a result of the test duration and the period of time available for diffusion.

Table 4.15. Breakdown of hardness data in relationship to microstructure for 0.92wt%C steel electropulsed at current density of the order 10^9 A·m^{-2}, pulse frequency 100Hz and pulse duration 80µs.

Sample code	Microstructure	$HV_{0.5-1}$
9-100-80-2s-1	Fine spheroidisation	345±10
9-100-80-2s-2	Proeutectoid cementite	322±30
9-100-80-2s-3	Fine spheroidisation	305±13
9-100-80-2s-4	Fine spheroidisation / recrystallisation	333±13
9-100-80-2s-5	Proeutectoid cementite	297±15
9-100-80-5s-1	Proeutectoid cementite	319±22
9-100-80-5s-2	Proeutectoid cementite / spheroidisation	278±14
9-100-80-5s-3	Fine spheroidisation	336±5
9-100-80-5s-4	Proeutectoid cementite	285±17

Resistivity

Resistivity values for samples electropulsed at current density of the order 10^9 A·m^{-2} are shown in Figure 4.20 G. Of 42 samples tested, only two showed any significant change in resistivity. The samples, treated with a single pulse (9-1-80-S-6) and 10 pulses (9-1-80-10s-5), were found to have a higher electrical resistivity after electropulsing. No microstructure change was observed in either sample through SEM but all samples treated with these parameters showed a reduction in hardness. No other samples treated at the same parameters showed either morphological or electrical property variation. These resistivity values are likely anomalous, possibly resulting from surface oxidation or contamination before resistance testing.

A slight change in resistivity was found to occur in samples that contained proeutectoid cementite. The increases involved were small (see Table 4.16) but occur in each of the three proeutectoid samples that underwent resistance tests.

Table 4.16. Resistivity variation in samples electropulsed at current density of the order 10^9 A·m^{-2} and found to contain proeutectoid cementite.

Sample code	**ρ** *(x10^{-7} Ω·m)*		**%Increase**
	Before	*After*	
9-100-80-2s-2	1.85	1.90	2.7
9-100-80-5s-1	1.44	1.52	5.6
9-100-80-5s-2	1.65	1.71	3.6

The variation observed is a result of the change in carbon distribution in the samples caused by the electropulsing treatment. Before electropulsing the ferrite-pearlite dual-phase microstructure offered a clear path of least resistance for electron flow through the single phase ferrite grains, which have significantly better electrical conductivity properties than the non-metallic cementite regions (see Table 4.17). After electropulsing the carbon was more widely distributed through the microstructure and thus the flow of electrons was retarded.

Summary

Electropulsing treatments at current density of the order 10^9 Am^{-2}, pulse duration 80µs and frequency ranging between 1 and 100Hz were found to reduce the hardness of all samples tested compared to the as-received cold-rolled condition. The hardness reductions observed were a result of structural relaxation at lower frequencies, and morphological changes at higher frequencies.

The associated electrical resistivity values were not observed to change significantly, although samples found by SEM analysis to contain proeutectoid cementite had undergone a small increase in resistivity.

The change in cementite distribution in these samples altered the path of least resistance for electron flow and increased the resistivity of the samples.

4.3. Discussion

4.3.1. Distribution of microstructure effects

The distribution of microstructure effects observed in the large number of samples tested at ambient conditions can be clearly linked to the applied electropulsing conditions. Figure 4.21 shows a graphical representation of the distribution of electropulsing effects. Electropulse-induced heating for a single pulse (calculated using Equation 3.18) is plotted against the applied pulse time. Applied pulse time is defined as the total duration of electric current flow through the sample, i.e. the product of the number of pulses and the pulse duration. The figure is shown in three parts (large overview, and two smaller close-up plots) due to the large number of data points and the wide range of values.[22] The overview graph gives a broad indication of the microstructure distribution, showing that:

- No microstructure change is observed when both the applied pulse time and the Joule heating effect are low.
- Martensitic transformations occurred at the extremes of high Joule heating effect or long applied pulse time, as a result of high frequency and pulse duration treatments.
- Spheroidised cementite and equiaxed ferrite occurred in an intermediate region in which the applied pulse time and the Joule heating effect were moderate.
- A region of variable microstructure effects exists at lower applied pulse times and Joule heating values. This region contains samples with fine lamellar breakdown (~0.1-1.5s, 3°C per pulse), proeutectoid cementite microstructures (0.02-0.04s, 2-8°C per pulse) and multiple morphologies (0.01s, 5.5-10°C per pulse).

All electropulse-induced microstructure effects occurred when the treatment parameters could be described as:

- High current density (10^9 A·m^{-2}), low to high frequency (20 - 100Hz), moderate pulse duration (80µs)
- Moderate current density (10^8 A·m^{-2}), moderate to high frequency (50 - 100Hz), moderate to high pulse duration (80 - 160µs)
- Moderate current density (10^8 A·m^{-2}), low frequency (20Hz), high pulse duration (160µs).

[22] For completeness, ambient temperature samples described in Chapter 6 are also included in the figures.

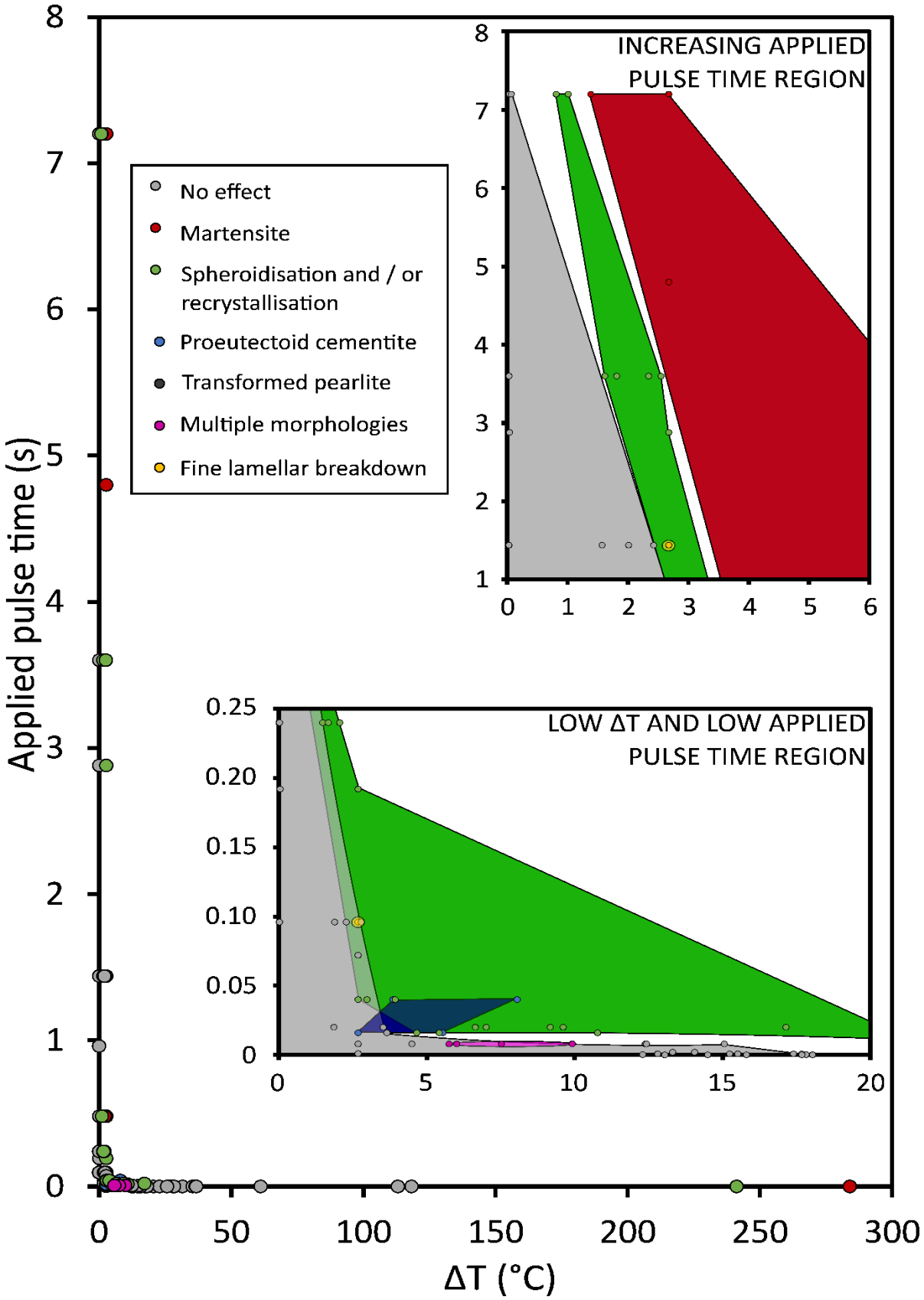


Figure 4.21. Summary of observed electropulse-induced microstructure effects. ΔT is the Joule heating effect for a single pulse calculated for each sample plotted. The applied pulse time is the actual time that the applied electric current was "on" for each sample. Note that six results with high electropulse-induced heating effects (described in Chapter 6) are also included.

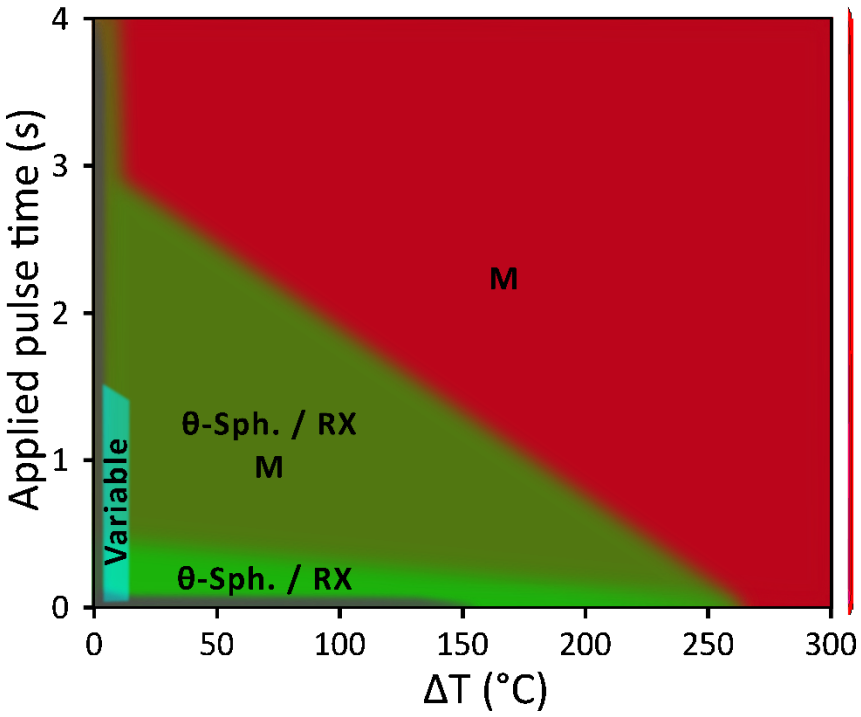


Figure 4.22. Transformation regions of electropulse-induced microstructure effects.

The low energy effects (those achieved at low to moderate pulsing parameters) were also treatment time sensitive, with longer treatments generally inducing more developed microstructures. This was also true for high energy treatments, though on a smaller timescale. No microstructure effects were observed when the combination of current density, frequency and pulse duration was insufficient to induce a heating effect.

The distribution of phases correlates to the heating effects induced by the electropulsing treatment (see Figure 4.22). Lower energy treatments generally experienced a smaller Joule heating effect, a smaller number of pulses (and as a result a lower cumulative heating effect), and a longer cooling period between pulses. Higher energy treatments experienced a significantly higher Joule heating effect, a larger number of pulses and less cooling time between pulses, resulting in a greater temperature increase. Grain size analysis also revealed that electropulse-induced annealing morphologies had comparable geometries to furnace-annealed microstructures. This suggests that the transformation mechanism associated with the electropulsing treatment in these samples was purely heat-based.

Some electropulsed samples were found to contain extremely fine cementite spheroidisation, and it is possible that grain refinement using the electropulsing method could be applied to small-cross section samples (i.e. drawn wire). However, the microstructures observed are again simply a result of the heating profile applied – a very high temperature over a few seconds, or a moderate temperature over minutes. In these cases the pulsed nature of the process may facilitate the grain refinement. The

cooling time between current pulses inhibits continuous grain growth, which could produce finer spheroidised grains. However, no similarly refined control sample was available for comparative analysis to confirm this assertion. Furthermore, the number and scale of the particles under consideration may have limited the accuracy of any measurements taken had a comparison been undertaken.

4.3.2. Formation mechanisms of observed phases

Several morphologies were observed to occur as a result of electropulse-induced heating, as shown in Figure 4.22. Given that the microstructure transformations were a result of heating effects and as such are broadly comparable with traditionally annealed structures, a brief discussion of the formation mechanisms involved follows.

Cementite spheroidisation and α-ferrite recrystallisation

The subcritical annealing morphologies of spheroidised cementite and equiaxed α-ferrite occur at temperatures below the eutectoid point in cold-worked pearlitic steels, as shown in Figure 4.23. The calculated eutectoid temperature for the 0.92wt%C composition used in these experiments was 728°C.[23] This would suggest that the temperatures achieved by the electropulsing process in spheroidised and recrystallised samples can be estimated to be between 600 and 728°C. Finer cementite spheroidisation would have occurred at lower temperatures within this range, where there is lower driving force for Ostwald ripening (grain growth by diffusion of carbon away from small particles towards larger ones, resulting in coarse spheroidised microstructure) [186]. Both the small sample size and the severe cold-rolling applied before electropulsing allowed cementite spheroidisation and equiaxed ferrite to be observed after treatments of only a few seconds. The high rate heating provided by the electropulsing treatment was sufficient to induce subcritical annealing.

Proeutectoid grain boundary cementite

Proeutectoid cementite forms in hypereutectoid steels inside the austenite-cementite phase field region. For this steel composition, the phase field region in question is calculated to be between 728 and 811°C. When proeutectoid cementite forms the remaining austenite is at the equilibrium eutectoid composition, having ejected the excess cementite to the grain boundaries. On slow cooling the austenite transforms to pearlite while the cementite remains at the grain boundaries [42]. However, in each sample that contained proeutectoid cementite, the matrix phase was ferrite rather than pearlite.

[23] Note that this value may be lower due to decarburisation in samples pulsed at 10^9 A·m^{-2}, see Methods section 3.3.2.2.

This behaviour occurred in one sample at moderate current density, 8-100-80-2s-1, and multiple samples at high current density. Critically, the microstructure only occurred in samples that underwent the augmented rolling process described in Methods section 3.3.2.2, which produced a dual-phase pearlite-ferrite microstructure (Figure 4.24 (top)). As a result, carbon in the as-received cold-rolled microstructure was concentrated in the dispersed pearlite colonies.

When the metal was heated to the austenite-cementite phase field, proeutectoid cementite formed at the grain boundaries and appears to have enveloped the pearlite (now austenite) colonies (Figure 4.24 (middle)). On cooling the remaining small regions of austenite reverted to pearlite Figure 4.24 (bottom)).

The treatment times involved were not sufficient for long range diffusion of carbon into the original ferrite grains, and the treatment temperature was not high enough to induce austenitisation at a very low carbon content. As a result the original ferrite grains remained as such on cooling.

Martensite

Fully transformed martensitic microstructure was produced as a result of high rate heating in samples composed of the original cold-rolled lamellar microstructure. In order for single phase martensite to form, complete austenitisation was achieved. This indicates

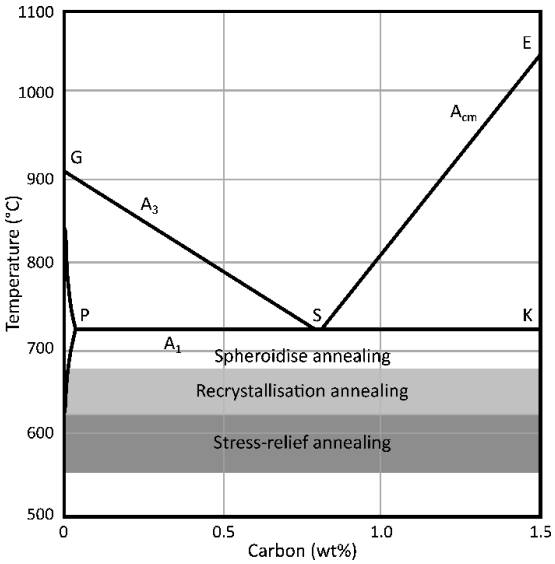


Figure 4.23. Subcritical annealing regions overlaid on the Fe-C phase diagram. Modified from [42], originally [187].

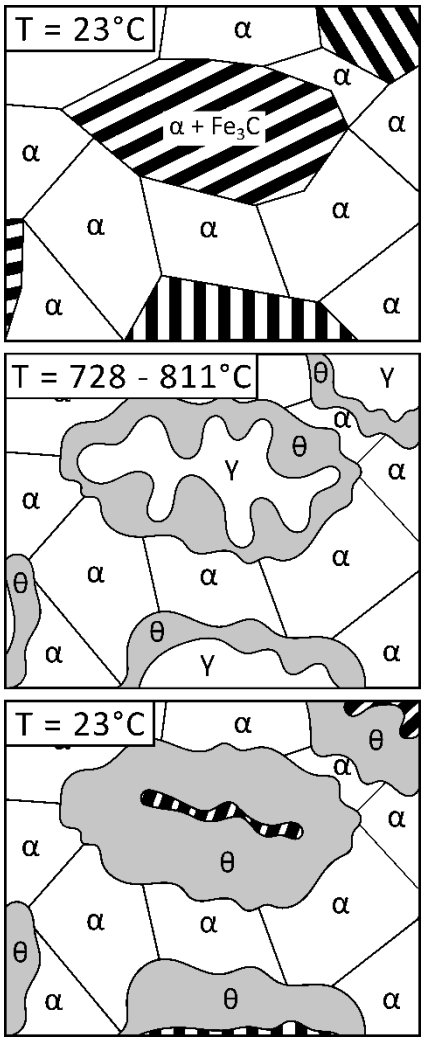


Figure 4.24. Schematic showing transformation of proeutectoid cementite microstructure.

that the temperatures achieved in martensitic samples were in excess of 811°C, based on the calculated phase diagram (see Methods, pp.55). Rapid withdrawal of electric current at the end of each test produced significant undercooling at ambient temperature that was sufficient to induce diffusionless martensitic transformation. As with the previous microstructures, small sample size and prior cold work enabled the electropulsing treatment to achieve the required temperatures for austenitisation with appropriate pulsing parameters. The martensite transformation was not the focus of this research and as such, its morphology was not scrutinised in the same manner as the subcritical annealing morphologies. However, its appearance in multiple samples goes some way towards highlighting the significant heating effect that electropulsing treatment is capable of inducing in very short treatment times.

4.3.3. Phase-related Joule heating variation

As a dual-phase material, electropulse-induced transformations in pearlitic steel could be affected by electrical conductivity variations in its components. This is particularly true when the base elements of the phases are considered – non-metallic cementite has an electrical resistivity seven-times greater than metallic iron, as shown in Table 4.17. The difference in electrical resistivity results from the variation in free electrons in the valence shells of the two elements, as shown in Figure 4.25. Iron has more free electrons than carbon, and is therefore more readily able to conduct electricity through the movement of free electrons between atoms [188].

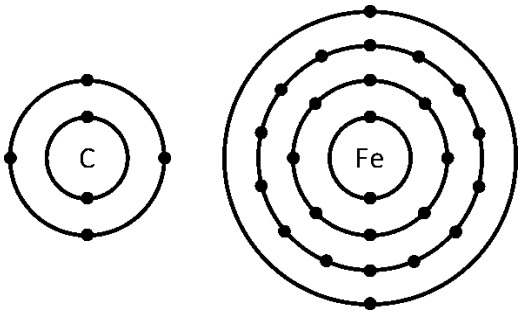


Figure 4.25. Electron configuration of iron and carbon.

Table 4.17. Theoretical heating effects by phase resulting from a single electropulse of current density 10^9 A·m^{-2} and pulse duration 80µs.

Phase	δ (kg·m^{-3})	ρ (x10^{-7} Ω·m)	C_p (J·kg^{-1}·K^{-1})	d (µs)	J (x10^9 A·m^{-2})	ΔT (°C)
α-ferrite (BCC Fe)	7860 [189]	0.98 [140]	461 [189]	80	1	2.2
Cementite (Fe_3C)	7660 [189]	7.87 [141]	594[24] [141]	80	1	13.8

[24] Specific heat capacity given by Umemoto *et al.* (2001) as 106.6 J·mol^{-1}·K^{-1} at 100°C. Conversion to J·kg^{-1}·K^{-1} using molar mass 179.5457 g/mol (atomic mass 3 x Fe 55.845 g/mol, C 12.0107 g/mol).

Table 4.17 also shows the calculated change in temperature due to Joule heating for a single electropulse by phase, using Equation 3.18. The idealised conditions apply a pulse of $1x10^9$ $A{\cdot}m^{-2}$ to α-ferrite and cementite, with the phase variation represented through differences in the material parameters electrical resistivity, density and specific heat capacity. As expected, the calculations show that the heating effect of electropulsing is most significant in the cementite phase. However, as the volume of carbon in the bulk material is much smaller than that of ferrite (0.92wt%C to 97.2wt%Fe) its detrimental effect on the electrical properties will be mitigated. Under the same pulsing conditions as described in Table 4.17, the bulk material (undeformed, for accurate comparison with the individual phases) experiences a resistive heating temperature increase of 6°C.

The higher resistivity of cementite raises questions over the current flow during electropulsing. Choosing a path of least resistance, electrons might be expected to preferentially travel through the ferrite phase. However, the varied orientation of pearlite colonies in the as-received material prevents a completely uninhibited path. In addition, a hypereutectoid steel is expected through normal annealing processes to consist of pearlite colonies and proeutectoid cementite along the prior austenite grain boundaries. Using the lever rule as shown in Equation 4.2, where C_0 is the steel carbon composition, C_E the eutectoid carbon composition (0.77wt%C) and C_θ the cementite upper phase boundary [25], a 0.92wt%C steel would be estimated to contain 2.5wt% of proeutectoid cementite.

$$wt\%\ Fe_3C = \frac{C_O - C_E}{C_\theta - C_E} \times 100 = \frac{0.92 - 0.77}{6.67 - 0.77} \times 100 = 2.5 \qquad 4.2$$

Electron flow through cementite is unavoidable, particularly in a hypereutectoid steel. This could then result in localised heating effects at cementite lamellae and prior austenite grain boundaries, and explains the heating and transformation effects observed in both phases regardless of composition.

4.3.4. Classical thermomechanical heating estimations

The heating behaviour of electropulse-transformed samples can be approximated using classical thermodynamics theory. This gives a theoretical understanding of the conditions required to achieve the observed microstructure change without electropulsing treatment. The convective heating equation is shown in Equation 4.3, where T is the target temperature of the sample (K), T_∞ the temperature inside the furnace (K), T_O the ambient temperature of the sample before insertion into the furnace (K), h the convection heat transfer coefficient ($W{\cdot}m^{-2}{\cdot}K^{-1}$), δ the density of the material ($kg{\cdot}m^{-3}$), C_p the specific heat capacity ($J{\cdot}kg^{-1}{\cdot}K^{-1}$), L_c the characteristic length (m) and τ the time required to reach T (s). The characteristic length is defined in Equation 4.4, where V is the volume of the workpiece (m^3) and A_s its surface area (m^2) [190].

$$\frac{T - T_\infty}{T_o - T_\infty} = e^{\left(\frac{h}{\delta \cdot C_p} \times \frac{1}{L_c} \tau\right)}$$

4.3

$$L_c = \frac{V}{A_s} = \frac{L \times W \times D}{2 \times L \times D + 2 \times L \times W + 2 \times W \times D}$$

4.4

Using the above equations, the time required for a small sample (approximately 40 x 0.65 x 0.2mm) to reach 740°C (within the austenite-cementite phase field for the 0.92wt%C steel composition) from ambient temperature is estimated at 49 seconds, with a heating rate of 14.5°C·s^{-1}. The full calculation is detailed in Appendix B. This estimate shows that electropulsing treatments at high current density involve much shorter heating times and significantly faster heating rates. The heating profile is then key to the rapid microstructure changes induced in the steel samples as a result of electropulsing.

4.3.5. Consistency of results

The results presented here show that electropulsing treatments can induce a variety of microstructures and are capable of producing very high parameter-dependent heating rates. However the results have also shown that the consistency of the microstructures achieved varies. Electropulsing at high pulsing parameters and very short treatment times produces the most inconsistent microstructure changes, and depends heavily on small variations in treatment time, sample geometry and ambient temperature cooling conditions as well as the quality of the connection between sample and electrode. Should electropulsing be considered as a processing treatment, it would be necessary to optimise the technique to remove environmental factors and develop a consistent method for sample connection (as found in the Gleeble equipment described in Methods section 3.4.6) and mechanical timing of test duration. It may also be necessary to optimise treatment parameters by sample, or to standardise sample size through industrial manufacturing methods.

4.4. Summary

Electropulsing treatments of current density ranging between 10^7 and 10^9 A·m^2, frequency 1 to 100Hz, pulse duration 80 to 160µs and test durations of single pulse up to 15 minutes were applied to cold-rolled 0.92wt%C pearlitic steel plate. No microstructure, mechanical or electrical property change was observed in samples electropulsed at current density of the order 10^7 A·m^2, independent of elevated test time, frequency or pulse duration parameters. A range of microstructures were observed to occur as a result of electropulsing treatment between 10^8 and 10^9 A·m^2, including:

- subcritical annealing microstructures of spheroidised cementite and equiaxed ferrite at current density between 10^8 and 10^9 A·m^2, and moderate combinations of frequency and pulse duration

- austenitised microstructures containing proeutectoid cementite or martensite at current density between 10^8 and 10^9 A·m^2, and high combinations of frequency and pulse duration.

The microstructures were induced by high rate heating as a result of the electropulsing process. No microstructure change was observed when the combined electropulsing parameters were insufficiently high to induce a heating effect. The effects induced by the electropulsing treatments were inconsistent and extremely sensitive to variations in ambient temperature, sample size and electrode connection quality. An optimised electropulsing process must be developed with similar characteristics to the Gleeble resistive heating simulator if the technique were to be used in any commercial setting.

5. Electropulsing at elevated temperature

5.1. Experimental parameters

Electropulsing at elevated temperature was conducted across a temperature range between 660 and 740°C in increments of 20°C. This temperature range was selected based on the theoretical eutectoid temperature obtained using Thermo-Calc software, as shown in the Methods section, Figure 3.4. Within this temperature range it was expected that cementite spheroidisation and recrystallisation or grain growth of α-ferrite should occur, switching to austenitisation at approximately 720 to 740°C. The premise of the experiment was to apply electropulsing to samples simultaneously undergoing traditional furnace treatment. An assessment could then be made as to whether electric current was able to induce microstructure variation as a secondary driving force to the furnace heating through thermal and athermal effects, based on grain morphology and mechanical properties.

Pre-drawn pearlitic steel rods of carbon composition 0.73wt%C were supplied by Tata Steel, having a diameter of 2mm and a cross-sectional area reduction of approximately 60%. As the salt bath treated rod was annealed after drawing, this sample can be described as undeformed. The average sample length used for experimental work was 30mm. Three initial microstructure conditions were tested - still air (SA), forced air (FA) and salt bath (SB540) cooled, as described in the Methods section, pp.51. The use of three different microstructure conditions was intended to allow the assessment of electropulsing effects on samples of varying interlamellar spacing and cementite globularisation.

After preheating the furnace to the target temperature (T_T) two samples were inserted, one control sample and one sample for electropulse treatment. The experimental configuration is shown in Figure 5.1. A K-type high temperature thermocouple probe was used to measure the internal furnace temperature (T_A) for comparison with the target temperature. Electropulsing treatment was initiated immediately on insertion into the furnace and stopped after 30 minutes, at

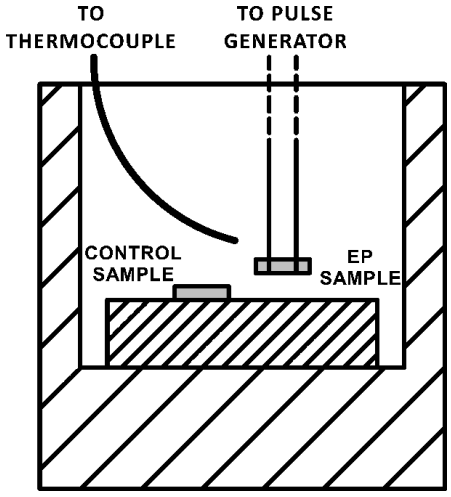


Figure 5.1. Schematic showing experimental configuration inside the furnace.

which point both samples were removed from the furnace to cool in air.

The electropulsing treatment was conducted at current density of the order 10^7 A·m^{-2}. This value was dictated by the geometry of the rod samples. The pulse frequency was set at 1Hz for all samples, in order to avoid the risk of sparking inside the furnace which may occur at higher frequencies. Pulse duration and test duration were 80μs and 30 minutes, respectively. Full electropulsing and heating parameters are described in Table 5.1.

Table 5.1. Electropulsing parameters for elevated temperature tests at J ~ 10^7 A·m^{-2}.

Condition	Sample code	T_T (°C)	T_A (°C)	J (x10^7 A·m^{-2})	f (Hz)	d (μs)	t (mins)	N (#)
SA	SA-F660-EP-30	660	660	5.8	1	80	30	1800
	SA-F680-EP-30	680	681	4.9	1	80	30	1800
	SA-F700-EP-30	700	699	5.6	1	80	30	1800
	SA-F720-EP-30	720	717	6.5	1	80	30	1800
	SA-F740-EP-30	740	737	6.2	1	80	30	1800
FA	FA-F660-EP-30	660	660	5.3	1	80	30	1800
	FA-F680-EP-30	680	678	5.3	1	80	30	1800
	FA-F700-EP-30	700	697	5.6	1	80	30	1800
	FA-F740-EP-30	740	739	6.5	1	80	30	1800
SB540	SB540-F660-EP-30	660	659	6.9	1	80	30	1800
	SB540-F680-EP-30	680	678	8.1	1	80	30	1800
	SB540-F700-EP-30	700	700	5.9	1	80	30	1800
	SB540-F720-EP-30	720	719	7.2	1	80	30	1800
	SB540-F740-EP-30	740	738	7.5	1	80	30	1800

5.2. Results

5.2.1. Microscopy and grain size analysis

Microscopy and grain size analysis is presented by initial microstructure condition, SA, FA or SB540. The SA condition includes images and analysis for all temperatures in 20°C intervals between 660 and 740°C. The FA and SB540 conditions are reduced for clarity, and include images for 660, 700 and 740°C only.

5.2.1.1. Still air (SA) condition

The still air (SA) cooled initial untreated microstructure was fully transformed lamellar pearlite aligned along the drawing direction. In the drawn condition the interlamellar spacing was measured to be 99±17nm. The cold-drawing applied was severe, with a cross sectional area reduction of 58%. Further details of the initial sample conditions can be found in the Methods section, pp.51.

Microscopy

Figures 5.2, 5.3 and 5.4 show high resolution etched secondary mode (SEM) imaging of samples with initial lamellar microstructure produced by still air (SA) cooling, treated simultaneously with

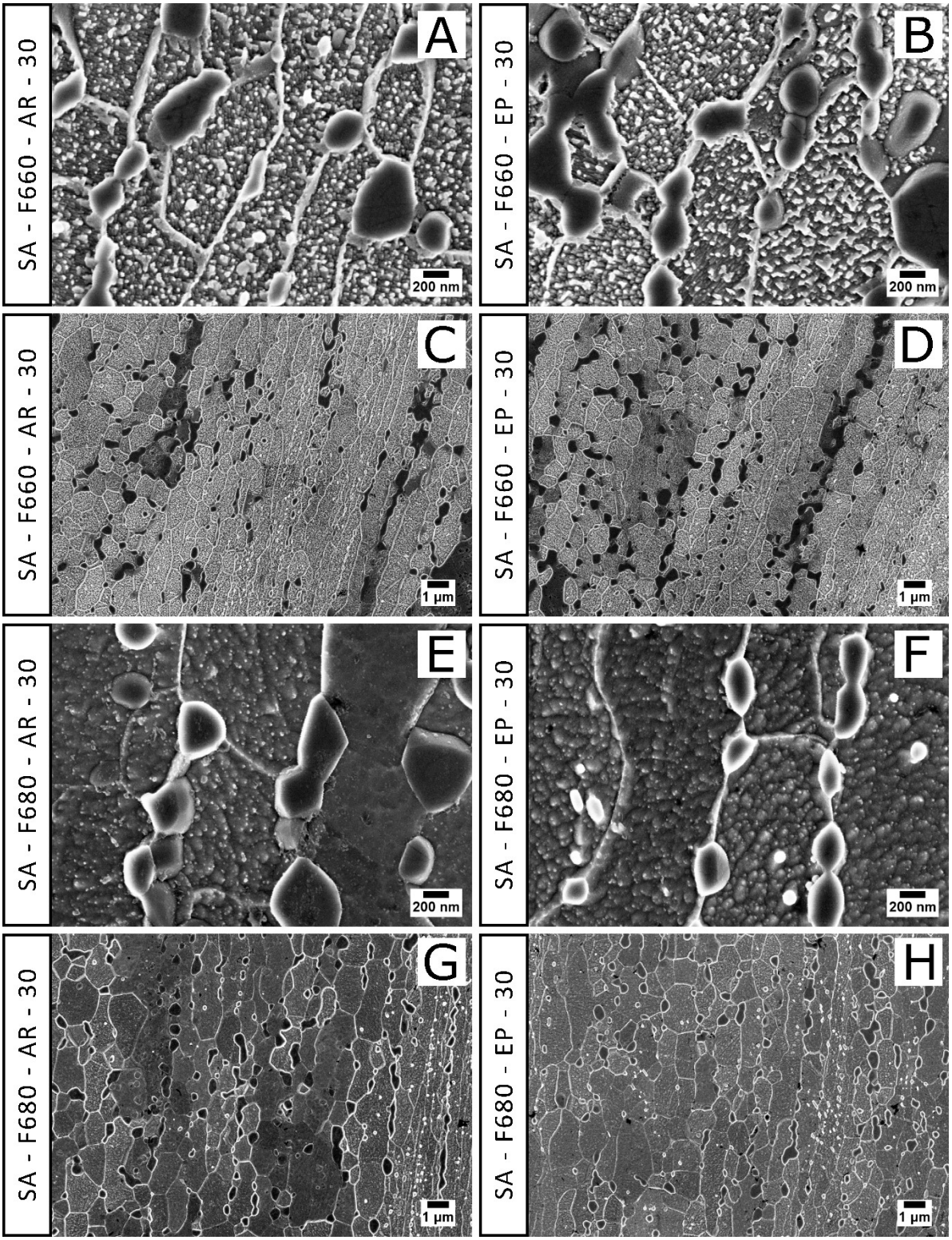


Figure 5.2. High resolution SEM microscopy of furnace annealed 0.73wt%C pearlitic steel (still air cooled condition) with or without simultaneous electropulsing treatment. A,C) annealing only, 660°C; B,D) annealing and electropulsing, 660°C; E,G) annealing only, 680°C; F,H) annealing and electropulsing, 680°C.

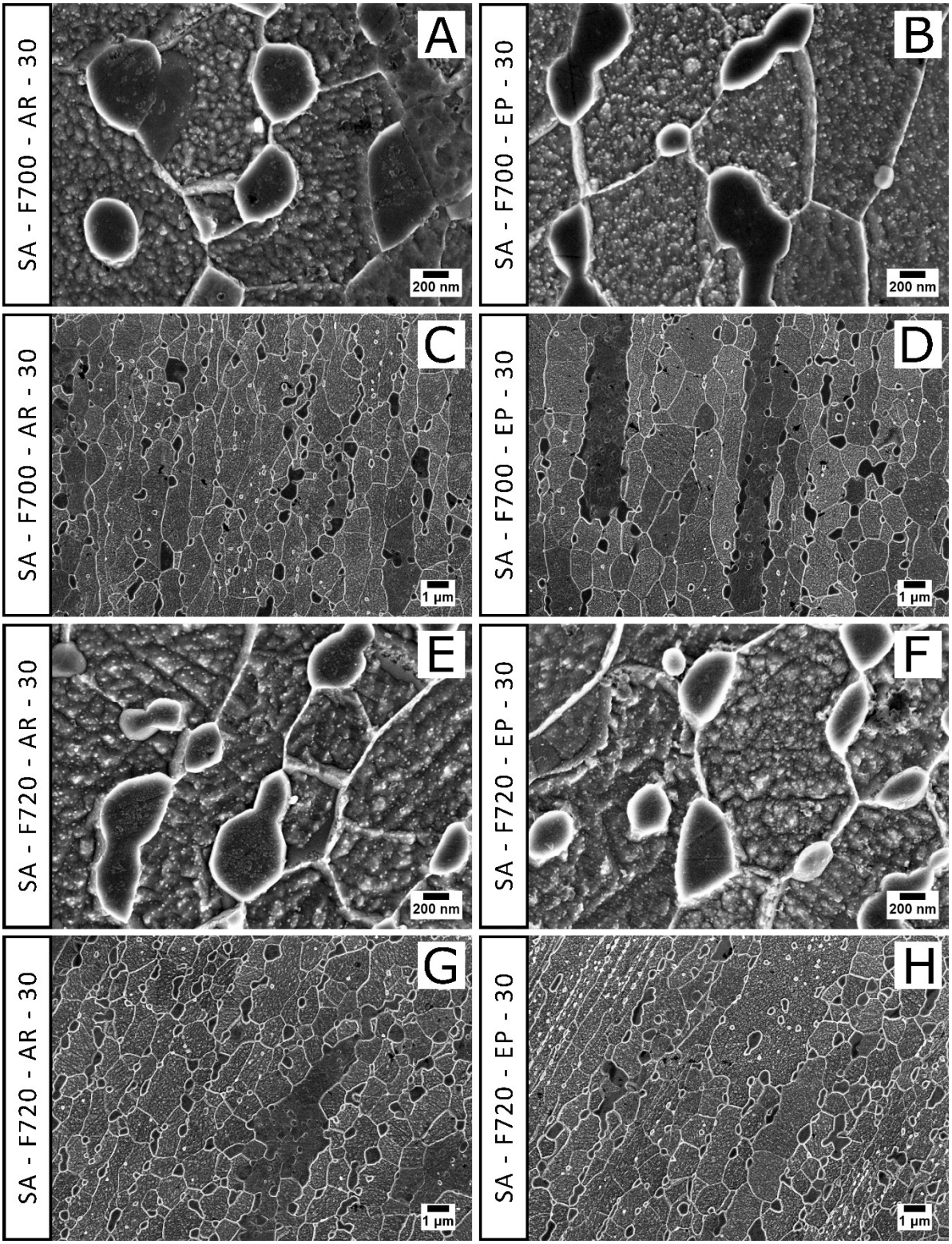


Figure 5.3. High resolution SEM microscopy of furnace annealed 0.73wt%C pearlitic steel (still air cooled condition) with or without simultaneous electropulsing treatment. A,C) annealing only, 700°C; B,D) annealing and electropulsing, 700°C; E,G) annealing only, 720°C; F,H) annealing and electropulsing, 720°C.

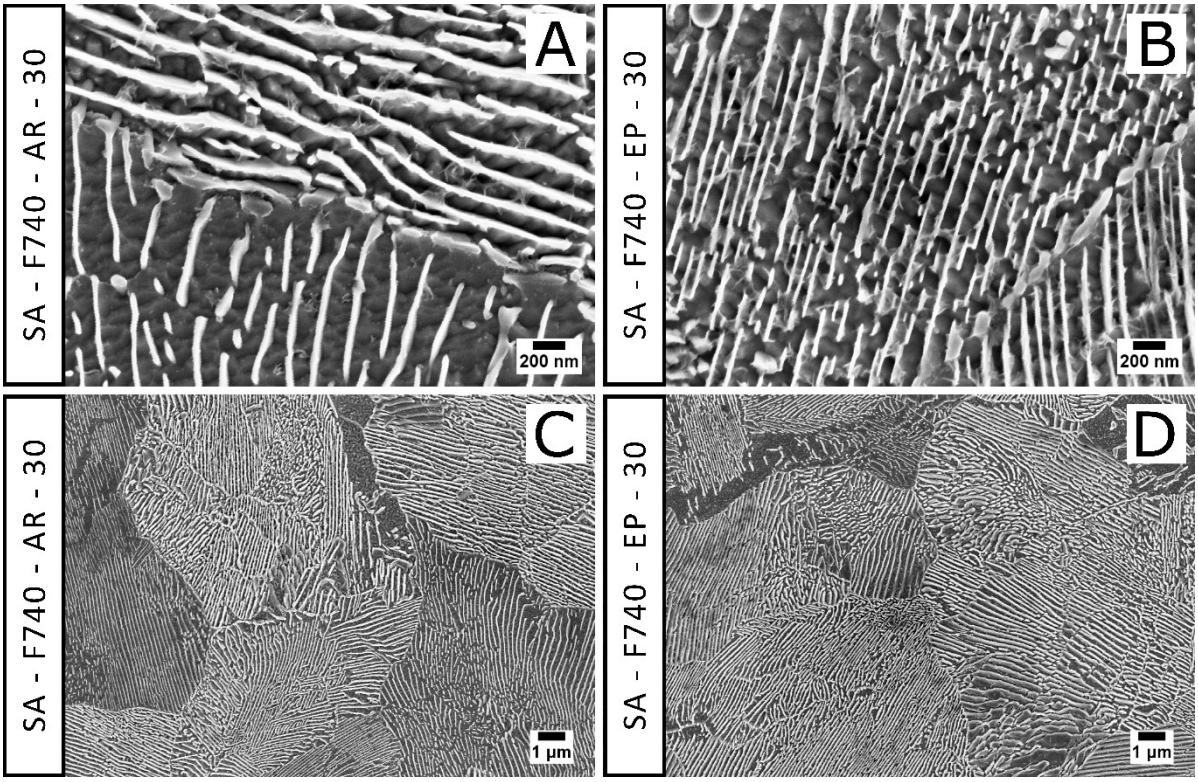


Figure 5.4. High resolution SEM microscopy of furnace annealed 0.73wt%C pearlitic steel (still air cooled condition) with or without simultaneous electropulsing treatment. A,C) annealing only, 740°C; B,D) annealing and electropulsing, 740°C.

electropulsing and furnace annealing. The electropulsed samples are presented for comparison with control samples, furnace annealed concurrently but without electropulsing treatment. In Figures 5.2 to 5.4 the control samples are shown on the left, while electropulsed samples appear on the right.

All samples, electropulsed with furnace treatment or furnace treated only, showed varying degrees of equiaxed α-ferrite grain growth and globular cementite spheroidisation between 660 and 720°C. Cementite globularisation was focused on the α-ferrite grain boundaries, with some occurrences of intragranular spheroidisation. At lower temperatures (660 – 680°C) regions of elongated grain structure were observed concurrently with annealed features, showing incomplete recrystallisation of the parent deformed lamellar microstructure.

At 740°C (Figure 5.4) the austenitisation temperature was surpassed and on cooling the microstructure transformed to that of undeformed lamellar pearlite. Upon visual examination at high magnification it might be suggested that the pearlite was finer in the electropulsed condition. However, measurements revealed that electropulsing did not affect the average interlamellar spacing (ILS) in the SA condition at 740°C. The furnace only sample was found to have an average ILS of 100±18nm, while the electropulse and furnace treatment sample was 96±27nm. ILS values for all conditions, SA, FA and SB540, are shown in Figure 5.5.

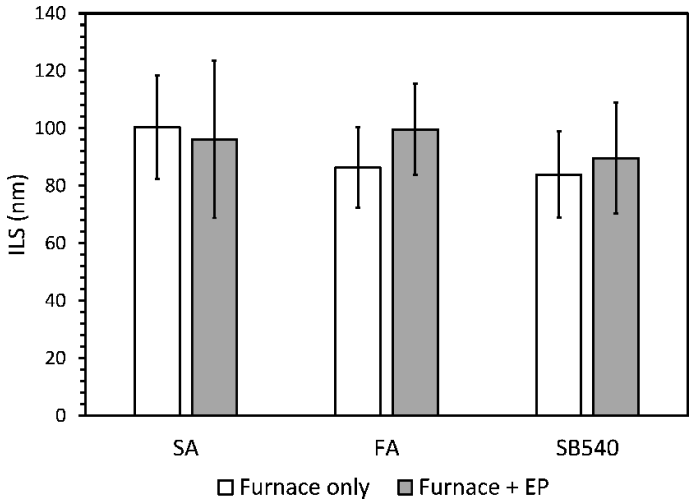


Figure 5.5. Interlamellar spacing of 0.73wt%C pearlitic steel with SA, FA and SB540 initial microstructure, after austenitisation and eutectoid transformation. Comparison is made after furnace annealing, or furnace annealing with simultaneous electropulsing treatment.

Grain size analysis parameters

Grain size analysis of both equiaxed ferrite and spheroidised cementite was conducted using ImageJ software and the techniques as described in the Methods section, pp.73. Measurement of equiaxed ferrite was conducted on images with a magnification of 14000X, while cementite spheroidisation was measured at 30000X. The variation in magnification is due to the difference in scale between the artefacts under consideration. The number of grains measured (n) is included with each graph. At each temperature step the n values are comparable, with any variation observed attributed to slight differences in etch quality and therefore visibility of the annealed features.

The equiaxed ferrite grains were assessed using three geometry descriptors – grain cross-sectional area, major axis length and aspect ratio. Cementite spheroidisation was assessed using two. Partially annealed lamellar cementite can take a range of shapes, from small spherical particles to large fragmented lamellar sections. Furthermore, lamellar fragments are not fully represented by two-dimensional SEM imaging as the grinding and polishing process can distort the appearance of the interpenetrating three-dimensional lamellae. This factor does not affect the measurement of equiaxed ferrite as its three-dimensional configuration is inherently different. As such it was determined that grain size analysis of cementite would not include area measurements, and would instead focus on the descriptors of aspect ratio and major axis length. The following sections describe the results of the analysis.

Grain size analysis - Equiaxed ferrite

Equiaxed α-ferrite was observed in both electropulsed and control samples between 660 and 720°C. A comparison between the electropulsed and control sample grain size characteristics is presented in Figures 5.6 to 5.8. Figure 5.6 shows the distribution of grain cross-sectional area by temperature,

Figure 5.7 describes the distribution of grain major axis length, and Figure 5.8 presents the distribution of aspect ratio (circularity). In each figure the control samples appear on the left and electropulsed samples on the right. A summary of geometry descriptors for the 660 and 720°C conditions is provided in Table 5.2. A Weibull curve is overlaid on each plot to show the distribution of the data points, as described in Methods section 3.5.3.2.

From Figure 5.6 it can be seen that at each temperature step the distribution of grain cross-sectional area is comparable between the electropulsed and control samples. The area can be seen to increase with temperature, with the tail of the Weibull distribution curve extending from approximately 3µm^2 at 660°C to 5µm^2 at 720°C. This behaviour correlates with the known annealing behaviour of steel, as grain growth occurs with increasing temperature or treatment time as a result of enhanced atomic diffusion [25]. At 660°C, 75% of equiaxed ferrite grains in both the electropulsed and control samples were measured to have a cross-sectional area of 0.9µm^2 or less. At 720°C, 75% of grains were found to have a cross-sectional area of 1.9µm^2 or less in the control sample and 1.5µm^2 or less in the electropulsed sample.

The distribution of major axis length was observed to increase slightly across the temperature range in a similar manner to the grain area, as shown in Figure 5.7. The major axis of equiaxed ferrite grains were found to have lengths of approximately 3µm or less at 660°C, rising incrementally to approximately 4µm or less at 720°C. This behaviour correlates with both the grain area findings and the previously stated known annealing behaviours. At 660°C, 75% of equiaxed ferrite grains were measured to have a major axis length of 1.8µm^2 or less in the control sample and 1.7µm^2 or less in the electropulsed sample. At 720°C, 75% of grains were found to have a major axis length of 2.3µm^2 or less in the control sample and 1.9µm^2 or less in the electropulsed sample.

Table 5.2. Summary of equiaxed ferrite geometry descriptors (assessed for approximately 75% of measured grains in samples with initial still air cooled microstructure).

Geometry descriptor	**T = 660°C**		**T = 720°C**	
	Control	*Electropulsed*	*Control*	*Electropulsed*
Area *(µm^2)*	≤0.9 *(76%)*	≤0.9 *(74%)*	≤1.9 *(75%)*	≤1.5 *(76%)*
Major axis length *(µm)*	≤1.8 *(76%)*	≤1.7 *(76%)*	≤2.3 *(76%)*	≤1.9 *(76%)*
Aspect ratio	≤2.8 *(74%)*	≤2.8 *(77%)*	≤2.5 *(76%)*	≤2.2 *(75%)*

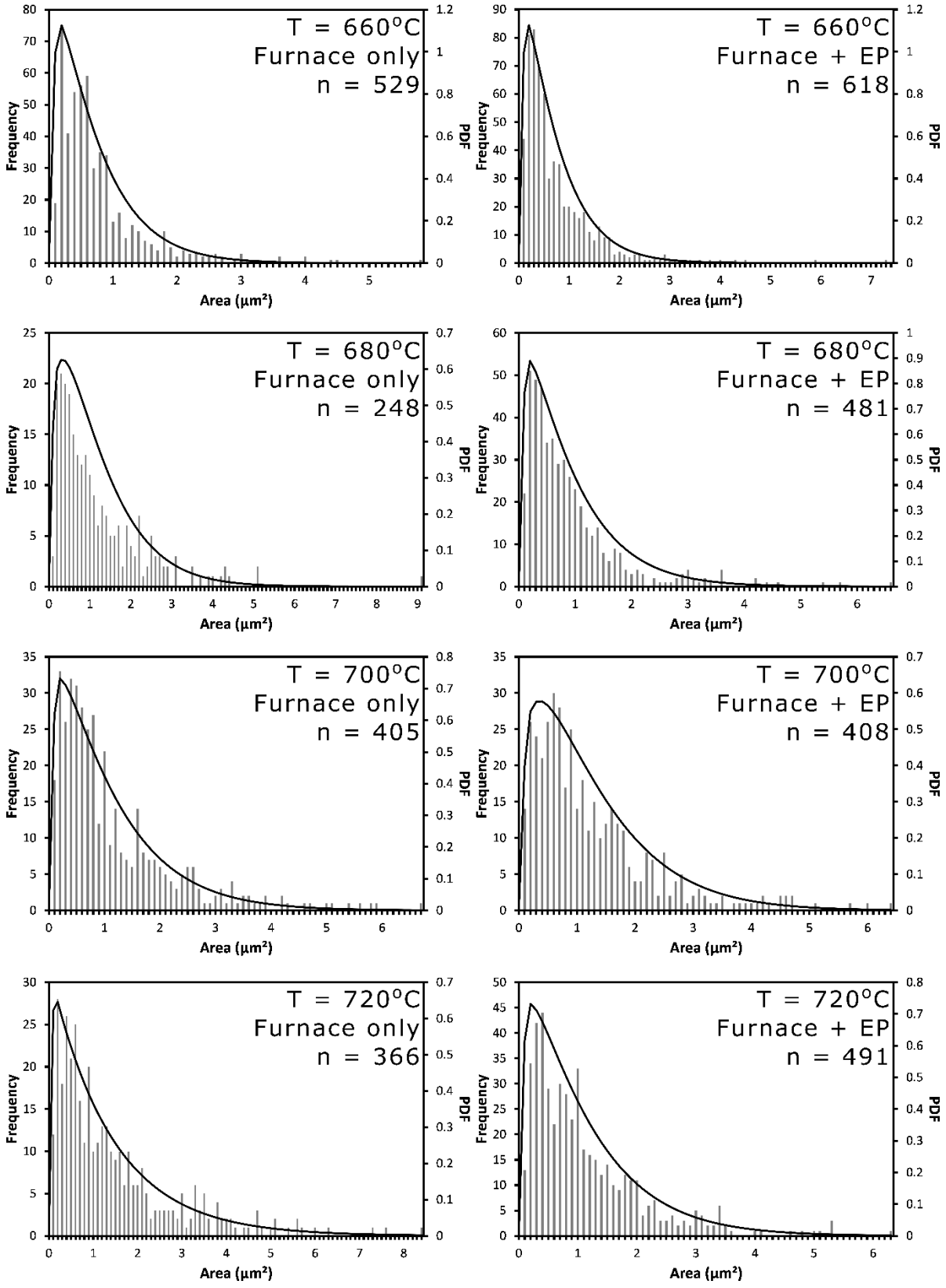


Figure 5.6. Ferrite grain area comparison (still air cooled condition) for temperatures 660 – 720°C.

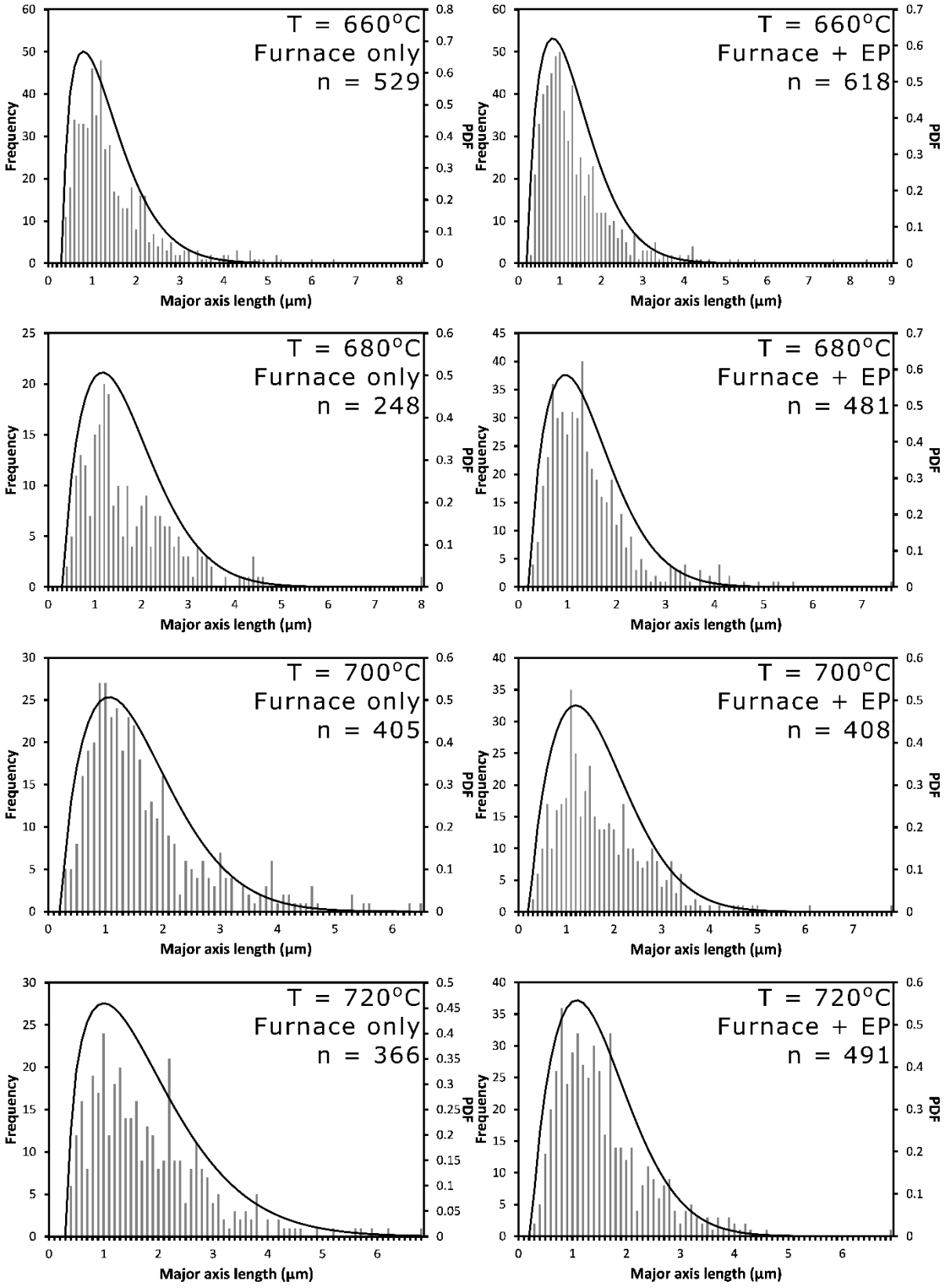


Figure 5.7. Ferrite grain major axis length comparison (still air cooled condition) for temperatures 660 – 720°C.

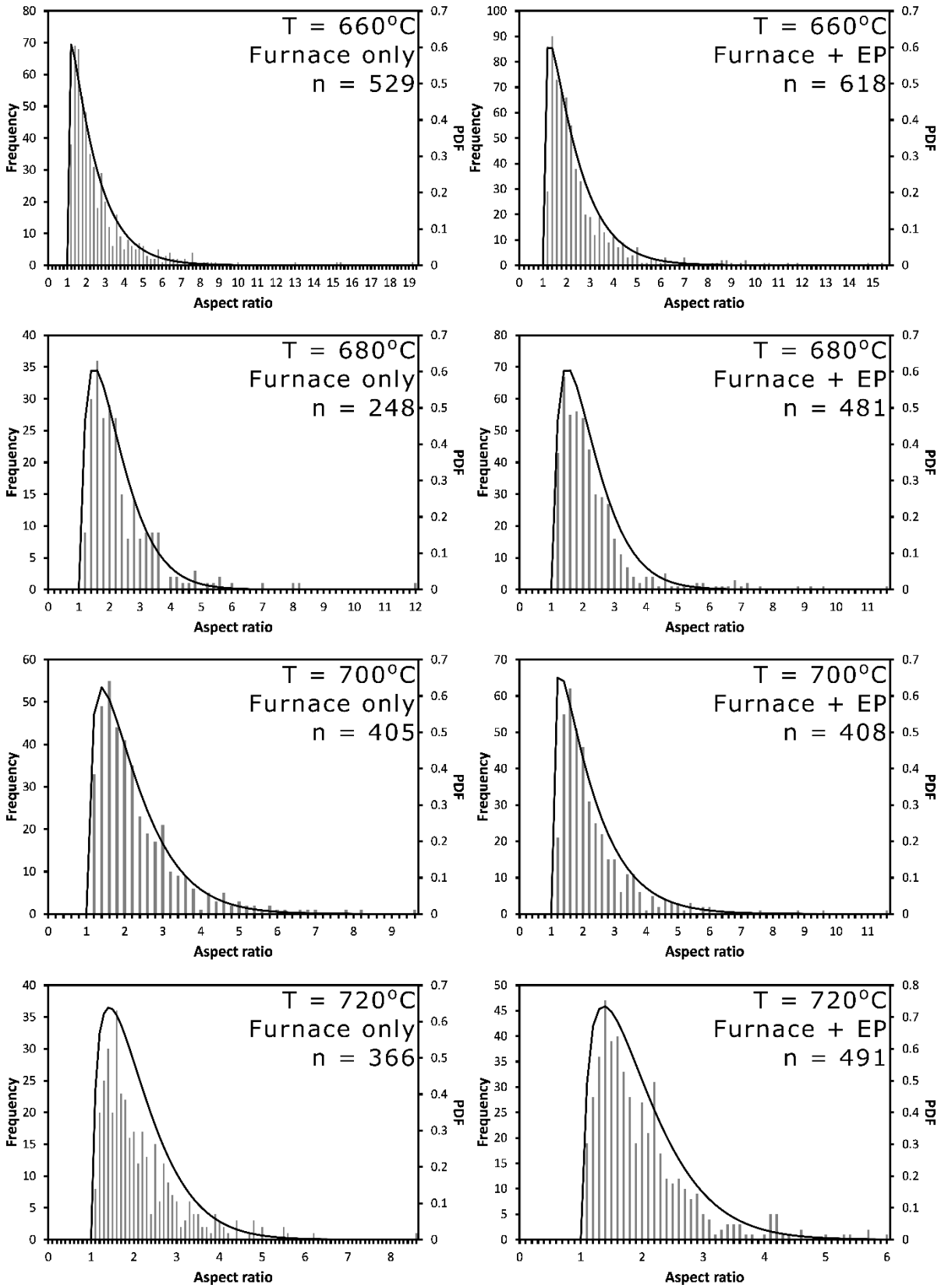


Figure 5.8. Ferrite grain aspect ratio comparison (still air cooled condition) for temperatures 660 – 720°C.

The aspect ratio of equiaxed ferrite grains was not found to change significantly over the applied treatment parameters, as shown in Figure 5.8. At 660°C, 75% of equiaxed ferrite grains in both the electropulsed and control samples were measured to have an aspect ratio of 2.8µm^2 or less. At 720°C, 75% of grains were found to have an aspect ratio of 2.5µm^2 or less in the control sample and 2.2µm^2 or less in the electropulsed sample. The very slight decrease observed between the 660 and 720°C conditions is not unexpected – with increasing temperature, a greater driving force for transformation is provided and as a result more equiaxed grains (with aspect ratio closer to 1) would be predicted.

No significant variation was observed in aspect ratio, major axis length or area measurements between the control and electropulsed samples at 660°C. However, at 720°C the electropulsed sample was found to have a slightly smaller area, aspect ratio and major axis length than the control sample. It might be expected that additional driving force provided by electropulsing would accelerate the recrystallisation and grain growth, therefore producing larger grains. As this is not the case, it is possible that some experimental artefact affected the microstructure, or that some other electropulsing effect caused a reduction in grain size.

Grain size analysis - Spheroidised cementite

Cementite spheroidisation was observed in all still air cooled samples in the temperature range 660 to 720°C. Figures 5.9 and 5.10 show a comparison of major axis length and aspect ratio between the control and electropulsed samples. Each temperature step is represented by a single graph, giving a direct comparison between the electropulsed and control samples.

The measured grains were filtered before analysis using a ratio devised by Chattopadhyay and Sellars [191]. This ratio provides a definition based on aspect ratio that allows differentiation between spheroidised and non-spheroidised cementite. According to the definition, cementite grains can be referred to as spheroidised if they have an aspect ratio of 8:1 or less. Accordingly, a small number of grains were not included in the plots shown in Figures 5.9 and 5.10.

The distribution of major axis length in annealed cementite is shown in Figure 5.9. The major axis length of spheroidised cementite was found to increase slightly with increasing temperature. At 660°C the majority of grains were measured to have major axis length of 0.5µm or less, while at 720°C this value had increased to 0.75µm. This behaviour was observed in both control and electropulsed samples (see Table 5.3), and was expected to occur based on previously described grain growth mechanisms.

It can be observed that there is some variation between the electropulsed and control samples in the frequency of grains with major axis length of 0.5µm or less at 660, 700 and 720°C. This correlates with a larger total number of grains measured in the electropulsed samples at 660, 700 and 720°C. When the number of grains measured was comparable between the electropulsed and control conditions as at 680°C, the distribution of major axis length is almost identical.

Furthermore, at each temperature step the shape of the distribution curve was comparable between the electropulsed and control sample. These findings imply that electropulsing did not induce any variation in major aspect length of spheroidised cementite grains in the still air cooled condition.

Analysis of the aspect ratio of spheroidised cementite particles gave similar results, producing highly comparable distribution curves. In all cases the majority of grains had an aspect ratio of between 1 and 2, which corresponds to circular rather than elongated grains. This behaviour was observed in both control and electropulsed samples.

As summarised in Table 5.3, the aspect ratio was not found to alter dramatically between the 660 and 720°C temperature conditions.

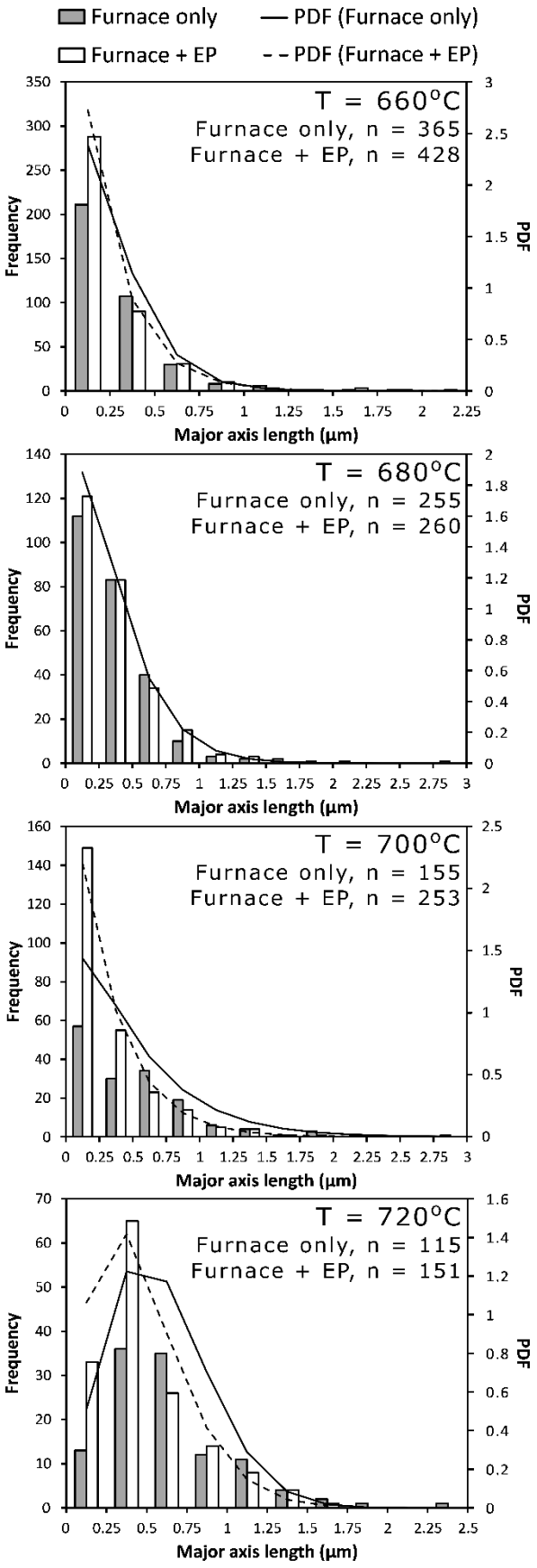


Figure 5.9. Spheroidised cementite major axis length comparison (still air cooled condition) for temperatures 660 – 720°C.

An increase in major axis length while aspect ratio remained constant shows that after achieving a spherical configuration the cementite grains continued to grow equiaxially.

Therefore, electropulsing during furnace treatment was not found to have any quantifiable effect on the geometry of spheroidised cementite particles in still air cooled pearlitic steel.

Table 5.3. Summary of spheroidised cementite geometry descriptors (assessed for approximately 75% of measured grains).

Geometry descriptor	T = 660°C		T = 720°C	
	Control	*Electropulsed*	*Control*	*Electropulsed*
Major axis length *(μm)*	≤0.5 *(87%)*	≤0.5 *(88%)*	≤0.75 *(73%)*	≤0.75 *(82%)*
Aspect ratio	≤2 *(79%)*	≤2 *(83%)*	≤2 *(78%)*	≤2 *(89%)*

Note: Percentage of grains within a particular size range are determined by the bin size of the related histogram. Larger bin size produces less granular percentage descriptor, resulting in the larger percentage values shown in this table.

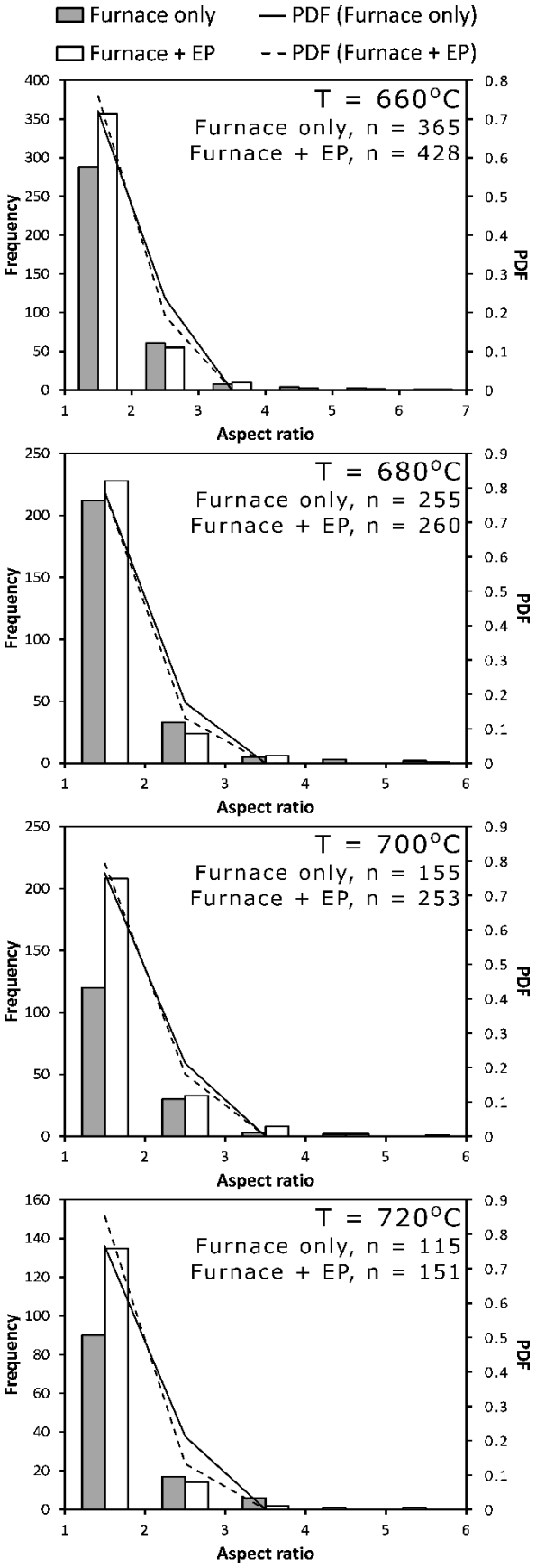


Figure 5.10. Spheroidised cementite aspect ratio comparison (still air cooled condition) for temperatures 660 – 720°C.

5.2.1.2. Forced air (FA) condition

The initial untreated microstructure of the forced air (FA) cooled steel was fully transformed lamellar pearlite aligned along the drawing direction. In the drawn condition the interlamellar spacing was measured to be 66±4nm. This spacing is finer than that measured in the SA material due to the faster cooling rate applied to the FA rod in pre-treatment. The rod underwent a cross-sectional area drawing reduction of 61%. Further details of the initial sample conditions can be found in the Methods section, pp.51.

Microscopy

Scanning Electron Microscopy imaging of samples with initial forced air cooled microstructure is shown in Figure 5.11. Samples treated by furnace annealing only are shown on the left, while those that underwent simultaneous furnace and electropulsing treatment appear on the right. As the results are similar to those of the still air cooled condition, only the temperature steps 660, 700 and 740°C are shown.

The effects of transition through the annealing process by temperature are clear, with grain structure transforming from initial lamellar microstructure to equiaxed α-ferrite and spheroidised cementite between 660 and 700°C (Figure 5.11 A-D). Recrystallisation and grain growth is more pronounced at the higher temperature, with greater driving force supplied. Similarly, cementite appears larger and more globular at 700°C than at 660°C. No variation between the control and electropulsed samples is obviously discernible from the SEM imaging. Further analysis of grain size is presented in the following sections.

At 740°C austenitisation of the samples was achieved, and lamellar pearlite reformed on air cooling. This behaviour was observed in both electropulsed and control samples, and the interlamellar spacing of the samples treated at this temperature was comparable (see Figure 5.5, pp.130). The control furnace sample was measured to have an ILS of 86±14nm, while the simultaneous furnace and electropulse treated sample had a value of 100±16nm. Based on the microscopy presented, electropulsing did not affect the austenitisation process during furnace annealing.

Grain size analysis parameters

Grain size analysis was conducted in an identical manner to that described for the still air cooled condition, using the same geometry descriptors and image magnification. For further information, refer to pp.130. As the results are again similar to those obtained for the still air cooled condition, grain size analysis is presented only for selected temperature steps.

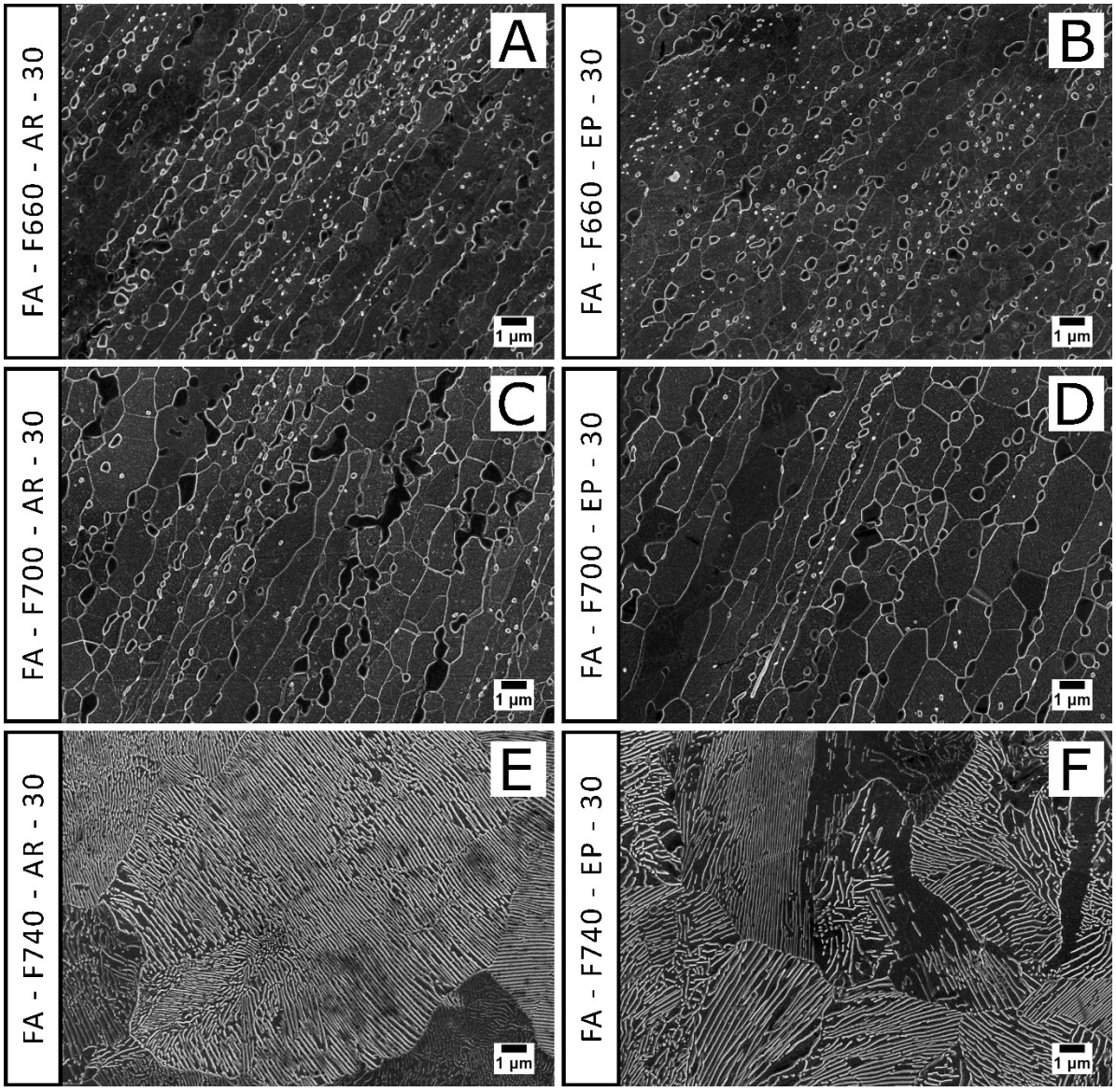


Figure 5.11. SEM microscopy of furnace annealed 0.73wt%C pearlitic steel (forced air cooled condition) with or without simultaneous electropulsing treatment. A) annealing only, 660°C; B) annealing and electropulsing, 660°C; C) annealing only, 700°C; D) annealing and electropulsing, 700°C; E) annealing only, 740°C; F) annealing and electropulsing, 740°C.

Grain size analysis - Equiaxed ferrite

Cross-sectional area, major axis length and aspect ratio of equiaxed α-ferrite grains from electropulsed and control samples are shown in Figures 5.12, 5.13 and 5.14, respectively. Data is shown for two temperature steps, 660 and 700°C.

Grain surface area was found to be comparable between the control and electropulsed samples at each temperature step. The distribution curves follow similar profiles, showing a frequency peak below approximately 1.5µm^2 in each case across the temperature range. At the lower temperatures grains with cross-sectional area up to approximately 4µm^2 were observed. The higher temperature of

700°C produced a greater frequency of larger grains, with the distribution curve extending up to approximately 5µm^2.

At 660°C, approximately 75% of equiaxed ferrite grains were measured to have a cross-sectional area of 1.3µm^2 in the control sample and 1.2µm^2 in the electropulsed sample (Table 5.4). At 700°C this number increased to 1.8µm^2 in both the control and electropulsed samples. As stated previously, this behaviour is predicted by and concurs with grain growth mechanics. The number of grains measured at each temperature step are also comparable, removing any frequency effects on the distribution curve. No significant or quantifiable variation in cross-sectional area of equiaxed ferrite was measured between the control and electropulsed samples at any temperature.

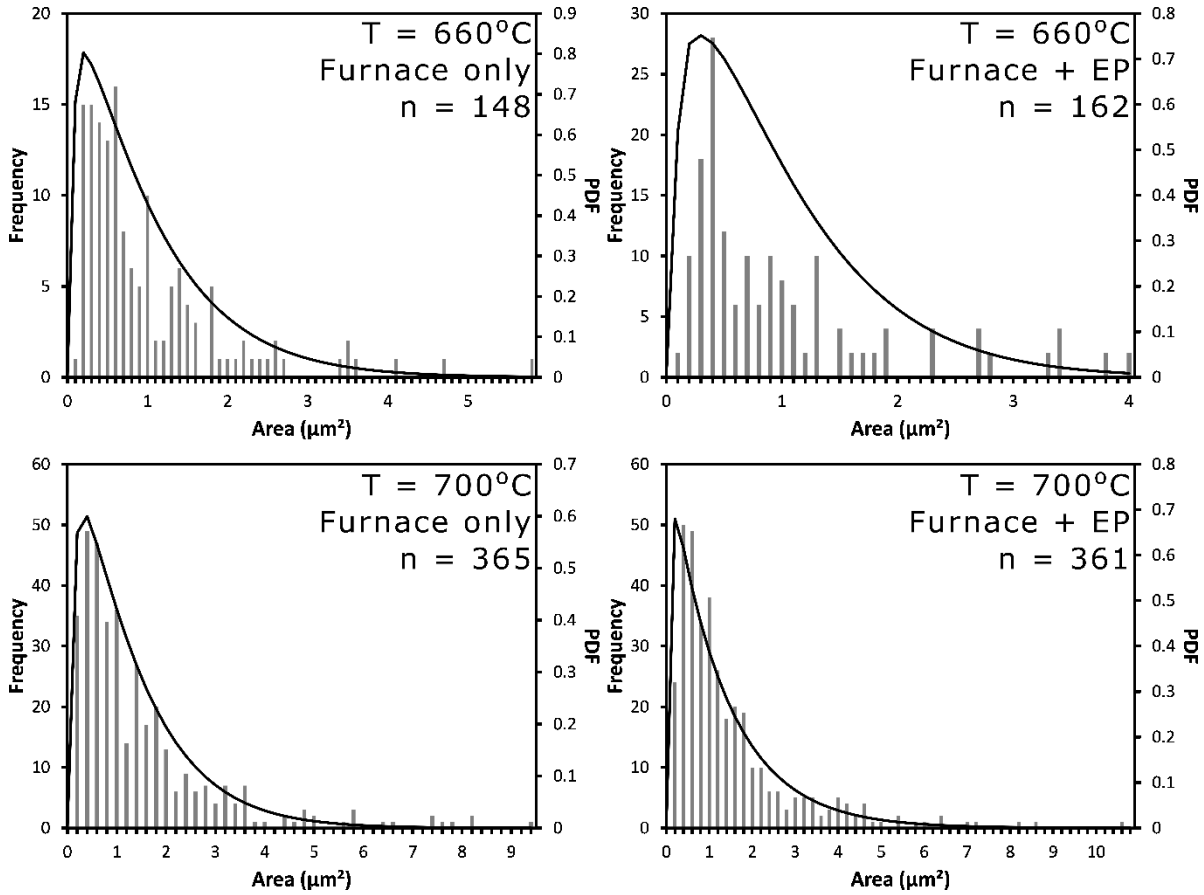


Figure 5.12. Ferrite grain area comparison (forced air cooled condition) for temperatures 660 and 700°C.

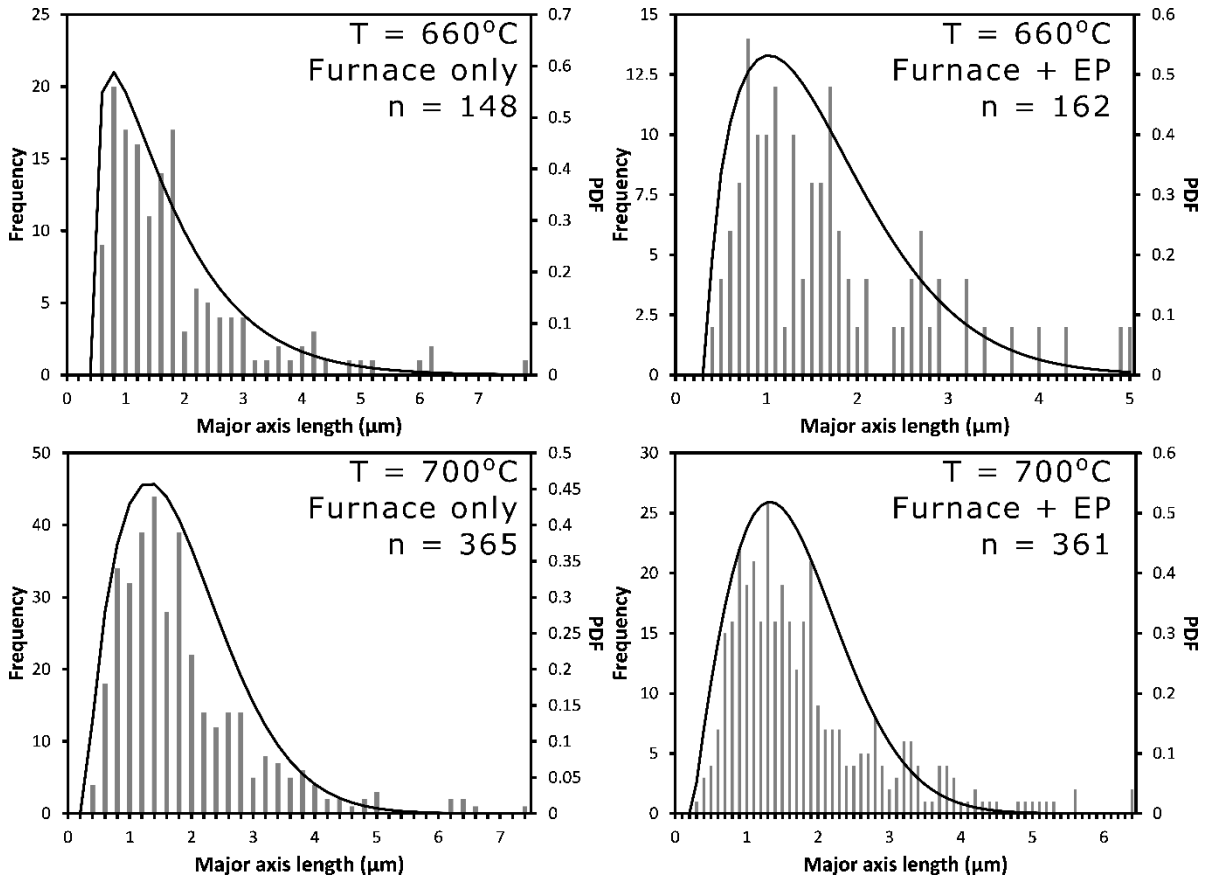


Figure 5.13. Ferrite grain major axis length comparison (forced air cooled condition) for temperatures 660 and 700°C.

Major axis length was also found to be comparable between control and electropulsed samples at each temperature step between 660 and 700°C, as shown in Figure 5.13. The distribution profiles of the electropulsed samples closely resemble their associated control samples. Very little variation in major axis length was measured between temperature steps – at both 660 and 700°C the distribution curve extends up to approximately 5µm. At both 660 and 700°C, approximately 75% of equiaxed grains in both the control and electropulsed samples were measured to have a major axis length of 2 - 2.2µm or less (see Table 5.4). No quantifiable electropulsing effect on the major axis length of the equiaxed α-ferrite was observed.

Table 5.4. Summary of equiaxed ferrite geometry descriptors (assessed for approximately 75% of measured grains in samples with initial forced air cooled microstructure).

Geometry descriptor	**T = 660°C**		**T = 700°C**	
	Control	*Electropulsed*	*Control*	*Electropulsed*
Area *(μm^2)*	≤1.3 *(76%)*	≤1.2 *(73%)*	≤1.8 *(76%)*	≤1.8 *(77%)*
Major axis length *(µm)*	≤2.2 *(76%)*	≤2 *(75%)*	≤2.2 *(75%)*	≤2.2 *(76%)*
Aspect ratio	≤3.75 *(76%)*	≤2.8 *(74%)*	≤2.6 *(76%)*	≤2.5 *(75%)*

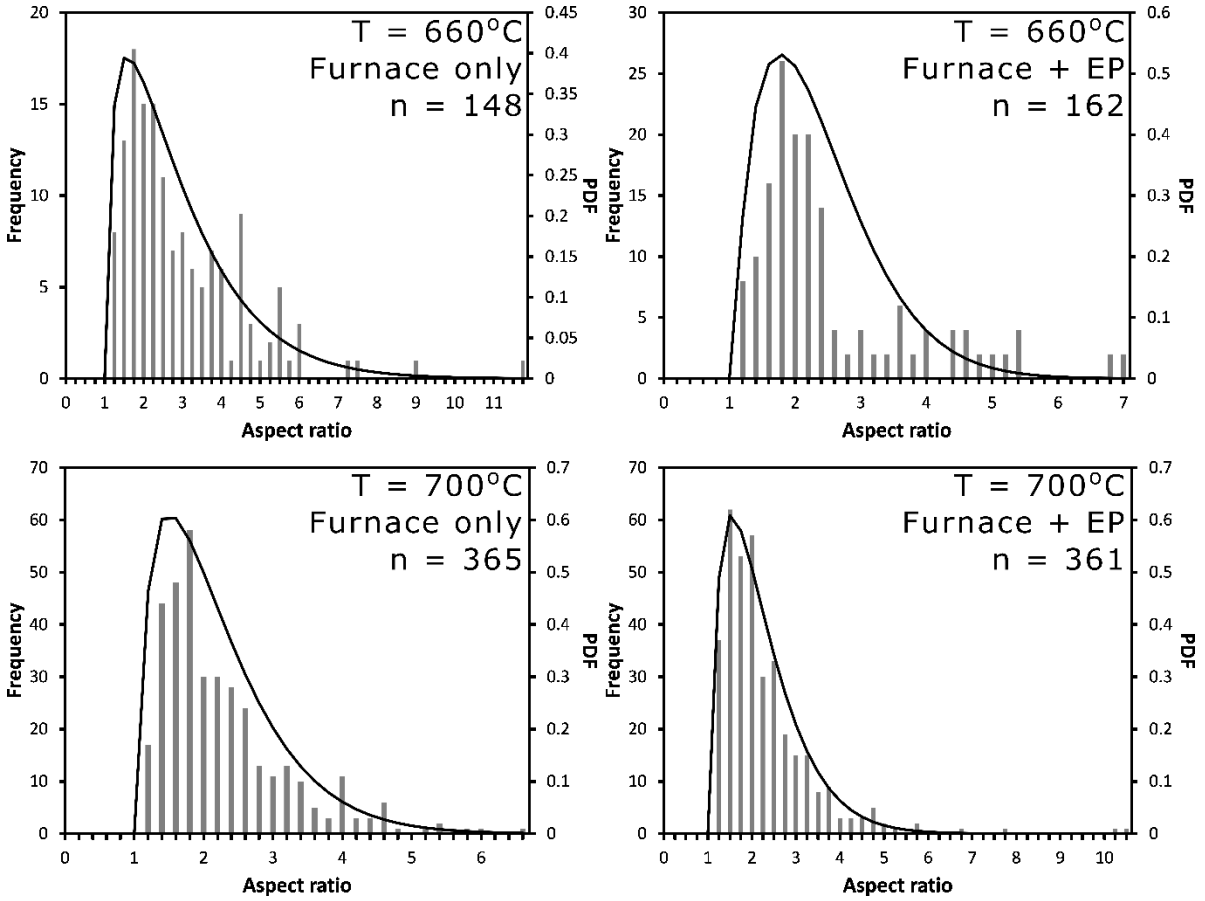


Figure 5.14. Ferrite grain aspect ratio comparison (forced air cooled condition) for temperatures 660 and 700°C.

The aspect ratio measurements of equiaxed ferrite grains at 660 and 700°C are shown in Figure 5.14. The distribution curves again have similar profiles at each temperature, extending up to approximately 5 to 6 at 660°C and 5 at 700°C. A variation between the control and electropulsed samples at 660°C was observed, as summarised in Table 5.4. At 660°C approximately 75% of equiaxed grains were found to have an aspect ratio of 3.75, while 75% of grains in the electropulsed sample had an aspect ratio of 2.8 or lower. At 700°C no variation is observed - approximately 75% of equiaxed grains in the control sample had an aspect ratio of 2.6 or lower, while the value for the electropulsed condition was 2.5.

The difference observed in the samples at 660°C is similar to effects observed in the SA condition, although those effects occurred at 720°C. While the results suggest that electropulsing may reduce the grain size during furnace annealing, they do not show good correlation and the majority of samples analysed thus far do not show any comparable effects. The differences measured may be a result of variable etch quality (upon which this measurement technique relies) or natural variability in the samples. The aspect ratio is observed to decrease slightly between 660 and 700°C independent of the anomalous result, which once again is an expected effect of the furnace treatment applied.

Grain size analysis - Spheroidised cementite

Cementite spheroidisation in initial forced air cooled microstructure samples is described by major axis length and aspect ratio in Figures 5.15 and 5.16. Data for three temperature conditions (660, 680 and 700°C) is included.

The effects of temperature on major axis length were only clearly observed at smaller grain diameters. The distribution curves at 660, 680 and 700°C were comparable and extend up to between approximately 1.5 and 1.75µm. The major axis length at 700°C is more widely distributed at smaller grain diameters, as summarised in Table 5.5. More than 80% of spheroidised grains were found to have a major axis length of 0.5µm in both the control and electropulsed conditions, while only 64% of grains at 700°C met the same criteria. This suggests that spheroidised cementite major axis length grew with increasing annealing temperature, which agrees with previously stated grain growth mechanics.

Table 5.5. Summary of spheroidised cementite geometry descriptors (assessed for approximately 75% of measured grains).

Geometry descriptor	T = 660°C		T = 700°C	
	Control	*Electropulsed*	*Control*	*Electropulsed*
Major axis length *(µm)*	≤0.5 *(82%)*	≤0.5 *(86%)*	≤0.5 *(64%)*	≤0.5 *(64%)*
Aspect ratio	≤2 *(85%)*	≤2 *(79%)*	≤2 *(74%)*	≤2 *(76%)*

See note: Table 5.3, pp.137

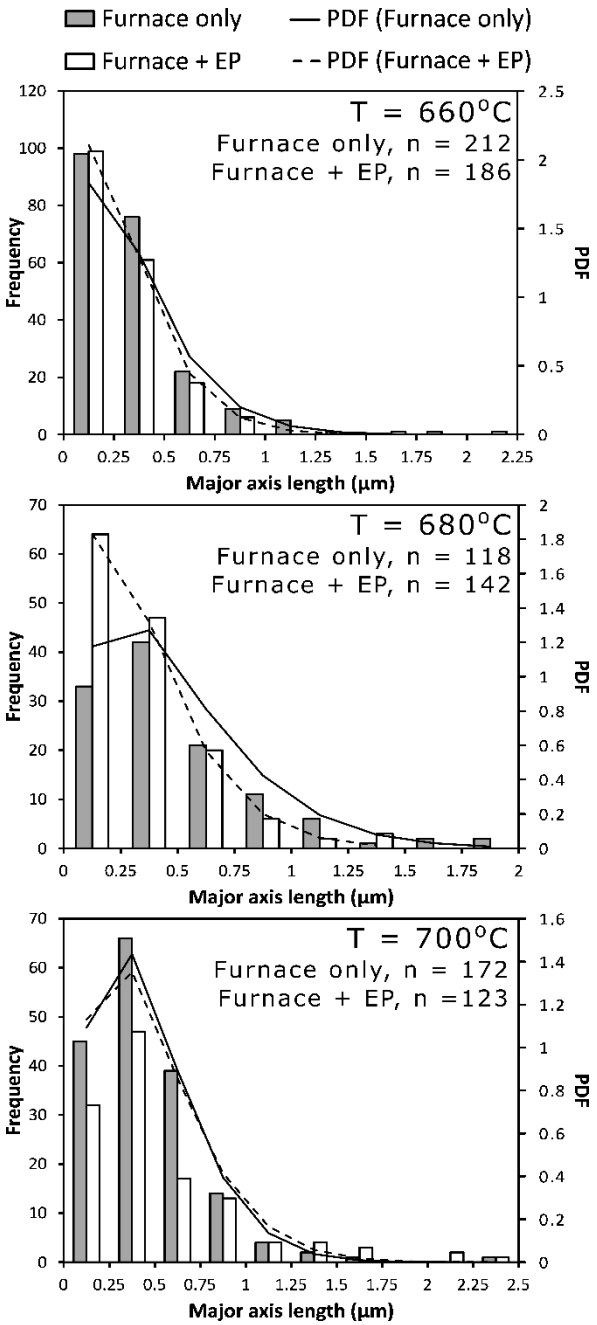


Figure 5.15. Spheroidised cementite major axis length comparison (forced air cooled condition) for temperatures 660 – 700°C.

A slight variation in distribution curve profile was observed at 680°C. The major axis length of spheroidised cementite in the control sample peaked between 0.25 and 0.5µm, while the electropulsed sample peaked between 0 and 0.25µm.

As shown by simulation (see pp.55, Figure 3.4) and experimental results, the transition temperature for this steel composition and initial microstructure occurs between 720 and 740°C. If electropulsing were to have an effect, it might be expected to occur at the transition temperature. However, the variation in major axis length occurred at 680°C, and no difference in distribution profile was observed between control and electropulsed samples at 660 or 700°C. As for previously described variations in the SA and FA conditions, the correlation seems random and no consistent trend has emerged.

As shown in Figure 5.16, no variation in aspect ratio was observed between control and electropulsed samples at any temperature step. At each temperature the distribution curve profiles have high correlation, and limited variation between temperatures was measured as summarised in Table 5.5. No evidence of electropulse-induced microstructure change was observed in aspect ratio measurements of spheroidised cementite.

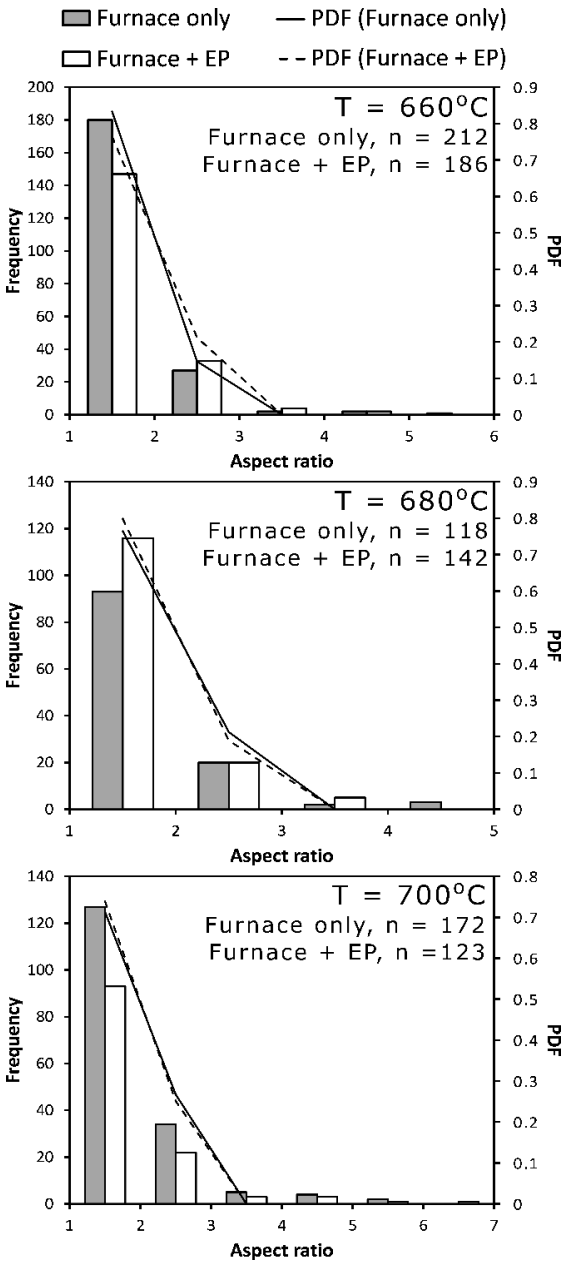


Figure 5.16. Spheroidised cementite aspect ratio comparison (forced air cooled condition) for temperatures 660 – 700°C.

5.2.1.3. Salt bath (SB540) condition

The salt bath treated (SB540) initial microstructure contained regions of fine spheroidised cementite particles interspersed with colonies of lamellar pearlite. The orientation of the pearlite was varied, unlike that of the drawn SA and FA conditions. Data supplied by the manufacturer states the average interlamellar spacing as 43nm. As the salt bath treatment occurred after the wire was drawn, the microstructure is observed in an undeformed state. Further details of the initial sample conditions can be found in the Methods section, pp.51.

Microscopy

Figure 5.17 shows SEM imaging of initial salt bath transformed (SB540) microstructure samples after furnace annealing or simultaneous furnace and electropulsing treatment. The furnace only control samples appear on the left, and electropulsed samples on the right. Imaging for treatment temperatures of 660, 700 and 740°C are presented.

The initial SB540 microstructure was significantly more fragmented and granular than the still air and forced air cooled conditions (see Methods pp.53, Figure 3.2) and the annealed samples were also found to have a differing microstructure as a result. Figure 5.17 A and B show a large volume of fine spheroidised cementite interspersed with some microscale grain boundary cementite and long ferrite grain boundaries at 660°C. Images C and D show more fully developed cementite spheroidisation and equiaxed α-ferrite at 700°C. The cementite grains were larger and more globular, while the equiaxed ferrite was more distinct than at 660°C. The ferrite grains appeared larger than those found in the still and forced air cooled conditions. Grain boundary pinning of ferrite grains by large cementite spheroids was observed in both the electropulsed and control samples. Intragranular cementite was also visible inside the ferrite grains, having nucleated during the initial salt bath treatment and continued to grow in the subsequent annealing treatment. No clear variation between control and electropulsed samples at 660 or 700°C was visible from initial observations. Detailed grain size analysis is described in the following sections.

Figure 5.17 E and F show control and electropulsed samples treated at 740°C. At this temperature transformation from pearlite to austenite occurred, and on cooling lamellar pearlite was reformed. Unlike the still and forced air cooled conditions, this transformation was also observed at 720°C in both the control and electropulsed samples in SB540 material. This is due to the finer, more fragmented initial microstructure observed in the salt bath transformed samples. Austenite is known to preferentially nucleate at the interface between ferrite and cementite grains in dual phase spheroidised iron-carbide microstructure [192]. In addition, the morphology and scale of pearlitic microstructure has been found to affect the austenitisation temperature, with finer microstructures

austenitising at lower temperatures [193]. The finer microstructure of the SB540 steel provided a greater number of grain boundary interface regions and therefore more preferential austenite nucleation points. The austenite transformation was also accelerated by enhanced carbon diffusion in the SB540 samples compared to the still and forced air cooled conditions, again due to a higher volume of carbon-ferrite interface points. As a result, SB540 samples austenitised at a lower temperature than those in the still and forced air cooled conditions.

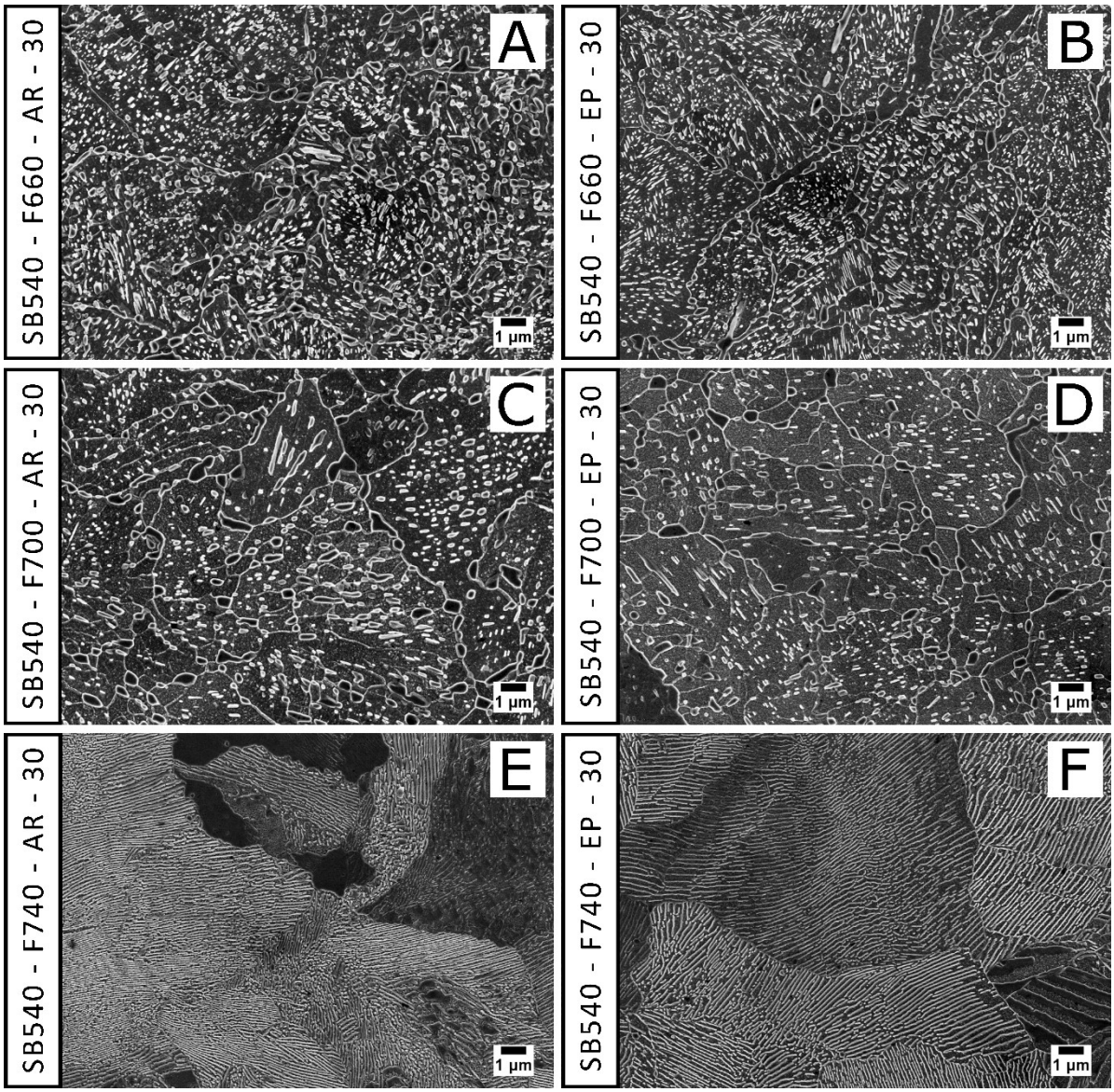


Figure 5.17. SEM microscopy of furnace annealed 0.73wt%C pearlitic steel (salt bath condition) with or without simultaneous electropulsing treatment. A) annealing only, 660°C; B) annealing and electropulsing, 660°C; C) annealing only, 700°C; D) annealing and electropulsing, 700°C; E) annealing only, 740°C; F) annealing and electropulsing, 740°C.

The volume fractions of lamellar pearlite and spheroidised or fragmented cementite regions obtained during testing at 740°C are shown in Table 5.6. A slight variation was observed between the samples, with the electropulsed sample having a higher proportion of fragmented regions than the furnace only control sample.

Table 5.6. Volume fraction analysis of 0.73wt%C SB540 samples annealed at 740°C with and without simultaneous electropulsing treatment.

Condition	**Volume fraction**	
	Lamellar pearlite	*Spheroidised / fragmented cementite*
Furnace only	0.85	0.15
Furnace and electropulsing	0.75	0.25

Additionally, interlamellar spacing measurements were made at 720 and 740°C and are summarised in Table 5.7. Samples treated at 720°C were found to have a larger interlamellar spacing than those at 740°C. No significant variation was found between the control and electropulsed samples at either temperature step, as the region of error of each sample pair overlapped.

Table 5.7. Interlamellar spacing of 0.73wt%C SB540 samples annealed at 720 and 740°C with and without simultaneous electropulsing treatment.

T *(°C)*	**ILS** *(nm)*	
	Furnace only	*Furnace + electropulsing*
720	126±31	142±30
740	84±15	90±19

As described in the Methods section, pp.74 the interlamellar spacing depends on the cooling rate from austenite through the pearlite transformation [142]. A faster cooling rate limits diffusion and prevents the lamellae from thickening, resulting in a fine interlamellar spacing. A larger interlamellar spacing at the lower temperature of 720°C is likely a result of slight variation in the cooling rate at ambient temperature between the 720 and 740°C samples. This could potentially result from environmental differences or a slight delay between opening the furnace door and full removal of the samples from the heat source. As the result was not observed in lamellar samples in the still and forced air conditions, and the coarser interlamellar spacing was observed in both the control and electropulsed samples at 720°C, the effect is not thought to result from electropulsing treatment.

Grain size analysis parameters

Grain size analysis of salt bath transformed samples was affected by the nature of the microstructure under consideration. The highly fragmented, fine spheroidised microstructure demonstrated in Figure 5.17 A and B could not be successfully analysed using ImageJ software due to limitations in

thresholding. A manual grain size count was determined to be impractical due to the scale of the task when considered with time constraints. As a result, cementite spheroidisation analysis at 660 and 680°C was conducted on images at 14000X to assess the largest grains, and 85000X to assess the smallest. This method was intended to give an indication of the range of cementite grain sizes present in each sample, but cannot be used to describe the distribution of grain size. Analysis of cementite spheroidisation at 700°C was conducted in the same manner as for the still and forced air conditions as the grains were larger, more easily distinguishable and appeared in smaller numbers. Equiaxed ferrite measurements were unaffected by the appearance of the cementite and were conducted as described in previous sections.

Grain size analysis - Equiaxed ferrite

Equiaxed ferrite geometry of SB540 samples that underwent furnace treatment at 660 and 700°C are shown in Figures 5.18 to 5.20. Control samples appear on the left, and simultaneous furnace and electropulse treated samples on the right.

As observed in previous initial microstructure conditions, the distribution profiles have good resemblance between control and electropulsed samples at each temperature step. The ferrite grain cross-sectional area, shown in Figure 5.18, appears to fall slightly between the 660 and 700°C conditions. At 660°C the distribution curve extends up to between approximately 5 and 6µm^2 in both the control and electropulsed conditions. At 700°C both the control and electropulsed distribution curves extend up to 3.5µm^2.

The drop in grain surface area between the temperatures is a result of a greater number of equiaxed grains in the sample. The grains measured at 660°C are more likely to be large fragmented ferrite regions or a result of prior austenite grain boundaries rather than recrystallisation or grain growth. At 700°C the grains are a result of the annealing treatment and are smaller than the previous temperature step as grain growth was not complete. Electropulsing treatment was not observed to have affected the ferrite grain cross-sectional area at either temperature step.

The distribution of major axis length in equiaxed ferrite grains is shown in Figure 5.19. As with all previous results, the distributions are comparable between control and electropulsed samples at each temperature step. At 660°C approximately 75% of equiaxed ferrite grains in the control sample had a major axis length of 1.9µm or less, and in the electropulsed sample this value was 1.7µm or less. At 700°C approximately 75% of equiaxed grains in the control sample had a major axis length of 1.5µm or less, and the electropulsed sample 1.6µm or less (see Table 5.8).

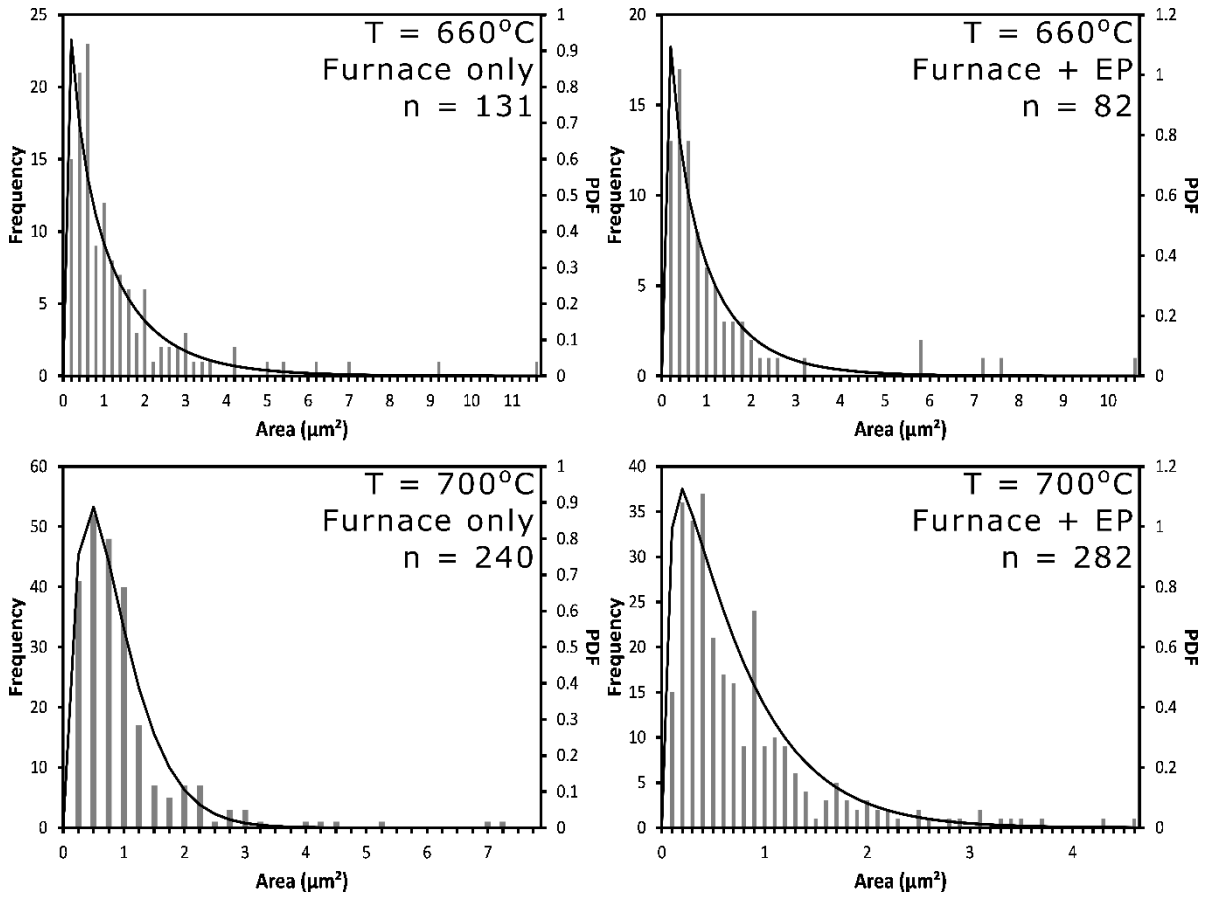


Figure 5.18. Ferrite grain area comparison (salt bath condition) for temperatures 660 and 700°C.

The major axis length appears to be slightly smaller in the samples treated at a higher temperature, which does not necessarily agree with grain growth behaviour in annealing processes. This suggests that as in the cross-sectional area measurements, larger ferrite regions and prior austenite grain boundaries have skewed the results. However, based on comparison with the control samples it cannot be concluded that electropulsing treatment has affected the major axis length of ferrite grains, equiaxed or otherwise.

The aspect ratio of α-ferrite grains is largely unaltered by temperature variation between 660 and 700°C. In each case the aspect ratio was comparable between the control and electropulsed samples. Approximately 75% of grains measured in the control sample at 660°C had an aspect ratio of 2.1 or less, while the same percentage of grains in the electropulsed sample had aspect ratio of 2.4 or less. Similarly, the control sample at 700°C contained approximately 75% of grains with aspect ratio of 2.2 or less, and electropulsed sample contained a majority of grains with aspect ratio 2.3 or less. The distribution profiles of the control and electropulsed samples were comparable at each temperature step. Electropulsing was not found to affect the aspect ratio of ferrite grains during furnace treatment of SB540 samples.

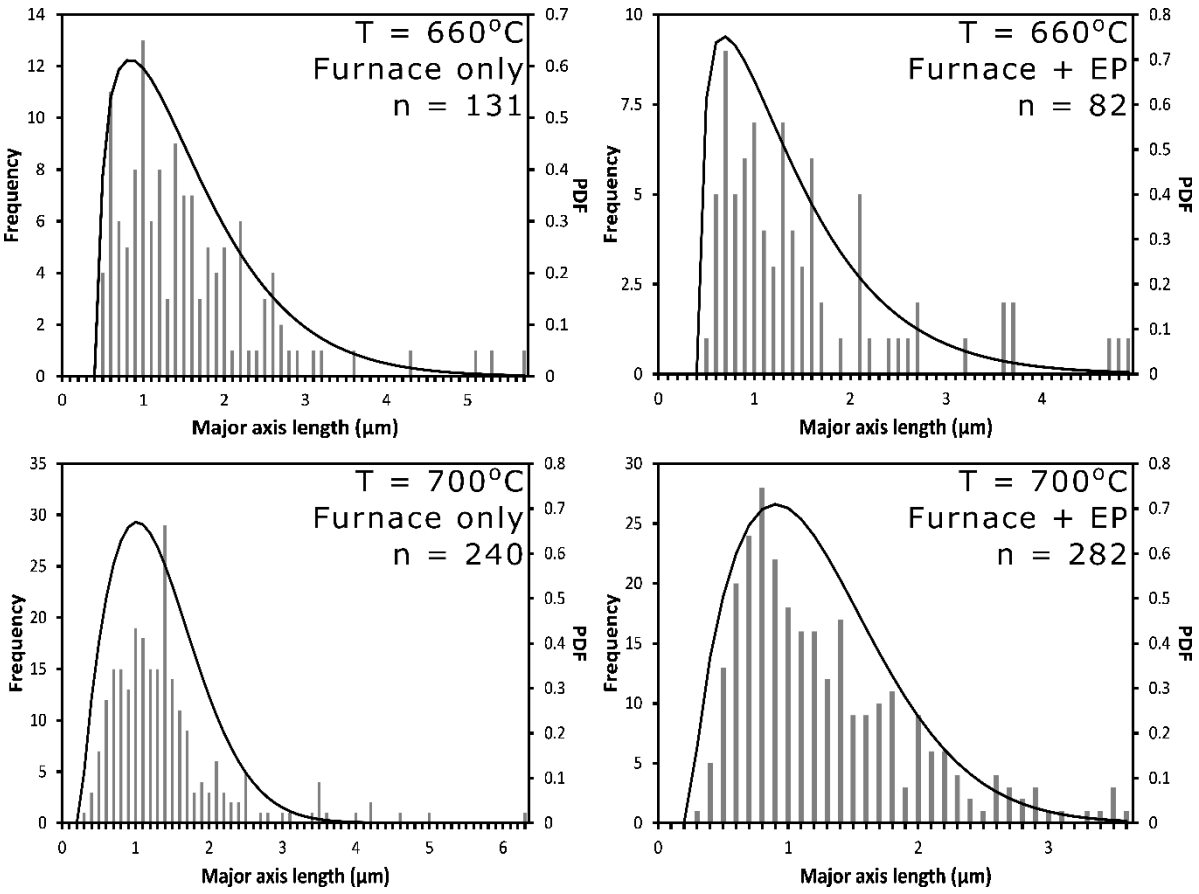


Figure 5.19. Ferrite grain major axis length comparison (salt bath condition) for temperatures 660 and 700°C.

Table 5.8. Summary of equiaxed ferrite geometry descriptors (assessed for approximately 75% of measured grains in samples with initial salt bath transformed microstructure).

Geometry descriptor	**T = 660°C**		**T = 700°C**	
	Control	*Electropulsed*	*Control*	*Electropulsed*
Area *(μm^2)*	≤1.6 *(77%)*	≤1.2 *(76%)*	≤1 *(75%)*	≤0.9 *(74%)*
Major axis length *(µm)*	≤1.9 *(76%)*	≤1.7 *(76%)*	≤1.5 *(73%)*	≤1.6 *(74%)*
Aspect ratio	≤2.1 *(76%)*	≤2.4 *(74%)*	≤2.2 *(74%)*	≤2.3 *(76%)*

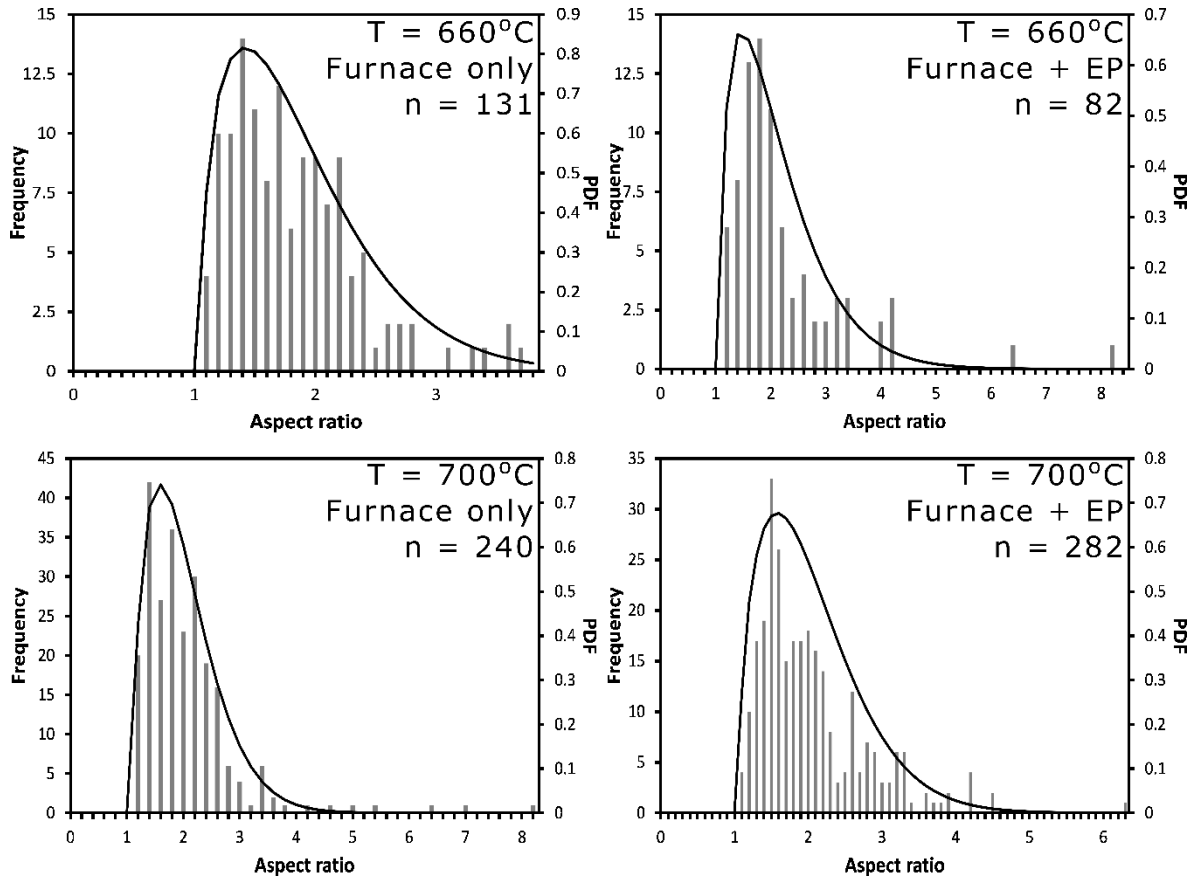


Figure 5.20. Ferrite grain aspect ratio comparison (salt bath condition) for temperatures 660 and 700°C.

Grain size analysis - Spheroidised cementite

As described previously, cementite spheroidisation was difficult to quantify in samples with large numbers of very fine grains. As a result the spheroidisation geometry of samples treated at 660°C and 680°C was assessed in a different manner to the previously described spheroidised samples. An assessment of the major axis length and aspect ratio of grains at the extremes of the size scale (i.e. very large and very small) was undertaken to give an indication of any electropulsing effects. The grains were filtered before analysis using the aspect ratio definition described on pp.135. The results are summarised in Table 5.9 (note that data for 680°C is included for comparative purposes due to the differing method used to obtain the measurements).

In both microscale and fine spheroidised cementite grains at 660°C the major axis length and aspect ratio were comparable between the control and electropulsed samples. The majority of large grains were found to have a major axis length of 0.5µm or less, and an aspect ratio of 3 or less. These values were consistent between the electropulsed and control samples. Similarly, fine grained cementite was observed to have highly comparable major axis length measurements. In both the control and electropulsed samples, 78% of fine cementite grains were found to have a major axis length of 0.2µm or less. A slight variation in the aspect ratio of fine grained cementite was observed between the

control and electropulsed samples, with the control sample cementite appearing to have a smaller aspect ratio.

Table 5.9. Summary of spheroidised cementite geometry descriptors in samples with very fine microstructures resulting from initial salt bath treatment.

Geometry descriptor	T = 660°C		T = 680°C	
	Control	*Electropulsed*	*Control*	*Electropulsed*
	Microscale spheroidisation			
	n = 210	n = 151	n = 188	n = 148
Major axis length *(μm)*	≤0.5 *(69%)*	≤0.5 *(72%)*	≤0.5 *(71%)*	≤0.5 *(69%)*
Aspect ratio	≤3 *(80%)*	≤3 *(83%)*	≤3 *(80%)*	≤3 *(87%)*
	Fine spheroidisation			
	n = 399	n = 364	n = 292	n = 332
Major axis length *(μm)*	≤0.2 *(78%)*	≤0.2 *(78%)*	≤0.2 *(76%)*	≤0.2 *(78%)*
Aspect ratio	≤2 *(69%)*	≤3 *(73%)*	≤2 *(72%)*	≤2 *(67%)*

Similar behaviour was observed at 680°C, with closely comparable major axis length values of both microscale and fine grains in the control and electropulsed samples. Some variation was observed in the aspect ratio, but when considered with the aspect ratio data at 660°C no trend emerges. This suggests that the aspect ratio variation is a result of natural and inherent statistical differences rather than an electropulse-induced effect.

At 700°C the scale and distribution of cementite spheroidisation was sufficient for the standard measurement technique applied in the still and forced air cooled sample analysis to be used. A comparison of major axis length and aspect ratio is shown in Figure 5.21.

In both cases the distribution profiles are closely comparable between the control and electropulsed samples. Both conditions show a frequency peak at major axis length of 0.25μm or less and aspect ratio between 1 and 2. The distribution curves extend up to approximately 1μm major axis length and an aspect ratio of 6. 90% of measured grains in the control sample were found to have a major axis length of 0.5μm or less, while in the electropulsed sample 88% of grains met the same criteria. 92% of grains in the control sample were reported to have an aspect ratio of 0.5 or less, while 86% of grains in the electropulsed sample fell within the same range.

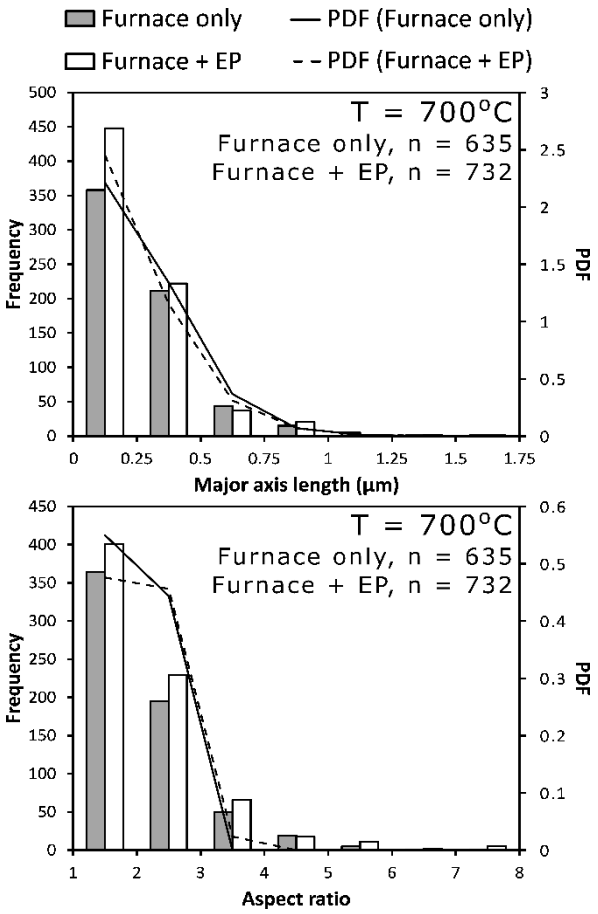


Figure 5.21. Spheroidised cementite major axis length and aspect ratio comparison (salt bath condition) for temperature 700°C.

While some variation was observed in the aspect ratio of spheroidised cementite grains measured in the three temperature steps 660, 680 and 700°C, no clear trend was observed and no other comparable effects were observed in the major axis length analysis. As a result it is concluded that electropulsing treatment had no effect on the cementite spheroidisation mechanism during high temperature annealing of 0.73wt%C steel rod with initial salt bath transformed microstructure.

5.2.2. Mechanical properties

The mechanical properties of samples from all three initial microstructure conditions were assessed using Vickers microhardness testing with a load of 2kg. Four hardness tests were conducted on each sample and an average value was generated. The results from the still air cooled (A), forced air cooled (B) and salt bath transformed (C) initial microstructure conditions with and without electropulsing are summarised in Figure 5.22. The as-received cold-drawn hardness of each condition is also included for comparison.

The microhardness of the still air cooled control condition was found to decrease from 251±1HV_2 after annealing at 660°C to 215±0.4HV_2 at 720°C. The electropulsed condition decreased from 255±2.3HV_2 at 660°C to 218±2.5HV_2 at 720°C. The degree of hardness reduction was very close between the

control and electropulsed samples, with the former falling by 36HV_2 and the latter by 37HV_2. The initial and final values were also comparable. A significant increase in hardness was observed after treatments at 740°C, corresponding with a return to lamellar pearlite after austenitisation. The control sample hardness increased to 336±1HV_2 while the electropulsed sample increased to 344±6.8HV_2.

Samples in the forced air cooled condition followed the same trend, with control sample microhardness falling from 264±3HV_2 after annealing at 660°C to 220±1.1HV_2 at 700°C (-44HV_2). The electropulsed condition decreased from 251±2.6HV_2 at 660°C to 223±1.2HV_2 at 720°C (-28HV_2). At 740°C the microhardness increased to 350±1.3HV_2 in the control sample and 319±11.8HV_2 in the electropulsed sample. Some slight variation was measured between the control and electropulsed samples at each temperature step but with no clear trend, and may have resulted from natural sample variability or localised effects during hardness testing such as surface microdefects.

The appearance of the microhardness plot of samples in the salt bath transformed initial microstructure condition differs slightly to the still and forced air cooled conditions. As in those conditions, the microhardness was observed to fall between 660 and 700°C in both the control and electropulsed samples. The control sample hardness was reduced from 266±2.2HV_2 to 237±2.9HV_2 (-29 HV_2), while the electropulsed hardness fell from 284±1.4HV_2 to 241±2.5HV_2 (-43HV_2). However, after 700°C the hardness was observed to increase, unlike the previous initial microstructure conditions which saw increased hardness only at 740°C. In the control sample the hardness increased from 282±6.5HV_2 at 720°C to 338±4.1HV_2 at 740°C (+56HV_2). The electropulsed sample hardness increased from 263±5.1HV_2 to 332±3.3HV_2 (+69HV_2) across the same temperature range. The increase in hardness at 720°C is a result of earlier austenitisation as described previously, resulting in a eutectoid transformation and lamellar microstructure.

The hardness characteristics of annealed and electropulsed SB540 initial microstructure samples vary somewhat, particularly at 660 and 720°C. However as in previous occurrences there is no apparent trend or supporting evidence from microstructural analysis.

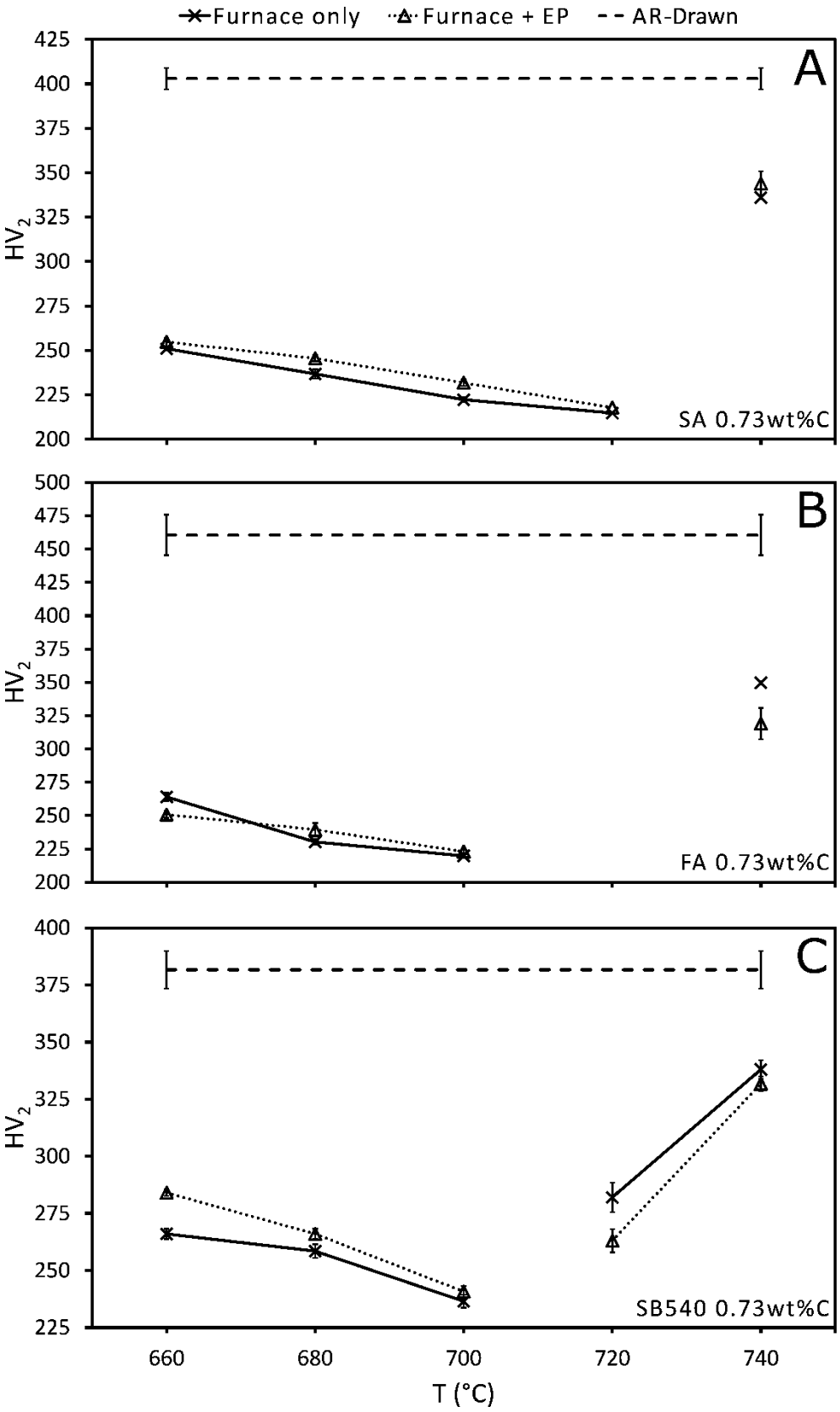


Figure 5.22. Comparison of microhardness characteristics of samples furnace treated and simultaneously electropulsed, and furnace treated only. A) SA samples; B) FA samples; C) SB540 samples. Note that hardness data is not provided for the electropulsed FA condition at 720°C due to a sample problem.

The hardness behaviour reported in all three microstructure conditions corresponds with the observed microstructures and known annealing behaviour of steel. Spheroidisation was observed between 660 and 720°C in the still air and forced air cooled conditions, and between 660 and 700°C in the salt bath transformed condition. At these temperatures, softening of the material was reported. Spheroidisation is a softening heat treatment intended to improve the workability of steel by increasing the ductility of the material. A reduction in grain boundary area per unit volume from lamellar to spheroidised microstructure reduces the resistance to dislocation motion, and hence the hardness of the steel [25]. The hardness of pearlitic steel is also known to decrease with increasing temperature [194] as the driving force for spheroidisation is increased and further softening occurs as a result.

Conversely, as the spheroidisation process is overtaken by the eutectoid transformation at 740°C (or 720°C in SB540 samples) the hardness would be expected to increase, as the grain boundary area increases with the formation of the lamellar structure and inhibits dislocation motion once more. This is evident in the results observed, with an increase in hardness reported in each material condition where the microstructure was observed to have transformed to lamellar pearlite. Both the control and electropulsed samples in the SB540 condition at 740°C have a higher hardness than those at 720°C, which is directly related to a smaller interlamellar spacing at the higher temperature as shown in Table 5.7.

Interlamellar spacing is a key factor governing the hardness of pearlitic steel, and is determined by the level of undercooling achieved below the eutectoid transformation temperature [142]. A finer interlamellar spacing is produced at a greater undercooling, and results in a harder steel due to a higher grain boundary area per unit volume than coarser lamellar structures. Both conductive and convective heat transfer are dependent on the temperature gradient between the hot body and the surrounding fluid [195]. It could therefore be expected that the larger temperature gradient produced at 740°C could induce a slightly more rapid cooling rate, leading to a finer interlamellar spacing than at 720°C.

While some microhardness variation was observed in the forced and salt bath treated initial microstructure conditions, overall there was no clear trend apparent from the results. Furthermore, the variations are relatively small and not thought to be significant. It is concluded that electropulsing treatment did not affect the mechanical properties of 0.73wt%C steel wire during furnace annealing.

5.3. Discussion

5.3.1. Electropulsing as a cooperative microstructure treatment

The aim of the experiments described in this chapter was to assess whether electropulsing at current density of 10^7 A·m^{-2} could be applied as a co-operative annealing treatment in order to induce microstructure effects different to those obtained through standard furnace treatments. The motivation for this study was based on the concept of electropulsing as a diffusion-enhancing process. Some studies have shown that electric current pulses can enhance diffusive phase transformations [20] and accelerate recrystallisation [67] and diffusive crack healing processes [61]. The eutectoid transformation and spheroidisation and recrystallisation mechanisms are diffusive [142], which led to the hypothesis that additional driving force provided by electropulsing may produce useful microstructure variations in furnace annealed pearlitic steel.

The critical point of the experiment lay in the theory of thermal and athermal components, which has been used in the literature to explain electropulsing effects observed in various materials [10, 28, 119, 196]. Research has also shown that a combination of thermal and athermal effects is required for electropulsing-induced transformation; athermal effects alone are not sufficient [136]. The combination of furnace annealing and electropulsing treatment was intended to remove the reliance on the electropulsing treatment itself to provide a large enough thermal effect in order to induce microstructure transformation, by providing an additional external heat source. Minimising the heating effect associated with the electropulsing treatment by applying a low current density would allow any consistently observed microstructure change to be inferred as a direct result of athermal effects associated with the electric current. A further beneficial side-effect of this method was facilitation of temperature selection, allowing consistent experimental temperatures in the subcritical eutectoid transformation range to be analysed.

5.3.2. Current density, thermal and athermal effects

Throughout the experimental results described in this chapter, no clear evidence of electropulse-induced microstructure or mechanical property change has emerged. Some variation in grain size were observed at various temperatures and material conditions, but no correlation or trend was observed in the data. Electropulsed grain sizes that diverged from the control sample grain size were observed to be both larger and smaller at various conditions. This would suggest that the effects were a result of inherent sample differences or furnace position, and that both the thermal and athermal effects were negligible at current densities of 10^7 A·m^{-2}.

Using Equation 3.18 (Methods pp.67) the temperature increase at ambient conditions of sample SB540-F680-EP-30, which achieved the highest current density value of $8.1\text{x}10^7$ A·m^{-2}, can be estimated at 0.02°C per pulse. Even taking into account an increase in resistivity due to the furnace

annealing,[25] the change in temperature generated by each pulse is estimated at only 0.08°C [197, 198]. These values are deemed insufficient to cause any variation in morphology due to thermal effects.

The athermal effect is more difficult to quantify, but it can be concluded that at the current densities applied the effect was not sufficient to alter the properties of the material either by independent mass transport or enhanced diffusion. Electromigration is known to occur at current densities in the region of 10^8 A·m^{-2} and above [199], half an order of magnitude higher than the majority of current density values obtained in this chapter. Electromigration due to pulsed electric current is also dependent on the time period over which the electric current is "on" and applied to the sample, and the frequency of pulses [200]. All tests in this chapter were conducted at a frequency of 1Hz and test duration of 30 minutes, which at a pulse duration of 80µs results in an applied current time of 0.144 seconds. A significantly longer treatment time may have induced an effect, as classical literature demonstrates through treatments in the order of days [124]. However, the electropulsing process is intended as an accelerating treatment and obtaining results at longer treatment times would have been impractical for this purpose. It would appear that the additional thermal driving force provided by the furnace did not facilitate the generation of lower current density athermal effects.

Some studies that demonstrate electropulsing effects also describe the interaction between the athermal "electron wind" and dislocations [10, 11, 119, 135], resulting in enhanced dislocation motion and therefore accelerated diffusion kinetics. The presence of dislocations within the crystal structure could therefore be an important factor affecting the success of current-induced microstructure change. The level of deformation in the steel samples must then be considered, both before treatment was initiated and during annealing. It is clear that inserting a deformed steel sample into a furnace at elevated temperature will reduce the volume of dislocations in the material through the process of recovery and recrystallisation [25]. This reduction may limit the effectiveness of the electric current to enhance diffusion by athermal methods. The literature shows that the effect of electropulsing treatments can in fact be altered by the level of prior deformation, with observations of enhanced cementite spheroidisation [7] and recrystallisation of copper [1] in variably deformed samples.

The initial drawing strain of the steel wire may also have limited the effectiveness of the electropulsing treatment. The deformation may not have been sufficiently severe to induce a high enough dislocation volume. Other studies that report electropulse-induced microstructure and/or mechanical property

[25] The increase in the resistivity of a metal ρ_T at elevated temperature T can be estimated using the equation $\rho_T = \rho_O\big(1 + \alpha(T - T_O)\big)$ where ρ_O is the resistivity at ambient temperature T_O and α is the temperature coefficient of resistivity (Rudnev *et al.*, 2002). SB540-F680-EP-30 was treated at 680°C, the ambient temperature was taken as 20°C and the ambient resistivity was experimentally determined to be 1.45x10^{-7} Ω·m. The temperature coefficient of resistivity was extrapolated from data available in Fischer (2009) relating to steel wire and is stated as 0.0048°C^{-1}.

effects were conducted on wires drawn to over 90% area reduction [7, 135, 201]. The wires tested in the current research were drawn to approximately 60% area reduction, and would be expected to contain a lower density of dislocations than those with significantly higher drawing reduction.

5.3.3. Limitations of the study

The experimental method was constrained by two key factors. The first relates to the sample dimensions, while the second involves applied current frequencies.

The material received from TATA Steel was pre-drawn to a diameter of approximately 2mm in all initial material conditions. As facilities for further drawing the wire were not available to the author, this resulted in a physical limitation on the maximum current density that could be applied to the samples during electropulsing. This current density was relatively low when compared to values obtained through cold rolling and milling of another steel composition. However, an important theme of the research described in this thesis was to ascertain whether low current density electropulsing could produce microstructural effects. Consequently, the experiments detailed in this chapter were completed with this hypothesis in mind.

Electropulsing at high frequency can produce very high temperatures as a result of Joule heating. It is also capable of producing sparks at the connection between wire and sample. It was determined that the most logical solution to these issues would be to conduct tests at the lowest possible frequency. This would not only remove health and safety issues associated with sparking at high frequencies, but also prevent electropulse-induced heating from affecting the results observed. Any athermal effects resulting from the electropulse treatment could then be confidently identified.

5.4. Summary

Samples of 0.73wt%C pearlitic steel wire in three initial microstructure configurations (still air cooled, forced air cooled and salt bath transformed) were subjected to simultaneous electropulsing and high temperature furnace annealing treatments. Furnace treatments ranged between 660 and 740°C, and electropulsing was conducted at current densities in the order of 10^7 $A{\cdot}m^{-2}$. The purpose of the experiments was to assess the capacity for low current density electropulsing to induce microstructure change with additional external driving force in the form of heat. The experiments did not reveal any consistent microstructure or mechanical property effects as a result of the electropulsing treatment when compared with control samples annealed at identical temperatures. This may have resulted from too low current density and therefore negligible athermal effect. Additionally, insufficient cold work prior to treatment may have limited the effectiveness of any athermal effect by reducing the volume of dislocations available for interaction with the so-called electron wind.

6. High current density electropulsing (non-UK)

6.1. Experimental parameters

Pearlitic steel plate of composition 0.92wt%C was cold-rolled to approximately 60% area reduction and milled to produce six samples of dimensions as described in Table 6.1. The samples were then transported to the Chinese Academy of Sciences (Hefei Institute of Physical Sciences) in Anhui, China by Prof. R.S. Qin. The electropulsing equipment at this location was significantly more powerful than that available to the author in the United Kingdom, and was able to consistently induce current densities of the order 10^9 A·m^{-2} in millimetre-scale samples. The purpose of the experiments was to assess whether a single powerful high current density electropulse could induce microstructure change in steel plate samples, and whether the mechanisms involved were purely thermal or contained an athermal component.

Table 6.1. Geometries of samples treated with a single electropulse at current density of the order 10^9A·m^{-2}.

Sample code	L (mm)	W (mm)	D (mm)	A (mm^2)
9-1-150-S-1	81.7	2.81	0.58	1.6
9-1-150-S-2	81.8	2.63	0.57	1.5
9-1-150-S-3	88.8	7.50	0.65	4.9
9-1-150-S-4	94.1	7.91	0.57	4.5
9-1-150-S-5	88.6	7.42	0.64	4.7
9-1-150-S-6	91.8	7.46	0.58	4.3

Each sample was treated with a single high current density pulse of electric current in an ambient environment, with a pulse duration of 150µs.[26] The current densities achieved ranged between 1.58 and 5.1x10^9 A·m^{-2}, and the samples were allowed to cool in air after treatment. The complete electropulsing parameters are detailed in Table 6.2. The samples were then returned to the UK, where electron microscopy and mechanical property testing were conducted by the author.

The heating effect generated in each sample can be estimated using the Joule heating equation, as derived in the Methods section, pp.67. As the treatments involved a single pulse, the equation has good validity. The results of the calculation are shown in Table 6.3, where ΔT is the temperature increase and T_{FINAL} the final temperature from ambient (taken as 23°C).

[26] Accurate pulse duration was not provided with the electropulsing data from the Hefei facility. The pulse duration stated here is estimated based on parameters from electropulsing literature originating from the same facility. Qin *et al.* (2011), Samuel *et al.* (2010).

Table 6.2. Electropulsing parameters for single pulse tests at current density J of the order 10^9 A·m^{-2}.

Sample code	Area reduction (%)	J ($x10^9$ A·m^{-2})	f (Hz)	d (µs)	N (#)
Control-1	65	-	-	-	-
9-1-150-S-1	65	4.7	1	150	1
9-1-150-S-2	65	5.1	1	150	1
Control-2	59	-	-	-	-
9-1-150-S-3	56	1.6	1	150	1
9-1-150-S-4	60	1.7	1	150	1
9-1-150-S-5	57	1.6	1	150	1
9-1-150-S-6	60	1.8	1	150	1

Table 6.3. Estimated Joule heating effect in single pulse tests at current density J of the order 10^9 A·m^{-2}.[27]

Sample code	J ($x10^9$ A·m^{-2})	ΔT (°C)	T_{FINAL} (°C)
9-1-150-S-1	4.7	241	264
9-1-150-S-2	5.1	284	307
9-1-150-S-3	1.6	28	51
9-1-150-S-4	1.7	32	55
9-1-150-S-5	1.6	28	51
9-1-150-S-6	1.8	35	58

6.2. Results

Microstructure change in the electropulsed samples was assessed using high resolution SEM, TEM and Atom Probe Tomography (APT). In addition, comparative resistive heating treatments were carried out on samples of the same composition and rolling reduction using a Dynamic Systems Inc. Gleeble 3800. The associated backscatter imaging and heating profiles are reported.

6.2.1. Electron microscopy microstructure characterisation

6.2.1.1. Scanning Electron Microscopy

Electropulsing treatment was observed to induce microstructure change in two of six samples, 9-1-150-S-1 and 9-1-150-S-2. Sample 9-1-150-S-1 was found to contain regions of both spheroidised cementite and recrystallised ferrite after treatment of a single electropulse of current density 4.7x10^9 A·m^{-2}. Figure 6.2 C-F shows high resolution SEM imaging of sample 9-1-150-S-1, with the control sample microstructure also presented for comparison (Figure 6.2 A,B).

The cementite spheroidisation observed in Figure 6.2 C and D was found to be in varying states of transformation. The microstructure after electropulsing contained regions of both fully spherical

[27] Resistivity was taken as 2.8x10^{-7} Ω·m, specific heat capacity 490 J·kg^{-1}·K^{-1}, density 7850kg·m^{-3} and pulse duration 150µs.

grains and partially transformed grains, emerging from fragmented cementite lamellae (see Figure 6.1). Both fine (Figure 6.2 C) and coarse (Figure 6.2 E) spheroidisation was present. The fully separated and spheroidised cementite was measured to have an average major axis length of 109nm (standard deviation of 107nm, ranging between 11 and 579nm) and aspect ratio 1.7±0.7 (n = 259).

The regions of recrystallised α-ferrite were visible due to the presence of carbon at the grain boundaries, which allowed the nital etch to delineate the ferrite. The grains were measured to have an average major axis length of 423±148nm and aspect ratio of 1.6±0.5 (n = 103). The recrystallised ferrite can be described as equiaxed as the aspect ratio was close to 1. The volume fractions of fragmented or spheroidised (partial or full) cementite, recrystallised ferrite and unchanged lamellar pearlite are summarised in Table 6.4.

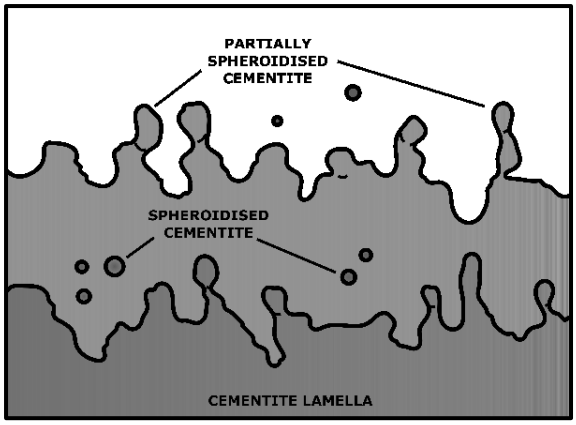


Figure 6.1. Schematic showing full and partial spheroidisation in cementite lamellae.

Table 6.4. Volume fraction analysis of sample 9-1-150-S-1 treated with a single electropulse of current density 4.7x10^{9} A·m^{-2}.

Morphology	Volume fraction
Lamellar pearlite	0.49
Spheroidised / fragmented cementite	0.29
Recrystallised ferrite	0.22

The microstructure of sample 9-1-150-S-2 is shown in Figure 6.3. After treatment with a single electropulse of current density 5.1x10^{9} A·m^{-2} the sample was found to have transformed from lamellar pearlite to martensitic laths. The current density applied to the sample was 8.5% higher than that applied to 9-1-150-S-1 which induced annealing-associated morphologies. The temperature increase induced in the martensitic sample 9-1-150-S-2 was consequently higher than that of the annealed 9-1-150-S-1. However, as shown in Table 6.3 the temperature of all samples estimated via the Joule heating equation did not exceed 307°C. This is clearly unusual, as the austenitisation temperature of the 0.92wt%C steel has been experimentally determined to be in excess of 720°C. After austenitisation a combination of high-rate heating and air cooling could have then produced sufficient undercooling to induce a diffusionless martensitic transformation.

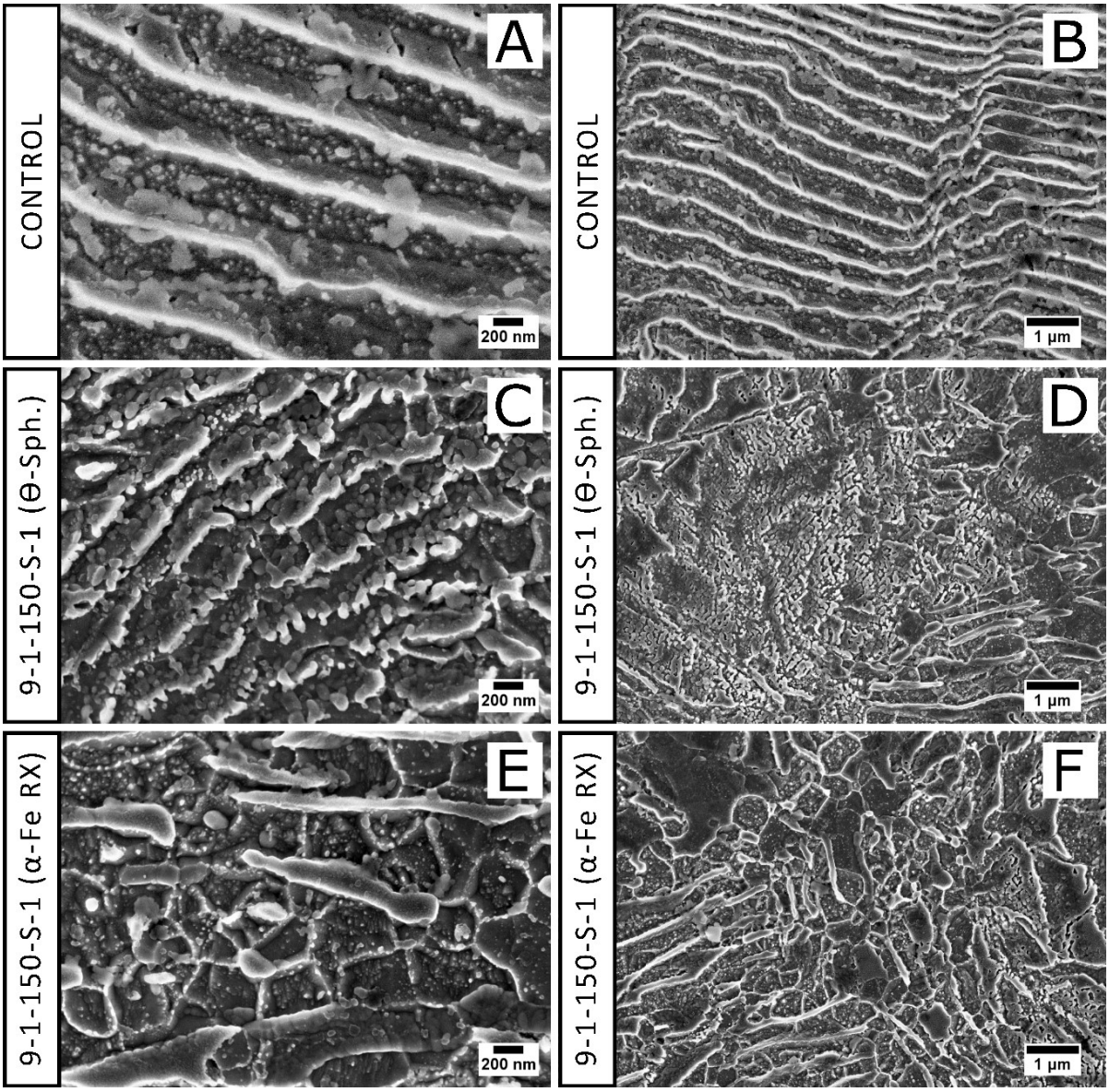


Figure 6.2. 0.92wt%C pearlitic steel treated with a single electropulse at $4.7x10^9$ A·m^{-2}. A,B) control sample, as-received cold-rolled; C,D) spheroidised cementite in electropulsed sample; E,F) recrystallised α-ferrite in electropulsed sample. Secondary electron imaging on samples etched in 2% nital solution (methanol balance).

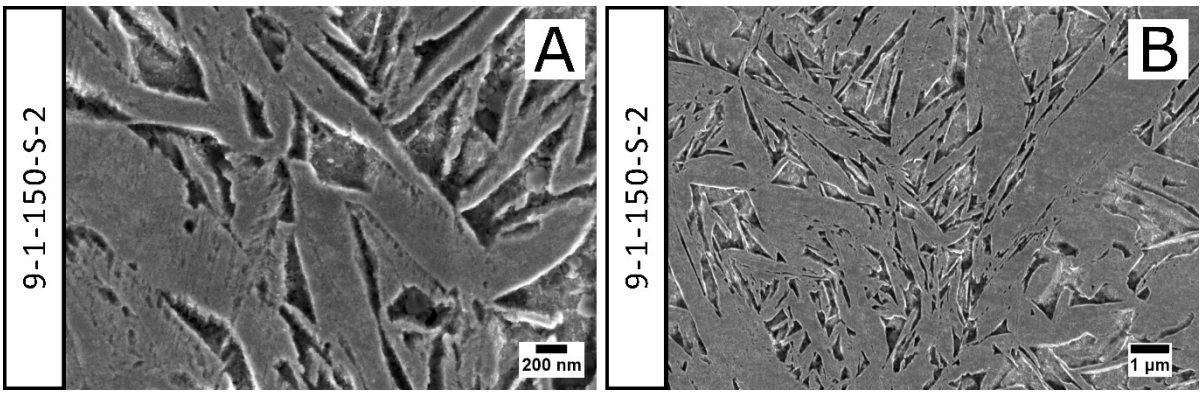


Figure 6.3. 0.92wt%C pearlitic steel treated with a single electropulse at $5.1x10^9$ A·m^{-2}, producing a fully martensitic microstructure. Secondary electron imaging on samples etched in 2% nital solution (methanol balance).

It is important to highlight a critical aspect of the results observed here. The spheroidisation, recrystallisation and austenitisation transformations are all diffusive, and therefore typically require heating for a certain duration before any effects can be observed. The microstructures found in two of the electropulsed samples were achieved with a single pulse, of pulse duration 150µs. This treatment time is significantly shorter than those typically used to obtain similar microstructures through furnace annealing. Spheroidisation treatments in some steels are known to require treatments up to 12 hours in duration [202]. In addition, the temperatures estimated by the Joule heating equation are significantly lower than those traditionally associated with the microstructures obtained [139]. Further discussion on the mechanisms for this accelerated microstructure transformation will be discussed in section 6.3.2.

No evidence of microstructure change was visible in the remaining four samples. As they were treated at lower current densities than samples 9-1-150-S-1 and 9-1-150-S-2 (but still of the order 10^9 $A{\cdot}m^{-2}$) it is likely that the driving force provided by the electropulsing treatment was not sufficient to induce transformation. The final temperatures estimated to have been generated by the electropulsing treatments associated with these samples did not exceed 58°C (Table 6.3). Further discussion on the variations associated with the treatment parameters applied will be given in section 6.3.2.

6.2.1.2. Transmission Electron Microscopy

Transmission Electron Microscopy (TEM) was used to further analyse and confirm the nature of the recrystallised α-ferrite grains observed through SEM imaging. The results of this analysis are shown in Figure 6.4, which includes TEM imaging of a control sample (top) and sample 9-1-150-S-1 (bottom). Selected Area Diffraction (SAD) patterns are also included for each image. A comparison of the TEM images clearly shows a microstructure of unbroken lamellar pearlite in the control sample, while the electropulsed sample is granular. The darker, narrower cementite lamellae are broken and intersected by equiaxed grains, strongly indicating that α-ferrite recrystallisation has occurred.

Contrast in TEM imaging of crystalline materials results from defects in the crystal lattice, phase variations, foil bending and thickness, and diffraction contrast. Both defects and phases alter the locally generated electron diffraction intensity in the region of the feature, leading to contrast in the TEM image [158]. As the phase composition of the steel shown in Figure 6.4 is known, the phases and regions of deformation can be differentiated.

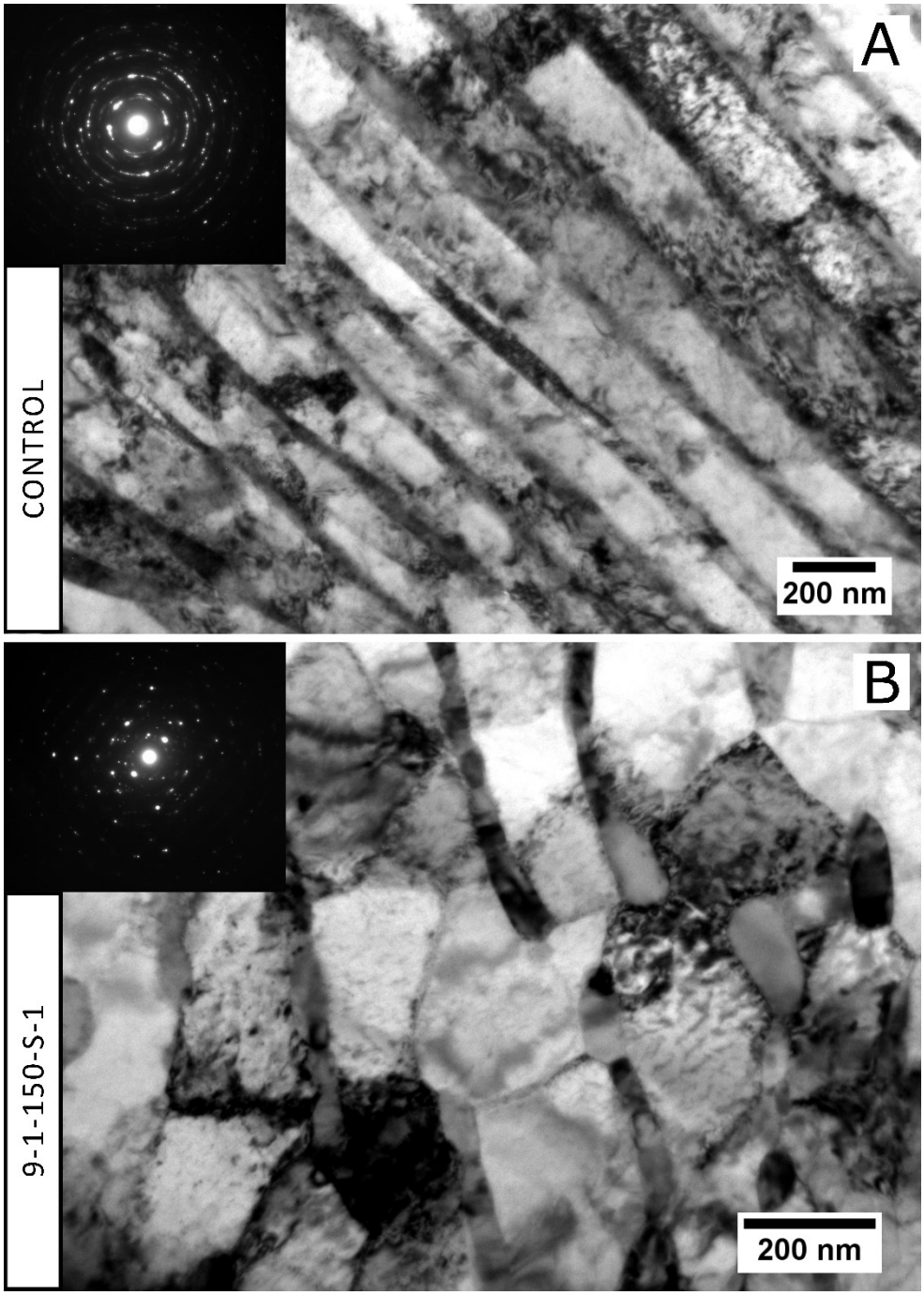


Figure 6.4. Transmission Electron Microscopy of 0.92wt%C pearlitic steel. A) as-received, cold-rolled lamellar microstructure; B) recrystallised α-ferrite in sample electropulsed at 4.7x10^{9} A·m^{-2}. Inset: associated Selected Area Diffraction patterns.

Between the dark cementite lamellae in the control sample image (A) defects can be identified as dark regions inside the lighter ferrite lamellae. Similarly areas of deformation can also be observed in the electropulsed sample, as well as ferrite grains that vary in contrast. This effect results from diffraction contrast caused by orientation variations between the grains. Additionally, the short electropulse treatment time may have prevented significant strain reduction through limited diffusion-based dislocation motion.

The SAD patterns are less indicative, as both show relatively well-defined diffraction rings containing many small grains. Both are consistent with patterns observed in polycrystalline materials, which produce more continuous and clear ring patterns the greater the volume of grains contained in the material [158]. The diffraction pattern associated with the cold-worked control sample appears slightly more continuous, which may be a result of deformation-induced phase fragmentation. Large deformations have been found to cause cementite decomposition in pearlitic steel, and formation of cell and subgrain boundaries in ferrite. The lamellar structure remains visible at very high deformations because a saturation limit exists for the decomposition process [109]. The effect can be difficult to observe through TEM imaging due to the atomic-scale nature of the cementite decomposition, and has been reported in the literature using APT. Deformation-induced phase decomposition in the control sample combined with grain growth in the electropulsed sample may have produced the variation observed in the crystalline SAD patterns.

6.2.2. Mechanical properties

The mechanical properties of the electropulsed samples were assessed through Vickers hardness testing. The results are summarised in Table 6.5. No significant variation was observed between control sample 2 and electropulsed samples 9-1-150-S-3 to 9-1-150-S-6.[28] The average values were measured to be between 444 and 464HV_{10} and the regions of error of the four electropulsed samples and control sample were indistinguishable from each other. This behaviour was expected based on SEM imaging, which showed no microstructure variation between the samples.

Similarly, control sample 1 and electropulsed sample 9-1-150-S-1 were closely comparable. The average values were 465 and 469$HV_{0.5}$ respectively, giving a difference of only 4HV. The regions of error were also comparable and overlapped. As cementite spheroidisation and α-ferrite recrystallisation were observed in sample 9-1-150-S-1 it was expected that some hardness variation between it and the control sample could have been observed. In this case a reduction of hardness was expected, due to the reduction of mechanical strain by microstructure reconfiguration. The lack of significant hardness variation in the results suggests that the microstructure transformation was limited to small regions, and was not significant enough to affect the bulk mechanical properties of the steel.

A significant change in hardness was measured in sample 9-1-150-S-2, with the average measured value recorded as 931±40$HV_{0.5}$. This is a large increase on the control sample hardness of 465±22$HV_{0.5}$, and is characteristic of a martensitic transformation as described in Chapter 4 [177, 178]. As the main

[28] Control sample 2 is used for comparison with samples 9-1-150-S-3 to 9-1-150-S-6 due to the comparable rolling reductions. Similarly, control sample 1 is compared with samples 9-1-150-S-1 and 9-1-150-S-2.

focus of this project was on the annealing microstructures of spheroidisation and recrystallisation, this hardness value was used as an indicator of the martensitic phase and no further testing was conducted on sample 9-1-150-S-2.

Table 6.5. Vickers hardness characteristics of 0.92wt%C pearlitic steel samples treated with a single high current density electropulse with current density J of the order 10^9 A·m^{-2}.

SAMPLE CODE	Area reduction *(%)*	DESCRIPTION	HV_{10}
Control-1	65	Deformed lamellar	465±22*
9-1-150-S-1	65	Recrystallised α-ferrite	469±21*
9-1-150-S-2	65	Martensite	931±40*
Control -2	59	Deformed lamellar	456±8
9-1-150-S-3	56	Deformed lamellar	464±6
9-1-150-S-4	60	Deformed lamellar	455±9
9-1-150-S-5	57	Deformed lamellar	451±10
9-1-150-S-6	60	Deformed lamellar	444±6

*$HV_{0.5}$

6.2.3. Confirmation of morphology change using Atom Probe Tomography

Atom Probe Tomography (APT) was employed in order to understand the distribution of elements in the electropulsed sample 9-1-150-S-1 and confirm the microstructure changes observed through SEM and TEM analysis. APT is used to pinpoint the 3D location of individual atoms in a sample using time-of-flight spectroscopy, and has been applied successfully in the literature to analyse pearlitic samples [4, 109, 203]. The process is described in full in Methods section 3.5.2.5. Several small sections were extracted at random from 9-1-150-S-1 using a FEI Helios NanoLab DualBeam 600 FIB system and milled into fine needle-shaped samples as shown in Figure 6.5 A.[29] The samples were then transported to the University of Oxford where APT analysis was conducted using a Local Electrode Atom Probe (LEAP) 3000X HR.[30] Three samples were tested, one of which failed during the APT analysis. The second and third samples completed successfully and detected cementite spheroids (both samples) and a grain boundary (one sample).

[29] APT sample milling was carried out by Dr. Anna Radecka using a customised preparation method. At the time of the experiment Dr. Radecka was a PhD student at Imperial College London working in the Department of Materials, conducting research with the APT group at the University of Oxford.

[30] APT analysis was conducted at the University of Oxford by Dr. Tomas L. Martin, in collaboration with Dr. Paul A.J. Bagot and Dr. Michael P. Moody. Dr. Anna Radecka was responsible for post-processing of the APT data and facilitated access to the University of Oxford group. Access to the APT facilities are restricted to fully trained members of the APT group at the university. The facilities are located in the Hume-Rothery Building of the Department of Materials (Parks Road, Oxford). Further information can be obtained from http://atomprobe.materials.ox.ac.uk/.

3D atomic reconstructions of the sample containing both spheroidisation and a grain boundary are shown in Figure 6.5. The needle before APT treatment is shown in Figure 6.5 A and the bulk reconstruction of all detected elements is shown in Figure 6.5 B. Individual atomic distributions of the elements known to comprise the 0.92wt%C steel are shown in Figure 6.5 C - H.

The 3D reconstructions show a high concentration of carbon in three regions – two spherical cementite particles and a grain boundary joining them. This is particularly clear in Figure 6.5 C, where a lower concentration of carbon in the bulk material can be seen. Increased concentrations of manganese and vanadium at the spheroidised grains was also observed. Segregation of elements during annealing treatments is well documented, and manganese and vanadium are known to have high solubility in cementite [139]. Partitioning of manganese into spheroidised cementite due to a solubility gradient has previously been observed through APT treatment [203]. Some phosphorus segregation to the grain boundary and carbide interface was also observed.

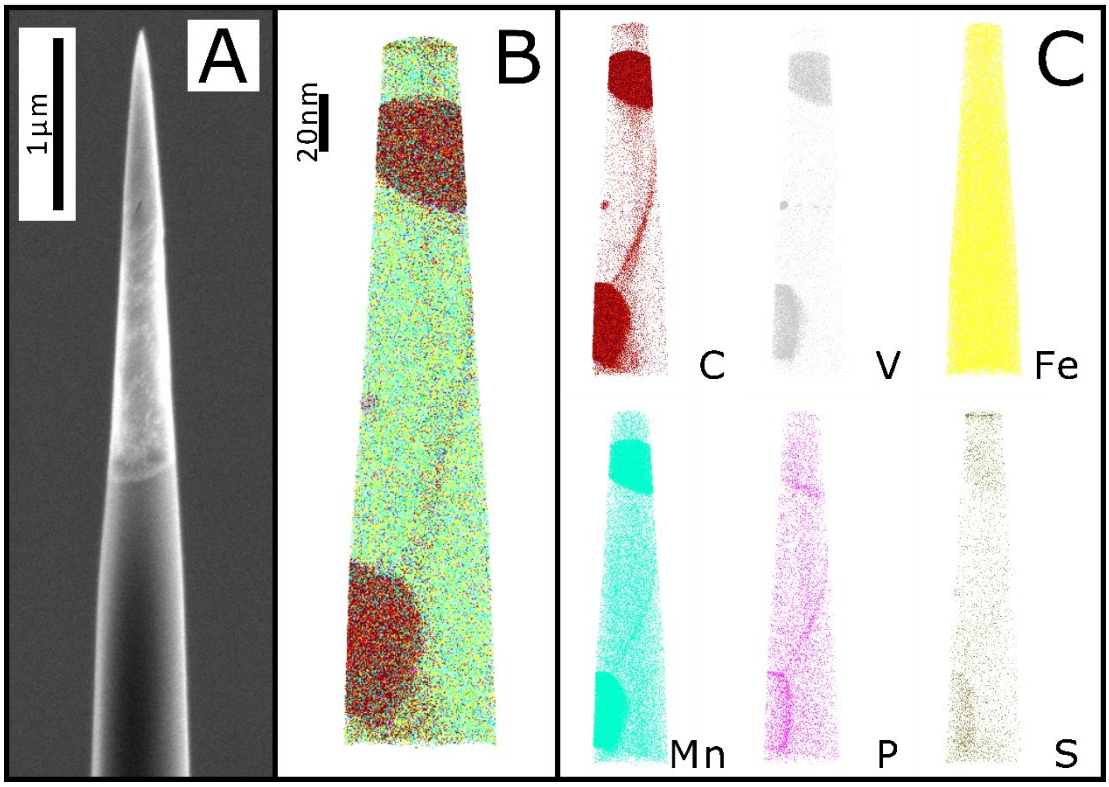


Figure 6.5. Atom Probe Tomography (APT) of 0.92wt%C pearlitic steel electropulsed at $4.7x10^{9}$ $A{\cdot}m^{-2}$. A) SEM imaging of APT needle after preparation in a Helios NanoLab 600. B-C) APT reconstruction of element distribution in needle (A). B) all elements; C) carbon; vanadium; iron; manganese; phosphorus; sulphur.

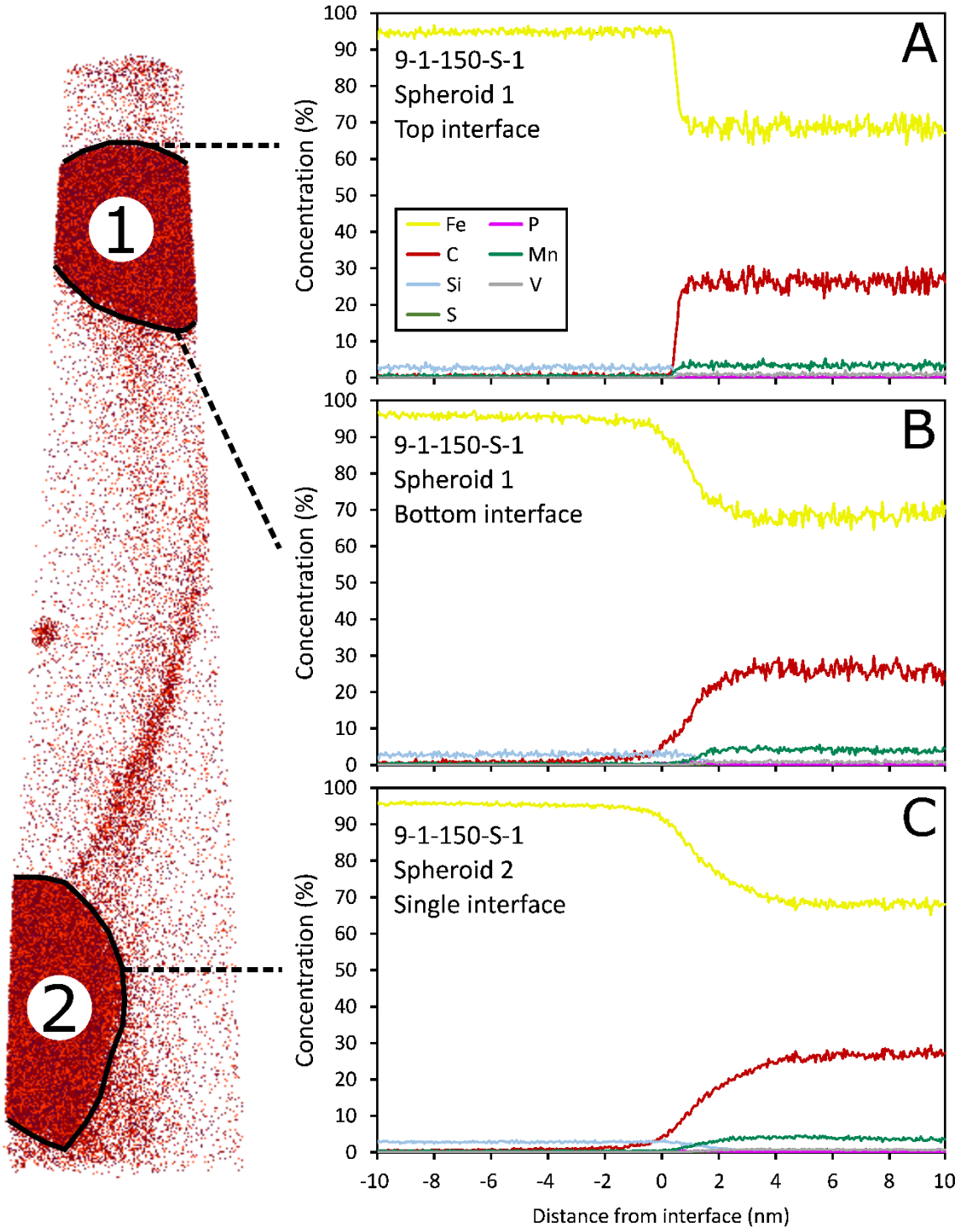


Figure 6.6. Proxigrams showing composition change at the interface between spheroidised cementite and the bulk matrix in 0.92wt%C steel after electropulsing at 4.7x10^{9} A·m^{-2}. The plots are shown in combination with the carbon distribution as shown in Figure 6.5 C, and the interfaces are highlighted.

Figure 6.6 shows proximity histograms, or proxigrams, for sample 9-1-150-S-1. The proxigrams show the change in composition at the interface between the carbon-rich grains and bulk matrix by plotting percent composition against distance from the interface. At each interface it can be seen that the concentration of ferrite drops, to be replaced by carbon. An increase in manganese at the interface is also observed. The proxigrams indicate the presence of a grain boundary, confirming that the carbon-rich particles shown in Figure 6.5 C are in fact spheroidised cementite. Note that the slope of the transition zone between the two regions is determined by the angle of the interface. A more curved surface will produce a less severe transition, as shown in Figure 6.6 B and C.

A proxigram could not be generated for the grain boundary joining the two spheroidised cementite grains. However, the compositional analysis clearly shows a peak in carbon, phosphorus and manganese along the length of the feature. Segregation of alloying elements to grain boundaries is a well-established phenomenon and occurs as a result of a free energy imbalance in the material system [204-206]. Equilibrium segregation refers to reduction in free energy by reducing local lattice strain resulting from over- or under-sized atoms relative to the matrix. Non-equilibrium segregation describes vacancy-element interactions and pile-up during rapid cooling, causing a concentration gradient at the grain boundary [142, 207]. The presence of a concentration gradient of multiple elements along a linear feature as observed in Figure 6.5 C is a strong indication that the feature is a grain boundary.

APT successfully confirmed that sample 9-1-150-S-1 contained both spheroidised cementite and non-lamellar ferrite grain boundaries after electropulsing treatment.

6.2.4. Resistive heating microstructure comparison

In order to more accurately compare the effects of electropulsing with other high rate heating methods, a Dynamic Systems Inc. Gleeble 3800 resistive heating unit was employed to treat five cold-rolled 0.92wt%C steel samples.[31] The experimental setup inside the Gleeble chamber is shown in Figure 6.7, and further information on the equipment used is included in the Methods section, pp.68. The samples and treatment parameters are described in Table 6.6. Sample GL 1 was used to calibrate the Gleeble equipment.

The dimensions of Gleeble samples 2 to 5 were comparable to those of samples 9-1-150-S-1 and 9-1-150-S-2. In short duration tests such as those undertaken here, it is more difficult to control the heating parameters using the Gleeble 3800. As a result a range of temperatures and heating rates

[31] Gleeble experiments were conducted in the Department of Mechanical Engineering at Imperial College London. As access to the equipment is restricted the experiments were carried out by postgraduate researcher Kang Ji, with the permission of research fellow Dr. Zhusheng Shi. The author was able to observe the experiments and data collection. More information can be found at http://www.imperial.ac.uk/avic-design/equipment/.

were achieved. The maximum peak temperature, heating and cooling rate all occurred during treatment of sample GL 4. However, the temperature profile of GL 5 was more uniform and the heating characteristics were similar between the two samples. As a result, GL 5 was selected as an appropriate candidate for comparison with the electropulsed samples.

The heating parameters associated with GL 5 (or any of the samples in Table 6.6) are not a perfect comparison for the electropulsing parameters applied to samples 9-1-150-S-1 and 9-1-150-S-2 (summarised in Table 6.7). The peak temperature of the Gleeble samples was 655°C, 348°C hotter than the highest estimate of electropulse-induced Joule heating. Furthermore the heating rate applied to the Gleeble samples was of the order 10^3 °C·s^{-1}, several orders of magnitude smaller than the electropulsing Joule heating rate of 10^6 °C·s^{-1}.[32] The cooling rates cannot be compared, as the values are not known for the electropulsed samples.

Table 6.6. Gleeble sample treatment parameters. The heating rate to T_{PEAK} (dT_{PEAK}/dt) and cooling rate from T_{PEAK} to T_{COOL} (dT_{COOL}/dt) are shown.

Sample code	**Area reduction** *(%)*	**L** *(mm)*	**W** *(mm)*	**D** *(mm)*	**A** *(mm^2)*	**T_{PEAK}** *(°C)*	**dT_{PEAK}/dt** *(°C·s^{-1})*	**T_{COOL}** *(°C)*	**dT_{COOL}/dt** *(°C·s^{-1})*
GL 1	--- Calibration sample ---								
GL 2	77	87.1	2.0	0.84	1.7	462	656	209	13
GL 3	77	87.3	2.0	0.81	1.6	545	790	181	18.6
GL 4	77	87.0	2.0	0.79	1.6	655	7906	123	26.4
GL 5	77	87.1	2.0	0.83	1.7	634	2919	115	25.9

However, the comparison of Gleeble and electropulse-induced microstructures provides some indication of the mechanisms involved in the observed transformations. The electropulsed samples have a high heating rate but low peak temperature, while the Gleeble samples have a lower heating rate but higher peak temperature. As such, the experiment can be used to indicate whether the heating rate is critical, or whether temperature can induce the same effects.

Figure 6.8 A and B shows backscatter imaging of sample GL 5, while C shows the applied heating profile. Backscatter imaging was selected for the Gleeble sample analysis, in order to more clearly delineate any recrystallisation or grain growth that may have occurred. From the images it can clearly be observed that the microstructure has maintained its lamellar structure. The cementite lamellae appear darker and are thinner than the lighter ferrite lamellae. Regions of darker contrast inside the ferrite lamellae are also visible. Contrast in backscattered electron imaging varies with surface topography, orientation and phase composition [158], and as such these darker regions could result

[32] The maximum heating rate of the Gleeble 3800 (depending on sample dimensions and material) is 10000 °C·s^{-1} (*Gleeble® 3800 System*. Dynamic Systems Inc. (2015) Online resource accessed on 04/08/2016 at http://gleeble.com/products/gleeble-3800.html).

from localised orientation variations or dislocations due to the cold work applied before Gleeble treatment. Rolling kinks are also still visible in the lamellae, particularly in Figure 6.8 A.

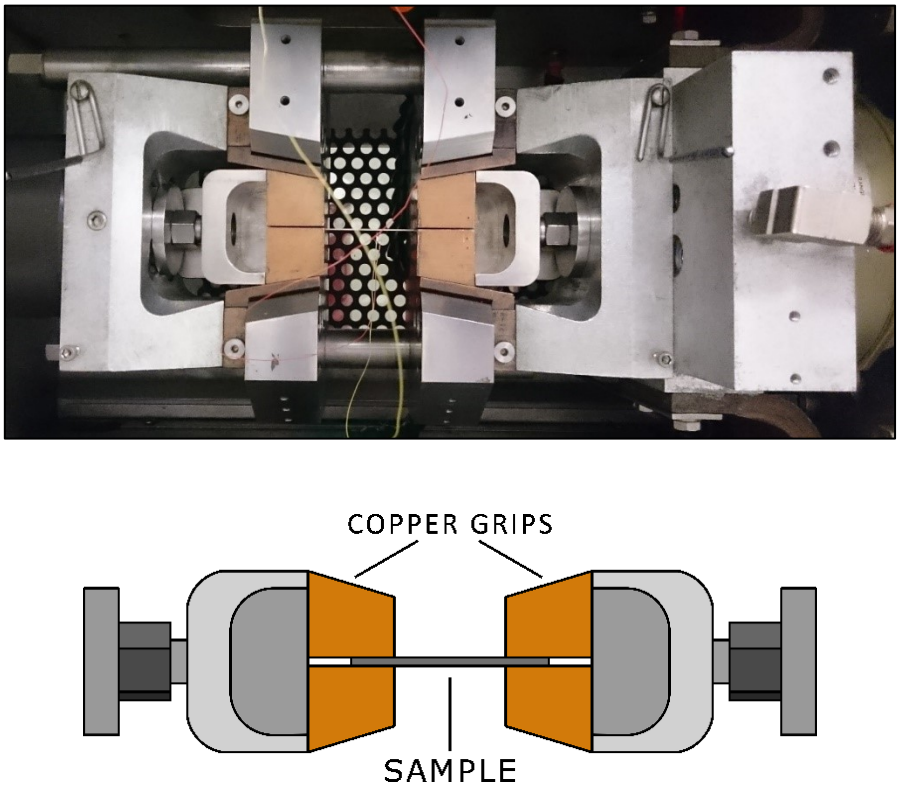


Figure 6.7. Gleeble 3800 experimental setup (top). The steel sample is held between two clamps, through which resistive heating is applied (bottom).

Table 6.7. Electropulsing and Gleeble parameter comparison.

Sample code	**T_{PEAK}** *(°C)*	**dT_{PEAK}/dt** *(°C·s^{-1})*	**dT_{COOL}/dt** *(°C·s^{-1})*
9-1-150-S-1	264	1,610,000	-
9-1-150-S-2	307	1,890,000	-
GL 4	655	7906	26.4
GL 5	634	2919	25.9

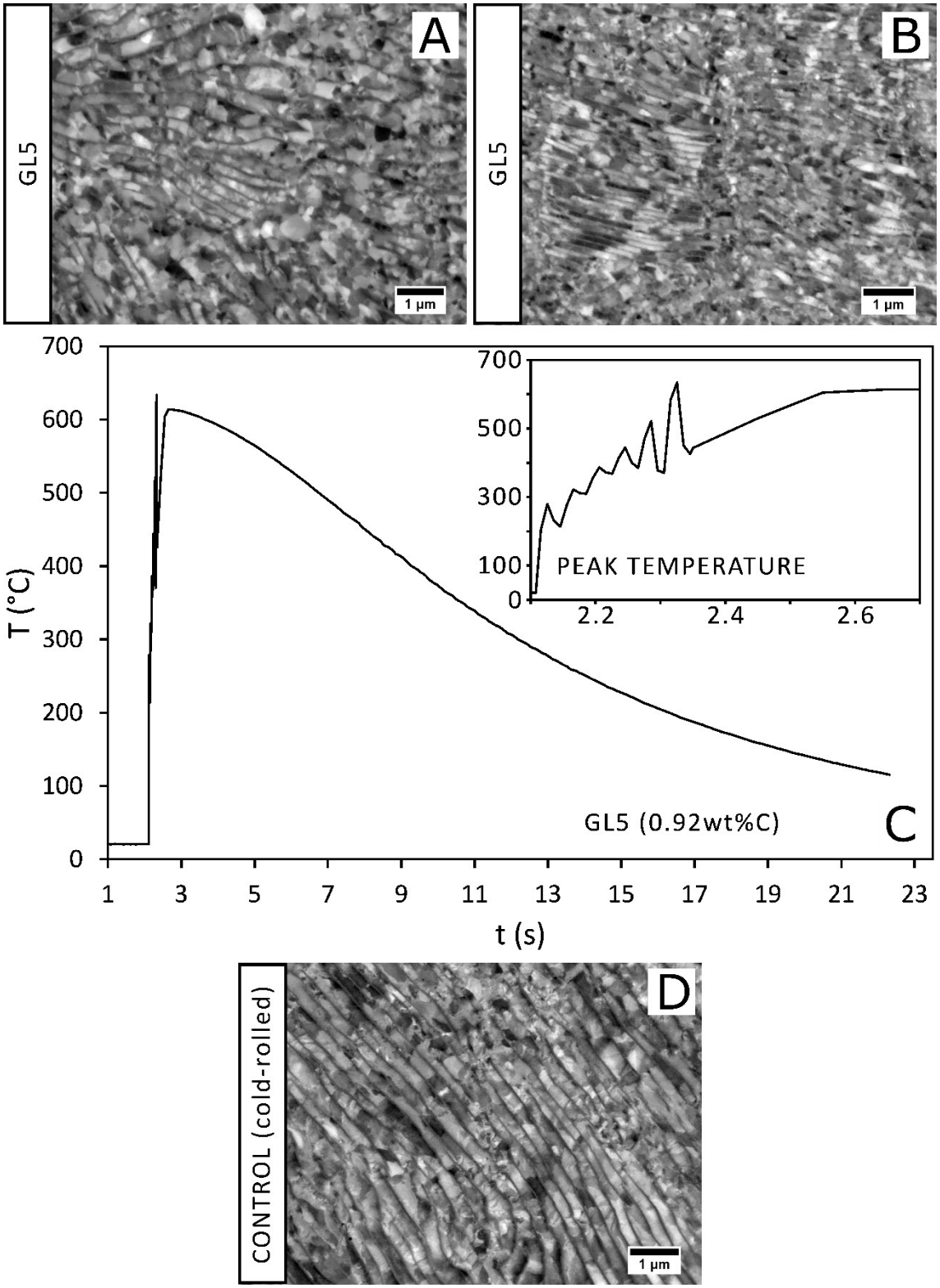


Figure 6.8. 0.92wt%C pearlitic steel heat treated in a Gleeble 3800 (Dynamic Systems Inc.) resistive heating unit to a peak temperature of 634°C. A,B) Backscatter electron imaging of post-treatment lamellar microstructure; C) Heating profile showing temperature time relationship. Inset: detail of peak temperature region; D) backscatter imaging of a control cold-rolled sample.

Evidence of equiaxed ferrite grains was observed in sample GL 5, where misorientation between grains is reflected by contrast variations. Regions of GL 5 were observed to contain small pockets of misoriented equiaxed grains, within the ferrite lamellae. The subgrains are highlighted in Figure 6.9 and resemble those observed in the electropulsed sample 9-1-150-S-1. The presence of equiaxed ferrite in sample GL 5 suggests that Gleeble resistive heating can induce similar microstructures to electropulsing treatments, indicating that the major driving force for transformation in both cases may be Joule heating.

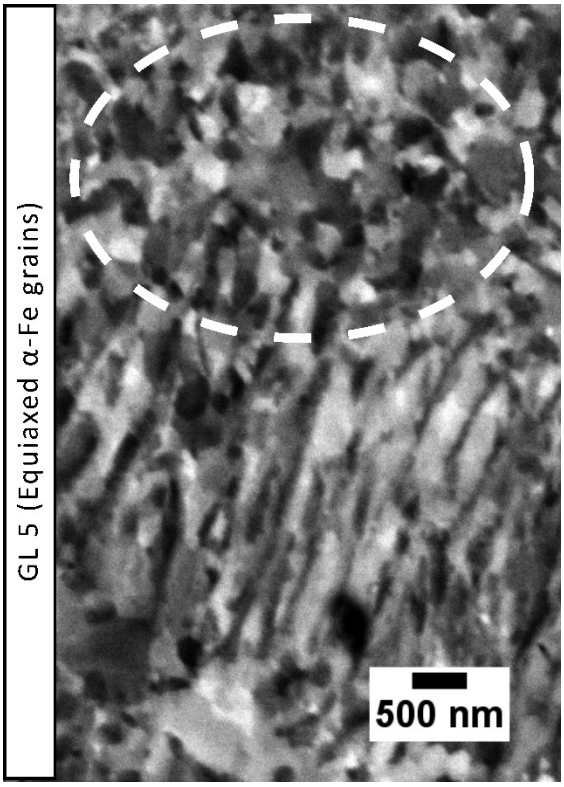


Figure 6.9. Backscatter electron imaging of sample GL 5 showing lamellar and equiaxed regions. Equiaxed grains are circled.

TEM examination of the microstructure confirmed the presence of equiaxed grains, as shown in Figure 6.10. The two regions shown are closely comparable to those found in the electropulsed sample (Figure 6.4). Sections of the lamellar microstructure were visible but disrupted by the presence of angular equiaxed grains of varying contrast, which are particularly evident in Figure 6.10 B. The selected area diffraction patterns were found to contain numerous reflections and were characteristic of polycrystalline material.

The average microhardness of the GL5 sample containing equiaxed ferrite grains was measured to be 505±9HV_2. This value is slightly higher than that of the electropulsed sample and is accounted for by the marginally higher rolling reduction of the Gleeble-treated sample. The average as-received cold-rolled hardness of the Gleeble sample material was 503±45HV_1, a difference of only 2HV. This behaviour is comparable to that observed in the electropulsed sample, which saw little variation between the as-received cold-rolled and electropulsed materials. As stated previously, the lack of hardness variation suggests that the microstructure changes observed were not sufficiently widespread to have a significant effect on the bulk mechanical properties.

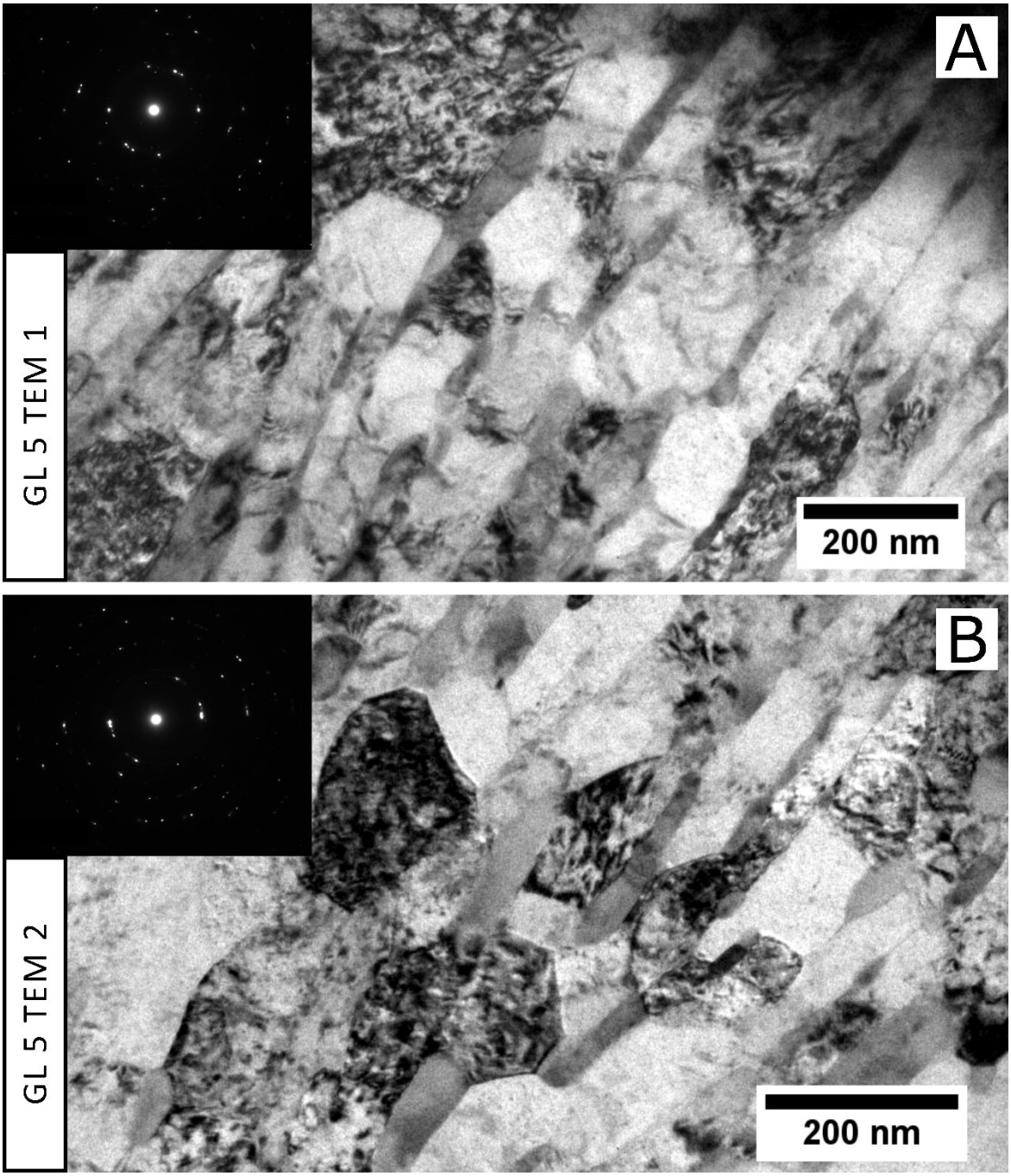


Figure 6.10. Transmission Electron Microscopy of recrystallised grains in 0.92wt%C pearlitic steel sample GL5, subjected to resistive heating in a Gleeble 3800. Inset: associated Selected Area Diffraction patterns.

6.3. Discussion

6.3.1. Driving force for transformation

The results described in the preceding pages showed that high current density single pulse electropulsing treatment can induce microstructure change in pearlitic steel samples. Of the six samples tested, no change was observed in four. The remaining two were found to contain martensitic or spheroidised and recrystallised microstructures. The treatment parameters applied give a clear indication of current density as a key parameter. At current densities lower than 1.8×10^{9} $A \cdot m^{-2}$, no

microstructure effects were visible. When the current density increased to $4.7x10^9$ $A{\cdot}m^{-2}$, subcritical annealing microstructures including recovered and partially recrystallised α-ferrite grains were formed. At a current density of $5.1x10^9$ $A{\cdot}m^{-2}$, a martensitic transformation occurred. Microstructure change was observed in only the highest current density conditions.

The pulse frequency, duration and number were identical between treatments, and the rolling reduction in each case was high (between 56 and 65% cross-sectional area reduction). Current density was the only significantly varied parameter and as a result is identified as the critical driving force for transformation in single pulse electric current treatments.

6.3.2. Mechanisms of accelerated microstructure transformation

Current density was the key factor in determining the occurrence and form of microstructure change in the pearlitic steel samples. However, it is less simple to identify the mechanisms involved in the electropulsing treatment. It is useful here to restate the phenomena observed in the two samples 9-1-150-S-1 and 9-1-150-S-2:

- Spheroidised and recrystallised microstructure was induced in sample 9-1-150-S-1 by a single electropulse with estimated Joule heating of 241°C (final T = 264°C).
- A martensitic transformation was induced in sample 9-1-150-S-2 by a single electropulse with estimated Joule heating of 284°C (final T = 307°C).
- The duration of each electropulse was 150µs.
- No effects were visible in four samples treated with electropulsing that induced Joule heating of 35°C or less.

The microstructure changes observed occurred at significantly lower temperatures and treatment times than those normally associated with diffusive transformations [202]. The treatment therefore appears to have accelerated both the spheroidisation and austenitisation transformations. The theoretical diffusion distance of carbon in α-ferrite produced by electropulse-induced heating can be calculated using Equations 6.1 and 6.2, where D is the diffusion coefficient ($m^2{\cdot}s^{-1}$), D_o a material-specific diffusion constant ($m^2{\cdot}s^{-1}$), Q the activation energy ($J{\cdot}mol^{-1}$), R the gas constant, T the absolute temperature (K), r the radial diffusion distance of an atom from origin (m) and t the time (s) [25].

$$\ln(D) = ln(D_o) - \frac{Q}{R}\left(\frac{1}{T}\right) \qquad 6.1$$

$$r = 2.4\sqrt{Dt} \qquad 6.2$$

Under the electropulsing parameters described for sample 9-1-150-S-1 (T = 264°C, t = 150µs) with a diffusion coefficient of $6.2x10^{-7}$ $m^2 \cdot s^{-1}$ and activation energy of 80 kJ·mol, the diffusion distance of carbon in the steel is calculated to be 3.0nm. For sample 9-1-150-S-2, this distance is increased to 5.8nm.

Short duration diffusive transformations are documented in the literature, but tend to involve standard annealing temperatures. For example, rapid austenitisation has previously been reported in the literature as early as 1967. Wallbridge and Parr [131] also used resistive heating to produce martensitic structures in low carbon steels using a direct current generated by battery storage equipment. Samples were heated at a rate of approximately $1000°C \cdot s^{-1}$, held at 975°C for 0.5 seconds and quenched to produce a cooling rate of more than $2000°C \cdot s^{-1}$. Grange [208] used lead bath heating to produce martensitic microstructure in steels with varying carbon compositions, including a 0.99wt%C steel. In each steel composition a treatment of 20 seconds duration produced austenitisation, with the completeness of the transformation affected by carbon composition and hence temperature. The temperatures applied through the lead bath ranged between 810 and 925°C, and the samples were 5 x 12 x 25mm. A later investigation on flash processing of 0.21wt%C steel sheets by Lolla *et al.* [209] also found that rapid heat treatments using either electrical induction or oxypropane flame could induce austenitisation, leading to a microstructure of martensite, bainite and carbides. The dwell time at the peak temperature of 1100°C (measured for induction flash processing) was 2 seconds.

Techniques for accelerated spheroidisation using induction heating are also found in the literature. Hauserova *et al.* [210] applied a pulsed induction treatment to 0.98wt%C bearing steel at various heating rates and intercritical holding temperatures, achieving spheroidised microstructure in two to three minutes at the highest heating rate.

The literature shows that short duration annealing treatments are not unusual, and that various microstructures can be achieved at elevated temperatures. The low temperature transformations observed in samples 9-1-150-S-1 and 9-1-150-S-2 must then become the focus of investigation. Alloying elements [139, 211] are known to affect the spheroidisation and austenitisation transformations, but this is not a variable in this study. Similarly, cold work can accelerate the spheroidisation of cementite [212] but the deformations applied to the samples here are comparable. The mechanism of the low temperature transformations cannot be accurately identified from the results obtained, but some speculation can be made on their nature.

Previous research in the literature has described electropulse-induced effects through the thermal and athermal components [10, 11, 119, 135]. The combination of heat and electron-crystal lattice

interactions was thought to enhance dislocation motion and diffusion of elements. High rate heating would provide the driving force for the transformation, while athermal interactions would reduce the transformation temperature by enhancing the diffusive capacity of the material. The athermal effect would enhance diffusion via momentum transfer between accelerated electrons and components of the crystal lattice. A higher current density would introduce a larger volume of electrons per cross-sectional area of sample, producing a greater number of electron-atom collisions. The martensitic 9-1-150-S-2 sample was treated with a higher current density than the annealed 9-1-150-S-1 sample, and therefore may have experienced not only a higher thermal effect but also a greater athermal diffusion enhancement effect to achieve austenitisation.

The heating rate associated with the treatments may also be significant. An extremely rapid heating rate as shown in Table 6.7 can produce thermal shock. A rapid temperature increase can produce stress in a material [213] due to localised thermal expansion gradients, and could provide an increased driving force for energy equilibrium transformations such as spheroidisation. Note that the skin effect (current crowding at the surface of the conductor due to internal induction effects) is not a contributing factor in the results observed. The skin effect can produce increased surface heating in high frequency AC circuits featuring large conducting samples [214]. As the electropulsing treatment is applied through capacitor discharge and the sample size is small, the skin effect does not affect the microstructure.

6.3.3. Repeatability of results

Six samples were subjected to electropulsing treatments, of which two were successfully transformed. The dependence of electropulse-induced microstructure change on current density was clear, with transformations occurring only in the highest current density samples. However, the equipment used to produce electric current pulses is problematic. The pulsing parameters become increasingly difficult to control as the power of the equipment used increases. The majority of electropulsing experiments described in this thesis were conducted on a smaller unit specifically so that the pulsing parameters could be closely controlled. However, the equipment used for the results presented in this chapter was extremely powerful and as a result the repeatability of the results may be limited. The dependence of electropulsing treatment on current density is a limiting factor that may prove difficult if not impossible to overcome, in terms of scalability and power requirements.

6.4. Summary

Application of a single high current density electropulse to two 0.92wt%C pearlitic steel samples successfully produced microstructure change. At current density of 4.7×10^9 A·m^{-2} regions of spheroidised cementite and recrystallised α-ferrite were observed, while at 5.1×10^9 A·m^{-2} a complete martensitic transformation occurred. The Joule heating equation was used to estimate the heating

effect associated with the treatments, and the temperature increase was found to be significantly lower than that normally required to achieve the described transformations. The test duration was also much shorter than standard treatments, although other rapid heating techniques in the literature are reported to produce similar annealing behaviours albeit at higher temperatures. Current density was found to be the key driving force for the transformations, as no microstructure change was observed in samples treated at lower current densities but otherwise identical parameters. The underlying mechanism for the low temperature transformations cannot be clearly identified from the results. High rate heating is likely the dominant factor but diffusion-enhancing athermal effects cannot be ruled out.

7. Conclusion

In this thesis, the effect of the application of pulsed electric current to heavily cold-worked pearlitic steel rod and plate has been examined, with an emphasis on the microstructures and associated hardness obtained. The electropulsing treatments were typically of pulse frequency between 1 and 100Hz, with a pulse duration of 80 to 160µs and a current density between 10^7 and 10^9 $A{\cdot}m^{-2}$. The applied predeformation was approximately a 60% cross-sectional area reduction or greater.

In Chapter 4, electropulsing was examined in 0.92wt%C steel plate at ambient (room) temperature. It was found that a variety of microstructures can be obtained by electropulsing treatment. These have been rationalised in terms of the total energy deposited in the sample by electropulsing, based on the calculated theoretical resistive heating and the actual applied pulse time.

At low current densities ($J \sim 10^7$ $A{\cdot}m^{-2}$) and combinations of low pulse duration and low frequency, the microstructure was essentially unaltered. The lamellar cementite plates remained visible, and no spheroidisation, fragmentation or equiaxed ferrite were found. The mechanical and electrical properties were also unchanged, with hardness and resistivity values found to be comparable to the as-received cold-worked state.

At higher deposited energy levels (current densities of 10^8 to 10^9 $A{\cdot}m^{-2}$, with varying combinations of pulse frequency and duration) microstructure change was observed. The transformations generally correlated with the amount of applied Joule heating. At the highest resistive heating temperatures austenitisation occurred, resulting in martensitic transformation via rapid air cooling or grain boundary pro-eutectoid cementite formation. The exception was one of the most heavily heated samples, which evidently cooled slowly enough that a transformed pearlitic microstructure was obtained.

At lower resistive heating temperatures, spheroidisation of the cementite lamellae and some equiaxed ferrite were obtained. The cementite lamellae could be observed to partially globularise, with lengthscales as small as 100-200nm. The average diameter of the globular cementite was approximately similar to the original pearlite interlamellar spacing. Higher treatment times lead to larger spheroidised cementite as a result of grain growth. Submicron equiaxed α-ferrite was found to occur alongside cementite spheroidisation in some (but not all) cases.

It is therefore evident that electropulsing can result in varied microstructure change, albeit at very high current densities and heating rates in plate samples with substantial amounts of pre-treatment deformation.

In Chapter 5, elevated temperature electropulsing was examined in 0.73wt%C steel rod. This was achieved through simultaneous electropulsing and furnace treatment. The samples were externally heated to reduce the amount of driving force for transformation that must be supplied by electropulsing, in order to reveal whether any athermal effects were occurring as a result of the current.

In an alloy with a calculated eutectoid temperature of 714°C, furnace target temperatures of 600 to 740°C were applied. The samples used were cold-drawn wires in three conditions as supplied by the manufacturer. Annealing was followed by 1) still air cooling prior to drawing, 2) forced air cooling prior to drawing and 3) drawing, re-annealing and salt bath patenting. As received, the still and forced air cooled samples were lamellar while the salt bath patented samples were lamellar with some cementite fragmentation.

After simultaneous electropulsing and furnace treatment up to 720°C, the still and forced air cooled samples had recrystallised to a microstructure of coarse equiaxed ferrite and spheroidised pearlite. The salt bath patented samples were also spheroidised and recrystallised up to 700°C but with finer characteristics as a result of the initial fragmented microstructure. Above 720°C the still and forced air cooled samples had re-austenitised and reverted to unstrained lamellar pearlite. The same behaviour occurred in salt bath patented samples above 700°C. In each case, electropulsing had essentially no effect on the microstructures or hardness obtained when compared to control samples, despite extensive efforts in characterising the ferrite grain size distributions and interlamellar spacing.

In Chapter 6, 0.92wt%C plate samples treated at the Chinese Academy of Sciences (Hefei Institute of Physical Sciences) using a high powered electropulse generator were examined. Single pulse treatments were applied using this facility in order to minimise cumulative heating effects and assess the effectiveness of truly “short duration” electropulsing.

The most favourable recrystallised, “nanostructured” microstructure was obtained after single pulse treatment for 150µs with a current density of 4.7×10^{9} $A \cdot m^{-2}$. In this case, TEM characterisation found a recrystallised ferrite grain size on the order of 200nm. Atom probe tomography characterisation of the transformed microstructure was unremarkable, showing spheroidised cementite grains and

carbon segregation to a ferrite grain boundary. Segregation of vanadium to cementite, and phosphorus and sulphur to the grain boundaries could also be observed.

Assuming that typical cold-rolled sheet has a cross-sectional area of 1000mm x 1mm, applied currents of $1x10^4$ to $1x10^6$ A would be required to achieve current densities of 10^7 to 10^9 $A{\cdot}m^{-2}$ on a rolling mill. For comparison, the (continuous) current in modern Vacuum Arc Remelting (a process used to gradually melt a workpiece in order to control solidification) is less than $1x10^4$ A [215]. It would appear then that the required currents for industrial scale electropulsing might be attainable using capacitor discharge, if there were a strong motivation to do so.

The results in Chapters 4 and 6 therefore lead to the question of the microstructural transformation mechanism. According to the literature the effects observed could be due to an athermal electron wind and subsequent enhanced diffusion, or simply a consequence of resistive heating. In order to address this question samples of 0.92wt%C plate were examined using a Gleeble 3800 thermomechanical testing unit at a heating rate of approximately $7x10^3$ $°C{\cdot}s^{-1}$, compared to $1x10^6$ $°C{\cdot}s^{-1}$ as calculated for the highest current density recrystallising electropulsing treatment. The peak temperature in the Gleeble samples was also greater than that calculated for electropulsing. Nevertheless, similar recrystallised pearlite microstructures could be obtained that were essentially indistinguishable from those obtained by electropulsing.

Processes other than electropulsing or thermomechanical Gleeble treatments have been used to obtain similar microstructure configurations. Research by Raabe and co-workers on the atom probe tomography and micromechanical testing of cold-drawn pearlitic wire produced comparable microstructures [4, 40, 111], with very high strengths up to 7GPa being reported owing to the fine lengthscale of the process. ECAP has also been used to produce refined pearlite microstructure with submicron equiaxed α-ferrite [5], although the strengths obtained were less than those reported by Raabe and co-workers due to the inherent differences in the processing methods.

It therefore seems clear that electropulsing is essentially a clean, current-based flash annealing process similar to techniques such as induction annealing. No clear evidence for athermal effects (i.e. effects not attributable to Joule heating) was obtained based on the microstructures or mechanical properties produced. Similarly, simple energy deposition calculations did not reveal any variation that could have resulted from anything other than resistive heating when compared to the distribution of microstructures with treatment parameters, although athermal effects have not been completely ruled out. A rapid post-cold deformation flash annealing process might be attractive for the production of ductile, ultra-fine grained α-ferrite and cementite microstructures. However, the

electropulsing treatment does not offer any real advantage over similar flash annealing processes. The microstructures obtained were not found to be harder than cold-worked pearlite, but might allow for some ductility recovery and improved workability.

8. Further work

The work detailed in this thesis gives a comprehensive view of the application of electropulsing to pearlitic steel across a range of treatment parameters. The data was used to give an overview of the treatment envelope at ambient temperature, across which electropulse-induced microstructure change was indicated. However, the experiments described herein were not capable of identifying the existence of any individual effects of the thermal and athermal components of the current.

The Joule heating effect is generally unavoidable during ambient temperature electropulsing treatments at higher frequencies and pulse durations. As a result, it is difficult to distinguish the effects of heat from any other athermal effect, should microstructure or mechanical property changes occur. To fully assess the individual influence of potential athermal effects, and to understand the relationship (if any) between the thermal and electron wind components, it is necessary to have control over the Joule heating effect. A possible solution and area for further research lies in developing a repeatable method to tailor the thermal effect. This could be achieved using a cooling medium such as liquid nitrogen.

By immersing the sample in such a liquid, the thermal effect generated by the current could be reduced or removed. Furthermore, a sample of sufficient length could be placed in liquid nitrogen in such a way as to produce a thermal gradient, offering a range of treatment temperatures in a single sample. A method to record an accurate thermal profile during an experiment of this type should be considered. The addition of an electropulsing unit capable of consistently generating applied currents to achieve current densities of 2 – 9 $A \cdot m^{-2}$ would also offer a higher margin of control in terms of the applied treatment parameters. Furthermore, it would remove the requirement for very small samples to be produced, reducing the machining time needed to prepare samples for electropulsing.

The mechanical properties of electropulsed samples were characterised based on Vickers's hardness testing. However, it may also be beneficial to conduct tensile testing on certain samples. In particular, samples treated at lower frequencies and pulse durations (i.e. where the resistive heating effect is minimised) might be tested. A further mechanical property test could be capable of discerning more subtle microstructure change (such as structural relaxation) and may identify any advantageous ductility-strength trade-off compared to the as-received material. Tensile testing was not conducted during this project due to sample size requirements.

9. References

[1] H. Conrad, N. Karam, and S. Mannan, "Effect of prior cold work on the influence of electric current pulses on the recrystallization of copper," *Scripta Metallurgica,* vol. 18, no. 3, pp. 275-280, Mar, 1984.

[2] B. Ma *et al.*, "Formation of local nanocrystalline structure in a boron steel induced by electropulsing," *Journal of Alloys and Compounds,* vol. 549, no. 5, pp. 77-81, Feb, 2013.

[3] G. Q. Teng *et al.*, "Rapid nanocrystallization from amorphous Fe78 B13 SI9 by high-current density electropulsing," *Journal of Materials Science Letters,* vol. 14, no. 2, pp. 144-145, Jan, 1995.

[4] Y. J. Li *et al.*, "Evolution of strength and microstructure during annealing of heavily cold-drawn 6.3 GPa hypereutectoid pearlitic steel wire," *Acta Materialia,* vol. 60, no. 9, pp. 4005-4016, May, 2012.

[5] T. T. He *et al.*, "Microstructure of ultra-fine-grained high carbon steel prepared by equal channel angular pressing," *Materials Science and Engineering a-Structural Materials Properties Microstructure and Processing,* vol. 535, pp. 306-310, Feb, 2012.

[6] R. S. Qin, E. I. Samuel, and A. Bhowmik, "Electropulse-induced cementite nanoparticle formation in deformed pearlitic steels," *Journal of Materials Science,* vol. 46, no. 9, pp. 2838-2842, May, 2011.

[7] E. I. Samuel, A. Bhowmik, and R. S. Qin, "Accelerated spheroidization induced by high intensity electric pulse in a severely deformed eutectoid steel," *Journal of Materials Research,* vol. 25, no. 6, pp. 1020-1024, Jun, 2010.

[8] L. Pan, W. He, and B. Gu, "Effects of electric current pulses on mechanical properties and microstructures of as-quenched medium carbon steel," *Materials Science and Engineering: A,* vol. 662, pp. 404-411, Apr, 2016.

[9] Z. H. Lai *et al.*, "Hyperfine-structure changes in iron-base amorphous-alloys produced by high-current density electropulsing," *Journal of Materials Research,* vol. 10, no. 4, pp. 900-906, Apr, 1995.

[10] G. L. Hu *et al.*, "Effect of Electropulsing on Recrystallization and Mechanical Properties of Silicon Steel Strips," *Journal of Materials Science & Technology,* vol. 27, no. 11, pp. 1034-1038, Nov, 2011.

[11] A. F. Sprecher, S. L. Mannan, and H. Conrad, "Overview no. 49: On the mechanisms for the electroplastic effect in metals," *Acta Metallurgica,* vol. 34, no. 7, pp. 1145-1162, Jul, 1986.

[12] Y. B. Jiang *et al.*, "Influence of electropulsing treatment on microstructure and mechanical properties of cold-rolled Mg-9Al-1Zn alloy strip," *Materials Science and Engineering a-Structural Materials Properties Microstructure and Processing,* vol. 528, no. 16-17, pp. 5627-5635, Jun, 2011.

[13] A. Rahnama, and R. S. Qin, "Electropulse-induced microstructural evolution in a ferritic–pearlitic 0.14% C steel," *Scripta Materialia,* vol. 96, pp. 17-20, Feb, 2015.

[14] Y. Tang *et al.*, "Effect of High-Density Electric Current on the Microstructure and Fatigue Crack Initiation of Stainless Steel," *Materials Transactions,* vol. 54, no. 11, pp. 2085-2092, 2013.

[15] Y. Z. Zhou *et al.*, "Grain refinement and formation of ultrafine-grained microstructure in a low-carbon steel under electropulsing," *Journal of Materials Research,* vol. 17, no. 8, pp. 2105-2111, Aug, 2002.

[16] X. Ye *et al.*, "Influence of electropulsing globularization on the microstructure and mechanical properties of Ti–6Al–4V alloy strip with lamellar microstructure," *Materials Science and Engineering-a,* vol. 622, pp. 1-6, Jan, 2015.
[17] Z. H. Lai *et al.*, "Nanocrystallization of amorphous Fe-Si-B alloys using high current density electropulsing," *Materials Science and Engineering a-Structural Materials Properties Microstructure and Processing,* vol. 287, no. 2, pp. 238-247, Aug, 2000.
[18] H. Conrad, N. Karam, and S. Mannan, "Effect of electric current pulses on the recrystallization of copper," *Scripta Metallurgica,* vol. 17, no. 3, pp. 411-416, Mar, 1983.
[19] H. Conrad *et al.*, "Effect of electric current pulses on the recrystallization kinetics of copper," *Scripta Metallurgica,* vol. 22, no. 2, pp. 235-238, Jan, 1988.
[20] Y. Z. Zhou *et al.*, "Diffusive phase transformation in a Cu-Zn alloy under rapid heating by electropulsing," *Philosophical Magazine Letters,* vol. 84, no. 5, pp. 341-348, May, 2004.
[21] X. F. Zhang, W. J. Lu, and R. S. Qin, "Removal of MnS inclusions in molten steel using electropulsing," *Scripta Materialia,* vol. 69, no. 6, pp. 453-456, Sep, 2013.
[22] Y. Z. Zhou *et al.*, "Reversing effect of electropulsing on damage of 1045 steel," *Journal of Materials Research,* vol. 15, no. 5, pp. 1056-1061, May, 2000.
[23] H. Song, Z. J. Wang, and T. J. Gao, "Effect of high density electropulsing treatment on formability of TC4 titanium alloy sheet," *Transactions of Nonferrous Metals Society of China,* vol. 17, no. 1, pp. 87-92, Jan, 2007.
[24] H. Song, and Z. J. Wang, "Microcrack healing and local recrystallization in pre-deformed sheet by high density electropulsing," *Materials Science and Engineering a-Structural Materials Properties Microstructure and Processing,* vol. 490, no. 1-2, pp. 1-6, Aug, 2008.
[25] W. D. Callister, and D. G. Rethwisch, *Fundamentals of Materials Science and Engineering: An Integrated Approach*, 3rd ed., Hoboken, NJ: John Wiley & Sons, 2008.
[26] R. Z. Valiev, and T. G. Langdon, "Principles of equal-channel angular pressing as a processing tool for grain refinement," *Progress in Materials Science,* vol. 51, no. 7, pp. 881-981, Sep, 2006.
[27] Y. Xiong *et al.*, "Mechanical properties and fracture characteristics of high carbon steel after equal channel angular pressing," *Materials Science and Engineering-a,* vol. 563, no. 15, pp. 163-167, Feb, 2013.
[28] L. Guan *et al.*, "Texture evolution in cold-rolled AZ31 magnesium alloy during electropulsing treatment," *Journal of Alloys and Compounds,* vol. 487, no. 1-2, pp. 309-313, Nov, 2009.
[29] H. Gleiter, "Nanocrystalline materials," *Progress in Materials Science,* vol. 33, no. 4, pp. 223-315, 1989.
[30] R. A. Masumura, P. M. Hazzledine, and C. S. Pande, "Yield stress of fine grained materials," *Acta Materialia,* vol. 46, no. 13, pp. 4527-4534, 1998.
[31] C. S. Pande, R. A. Masumura, and R. W. Armstrong, "Pile-up based hall-petch relation for nanoscale materials," *Nanostructured Materials,* vol. 2, no. 3, pp. 323-331, 1993.
[32] S. Takaki, K. Kawasaki, and Y. Kimura, "Mechanical properties of ultra fine grained steels," *Journal of Materials Processing Technology,* vol. 117, no. 3, pp. 359-363, 2001.
[33] M. A. Meyers, A. Mishra, and D. J. Benson, "Mechanical properties of nanocrystalline materials," *Progress in Materials Science,* vol. 51, no. 4, pp. 427-556, 2006.
[34] Y. Fukuda *et al.*, "Processing of a low-carbon steel by equal-channel angular pressing," *Acta Materialia,* vol. 50, no. 6, pp. 1359-1368, 2002.
[35] J. C. Pang *et al.*, "Tensile and fatigue properties of ultrafine-grained low-carbon steel processed by equal channel angular pressing," *Materials Science and Engineering-a,* vol. 553, no. 15, pp. 157-163, Sep, 2012.
[36] N. Tsuji *et al.*, "Ultra-fine grained bulk steel produced by accumulative roll-bonding (ARB) process," *Scripta Materialia,* vol. 40, no. 7, pp. 795-800, Mar, 1999.
[37] N. Tsuji *et al.*, "Toughness of ultrafine grained ferritic steels fabricated by ARB and annealing process," *Materials Transactions,* vol. 45, no. 7, pp. 2272-2281, 2004.

[38] C. Borchers, and R. Kirchheim, "Cold-drawn pearlitic steel wires," *Progress in Materials Science,* vol. 82, pp. 405-444, Sep, 2016.
[39] K. Hono *et al.*, "Cementite decomposition in heavily drawn pearlite steel wire," *Scripta Materialia,* vol. 44, no. 6, pp. 977-983, 2001.
[40] Y. J. Li *et al.*, "Atom probe tomography characterization of heavily cold drawn pearlitic steel wire," *Ultramicroscopy,* vol. 111, no. 6, pp. 628-632, May, 2011.
[41] J. Languillaume, G. Kapelski, and B. Baudelet, "Evolution of the tensile strength in heavily cold drawn and annealed pearlitic steel wires," *Materials Letters,* vol. 33, no. 3, pp. 241-245, 1997.
[42] G. Krauss, *Steels: Processing, Structure, and Performance, Second Edition*: ASM International, 2015.
[43] O. A. Troitskii, "Electromechanical effect in metals," *ZhETF Pisma Redaktsiiu,* vol. 10, pp. 18, 1969.
[44] O. Troitskii, "Electroplastic Deformation of Metals," *Problemy Prochnosti*, no. 12, pp. 88-93, 1976.
[45] S. H. Xiao *et al.*, "Recrystallization in fatigued copper single crystals under electropulsing," *Scripta Materialia,* vol. 46, no. 1, pp. 1-6, Jan, 2002.
[46] G. L. Hu *et al.*, "Electropulsing Induced Texture Evolution in the Recrystallization of Fe-3 Pct Si Alloy Strip," *Metallurgical and Materials Transactions a-Physical Metallurgy and Materials Science,* vol. 42A, no. 11, pp. 3484-3490, Nov, 2011.
[47] H. Song, and Z. J. Wang, "Grain refinement by means of phase transformation and recrystallization induced by electropulsing," *Transactions of Nonferrous Metals Society of China,* vol. 21, pp. S353-S357, Aug, 2011.
[48] Z. Xu *et al.*, "The effect of multiple pulse treatment on the recrystallization behavior of Mg-3Al-1Zn alloy strip," *Applied Physics a-Materials Science & Processing,* vol. 88, no. 2, pp. 429-433, Aug, 2007.
[49] Q. Xu *et al.*, "Accumulation and annihilation effects of electropulsing on dynamic recrystallization in magnesium alloy," *Materials Science and Engineering a-Structural Materials Properties Microstructure and Processing,* vol. 528, no. 7-8, pp. 3249-3252, Mar, 2011.
[50] Y. B. Jiang *et al.*, "Microstructure and texture evolution of the cold-rolled AZ91 magnesium alloy strip under electropulsing treatment," *Journal of Alloys and Compounds,* vol. 509, no. 11, pp. 4308-4313, Mar, 2011.
[51] S. R. Qiao *et al.*, "Damage healing of aluminum alloys by D.C. electropulsing and evaluation by resistance," *Rare Metal Materials and Engineering,* vol. 38, no. 4, pp. 570-573, Apr, 2009.
[52] R. Takemoto, and H. Mizubayashi, "Effects of passing electric-current on structural relaxation, crystallization and elastic property an amorphous Cu50 Ti50," *Acta Metallurgica Et Materialia,* vol. 43, no. 4, pp. 1495-1504, Apr, 1995.
[53] J. P. Barnak, A. F. Sprecher, and H. Conrad, "Colony (grain) size reduction in eutectic Pb-Sn castings by electropulsing," *Scripta Metallurgica Et Materialia,* vol. 32, no. 6, pp. 879-884, Mar, 1995.
[54] H. Song, and Z. J. Wang, "Effect of electropulsing on dislocation mobility of titanium sheet," *Transactions of Nonferrous Metals Society of China,* vol. 22, no. 7, pp. 1599-1605, Jul, 2012.
[55] H. Song, and Z. J. Wang, "Improvement of mechanical properties of cold-rolled commercially pure Ti sheet by high density electropulsing," *Transactions of Nonferrous Metals Society of China,* vol. 22, no. 6, pp. 1350-1355, Jun, 2012.
[56] Z. H. Lai *et al.*, "Effect of electropulsing on the microstructure and properties of iron-based amorphous alloys," *Scripta Metallurgica,* vol. 23, no. 3, pp. 305-310, Mar, 1989.
[57] Z. S. Xu, Z. H. Lai, and Y. X. Chen, "Effect of electric current on the recrystallization behavior of cold worked α - Ti," *Scripta Metallurgica,* vol. 22, no. 2, pp. 187-190, Jan, 1988.

[58] Y. Z. Zhou, S. H. Xiao, and J. D. Guo, "Recrystallized microstructure in cold worked brass produced by electropulsing treatment," *Materials Letters,* vol. 58, no. 12-13, pp. 1948-1951, May, 2004.
[59] R. S. Qin, and S. X. Su, "Thermodynamics of crack healing under electropulsing," *Journal of Materials Research,* vol. 17, no. 8, pp. 2048-2052, Aug, 2002.
[60] Y. Z. Zhou *et al.*, "The healing of quenched crack in 1045 steel under electropulsing," *Journal of Materials Research,* vol. 16, no. 1, pp. 17-19, Jan, 2001.
[61] Y. Z. Zhou *et al.*, "Crack healing in a steel by using electropulsing technique," *Materials Letters,* vol. 58, no. 11, pp. 1732-1736, Apr, 2004.
[62] H. Conrad *et al.*, "Effect of electric-current pulses on fatigue characteristics of polycrystalline copper," *Materials Science and Engineering a-Structural Materials Properties Microstructure and Processing,* vol. 145, no. 1, pp. 1-12, Sep, 1991.
[63] Y. Ivanov *et al.*, "Evolution of Al–19· 4Si alloy surface structure after electron beam treatment and high cycle fatigue," *Materials Science and Technology,* vol. 31, no. 13, pp. 1523-1529, 2015.
[64] X. Ye *et al.*, "Enhanced grain refinement and microhardness of Ti–Al–V alloy by electropulsing ultrasonic shock," *Journal of Alloys and Compounds,* vol. 621, pp. 66-70, 2015.
[65] R. S. Qin, "Critical assessment 8: outstanding issues in electropulsing processing," *Materials Science and Technology,* vol. 31, no. 2, pp. 203-206, 2015.
[66] W. Zhang *et al.*, "Martensitic transformation from alpha-Ti to beta-Ti on rapid heating," *Applied Physics Letters,* vol. 84, no. 24, pp. 4872-4874, Jun, 2004.
[67] T. Hao, H. Tanimoto, and H. Mizubayashi, "Transformation to nanocrystallites in amorphous alloys induced by resonant electropulsing," *Materials Transactions,* vol. 46, no. 12, pp. 2898-2907, Dec, 2005.
[68] H. Mizubayashi, T. Hao, and H. Tanimoto, "Low temperature crystallization of amorphous alloys under electropulsing," *Journal of Non-Crystalline Solids,* vol. 312-14, pp. 581-584, 2002.
[69] H. Conrad, "Electroplasticity in metals and ceramics," *Materials Science and Engineering a-Structural Materials Properties Microstructure and Processing,* vol. 287, no. 2, pp. 276-287, Aug, 2000.
[70] I. S. Valeev, and Z. G. Kamalov, "Structure evolution in copper resulting from the effect of powerful current pulses," *Journal of Materials Engineering and Performance,* vol. 12, no. 3, pp. 272-278, Jun, 2003.
[71] D. Zhang *et al.*, "Dynamic electropulsing induced phase transformations and their effects on single point diamond turning of AZ91 alloy," *Journal of Surface Engineered Materials and Advanced Technology,* vol. 2, no. 1, pp. 16-21, 2012.
[72] S. To *et al.*, "Dynamic electropulsing induced phase transformations in a furnace cooled Zn-Al based alloy (ZA22)," *Materials Transactions,* vol. 51, no. 11, pp. 1997-2004, Nov, 2010.
[73] Z. C. Cordero, B. E. Knight, and C. A. Schuh, "Six decades of the Hall–Petch effect – a survey of grain-size strengthening studies on pure metals," *International Materials Reviews,* vol. 61, no. 8, pp. 495-512, Nov, 2016.
[74] R. Song *et al.*, "Overview of processing, microstructure and mechanical properties of ultrafine grained bcc steels," *Materials Science and Engineering: A,* vol. 441, no. 1–2, pp. 1-17, 2006.
[75] Z. Horita *et al.*, "Equal-channel angular pressing of commercial aluminum alloys: Grain refinement, thermal stability and tensile properties," *Metallurgical and Materials Transactions A,* vol. 31, no. 3, pp. 691-701, 2000.
[76] C. E. Carlton, and P. J. Ferreira, "What is behind the inverse Hall–Petch effect in nanocrystalline materials?," *Acta Materialia,* vol. 55, no. 11, pp. 3749-3756, 2007.
[77] A. S. Argon, and S. Yip, "The strongest size," *Philosophical Magazine Letters,* vol. 86, no. 11, pp. 713-720, Nov, 2006.

[78] D. J. Dunstan, and A. J. Bushby, “Grain size dependence of the strength of metals: The Hall–Petch effect does not scale as the inverse square root of grain size,” *International Journal of Plasticity,* vol. 53, pp. 56-65, 2014.
[79] Y. Li, A. J. Bushby, and D. J. Dunstan, “The Hall–Petch effect as a manifestation of the general size effect,” *Proceedings of the Royal Society A,* vol. 472, 2016.
[80] S. Divinski *et al.*, "Chapter 1 - Functional Nanostructured Materials – Microstructure, Thermodynamic Stability and Atomic Mobility," *Frontiers of Nanoscience*, pp. 1-50: Elsevier, 2009.
[81] D. H. Shin *et al.*, “Effect of pressing temperature on microstructure and tensile behavior of low carbon steels processed by equal channel angular pressing,” *Materials Science and Engineering-a,* vol. 323, no. 1–2, pp. 409-415, 2002.
[82] A. Yamashita *et al.*, “Influence of pressing temperature on microstructural development in equal-channel angular pressing,” *Materials Science and Engineering-a,* vol. 287, no. 1, pp. 100-106, 2000.
[83] W. H. Huang *et al.*, “The effect of strain path and temperature on the microstructure developed in copper processed by ECAE,” *Materials Science and Engineering-a,* vol. 366, no. 2, pp. 221-228, 2004.
[84] R. Z. Valiev, A. P. Zhilyaev, and T. G. Langdon, *Bulk Nanostructured Materials: Fundamentals and Applications*: Wiley, 2013.
[85] V. M. Segal, “Engineering and commercialization of equal channel angular extrusion (ECAE),” *Materials Science and Engineering-a,* vol. 386, no. 1–2, pp. 269-276, Nov, 2004.
[86] G. Yang *et al.*, “Enhancement of mechanical properties of heat-resistant martensitic steel processed by equal channel angular pressing,” *Materials Science and Engineering-a,* vol. 515, no. 1–2, pp. 199-206, 2009.
[87] R. G. Narayanan, and U. S. Dixit, *Advances in Material Forming and Joining: 5th International and 26th All India Manufacturing Technology, Design and Research Conference, AIMTDR 2014*: Springer India, 2015.
[88] J. Lemus-Ruiz *et al.*, “Production, characterization, and mechanical evaluation of dissimilar metal/ceramic joints,” *Nanocomposites with Unique Properties and Applications in Medicine and Industry. InTech, Croatia*, pp. 205-224, 2011.
[89] L. Li, K. Nagai, and F. Yin, “Progress in cold roll bonding of metals,” *Science and Technology of Advanced Materials,* vol. 9, no. 2, pp. 023001, Apr, 2008.
[90] G. P. Dinda, H. Rösner, and G. Wilde, “Synthesis of bulk nanostructured Ni, Ti and Zr by repeated cold-rolling,” *Scripta Materialia,* vol. 52, no. 7, pp. 577-582, 2005.
[91] N. Tsuji *et al.*, “ARB (Accumulative Roll-Bonding) and other new Techniques to Produce Bulk Ultrafine Grained Materials,” *Advanced Engineering Materials,* vol. 5, no. 5, pp. 338-344, 2003.
[92] Y. Saito *et al.*, “Novel ultra-high straining process for bulk materials—development of the accumulative roll-bonding (ARB) process,” *Acta Materialia,* vol. 47, no. 2, pp. 579-583, 1999.
[93] R. M. Brick, “Hot roll bonding of steel,” *Welding Journal,* vol. 49, no. 9, pp. S440, 1970.
[94] Z. Dhib *et al.*, “Cladding of low-carbon steel to austenitic stainless steel by hot-roll bonding: Microstructure and mechanical properties before and after welding,” *Materials Science and Engineering-a,* vol. 656, pp. 130-141, Feb, 2016.
[95] D. Terada, S. Inoue, and N. Tsuji, “Microstructure and mechanical properties of commercial purity titanium severely deformed by ARB process,” *Journal of Materials Science,* vol. 42, no. 5, pp. 1673-1681, 2007.
[96] S. Ohsaki *et al.*, “Bulk mechanical alloying of Cu–Ag and Cu/Zr two-phase microstructures by accumulative roll-bonding process,” *Acta Materialia,* vol. 55, no. 8, pp. 2885-2895, 2007.
[97] N. Tsuji *et al.*, “Strength and ductility of ultrafine grained aluminum and iron produced by ARB and annealing,” *Scripta Materialia,* vol. 47, no. 12, pp. 893-899, 2002.

[98] N. Kamikawa, N. Tsuji, and Y. Minamino, “Microstructure and texture through thickness of ultralow carbon IF steel sheet severely deformed by accumulative roll-bonding,” *Science and Technology of Advanced Materials,* vol. 5, no. 1, pp. 163-172, 2004.

[99] A. L. d. M. Costa *et al.*, “Ultra grain refinement and hardening of IF-steel during accumulative roll-bonding,” *Materials Science and Engineering-a,* vol. 406, no. 1, pp. 279-285, 2005.

[100] G. Krallics, and J. G. Lenard, “An examination of the accumulative roll-bonding process,” *Journal of Materials Processing Technology,* vol. 152, no. 2, pp. 154-161, 2004.

[101] T. Tarui *et al.*, “High strength galvanized steel wire for bridge cables,” *Structural Engineering International,* vol. 12, no. 3, pp. 209-213, 2002.

[102] L. Li, and J. Virta, “Ultrahigh strength steel wires processed by severe plastic deformation for ultrafine grained microstructure,” *Materials Science and Technology,* vol. 27, no. 5, pp. 845-862, 2011.

[103] J. Toribio *et al.*, “Role of drawing-induced residual stresses and strains in the hydrogen embrittlement susceptibility of prestressing steels,” *Corrosion Science,* vol. 53, no. 10, pp. 3346-3355, 10, 2011.

[104] A. R. Marder, and B. L. Bramfitt, “The effect of morphology on the strength of pearlite,” *Metallurgical Transactions A,* vol. 7, no. 3, pp. 365-372, Mar, 1976.

[105] J. M. Hyzak, and I. M. Bernstein, “The role of microstructure on the strength and toughness of fully pearlitic steels,” *Metallurgical Transactions A,* vol. 7, no. 8, pp. 1217-1224, 1976.

[106] J. Toribio, and E. Ovejero, “Effect of cumulative cold drawing on the pearlite interlamellar spacing in eutectoid steel,” *Scripta Materialia,* vol. 39, no. 3, pp. 323-328, Mar, 1998.

[107] J. D. Embury, and R. M. Fisher, “The structure and properties of drawn pearlite,” *Acta Metallurgica,* vol. 14, no. 2, pp. 147-159, 1966.

[108] M. Zelin, “Microstructure evolution in pearlitic steels during wire drawing,” *Acta Materialia,* vol. 50, no. 17, pp. 4431-4447, Sep, 2002.

[109] Y. J. Li *et al.*, “Atomic-scale mechanisms of deformation-induced cementite decomposition in pearlite,” *Acta Materialia,* vol. 59, no. 10, pp. 3965-3977, Jun, 2011.

[110] V. G. Gavriljuk, “Decomposition of cementite in pearlitic steel due to plastic deformation,” *Materials Science and Engineering-a,* vol. 345, no. 1–2, pp. 81-89, Mar, 2003.

[111] Y. Li *et al.*, “Segregation stabilizes nanocrystalline bulk steel with near theoretical strength,” *Physical Review Letters,* vol. 113, no. 10, pp. 106104 1-5, 2014.

[112] J. Languillaume, G. Kapelski, and B. Baudelet, “Cementite dissolution in heavily cold drawn pearlitic steel wires,” *Acta Materialia,* vol. 45, no. 3, pp. 1201-1212, Mar, 1997.

[113] R. Sandström, “On recovery of dislocations in subgrains and subgrain coalescence,” *Acta Metallurgica,* vol. 25, no. 8, pp. 897-904, Aug, 1977.

[114] H. Conrad, “Effects of electric current on solid state phase transformations in metals,” *Materials Science and Engineering a-Structural Materials Properties Microstructure and Processing,* vol. 287, no. 2, pp. 227-237, Aug, 2000.

[115] K. Okazaki, M. Kagawa, and H. Conrad, “An evaluation of the contributions of skin, pinch and heating effects to the electroplastic effect in titanium,” *Materials Science and Engineering,* vol. 45, no. 2, pp. 109-116, Sep, 1980.

[116] Y. S. Chao *et al.*, “Microstructural relaxation of amorphous alloy Fe79 Si7 B14 during electropulsing,” *Materials Science and Engineering a-Structural Materials Properties Microstructure and Processing,* vol. 182, pp. 982-985, May, 1994.

[117] W. Zhang *et al.*, “Formation of nanoscale α-Al in a superdralumin under high current density electropulsing,” *Journal of Materials Science Letters,* vol. 21, no. 24, pp. 1923-1925, 2002.

[118] Y. H. Zhu *et al.*, “Effects of dynamic electropulsing on microstructure and elongation of a Zn-Al alloy,” *Materials Science and Engineering a-Structural Materials Properties Microstructure and Processing,* vol. 501, no. 1-2, pp. 125-132, Feb, 2009.

[119] Q. Xu *et al.*, “Improved plasticity of Mg-Al-Zn alloy by electropulsing tension,” *Materials Letters,* vol. 64, no. 9, pp. 1085-1087, May, 2010.

[120] Y. H. Zhu *et al.*, "Effect of Static Electropulsing on Microstructure and Elongation of a Zn-Al Alloy (ZA22)," *Metallurgical and Materials Transactions a-Physical Metallurgy and Materials Science,* vol. 42A, no. 7, pp. 1933-1940, Jul, 2011.
[121] D. Zhang *et al.*, "Static Electropulsing-Induced Microstructural Changes and Their Effect on the Ultra-Precision Machining of Cold-Rolled AZ91 Alloy," *Metallurgical and Materials Transactions a-Physical Metallurgy and Materials Science,* vol. 43A, no. 4, pp. 1341-1346, Apr, 2012.
[122] V. B. Fiks, "On the mechanism of the mobility of ions in metals," *Soviet Physics-Solid State,* vol. 1, no. 1, pp. 14-28, 1959.
[123] H. Ceric, and S. Selberherr, "Electromigration in submicron interconnect features of integrated circuits," *Materials Science and Engineering: R: Reports,* vol. 71, no. 5, pp. 53-86, 2011.
[124] H. B. Huntington, and A. R. Grone, "Current-induced marker motion in gold wires," *Journal of Physics and Chemistry of Solids,* vol. 20, no. 1, pp. 76-87, Jan, 1961.
[125] A. S. Nowick, *Diffusion in Solids: Recent Developments*: Elsevier Science, 2012.
[126] R. J. Gleixner, and W. D. Nix, "A physically based model of electromigration and stress-induced void formation in microelectronic interconnects," *Journal of applied physics,* vol. 86, no. 4, pp. 1932-1944, 1999.
[127] J. R. Black, "Electromigration failure modes in aluminum metallization for semiconductor devices," *Proceedings of the IEEE,* vol. 57, no. 9, pp. 1587-1594, 1969.
[128] L. Zhang *et al.*, "Effect of current crowding on void propagation at the interface between intermetallic compound and solder in flip chip solder joints," *Applied physics letters,* vol. 88, no. 1, pp. 012106, 2006.
[129] H. Conrad, "Some effects of an electric field on the plastic deformation of metals and ceramics," *Materials Research Innovations,* vol. 2, no. 1, pp. 1-8, May, 1998.
[130] H. Conrad, Z. Guo, and A. F. Sprecher, "Effects of electropulse duration and frequency on grain-growth in Cu," *Scripta Metallurgica Et Materialia,* vol. 24, no. 2, pp. 359-362, Feb, 1990.
[131] J. M. Wallbridge, and J. G. Parr, "Effect of Rapid Heat Treating on Mechanical Properties of Low-Carbon Steel Sheet," *Journal of the Iron and Steel Institute,* vol. 205, pp. 750-755, 1967.
[132] Y. Z. Zhou *et al.*, "Ultrafine-grained microstructure in a Cu-Zn alloy produced by electropulsing treatment," *Journal of Materials Research,* vol. 18, no. 8, pp. 1991-1997, Aug, 2003.
[133] Y. Z. Zhou *et al.*, "Influence of electropulsing on nucleation during phase transformation," *Journal of Materials Research,* vol. 17, no. 12, pp. 3012-3014, Dec, 2002.
[134] Y. Z. Zhou *et al.*, "Formation of a nanostructure in a low-carbon steel under high current density electropulsing," *Journal of Materials Research,* vol. 17, no. 5, pp. 921-924, May, 2002.
[135] Z. H. Xu *et al.*, "Research on the engineering application of multiple pulses treatment for recrystallization of fine copper wire," *Materials Science and Engineering a-Structural Materials Properties Microstructure and Processing,* vol. 424, no. 1-2, pp. 300-306, May, 2006.
[136] Y. B. Jiang *et al.*, "Mechanism of electropulsing induced recrystallization in a cold-rolled Mg-9Al-1Zn alloy," *Journal of Alloys and Compounds,* vol. 536, pp. 94-105, Sep, 2012.
[137] H. M. Liao *et al.*, "Effect of thermo-electropulsing rolling on mechanical properties and microstructure of AZ31 magnesium alloy," *Materials Science and Engineering a-Structural Materials Properties Microstructure and Processing,* vol. 529, pp. 138-142, Nov, 2011.
[138] Z. J. Wang, and H. Song, "Effect of high-density electropulsing on microstructure and mechanical properties of cold-rolled TA15 titanium alloy sheet," *Journal of Alloys and Compounds,* vol. 470, no. 1-2, pp. 522-530, Feb, 2009.

[139] R. Honeycombe, *Steels: Microstructure and Properties*, 1st ed., Metals Park, Ohio: Edward Arnold (Publishers) Ltd. and the ASM, 1982.
[140] "Chapter 19 - Electrical properties," *Smithells Metals Reference Book (Seventh Edition)*, pp. 19-1-19-10, Oxford: Butterworth-Heinemann, 1992.
[141] M. Umemoto *et al.*, "Production of bulk cementite and its characterization," *Metallurgical and Materials Transactions A,* vol. 32, no. 8, pp. 2127-2131, 2001.
[142] D. A. Porter, K. E. Easterling, and M. Y. Sherif, *Phase Transformations in Metals and Alloys*, 3rd ed., Boca Raton, FL: CRC Press, 2009.
[143] X. Luo, and G. E. Totten, "Wire Cooling Curve Analysis, *Steel Heat Treating Technologies*," *ASM Handbook*, ASM International, 2013, pp. 310-314.
[144] A. Inoue, T. Ogura, and T. Masumoto, "Deformation and fracture behaviours of cementite," *Transactions of the Japan Institute of Metals,* vol. 17, no. 10, pp. 663-672, 1976.
[145] H. T. Angus, *Cast Iron: Physical and Engineering Properties*, 2 ed.: Elsevier Science, 2013.
[146] S. Tagashira *et al.*, "Deformation microstructure and tensile strength of cold rolled pearlitic steel sheets," *ISIJ International,* vol. 40, no. 11, pp. 1149-1156, 2000.
[147] G. Wei, W. Gao, and N. M. Sammes, *An Introduction to Electronic and Ionic Materials*: World Scientific, 1999.
[148] J. O. Linde, "The effect of cold-work on the electrical resistivity of alloys and the law of recovery," *Applied Scientific Research, Section B,* vol. 4, no. 1, pp. 73-86, 1955.
[149] G. F. Vander Voort, "Understanding and measuring decarburization," *Advanced Materials and Processes*, Feb, 2015.
[150] F. E. Purkert, "Prevention of decarburization in Annealing of high carbon steel," *Journal of Heat Treating,* vol. 2, no. 3, pp. 225-231, 1982.
[151] L. G. Gol'dshtein, B. Y. Lyubov, and L. A. Shvartsman, "Method for approximate calculation of surface decarburizing of steel," *Metal Science and Heat Treatment,* vol. 14, no. 7, pp. 578-580, 1972.
[152] "Instructions: Model AV-108F-3A-B-P," https://www.avtechpulse.com/manuals/AV-108F-3A-B-P,ed7.pdf.
[153] A. von Meier, "Electric Power Systems: A Conceptual Introduction," Wiley, 2006, p. 328.
[154] D. Ferguson *et al.*, "A look at physical simulation of metallurgical processes, past, present and future," *Materials Science and Engineering-a,* vol. 499, no. 1–2, pp. 329-332, 2009.
[155] B. L. Bramfitt, and S. J. Lawrence, "Metallography and Microstructures of Carbon and Low-Alloy Steels," *Metallography and Microstructures, ASM Handbook*, pp. 608-626: ASM International, 2014.
[156] "ASTM Standard E407, 2007e1, Practice for Microetching Metals and Alloys," ASTM International, 2007.
[157] P. Breton, "From microns to nanometers: early landmarks in the science of scanning electron microscope imaging," *Scanning Microscopy,* vol. 13, no. 1, pp. 1-6, 1999.
[158] D. G. Brandon, and W. D. Kaplan, *Microstructural characterization of materials*, 2nd ed., Chichester: John Wiley, 2008.
[159] A. Agarwal, *Nobel Prize Winners in Physics*: APH Publishing Corporation, 2008.
[160] D. B. Williams, and C. B. Carter, *Transmission Electron Microscopy: A Textbook for Materials Science*: Springer US, 2009.
[161] C. G. Herbert, and R. A. W. Johnstone, *Mass Spectrometry Basics*: CRC Press, 2002.
[162] "ASTM Standard E112, 2013, Standard Test Methods for Determining Average Grain Size," ASTM International, 2013.
[163] W. Weibull, "A statistical distribution function of wide applicability," *Journal of Applied Mechanics,* vol. 103, pp. 293-297, 1951.
[164] Z. Fang, B. R. Patterson, and M. E. Turner, "Modeling particle size distributions by the Weibull distribution function," *Materials Characterization,* vol. 31, no. 3, pp. 177-182, Oct, 1993.

[165] H. Rinne, *The Weibull Distribution: A Handbook*: CRC Press, 2008.
[166] G. H. Zhang, and M. Enomoto, “Interlamellar spacing of pearlite in a near-eutectoid Fe-C alloy measured by serial sectioning,” *ISIJ International,* vol. 49, no. 6, pp. 921-927, 2009.
[167] "ASTM Standard E384, 2011e1, Standard Test Method for Knoop and Vickers Hardness of Materials," ASTM International, 2011.
[168] "Seaward DO5000 Series datasheet," Apr, 2016; http://www.seaward.co.uk/downloads/do5000_series_datasheet_rev_2_v2.pdf.
[169] B. L. Bramfitt, "Structure/Property Relationships in Irons and Steels," *Metals Handbook Desk Edition*, pp. 153-173: ASM International, 1998.
[170] H. Okamoto, and M. Oka, “Lower bainite with midrib in hypereutectoid steels,” *Metallurgical Transactions A,* vol. 17, no. 7, pp. 1113-1120, 1986.
[171] H. K. D. H. Bhadeshia, *Bainite in Steels: Transformations, Microstructure and Properties*: IOM Communications, 2001.
[172] H. I. Aaronson, *Decomposition of Austenite by Diffusional Processes*, New York: Interscience, 1962.
[173] C. A. Dube, “Doctoral Thesis,” Carnegie-Mellon, Pittsburgh, PA, 1948.
[174] C. A. Dube, H. I. Aaronson, and R. F. Mehl, “La formation de la ferrite proeutectoide dans les aciers au carbone,” *Revue de Metallurgie,* vol. 55, no. 3, pp. 201-210, 1958.
[175] G. Spanos, and M. V. Kral, “The proeutectoid cementite transformation in steels,” *International Materials Reviews,* vol. 54, no. 1, pp. 19-47, Jan, 2009.
[176] R. P. Todorov, and K. G. Khristov, “Widmanstatten structure of carbon steels,” *Metal Science and Heat Treatment,* vol. 46, no. 1, pp. 49-53, 2004.
[177] G. Krauss, “Martensite in steel: strength and structure,” *Materials Science and Engineering-a,* vol. 273–275, pp. 40-57, Dec, 1999.
[178] G. Krauss, "Martensitic transformation, structure and properties in hardenable steels," *Hardenability Concepts with Applications to Steel*, D. V. Doane and J. S. Kirkaldy, eds., pp. 229-248: AIME, 1978.
[179] Y. Ohmori, and R. W. K. Honeycombe, “The isothermal transformation of plain carbon austenite,” *Proceedings of ICSTIS, Supplementary Transactions of ISIJ,* vol. 11, pp. 1160-1164, 1971.
[180] S. M. C. van Bohemen, M. J. Santofimia, and J. Sietsma, “Experimental evidence for bainite formation below Ms in Fe–0.66C,” *Scripta Materialia,* vol. 58, no. 6, pp. 488-491, Mar, 2008.
[181] M. X. Zhang, and P. M. Kelly, “Crystallography and morphology of Widmanstätten cementite in austenite,” *Acta Materialia,* vol. 46, no. 13, pp. 4617-4628, Aug, 1998.
[182] R. L. Bodnar, and S. S. Hansen, “Effects of Widmanstätten ferrite on the mechanical properties of a 0.2 pct C-0.7 pct Mn steel,” *Metallurgical and Materials Transactions A,* vol. 25, no. 4, pp. 763-773, 1994.
[183] B. A. Leont'ev, and Y. N. Buzovskii, “Mechanical properties of steel with a Widmanstatten structure,” *Metal Science and Heat Treatment,* vol. 10, no. 11, pp. 930-932, 1968.
[184] G. E. Totten, *Steel Heat Treatment: Metallurgy and Technologies*, 2nd ed., Boca Raton, Fla. ; London: CRC, 2007.
[185] D. D. Pollock, *Physical Properties of Materials for Engineers*: CRC press, 1993.
[186] J. R. Groza, and J. F. Shackelford, *Materials Processing Handbook*: CRC Press, 2007.
[187] K. E. Thelning, *Steel and its Heat Treatment*: Butterworths, 1984.
[188] L. Solymar, D. Walsh, and R. R. A. Syms, *Electrical Properties of Materials*: OUP Oxford, 2014.
[189] L. R. Jenkins, and R. D. Forrest, "Ductile Iron," *Properties and Selection: Irons, Steels, and High-Performance Alloys, ASM Handbook*, ASM International, 1990, pp. 33–55.
[190] C. P. Kothandaraman, *Fundamentals of Heat and Mass Transfer*: New Age International, 2006.
[191] S. Chattopadhyay, and C. M. Sellars, “Quantitative measurements of pearlite spheroidization,” *Metallography,* vol. 10, no. 1, pp. 89-105, Feb, 1977.

[192] G. Miyamoto *et al.*, "Effects of Mn, Si and Cr addition on reverse transformation at 1073 K from spheroidized cementite structure in Fe–0.6 mass% C alloy," *Acta Materialia,* vol. 58, no. 13, pp. 4492-4502, Aug, 2010.
[193] F. G. Caballero, C. Capdevila, and C. García de Andrés, "Influence of scale parameters of pearlite on the kinetics of anisothermal pearlite-to-austenite transformation in a eutectoid steel," *Scripta Materialia,* vol. 42, no. 12, pp. 1159-1165, Jun, 2000.
[194] Ö. E. Atasoy, and S. Özbilen, "Pearlite spheroidization," *Journal of Materials Science,* vol. 24, no. 1, pp. 281-287, 1989.
[195] M. M. Rathore, and R. Kapuno, *Engineering Heat Transfer*: Jones & Bartlett Learning, LLC, 2011.
[196] X. Ye *et al.*, "Effect of electropulsing treatment on microstructure and mechanical properties of cold-rolled pure titanium strips," *Journal of Materials Processing Technology,* vol. 222, pp. 27-32, Aug, 2015.
[197] V. Rudnev *et al.*, *Handbook of Induction Heating*: CRC Press, 2002.
[198] T. Fischer, *Materials Science for Engineering Students*: Elsevier Science, 2009.
[199] K. N. Tu, "Recent advances on electromigration in very-large-scale-integration of interconnects," *Journal of Applied Physics,* vol. 94, no. 9, pp. 5451-5473, 2003.
[200] P. S. Ho, and T. Kwok, "Electromigration in metals," *Reports on Progress in Physics,* vol. 52, no. 3, pp. 301, 1989.
[201] A. J. Sánchez Egea *et al.*, "Mechanical and metallurgical changes on 308L wires drawn by electropulses," *Materials & Design,* vol. 90, pp. 1159-1169, Jan, 2016.
[202] J. R. Davis, and A. S. M. I. H. Committee, *ASM Specialty Handbook: Tool Materials*: ASM International, 1995.
[203] Y. J. Li *et al.*, "Mechanisms of subgrain coarsening and its effect on the mechanical properties of carbon-supersaturated nanocrystalline hypereutectoid steel," *Acta Materialia,* vol. 84, pp. 110-123, Feb, 2015.
[204] M. Herbig *et al.*, "Atomic-scale quantification of grain boundary segregation in nanocrystalline material," *Physical Review Letters,* vol. 112, no. 12, pp. 126103, 2014.
[205] D. Raabe *et al.*, "Grain boundary segregation engineering in metallic alloys: A pathway to the design of interfaces," *Current Opinion in Solid State and Materials Science,* vol. 18, no. 4, pp. 253-261, Aug, 2014.
[206] M. P. Seah, "Grain boundary segregation," *Journal of Physics F: Metal Physics,* vol. 10, no. 6, pp. 1043, 1980.
[207] R. G. Faulkner, "Non-equilibrium grain-boundary segregation in austenitic alloys," *Journal of Materials Science,* vol. 16, no. 2, pp. 373-383, 1981.
[208] R. A. Grange, "The rapid heat treatment of steel," *Metallurgical Transactions,* vol. 2, no. 1, pp. 65-78, 1971.
[209] T. Lolla *et al.*, "Development of rapid heating and cooling (flash processing) process to produce advanced high strength steel microstructures," *Materials Science and Technology,* vol. 27, no. 5, pp. 863-875, May, 2011.
[210] D. Hauserova, J. Dlouhy, and Z. Novy, "Effect of heating rate on accelerated carbide spheroidisation (ASR) in 100CrMnSi6-4 bearing steel," *Archives of Metallurgy and Materials,* vol. 59, no. 3, pp. 1199-1203, 2014.
[211] H. L. Yi *et al.*, "Acceleration of spheroidization in eutectoid steels by the addition of aluminum," *Scripta Materialia,* vol. 67, no. 7–8, pp. 645-648, Oct, 2012.
[212] L. E. Samuels, *Light Microscopy of Carbon Steels*: ASM International, 1999.
[213] C. M. Branco, R. Ritchie, and V. Sklenicka, *Mechanical Behaviour of Materials at High Temperature*: Springer Netherlands, 1996.
[214] R. K. Rajput, *Power System Engineering*: Laxmi Publications Pvt Limited, 2006.

[215] R. L. Williamson *et al.*, “Modern control strategies for vacuum arc remelting of segregation sensitive alloys,” *Proceedings of the International Symposium on Superalloys,* vol. 718, pp. 625-706, 1997.
[216] J. E. J. Staggs, and H. N. Phylaktou, “The effects of emissivity on the performance of steel in furnace tests,” *Fire Safety Journal,* vol. 43, no. 1, pp. 1-10, 2008.
[217] "AISI 1080 steel, as rolled," MatWeb LLC, 2016.

10. Appendix A

Decarburisation of a pearlitic steel sample

Fick's second law of diffusion (Equation 10.1) can be simplified to Equation 10.2 if the diffusion coefficient is independent of composition.

$$\frac{\partial C}{\partial t} = \frac{\partial}{\partial x}\left(D\frac{\partial C}{\partial x}\right)$$

10.1

$$\frac{\partial C}{\partial t} = D\frac{\partial^2 C}{\partial x^2}$$

10.2

Defining the following boundary conditions allow a solution to the equation of the form shown in Equation 10.3 (restated from Methods, pp.60).

- The distribution of carbon in the matrix is uniform before diffusion begins, and has concentration C_o
- The depth x is determined to be zero at the surface of the material and increases as it approaches the centre of the sample
- At the moment before diffusion begins the time is defined as zero.

$$\frac{C_s - C_x}{C_s - C_o} = erf\left(\frac{x}{2\sqrt{Dt}}\right)$$

10.3

C_o: original carbon composition, 0.92wt%C

C_s: carbon composition at the sample surface after decarburisation in wt%C (taken as 20% of C_x [151])

C_x: carbon composition at a depth x inside the sample in wt%C

x: depth inside the sample, taken as half of the total sample thickness for this estimate, 0.5mm

D: diffusion coefficient of carbon in austenite, $2.3 \times 10^{-5} mm^2 \cdot s^{-1}$ [25]

t: treatment time in seconds, 7200s

Taking the error function component,

$$erf\left(\frac{x}{2\sqrt{Dt}}\right) = \text{erf}\left(\frac{0.5}{2\sqrt{(2.3\times10^{-5})\cdot 7200}}\right) = \text{erf}(0.6143) = 0.6150$$

Then rearranging Equation 10.3 in terms of C_x, if $C_s = 0.2C_x$:

$$\frac{0.2C_x - C_x}{0.2C_x - C_o} = 0.6150$$

$$C_x + 0.123C_x - 0.2C_x = 0.6150C_o$$

$$0.923C_x = 0.6150C_o$$

$$C_x = \frac{0.6150C_o}{0.923}$$

If the original carbon content of the steel was 0.92wt%C, then after two hours the carbon content is estimated to have reduced by decarburisation to 0.61wt%C in the middle of the workpiece.

11. Appendix B

Convection heating of high carbon steel

Heating of a sample inside a convection furnace can be estimated using the lumped parameter method shown in Equation 11.1 [190].

$$\frac{T - T_\infty}{T_o - T_\infty} = e^{\left(\frac{h}{\delta \cdot C_p} \times \frac{1}{L_c} \tau\right)}$$

11.1

T: target temperature of the sample (K), 1013K (740°C)

T_∞: temperature inside the furnace (K), 1013.1K (740.1°C)

T_O: ambient temperature of the sample before insertion into the furnace (K), 296K (23°C)

h: convection heat transfer coefficient ($W \cdot m^{-2} \cdot K^{-1}$), 21.1 $W \cdot m^{-2} \cdot K^{-1}$. Average based on values at ambient (12.3 $W \cdot m^{-2} \cdot K^{-1}$) and T_∞ = 840.8K (29.9 $W \cdot m^{-2} \cdot K^{-1}$) from [216].

δ: material density ($kg \cdot m^{-3}$), 7850 $kg \cdot m^{-3}$

C_p: specific heat capacity ($J \cdot kg^{-1} \cdot K^{-1}$), 490 $J \cdot kg^{-1} \cdot K^{-1}$

L_c: characteristic length (m), 7.0×10^{-5} m.

τ: time to reach T (s)

The characteristic length is a geometry descriptor and is defined in Equation 11.2.

$$L_c = \frac{V}{A_s} = \frac{L \times W \times D}{2 \times L \times D + 2 \times L \times W + 2 \times W \times D}$$

11.2

V: volume of the workpiece (m^3)

A_s: surface area of the workpiece (m^2)

L: sample length (m), 0.038m

W: sample width (m), 0.00065m

D: sample depth (m), 0.00018m

The sample dimensions applied in this calculation are taken from the average values calculated for samples electropulsed at current density of the order 10^9 A·m^{-2} in Chapter 6.

The method is valid when the Biot number (Equation 11.3) is less than 0.1.

$$Bi = \frac{L_c h}{k} \qquad 11.3$$

k: thermal conductivity (W·m^{-1}·K^{-1}), 47.7 W·m^{-1}·K^{-1}. Thermal conductivity of AISI 1080 steel, as rolled [217].

For the applied parameters the Biot number is equal to 3.1x10^{-5}, which allows the lumped parameter method to be used:

$$\frac{1013 - 1013.1}{296 - 1013.1} = e^{\left(\frac{21.1}{7850 \cdot 490} \times \frac{1}{7.0 \times 10^{-5}} \tau\right)}$$

The equation gives the time to reach 740°C from ambient temperature as 49 seconds.